Magnetotransport experiments in GaAs 2D holes and RF-QPC readout in a lateral quantum dot device

by

Nicholas Cockton

A thesis
presented to the University of Waterloo
in fulfillment of the
thesis requirement for the degree of
Doctor of Philosophy
in
Physics

Waterloo, Ontario, Canada, 2024

© Nicholas Cockton 2024

Examining Committee Membership

The following served on the Examining Committee for this thesis. The decision of the Examining Committee is by majority vote.

External Examiner:	Cagliyan Kurdak Professor, Dept. of Physics, University of Michigan
Supervisor:	Jan Kycia Professor, Dept. of Physics and Astronomy, University of Waterloo
Internal Member:	Robert Hill Professor, Dept. of Physics and Astronomy, University of Waterloo
Internal-External Member:	Jonathan Baugh Professor, Dept. of Chemistry, University of Waterloo
Other Member(s):	Sergei Studenikin Adjunct Professor, Dept. of Physics and Astronomy, University of Waterloo

Author's Declaration

This thesis consists of material all of which I authored or co-authored: see Statement of Contributions included in the thesis. This is a true copy of the thesis, including any required final revisions, as accepted by my examiners.

I understand that my thesis may be made electronically available to the public.

Statement of Contributions

The contents of this thesis are the author's individual work, but the studies presented are the outcome of collaboration with several groups.

Specifically, the devices under investigation were designed and fabricated by several different groups. The GaAs/AlGaAs heterostructures studied in Chapters 4, 5 were grown at the University of Waterloo by Prof. Zbig Wasilewski's group (led by Dr. Man Chun Alan Tam) and at Sandia National Labs with contributions from Dr. Lisa Tracy, Dr. John Reno, and Dr. Terry Hargett. The fabrication of these heterostructures into Hall bar devices was carried out at the University of Waterloo by Prof. Jonathan Baugh's group, with contributions from Dr. François Sfigakis, Dr. Arjun Shetty, Dr. Brandon Buonacorsi, and Stephen Harrigan. The quantum dot device studied in Chapter 6 was designed and fabricated at the National Research Council Canada (NRC). The SQUID amplifier studied in Chapter 6 was purchased from *ez-SQUID*, founded by Dr. Michael Mück.

All chapters of this thesis were written solely by the author. The experiments were designed and conducted by the author, with guidance from Dr. Jan Kycia. Dr. François Sfigakis contributed to the interpretation of the data and provided feedback on the results presented in Chapter 4. Dr. Guy Austing reviewed and provided feedback on the results presented in Chapter 5.

Abstract

This thesis presents a set of experiments conducted on GaAs/AlGaAs heterostructures fabricated into Hall bars and a lateral quantum dot device. The Hall bar experiments seek to further the understanding of the complexity of the GaAs valence band of a two-dimensional hole gas (2DHG). Meanwhile, the quantum dot experiments aim to improve the performance of an RF-QPC readout employed for charge detection. These experiments are significant for the development of future quantum technologies that utilize spins in semiconductors, in fields such as spintronics and quantum computing.

Firstly, we study Hall bar devices formed in a 2DHG of a dopant-free GaAs/AlGaAs heterostructure. The hole sheet density (p_{2d}) is adjustable via a metal top-gate that induces and confines holes to the GaAs/AlGaAs interface. We employ magnetotransport measurements to assess both the device quality and the underlying physics of the valence band. By measuring several devices, we identify fabrication parameters that lead to parasitic parallel conduction and gate hysteresis. In our devices, featuring an asymmetric quantum well hosting a 2DHG, Rashba spin-orbit interaction (SOI) leads to a beating pattern in the Shubnikov-de Haas (SdH) oscillations of the two subbands of the heavy-hole (HH) valence band. We employ Fourier analysis to isolate the frequencies present in the SdH oscillations. The effective masses of the two spin-orbit split HH subbands are extracted via the temperature dependence of the isolated oscillations, without invoking assumptions regarding the band structure. This analysis is performed for different values of p_{2d} and ranges of magnetic field. The HH splitting induced by Rashba SOI is evaluated and compared to modulation-doped samples in literature. Moreover, we extract the out-of-plane g factor from thermal-activation measurements in the quantum Hall regime.

Secondly, we investigate non-linear magnetotransport in a Hall bar device, also formed in a 2DHG of a dopant-free GaAs/AlGaAs heterostructure. We observe the SdH phase inversion phenomenon and explore the empirical relationship between the hole temperature and applied dc current through the Hall bar. In the quantum Hall regime, comprehensive maps of the differential resistance (ρ_{xx} and r_{xy}) as a function of current and magnetic field (B) are generated to show the evolution of quantum Hall breakdown reaching filling factor $\nu = 1$. By adjusting the top-gate voltage, the hole sheet density (p_{2d}) is incremented to

reveal how the quantum Hall breakdown characteristics evolve with p_{2d}. A Zener-type tunneling model is employed to describe the size of the transport diamonds in current. We examine the magnetic field dependence of the critical current compiled for different values of p_{2d}. The zero current anomaly (ZCA) phenomenon is observed and discussed. Hysteresis observed in the quantum Hall breakdown regime of a two-dimensional electron gas (2DEG) has been linked with dynamic nuclear polarization (DNP) through the interplay of electron and nuclear spins via the hyperfine interaction. Motivated by examining the strength of the hyperfine coupling between hole and nuclear spins, we investigate hysteresis near breakdown in our 2DHG.

Finally, we present measurements on a lateral double quantum dot (DQD) device formed in a 2DEG of a modulation-doped GaAs/AlGaAs heterostructure. These devices demonstrate potential as a platform for advancing quantum information technologies, particularly when employed as single spin qubits. The fast, single-shot readout of spin states is crucial, and using spin-to-charge conversion techniques, only the charge state readout becomes essential. Thus, we design and setup an optimized radio frequency quantum point contact (RF-QPC) charge sensor for the quantum dot device. Charge sensitivity measurements are conducted using a standard QPC sensor, followed by the RF-QPC. Additionally, we characterize a superconducting quantum interference device (SQUID) amplifier for integration into the RF-QPC readout. We successfully demonstrate a carrier nulling technique, specifically to accommodate the SQUID amplifier's limited dynamic range, and enable its integration into the RF-QPC readout. After Incorporating the SQUID amplifier into the RF-QPC readout, critical issues are identified and future work to address them is discussed.

Acknowledgements

First and foremost, I would like to thank my supervisor, Dr. Jan Kycia. Your guidance and support throughout my graduate career has been indispensable. Your passion for experimental physics makes the lab an enjoyable place to work, learn, and succeed. I am profoundly grateful for the privilege of learning under your mentorship.

Next I would like to thank my advisory committee members: Dr. Jonathan Baugh, Dr. Sergei Studenikin, and Dr. Robert Hill, for their valuable insights and contributions to my research. Additionally, I am grateful to Dr. Marek Korkusinki and Dr. Guy Austing from NRC for their continuous feedback and support. Special thanks to Dr. Zbig Wasilewski's group and Sandia National Labs for providing the GaAs wafers, and to Dr. Jonathan Baugh's group for fabricating them into Hall bars. Huge thanks to Dr. François Sfigakis for engaging in numerous conversations addressing the complexity of holes in GaAs.

I also need to thank the past and present members of the Kycia Group: Dr. Jeffrey Mason, Dr. David Pomaranski, Clifford Plesha, Tianze Zou, Taylor Fraser, Andree Coschizza, Cody Nademi, and Carolyn Chen. Your collective assistance, insights, and camaraderie have made the lab an enriching and enjoyable place to work.

Finally, I would like to express my gratitude to my family. To my parents, Cheryl and Lee, and my brother Ryan, as well as my future in-laws Robert and Kathryn, your unwavering love and support throughout my entire educational journey have been immeasurable. Most importantly, I need to thank my partner, Gillian. Your belief in me and your constant encouragement were my pillars of strength, lifting me up whenever I had doubts. I could not have achieved this without your unwavering love and support.

Dedication

To Gillian and my parents, Cheryl and Lee

Table of Contents

Examining Committee ii

Author's Declaration iii

Statement of Contributions iv

Abstract v

Acknowledgements vii

Dedication viii

List of Figures xiv

List of Tables xix

List of Abbreviations xx

1 Introduction 1

1.1 Outline 2

2 Background concepts **4**

2.1 Introduction . . . 4

2.2 Band structure of GaAs . . . 4

2.2.1 2D confinement . . . 5

2.2.2 Spin-orbit interaction (SOI) . . . 7

2.3 Magnetotransport of 2D systems . . . 9

2.3.1 Shubnikov-de Haas Oscillations . . . 9

2.3.2 Integer quantum Hall effect . . . 12

2.4 Quantum dots and 1D constrictions . . . 14

2.4.1 Coulomb blockade . . . 14

2.4.2 Conductance quantization in quantum point contact . . . 15

2.5 SQUIDs . . . 17

2.5.1 Josephson junctions . . . 17

2.5.2 DC SQUID . . . 20

2.5.3 SQUID amplifiers . . . 22

3 Experimental methods **25**

3.1 Introduction . . . 25

3.2 2D devices . . . 25

3.2.1 Heterojunctions and quantum wells . . . 25

3.2.2 Modulation-doped devices . . . 27

3.2.3 Dopant-free induced devices . . . 28

3.3 Cryostat and experiment components . . . 30

3.3.1 Dilution refrigerator . . . 30

3.3.2 Shasta cryostat . . . 31
3.3.3 Superconducting magnet . . . 33
3.3.4 Sample cell and electrical filtering . . . 33

4 Spin-orbit splitting in dopant-free GaAs/AlGaAs two-dimensional hole gases 36

4.1 Introduction . . . 36
4.2 Literature review . . . 38
4.2.1 Spin-orbit splitting in 2DHGs . . . 38
4.2.2 Effective masses in 2DHGs . . . 41
4.3 Experimental methods . . . 43
4.3.1 Measurement setup . . . 43
4.3.2 Wafers and sample fabrication . . . 44
4.3.3 2DHG density and gate hysteresis . . . 45
4.3.4 Shubnikov-de Haas oscillations . . . 48
4.3.5 Parallel conduction . . . 53
4.3.6 2DHG Mobility . . . 56
4.3.7 HH-/HH+ effective masses . . . 57
4.3.8 Spin-orbit splitting . . . 62
4.3.9 Landau fan diagrams . . . 65
4.3.10 Thermal activation measurements . . . 66
4.4 Conclusions and future work . . . 71

5 Quantum Hall breakdown and nonlinear phenomena in a dopant-free GaAs/AlGaAs two-dimensional hole gas 74

5.1 Introduction . . . 74

5.2 Literature review . . . 76
5.2.1 History of quantum Hall breakdown . . . 76
5.2.2 Mechanisms of breakdown . . . 82
5.2.3 Breakdown phase diagrams . . . 84
5.2.4 Hysteresis near breakdown . . . 89
5.3 Experimental methods . . . 94
5.3.1 Sample details . . . 94
5.3.2 AC+DC measurement setup . . . 95
5.3.3 SdH phase inversion . . . 96
5.3.4 Current-induced heating of 2DHG . . . 98
5.3.5 Breakdown at integer filling factors . . . 101
5.3.6 Progression of colormaps with hole density . . . 109
5.3.7 Magnetic field dependence of critical current . . . 115
5.3.8 Zero current anomaly . . . 117
5.3.9 Investigation of hysteresis near breakdown . . . 119
5.4 Conclusions and future work . . . 128

6 RF-QPC readout of lateral quantum dot device 131
6.1 Introduction . . . 131
6.2 Literature Review . . . 132
6.2.1 Lateral quantum dot devices . . . 132
6.2.2 QPC charge sensor . . . 134
6.2.3 RF-QPC charge sensor . . . 135
6.3 Experimental Methods . . . 141

6.3.1 Matching network design . . . 141
6.3.2 Matching network characterization . . . 143
6.3.3 Readout circuit . . . 146
6.3.4 Charge sensitivity measurements . . . 148
6.3.5 Microstrip SQUID amplifier . . . 157
6.3.6 Carrier nulling . . . 162
6.3.7 Integrating the MSA into RF-QPC readout . . . 168
6.4 Conclusions and future work . . . 174

7 Summary and future work **176**
7.1 Summary . . . 176
7.2 Future work . . . 178

References **180**

Appendices **201**

A Fourier analysis of the SdH oscillations **201**

B Extended data **204**
B.1 Effective mass analysis at other hole densities . . . 204
B.2 Activation energies at other hole densities . . . 206
B.3 Temperature dependence of the low B-field positive magnetoresistance . . . 207

C RF-QPC readout noise temperature and power dependence **208**
C.1 RF-QPC noise temperature . . . 208
C.2 RF-QPC power dependence . . . 211

List of Figures

2.1 Schematic representations of the band structure of GaAs 6
2.2 Hall bar geometry with typical magnetotransport measurement scheme . . 10
2.3 2D density of states in a small perpendicular magnetic field 11
2.4 2D density of states in a large perpendicular magnetic field 13
2.5 Schematic representations to explain the integer quantum Hall effect 13
2.6 Capacitive model of a single quantum dot 15
2.7 Conductance quantization in a quantum point contact 16
2.8 Schematic of a resistively-shunted Josephson junction 19
2.9 Schematic of a dc SQUID in the RCSJ model 21
2.10 Diagram of a typical SQUID amplifier 23

3.1 Modulation-doped example 27
3.2 Schematic of a HIGFET structure 29
3.3 Schematic of the modified Shasta 106 cryostat 32
3.4 Pictures of the cryostat and sample cell 34

4.1 SdH oscillations from Eisenstein *et al.* - square and triangular QW 39
4.2 SdH oscillations from Papadakis *et al.* - tuning the QW asymmetry 40

4.3 SdH oscillations from Habib *et al.* - 2DHG effective masses 42
4.4 Circuit schematic for magnetotransport measurements 44
4.5 Layer structure of the five GaAs/AlGaAs heterostructures characterized . . 45
4.6 Hole density as a function of top-gate voltage 47
4.7 SdH oscillations and Fourier transforms for samples G522 and G265 49
4.8 Fourier spectra for samples G265 and VB1137 51
4.9 SdH oscillations as a function of inverse magnetic field 52
4.10 Parallel conduction - lifting of the SdH minima at high B-field 54
4.11 Parallel conduction - Comparison between hole densities extracted from the Hall effect and the SdH oscillations 55
4.12 2DHG mobility for all samples 57
4.13 Temperature-dependence of the SdH oscillations - effective mass analysis . 59
4.14 Effective masses and quantum scattering times over different magnetic field ranges and hole densities 61
4.15 Rashba coefficient and HH splitting as a function of hole density 63
4.16 Comparison of the SO splitting as a function of hole density to samples in literature 64
4.17 Landau fan diagrams 66
4.18 Temperature-dependence of the SdH oscillations in the quantum Hall regime - thermal activation analysis 68
4.19 Values of the g factor extracted for even- and odd-filling factor data at five hole densities 71

5.1 First measurement of breakdown by Ebert *et al.* 77
5.2 Breakdown measurements from Kuchar *et al.* 78
5.3 Breakdown data from Jeckelmann *et al.* 79

5.4 Breakdown measurements from Ebert *et al.* 80
5.5 Breakdown measurements from Eaves *et al.* 81
5.6 Bootstrap electron heating model for breakdown 83
5.7 Grayscale maps of breakdown from Studenikin *et al.* 85
5.8 Colormap of breakdown from Yu *et al.* 87
5.9 Critical currents as a function of B-field from Yu *et al.* 89
5.10 Electrical polarization of nuclear spins near breakdown 92
5.11 Hysteretic behaviour near breakdown from Kawamura *et al.* 93
5.12 AC+DC circuit setup used for the nonlinear measurements 95
5.13 Low B-field colormap of ρ_{xx} 96
5.14 Current-induced heating of 2DHG 99
5.15 Magnetoresistance of the 2DHG measured in the linear response regime . . 102
5.16 Breakdown colormaps of the 2DHG at $p_{2d} = 2.0 \times 10^{15}$ m^{-2} and 50 mK . . 103
5.17 Colormap of ρ_{xx} with white lines intersecting the tips of the transport diamonds 106
5.18 ρ_{xx}-I and r_{xy}-I traces through $\nu = 1$ and $\nu = 2$ transport diamonds 109
5.19 Colormaps of ρ_{xx} measured at $T_0 = 50$ mK and collected at four hole densities 110
5.20 Vertical traces through the transport diamonds for $p_{2d} = 2.0 \times 10^{15}$ m^{-2} and $p_{2d} = 1.3 \times 10^{15}$ m^{-2} 113
5.21 Vertical traces through the transport diamonds for filling factors $\nu = 1, 2$. 114
5.22 Critical current as a function of magnetic field 116
5.23 Selected traces of the zero current anomaly 118
5.24 Colormaps of ρ_{xx} for analyzing hysteresis 120
5.25 Removal of trivial hysteresis 121

5.26 Corrected hysteresis colormaps . . . 123
5.27 Quantifying the observed hysteresis near the $\nu = 1$ transport diamond . . . 124
5.28 Hysteresis measured with the DC1 technique . . . 126
5.29 Hysteresis measured with the DC2 technique . . . 127

6.1 SEM image of the NRC DQD device . . . 133
6.2 Quantum point contact measurements using the DQD device . . . 134
6.3 LC matching network design . . . 136
6.4 Matching network characterization . . . 144
6.5 RF-QPC readout circuit configured on the dilution refrigerator . . . 147
6.6 Single and double quantum dot circuits . . . 149
6.7 DC-QPC readout configuration and DQD stability diagram . . . 150
6.8 DC-QPC readout charge sensitivity measurements . . . 152
6.9 RF-QPC readout charge sensitivity measurements . . . 155
6.10 Diagram and electrical schematic of the MSA . . . 158
6.11 MSA gain as a function of frequency . . . 159
6.12 Noise temperature characterization of the MSA . . . 160
6.13 MSA gain and noise temperature as a function of rf power . . . 162
6.14 Simulated amplitude modulation of a carrier signal . . . 163
6.15 RF circuit for the carrier nulling experiment configured on the dilution refrigerator . . . 165
6.16 Carrier nulling experiment with the MSA . . . 167
6.17 RF-QPC readout with the nulling circuit and MSA configured on the dilution refrigerator . . . 169
6.18 RF-QPC readout and MSA interaction . . . 170

6.19 RF-QPC readout with the MSA and a 10 dB attenuator 173

A.1 Preparation of the SdH oscillations for the Fourier transform 202

B.1 Additional effective mass data and analysis at $p_{2d} = 1.9 \times 10^{15}$ m^{-2} 204

B.2 Additional effective mass data and analysis at $p_{2d} = 1.1 \times 10^{15}$ m^{-2} 205

B.3 Additional effective mass data and analysis at $p_{2d} = 0.7 \times 10^{15}$ m^{-2} 205

B.4 Additional thermal activation data 206

B.5 Temperature dependence of the low B-field positive magnetoresistance . . . 207

C.1 Shot noise of the RF-QPC readout 209

C.2 Power dependence of the RF-QPC readout 211

List of Tables

6.1 Matching network parameters 146
6.2 RF-QPC readout parameters 157

List of Abbreviations

2DEG two-dimensional electron gas

2DHG two-dimensional hole gas

BIA bulk-inversion asymmetry

HH heavy-hole

LH light-hole

PTR pulse tube refrigerator

QW quantum well

RF-QPC radio-frequency quantum point contact

SdH Shubnikov-de Haas

SIA structure-inversion asymmetry

SOI spin-orbit interaction

SQUID superconducting quantum interference device

Chapter 1

Introduction

Two-dimensional hole gases (2DHGs) are of significant interest for both fundamental studies [1, 2, 3] and potential applications in fields such as spintronics [4, 5, 6] and quantum computing [7, 8, 9]. Among 2DHGs, GaAs holes are particularly attractive candidates for spin-based qubits [10]. They are less prone to spin decoherence caused by hyperfine interactions compared to GaAs electrons [11, 12]. This is because their p-orbitals do not overlap with atomic nuclei [13]. Furthermore, their strong spin-orbit interactions enable rapid, electrically-driven qubit control through electric dipole spin resonance (EDSR) [9]. Additionally, GaAs's direct bandgap makes it suitable for applications such as spin-to-photon conversion [14] or photon-to-spin conversion [15, 16].

In contrast to simpler two-dimensional electron gases (2DEGs), the complex properties of 2DHGs mentioned above can be regarded as additional parameters for engineering novel devices based on hole spins. Inspired by recent advancements in the development of high-quality 2DHGs in dopant-free devices [17, 18], our objective is to expand current knowledge of the intricate properties of 2DHGs in the GaAs material system. In this thesis, we investigate pertinent phenomena of 2DHGs, including spin-orbit interaction, hyperfine interaction, as well as material properties such as effective mass and the Landé g factor. Furthermore, in the context of spin-based qubits, we develop a radio-frequency quantum point contact (RF-QPC) charge detector and explore integrating a superconducting quantum interference device (SQUID) amplifier to enhance its sensitivity.

1.1 Outline

This thesis is structured as follows:

Chapter 2 presents the background concepts relevant to the experiments in this work. We begin by reviewing the key aspects of the band structure of GaAs and spin-orbit coupling effects in solids. Next, we discuss the magnetotransport measurements used to characterize 2D systems and probe their interactions. We also provide an overview of Coulomb blockade for a single quantum dot and conductance quantization phenomena in quantum point contacts. This chapter concludes by examining the physics governing the superconducting quantum interference device (SQUID).

Chapter 3 briefly outlines the experimental methods. In this chapter, we describe the working principles of the relevant experimental devices, cryogenic equipment, and measurement cell employed in the experimental work of this thesis.

Chapter 4 is the first results chapter. In this chapter, we focus on the characterization of dopant-free, p-type GaAs/AlGaAs Hall bar devices. We identify fabrication parameters that result in undesired parallel conduction and gate hysteresis. We identify four successive and distinct SdH regimes at different magnetic field ranges, resulting from SOI and Zeeman spin splitting within the Heavy-hole (HH) valence band. Furthermore, we extract the effective masses and estimate the energy splitting of the heavy hole (HH) band under Rashba SOI. This chapter concludes with an estimation of the out-of-plane g factor for HH.

Chapter 5 is the second results chapter, which continues the measurements on dopant-free, p-type GaAs/AlGaAs Hall bar devices. We explore the non-linear magnetotransport characteristics of these devices. We present the SdH phase inversion phenomenon and explore the empirical relationship between the hole temperature and applied dc current through the Hall bar. The features of two-dimensional maps of differential resistance as a function of magnetic field and current in the quantum Hall breakdown regime are extensively described. The magnetic field dependence of the critical breakdown current and electric field is examined. The zero current anomaly (ZCA) phenomenon is observed and discussed. This chapter concludes with examining hysteresis behaviour in the quantum Hall regime.

Chapter 6 is the third results chapter. In this chapter, we focus on the development of an RF-QPC charge detector in a lateral quantum dot device. We conduct charge sensitivity measurements in the single electron regime using the RF-QPC readout and compare the sensitivity to other readouts in literature. Additionally, we demonstrate a nulling technique for RF-QPC readout, which is valuable for integrating a microstrip SQUID amplifier (MSA) with limited dynamic range. This chapter concludes with integrating the MSA into the RF-QPC readout.

Chapter 7 summarizes the results presented in this thesis. Additionally, we suggest some future research directions that can follow from this thesis.

Chapter 2

Background concepts

2.1 Introduction

In this chapter, we provide a comprehensive overview of the key concepts essential for the experiments conducted in this thesis. We begin by examining the properties of 2D holes within the GaAs material system. Following that, we outline the magnetotransport measurements used to characterize 2D systems. Subsequently, we discuss important phenomena relevant to lateral quantum dot devices. Lastly, we discuss the operating principles behind the superconducting quantum interference device (SQUID). Additionally, each experimental results chapter begins with a specialized literature review.

2.2 Band structure of GaAs

GaAs is a III-V semiconductor that has a zinc blende crystal structure. The tight-binding method approximates the electronic wave functions in a solid by using a superposition of the wave functions for isolated atoms at each atomic site. Using the tight-binding approximation, the conduction band of GaAs is predominately made up of atomic s orbitals. Atomic s orbitals have spherical symmetry and $\ell = 0$ orbital quantum number. In contrast, the valence band is reminiscent of atomic p orbitals. Atomic p orbitals have an anisotropic

spatial symmetry and have $\ell = 1$. The atomic p orbitals are three-fold degenerate with respect to the total angular momentum $J = L + S$, the sum of the orbital L and spin S angular momenta. With spin taken into account, the valence band becomes six-fold degenerate. In bulk crystals, spin-orbit interaction (SOI) lifts the six-fold degeneracy of the valence band into 3 bands: Heavy holes (HH), light holes (LH) and the split-off band (SO). In the basis of total angular momentum J and the projection along a $\hat{z}$ axis m_j, $|J, m_j\rangle$, HH have $|3/2, \pm 3/2\rangle$, LH have $|3/2, \pm 1/2\rangle$, and SO band has $|1/2, \pm 1/2\rangle$. Fig. 2.1a shows the bulk GaAs band structure. Although J and m_j are only approximately good quantum numbers, they are used nonetheless for nomenclature.

The HH and LH bands are degenerate for wave vector $k = 0$, but are non-degenerate for $k \neq 0$. The SO band lies lower in energy by the spin-orbit gap Δ_{SO}. In GaAs $\Delta_{SO} = 0.34$ eV [19]. In contrast to the conduction band, the valence band in bulk GaAs is highly anisotropic and non-parabolic. Therefore, it is not possible to accurately describe a hole system using a simple effective mass approximation, as is often the case for electrons.

2.2.1 2D confinement

The valence band becomes more complex due to size quantization in a 2DHG. In the case of a 2DHG hosted in a symmetric quantum well (QW), the degeneracy between the LH and HH bands at $k_z = 0$ is lifted with an energy gap Δ_{hh-lh}, as depicted in Fig. 2.1b. Here, k_z denotes the wave vector along the growth direction. For a 2DHG in an asymmetric QW, Rashba SOI lifts the degeneracy of the $m_j = \pm 3/2$ states in the HH band. This leads to a splitting of the HH band into two bands denoted as HH+ ($m_j = +3/2$) and HH- ($m_j = -3/2$) [20], as illustrated in Fig. 2.1c. Additionally, these two SOI-split bands exhibit different effective masses, with HH+ having a larger mass and HH- having a smaller one, both of which vary with k_z. Similarly, the total angular momentum degeneracy is also lifted in the LH and SO bands, resulting in LH-/LH+ and SO-/SO+.

In the context of transport in the 2DHG, at large values of the in-plane wavevector ($k_{||}$) corresponding to much higher hole densities $p_{2d} = k_F^2/2\pi$ (where k_F represents the Fermi wave vector) than those typically observed in transport experiments, an anti-crossing between the HH and LH occurs (see Fig. 2.1d). This leads to the hybridization of their

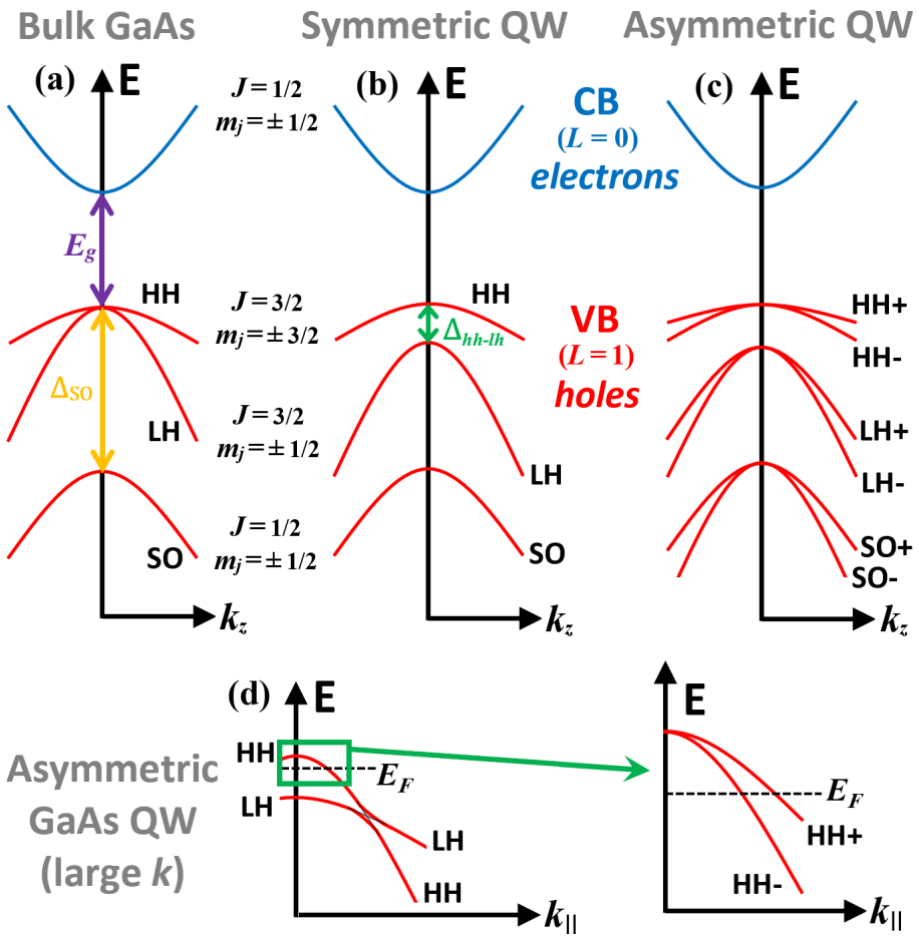


Figure 2.1: Schematic representations of the band structure of GaAs. (a) Conduction band (CB) and valence band (VB) of bulk GaAs. The valence band consists of the heavy hole (HH), light hole (LH) and split-off (SO) band. Band structure for (b) symmetric quantum well (QW) and (c) asymmetric QW as a function of the wavevector along the growth direction (k_z). (d) Dispersion relation as a function of in-plane wavevector ($k_{||}$) for LH and HH bands, illustrating their anti-crossing. (inset) Zoomed-in view of the HH+ and HH- dispersions, near a Fermi energy E_F typically achieved in experiments. Figure made by Dr. François Sfigakis.

wavefunctions. While the mixing between HH and LH bands reaches its maximum at the anti-crossing, and the LH band is unoccupied, hybridization is present to some extent for all values of $k_{||}$. This mixing/hybridization is the principal reason why J and m_j are not good (conserved) quantum numbers.

Furthermore, the LH-HH anti-crossing results in the effective masses of the 2DHG hosted in a QW becoming anisotropic in space. Along the growth direction (k_z), the effective masses correspond to the band names, with the HH effective mass being larger than LH. However, within the 2D plane ($k_{||}$), a mass inversion occurs and the LH effective mass becomes larger than HH. This is illustrated in Fig. 2.1d, where the curvature of the HH band before the anti-crossing is steeper than that of the LH band.

2.2.2 Spin-orbit interaction (SOI)

Spin-orbit interaction (SOI) is a relativistic effect that couples an electron's motion within a potential to its spin degree of freedom. In atomic physics, this effect is incorporated into the Hamiltonian through a non-relativistic approximation of the Dirac equation. SOI can be understood as an effective Zeeman interaction arising from a Lorentz transformation of electric and magnetic fields [21]. When an electron moves in a static electric field $\vec{E}$, it perceives, in its reference frame, an effective magnetic field $\vec{B}_{eff}$ oriented perpendicular to both its momentum $\vec{p}$ and the electric field $\vec{E}$

$$\vec{B}_{eff} = -\frac{1}{2m_0c^2}\vec{p} \times \vec{E} \tag{2.1}$$

where m_0 is the rest mass of the electron, and c is the velocity of light in vacuum. This magnetic field in the rest frame of the electron couples to the electron spin via the Zeeman interaction. The spin-orbit Hamiltonian for a free electron in an electric field $\vec{E} = -\nabla V(r)$ is given by [22]

$$H_{SO} = -\frac{\hbar}{4m_0^2c^2}\sigma \cdot \vec{p} \times (\nabla V(r)) \tag{2.2}$$

where $\hbar$ is Planck's constant and $\sigma = (\sigma_x, \sigma_y, \sigma_z)$ are the Pauli spin matrices.

SOI in semiconductors

The spin degeneracy of electrons and holes in semiconductors is a result of time reversal symmetry and spatial inversion symmetry [23]. In the presence of a finite magnetic field, time reversal symmetry is broken and the spin degeneracy is lifted. Alternatively, once spatial inversion asymmetry is introduced, spin degeneracy is lifted even for zero magnetic field.

Spatial inversion asymmetry in semiconductors can arise from three mechanisms: bulk-inversion asymmetry (BIA) [24], structure-inversion asymmetry (SIA) [25], or surface termination [26, 27]. The latter will not be explored in more detail, as it is significantly smaller than the BIA or SIA terms and is less important for heterojunctions (utilized in this work), where the wavefunction vanishes near the interface. The BIA term, also known as Dresselhaus SOI, is present when the underlying crystal structure lacks an inversion center. An electron moving through the asymmetric potential within the crystal lattice couples to the electron spin through SOI and lifts the spin degeneracy. The BIA is an intrinsic material property. Type III-V semiconductors that have a zinc blende crystal structure, such as GaAs, InAs and InSb, lack inversion symmetry. In contrast, type IV semiconductors like Si and Ge possess a diamond crystal structure with a center of inversion. For (100) zincblende materials, the Dresselhaus SOI in the 2×2 HH subspace is described by the following [28]

$$H_D = \gamma_D(k_+\sigma_- + k_-\sigma_+) + \beta_{D1}(k_+k_-k_+\sigma_- + k_-k_+k_-\sigma_+) + \beta_{D2}(k_-^3\sigma_- + k_+^3\sigma_+) \tag{2.3}$$

where $k_\pm = k_x \pm ik_y$ and γ_D, β_{D1} and β_{D2} are Dresselhaus parameters. The linear terms, γ_D, and β_{D1} dominate while the cubic term is much smaller. Meanwhile the SIA term, also known as Rashba SOI, occurs in 2D systems with inversion-asymmetric confinement potentials. The shape of the confinement potential is adjustable with an external gate, therefore Rashba SOI is tunable. The Rashba SOI for the 2×2 HH subspace is described by [28]

$$H_R = i\alpha_{R1}(k_+\sigma_+ - k_-\sigma_-) + i\alpha_{R2}(k_+^3\sigma_- - k_-^3\sigma_+) + i\alpha_{R3}(k_+\sigma_+ - k_-\sigma_-)k^2 \tag{2.4}$$

where the Rashba coefficients α_{Ri} are proportional to the shape of the asymmetric confinement potential. Using the axial approximation [29], α_{R1} and α_{R3} are zero, leaving only

the cubic term [28]. The Dresselhaus terms are smaller than the Rashba counterparts. In inversion-asymmetric systems (Chapter 4), the Rashba term dominates with a cubic dependence on wavevector.

2.3 Magnetotransport of 2D systems

Two-dimensional electron or hole systems are typically characterized by performing low-temperature magnetotransport experiments in a Hall-bar geometry, as depicted in Fig. 2.2. A current I is injected along the length of the Hall bar, and the longitudinal and transverse voltages (V_{xx} and V_{xy} respectively) are measured. The longitudinal resistivity of a 2D system for a Hall bar with width W and length L is given by $\rho_{xx} = V_{xx}/[(L/W)I]$. Meanwhile, the transverse resistivity is simply given by $\rho_{xy} = r_{xy} = V_{xy}/I$. The transverse resistivity (ρ_{xy}) in 2D does not depend on geometry because the voltage drop (V_{xy}) is not from a current directed along the width (W) of the Hall bar. V_{xy} is instead due to the induced electric field ($E_y = V_{xy}/W$) generated as a consequence of the Lorentz force resulting from the movement of charged particles in the presence of a magnetic field.

2.3.1 Shubnikov-de Haas Oscillations

In classical physics, when a charged particle moves within a magnetic field, it experiences a Lorentz force, resulting in cyclotron motion. The cyclotron radius depends on the particle's velocity and the strength of the magnetic field. At sufficiently low temperatures, the quantization of the motion of charged particles in a magnetic field becomes resolvable. Utilizing the effective mass approximation [22], we can treat a 2D system as having a parabolic dispersion, where the effective mass is independent of the wavevector k. In this framework, the Hamiltonian for a 2D system of non-interacting particles with charge q in the presence of a magnetic field B applied along the z-axis is given by

$$\hat{H} = \frac{1}{2m^*}(\hat{p} - q\hat{A})^2 \tag{2.5}$$

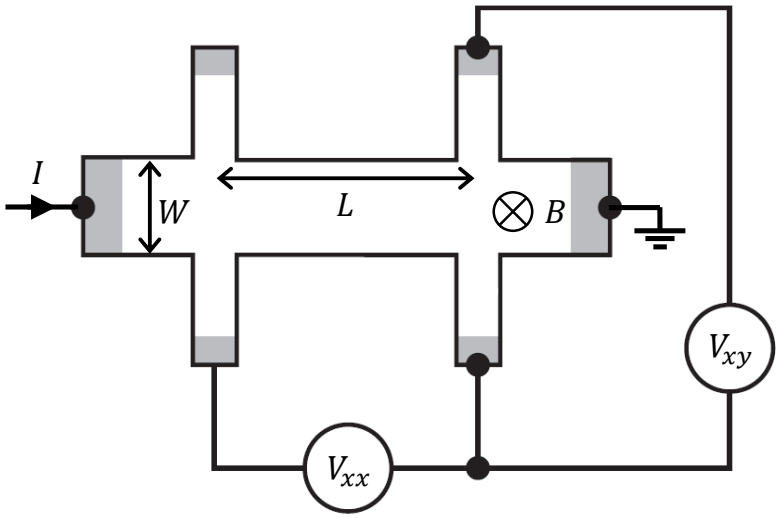


Figure 2.2: Hall bar geometry with the typical measurement scheme used for a magneto-transport measurement.

where $\hat{p}$ represents the canonical momentum, and $\hat{A}$ is the magnetic vector potential. Using the Landau gauge, $\vec{A} = B_z x\hat{y}$, we can derive the following

$$H = \frac{\hat{p}_x^2}{2m^*} + \frac{1}{2m^*}(\hat{p}_y - qB_z x\hat{y})^2 \tag{2.6}$$

Assuming a wavefunction of the form $\psi(x, y) = \psi(x)e^{ik_y y}$ such that the operator $\hat{p_y}$ commutes with this Hamiltonian, we can replace $\hat{p_y}$ with its eigenvalue $\hbar k_y$. Identifying the cyclotron frequency as $\omega_c = \frac{qB}{m^*}$, Eq. 2.6 becomes

$$\hat{H} = \frac{\hat{p}_x^2}{2m^*} + \frac{1}{2}m^*\omega_c^2\left(x - \frac{\hbar k_y}{m^*\omega_c}\right)^2 \tag{2.7}$$

The above Hamiltonian describes a one-dimensional quantum harmonic oscillator with a frequency of $\omega_c = \frac{eB_z}{m^*}$ centered around $\frac{\hbar k_y}{eB_z}$. The energy eigenvalues are therefore given by

$$E_n^{\pm} = \left(n + \frac{1}{2}\right)\hbar\omega_c \pm \frac{1}{2}g_{zz}\mu_B B_z \tag{2.8}$$

The first term in Eq. 2.8 breaks up the constant density of states of a 2D system into discrete levels, labeled by the index n. These levels are known as Landau levels, with an

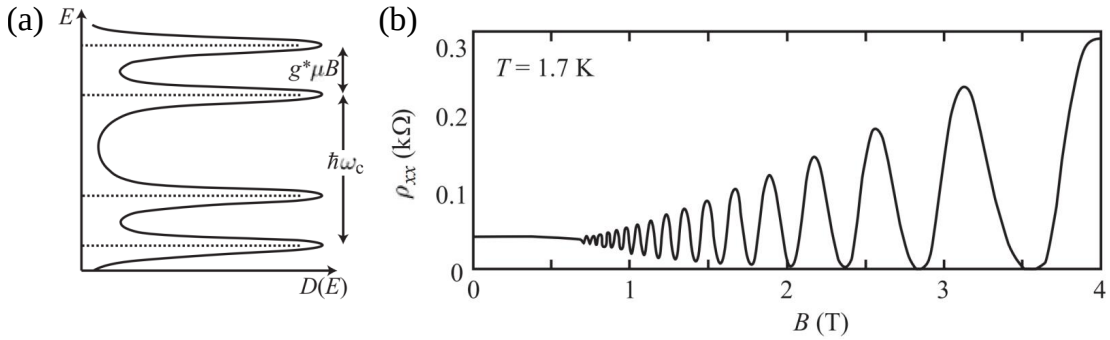


Figure 2.3: (a) Schematic representation of the density of states of a 2D system in the presence of a perpendicular magnetic field. The separation between Landau levels is given by the cyclotron energy $\hbar\omega_c$. The Zeeman energy further splits spin degenerate Landau levels by $g_{zz}\mu_B B$. (b) Longitudinal resistivity as a function of perpendicular magnetic field measured for a GaAs 2DEG in Hall bar geometry. Adapted from [30].

energy spacing of $\hbar\omega_c$. It is convenient to introduce the filling factor ν, which is defined as the number of occupied Landau levels at a given magnetic field. In an ideal 2D system without scattering, the Landau levels are true δ-functions. However, in a real system with disorder, the carriers undergo scattering from impurities, resulting in a broadening of the Landau levels with a width of Γ. Assuming a Lorentzian shape, the Landau level broadening is on the order of $\Gamma \sim \hbar/\tau_q$, where τ_q is the quantum lifetime. The second term in Eq. 2.8 describes the response of the spin to the magnetic field via the Zeeman interaction. The Zeeman energy additionally splits the Landau levels by an amount $g_{zz}\mu_B B$, where g_{zz} is the out-of-plane g-factor and μ_B is the Bohr magneton. The density of states for a 2D system in a perpendicular magnetic field is depicted in Fig. 2.3a.

In the limit of small magnetic fields for a single electric subband occupied, the oscillating density of states modulates the classical Drude resistivity ρ_0 according to [31]

$$\rho_{xx}(B,T) = \rho_0 \left[1 - 2e^{(-\pi/\omega_c\tau_q)} \frac{\chi(T)}{\sinh\chi(T)} \cos\left(2\pi \frac{hp_{2d}}{2eB}\right)\right] \tag{2.9}$$

The oscillations in the longitudinal resistivity as a function of perpendicular magnetic field are known as Shubnikov-de Haas (SdH) oscillations. From the cosine term, the oscillations are periodic in 1/B with a periodicity $2e/hp_{2d}$, where p_{2d} is the carrier density. The expo-

nential term reflects the broadening of the Landau levels through the quantum lifetime τ_q. Meanwhile, $\chi(T)/\sinh\chi(T)$ is the thermal dampening term that describes the temperature dependence of the oscillations, where $\chi(T) = 2\pi^2 k_B T/\hbar\omega_c$. Fig. 2.3b shows an example of SdH oscillations for a GaAs 2DEG measured at 1.7 K.

2.3.2 Integer quantum Hall effect

At large magnetic fields and low temperatures, the discrete density of states also begins to affect the transverse resistance, r_{xy}. This is a consequence of the Landau levels becoming sufficiently well-separated with no overlap, due to the larger cyclotron energy spacing $\hbar\omega_c$ and/or spin splitting $g_{zz}\mu_B B$. A plateau in the Hall resistance occurs when the Fermi energy is positioned halfway between two adjacent Landau levels, as depicted in Fig. 2.4a. The plateaus occur at values given by

$$r_{xy} = \frac{h}{e^2}\frac{1}{\nu} \tag{2.10}$$

where $\nu = \frac{hp_{2d}}{eB_z}$ is the filling factor. Every time ν Landau levels are completely filled, a plateau in the Hall resistance occurs. Concomitantly, the longitudinal resistivity ρ_{xx} goes to zero. These two properties are the hallmark features of the integer quantum Hall effect. Fig. 2.4b shows an example of the SdH oscillations and Hall plateaus in the quantum Hall regime for a GaAs 2DEG measured at 100 mK.

The microscopic explanation of the integer quantum Hall effect can be attributed to two mechanisms: disorder potential and the formation of edge channels. The disorder potential causes states in the bulk to become localized, resulting in suppressed bulk conductance at the Fermi level. Concomitantly, the confinement potential bends the Landau levels upward at the sample edges, giving rise to one-dimensional ballistic transport channels, as depicted in Fig. 2.5. The motion of these channels is chiral in nature, meaning they move in opposite direction on opposite edges of the sample. The number of edge states equals the filling factor ν, with each state (spin non-degenerate) contributing half of a conductance quantum (e^2/h).

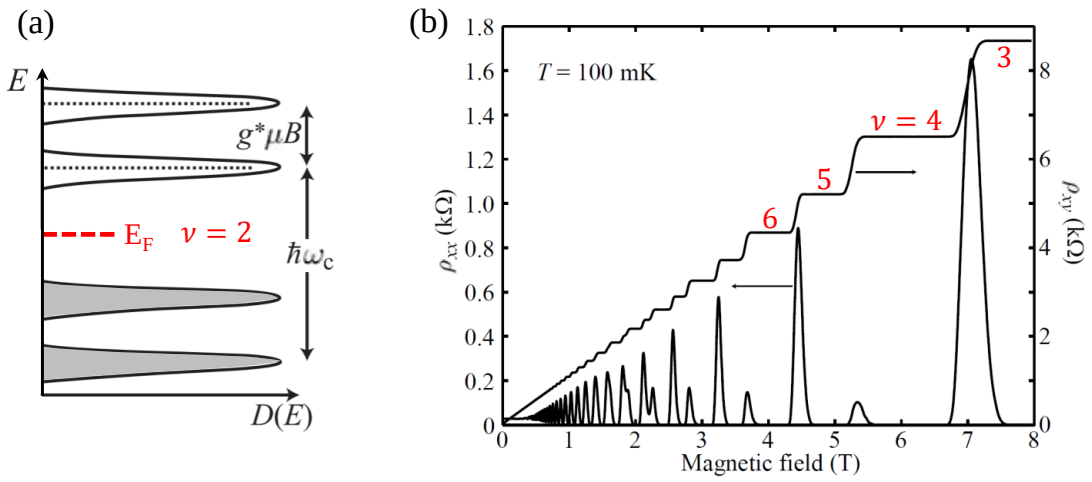


Figure 2.4: (a) Density of states in the strong quantum Hall regime for filling factor $\nu = 2$. The spin split Landau levels do not overlap and the Fermi level is in a clear spectral gap between the a fully occupied Landau level below (shaded gray) and empty level above. (b) SdH oscillations (left y-axis) and Hall resistance (right y-axis) of a GaAs 2DEG in a Hall bar geometry measured at 100 mK. The red numbers on the Hall plateaus indicate the corresponding filling factor ν. Adapted from [30].

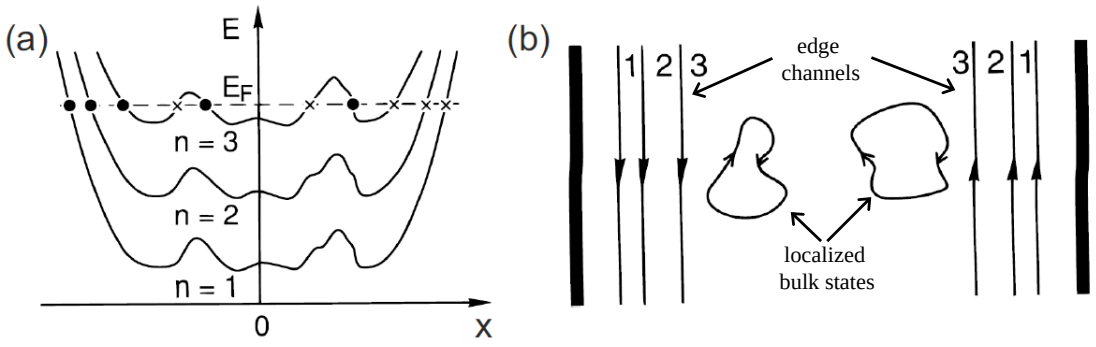


Figure 2.5: (a) A schematic representation illustrating the intersection of the Fermi level with the first three Landau levels along the width of the Hall bar. (b) A top-down view of the Hall bar displaying edge channels (numbered) and localized bulk states. The thick lines denote the edges of the sample. Adapted from [32].

2.4 Quantum dots and 1D constrictions

A quantum dot is a structure in which electrons or holes are confined in all three spatial dimensions. In semiconductor devices, quantum dots are created by introducing additional lateral confinement in a 2D electron or hole gas. This lateral confinement can also be utilized to form 1D channels known as quantum point contacts (QPCs). In this section, we will discuss the Coulomb blockade and conductance quantization phenomena that are relevant to laterally defined semiconductor devices.

2.4.1 Coulomb blockade

Quantum dots can be described using a capacitive model, as depicted in Figure 2.6a for a single quantum dot. The quantum dot, represented by a blue circle, is tunnel-coupled to both the source and drain leads and is also capacitively-coupled to a gate. Tunnel coupling implies that the dot is connected to the leads through a resistive connection, enabling the exchange of charges with the leads, in addition to capacitive coupling. The gate is used to shift the electrochemical potential of the quantum dot and consequently adjust the number of charge carriers.

The energy spectrum of a semiconductor quantum dot is primarily governed by two distinct energy scales. The first is the Coulomb repulsion experienced among charge carriers, which, in conjunction with the small size of the quantum dot, results in a charging energy given by $E_C = e^2/C_\Sigma$. This energy is required to add an additional charge carrier to the quantum dot, where C_Σ represents the total capacitance between the quantum dot and its environment (which includes the source and drain leads and the metallic gate). This effect leads to a suppression of the tunneling current, known as Coulomb blockade, which is purely classical and arises from the discrete nature of electric charge. The second energy scale pertains to the allowed orbital states of single-particle energies, denoted as E_N. The energy difference between adjacent electrochemical potentials, referred to as the addition energy, is given by

$$E_{add}(N) = \mu(N) - \mu(N-1) = \Delta E + E_C \tag{2.11}$$

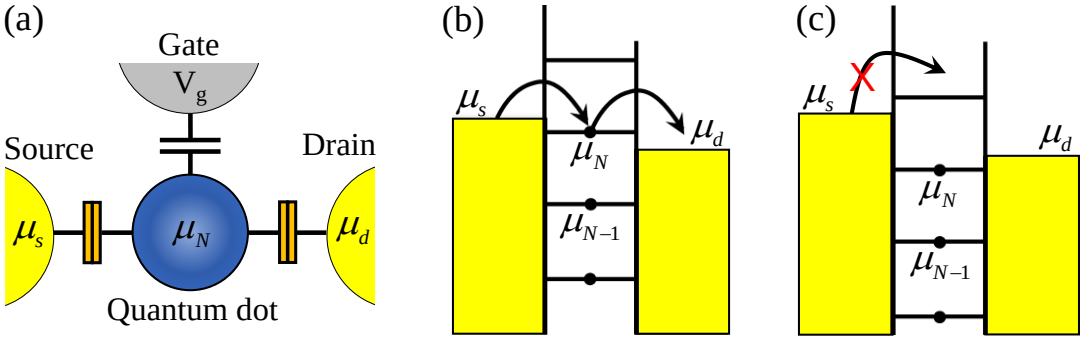


Figure 2.6: (a) Capacitive model of a single quantum dot. The quantum dot is tunnel coupled to source and drain leads and capacitively-coupled to a gate. Applying a voltage to the gate shifts the electrochemical potential, μ_N, of the QD relative to the leads. Energy level diagrams showing conditions for (b) single electron transport and (c) Coulomb blockade.

where ΔE represents the energy difference between two single-particle energy states. For quantum dots in GaAs/AlGaAs heterostructures, E_C is approximately 1 meV, and ΔE is approximately 0.1 meV [30].

Fig. 2.6b shows a schematic energy level diagram for a single quantum dot, where a ladder of levels is approximately equally spaced by E_C. A source-drain voltage bias produces an energy difference between the leads, $\mu_{sd} = \mu_s - \mu_d = -|e|V_{sd}$, which is known as the bias window. The voltage on the gate V_g positions the electrochemical potential of the N-electron quantum dot state μ_N within the bias window, enabling single charge transport. The magnitude of the current will depend on the dot-to-lead tunnel rate. In Fig. 2.6c, the Coulomb blockade phenomenon is observed, where μ_N lies outside the bias window, preventing the addition of a charge to the dot, and as a result, there is no current flow.

2.4.2 Conductance quantization in quantum point contact

A quantum point contact (QPC) is a narrow constriction obtained in a 2D electron or hole gas, with its width on the order of the Fermi wavelength and its length smaller than

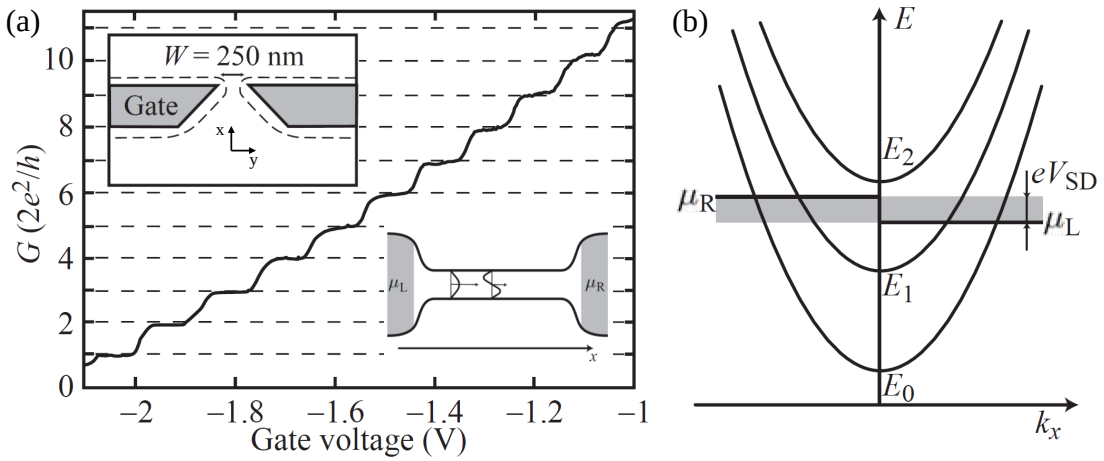


Figure 2.7: (a) (adapted from [33]) The first measurement of conductance quantization in a QPC. The upper inset shows the split-gate constriction on top a 2DEG used for the measurement. The lower inset (adapted from [30]) shows a voltage bias applied between two electron reservoirs. (b) (adapted from [30]) Parabolic dispersion for three subbands. Only the lowest two channels contribute to transport.

the elastic mean free path. By adjusting the width of the constriction using electrostatic gates, one can observe a step-like change in its conductance. The conductance values at these steps are multiples of the conductance quantum ($2e^2/h$). Since its initial discovery by Wees *et al.* in a GaAs 2DEG [33] (shown in Fig. 2.7a), quantized conductance in a narrow constriction has proven to be a universal effect, independent of fabrication technology and host material.

Consider the QPC as a long ballistic conductor of width W connected to two electron reservoirs, as illustrated in the lower right inset of Fig. 2.7a. The lateral confinement in the y-direction gives rise to a series of quantized transverse modes. Each of these modes can be approximated as having a parabolic dispersion relation given by

$$E_n(k_x) = E_n + \frac{\hbar^2 k_x^2}{2m^*}, \qquad E_n = \frac{\pi^2\hbar^2}{2m^* W^2} n^2 \tag{2.12}$$

with energy offset E_n as depicted in Fig. 2.7b. Applying a voltage $e(\mu_L - \mu_R)$ across the QPC results in a current flow. Using the Landauer-Büttiker formalism, the conductance

of a QPC with n occupied modes is given by [30]

$$G = g_s \frac{e^2}{h} \sum_n \int_{-\infty}^{+\infty} T_n(E)[f(E,\mu_L) - f(E,\mu_R)]\, dE \tag{2.13}$$

where $T_n(E)$ is an energy-dependent transmission probability that accounts for back-scattering, and $f(E,\mu_i)$ represents the Fermi functions for the left and right reservoirs. Each mode n contributes to the total conductance given by the integral in Eq. 2.13. The prefactor g_s accounts for spin degeneracy, with $g_s = 2$ being applicable to a GaAs 2DEG at zero magnetic field. In the limit of zero temperature the Fermi functions in the integral of Eq. 2.13 are replaced by step functions. For ideal transmission modes, the QPC conductance with N occupied modes is given by

$$G = 2N \frac{e^2}{h} \tag{2.14}$$

The conductance is quantized in integer multiples of the conductance quantum ($2e^2/h$). In the presence of a magnetic field, the spin degeneracy is broken, leading to plateaus at integer multiples of e^2/h.

2.5 SQUIDs

The operation of the superconducting quantum interference device (SQUID) relies on two key phenomena in superconductivity: the Josephson effect and the quantization of magnetic flux. In this section, we will present the theoretical principles underlying the SQUID operation.

2.5.1 Josephson junctions

A Josephson junction is composed of two superconductors connected by a very weak link. This weak link can take the form of an insulator (superconductor-insulator-superconductor, SIS), a normal metal (SNS), or a narrow constriction (ScS). The physical size of the weak link is significantly smaller than the coherence length of the Cooper pairs, which allows it

to couple the wave functions of the two superconductors. This coupling leads to distinctive electrical properties, such as a phase-dependent supercurrent or a sinusoidal alternating current across the junction. The current-voltage characteristics of Josephson junctions are defined by the two Josephson relations. The Josephson current-phase relation is given by

$$I_s = I_0 \sin(\delta) \tag{2.15}$$

where I_s represents the supercurrent carried by Cooper pairs passing through the junction, and I_0 denotes the maximum or critical current that the junction can support without experiencing any voltage drop. The critical current is dependent on the material, geometry, and temperature. $\delta = \theta_1 - \theta_2$ corresponds to the phase difference between the two macroscopic wave functions of the two superconductors. The Josephson voltage-phase relation is given by

$$\frac{d\delta}{dt} = \frac{2eV}{\hbar} \tag{2.16}$$

where V is the voltage drop across the junction, e is the elementary charge, and $\hbar$ is Planck's constant.

Resistively Capacitance Shunted Junction (RCSJ) model

When the current passing through the junction exceeds the critical current I_0, a voltage abruptly develops across the junction. However, this voltage only returns to zero for a current significantly lower than I_0. In other words, the Josephson junction alone exhibits a hysteretic current-voltage (I-V) relationship. To utilize a Josephson junction in a SQUID, this hysteresis must be eliminated. This is accomplished by incorporating a shunt resistor in parallel with the junction. In the case of insulating barriers in an SIS configuration, the junction areas are sufficiently large to yield junctions with adequate critical currents, resulting in an effective capacitance across the junction. Therefore, an accurate model of a non-hysteretic Josephson junction should include resistor and capacitor elements. The resistively and capacitively shunted junction (RCSJ) model incorporates these components, as shown in Fig. 2.8a. Using Kirchhoff's law, the sum of all currents flowing across the junction in the RCSJ model is given by [34]

$$I = I_0 \sin(\delta) + \frac{V}{R} + C\frac{dV}{dt} \tag{2.17}$$

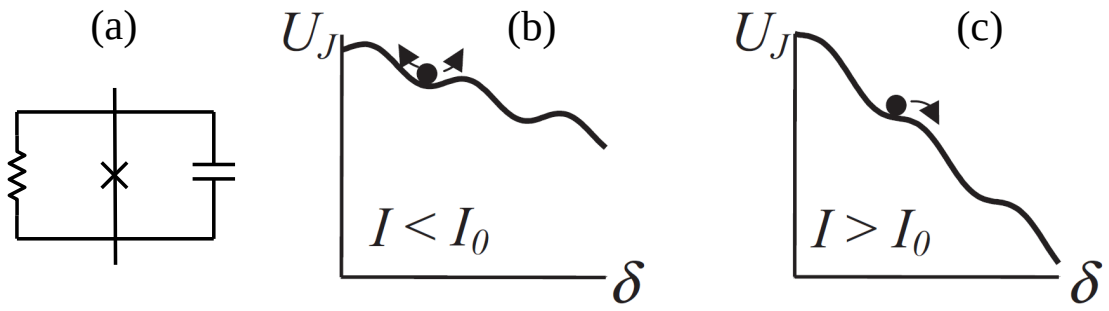


Figure 2.8: (a) Schematic of resistively-shunted Josephson junction. Tilted "washboard" potential derived from the RCSJ model depicting (a) $I < I_0$ and (b) $I > I_0$. Adapted from [34].

Using the Josephson voltage-phase relation (Eq. 2.16), Eq. 2.17 can be re-written as

$$I - I_0 \sin(\delta) = \frac{\hbar C}{2e}\ddot{\delta} + \frac{\hbar}{2eR}\dot{\delta} \tag{2.18}$$

which is a nonlinear second-order differential equation. One can recognize the similarity between Eq. 2.18 and the standard equation of motion for a particle moving in a one dimensional potential. In the mechanical analogue, the mass of the particle is equivalent to $m = \hbar C/2e$, the viscous drag component to $\gamma = \hbar/2eR$, and the non-linear force term to $F = I - I_0 \sin(\delta)$. The particle moves in a potential given by ($F = -\nabla U_J = -dU_J/d\delta$)

$$U_J = -I\delta - I_0 \cos(\delta) \tag{2.19}$$

resulting in an effective "washboard" potential. It can be parameterized by the ratio of the current to the critical current I/I_0. When $I/I_0 < 1$, the periodic potential wells of the washboard trap the phase (particle) δ at certain values, leading to no voltage drop across the junction. This situation is depicted in Fig. 2.8b.

When $I/I_0 > 1$, the washboard becomes tilted from the term $I\delta$ in Eq. 2.19, enabling the phase (particle) to advance down the "washboard" potential. We can parameterize the effect of the capacitance (mass) by introducing the Stewart–McCumber parameter, given by

$$\beta_c = \frac{2eI_0R^2C}{\hbar} \tag{2.20}$$

When $\beta_c \ll 1$, the junction is considered to be over-damped, which means that the viscous drag (resistive) term dominates over the inertia term. The over-damped solution results in a non-hysteretic I-V characteristic, which is necessary for the practical operation of a SQUID. As β_c increases and the junction enters the under-damped regime, the I-V curve exhibits hysteresis. In this case, once the phase (particle) starts to evolve, the dominant inertial term prevents the phase (particle) from becoming trapped in one of the washboard ripples, as depicted in Fig. 2.8c. Typically the junction is shunted with a damping resistor that is much smaller than the normal conductance of the junction. This reduces β_c and prevents hysteresis.

2.5.2 DC SQUID

A DC SQUID is a device that utilizes two shunted Josephson junctions connected in parallel within a closed superconducting loop. The DC SQUID primarily functions as a magnetic flux-to-voltage transducer. The device's operation relies not only on the Josephson effect but also on the quantization of magnetic flux within the superconducting loop.

Recall that the macroscopic wavefunction of a superconductor can be represented by a complex order parameter, described by $\Psi = \psi_0 e^{i\theta}$, where ψ_0 is the amplitude and θ is the phase. In the case of superconductors with non-trivial topologies, such as a loop, a boundary condition is imposed, ensuring that the wavefunction remains single-valued at every point along the loop. Consequently, a phase shift of 2π does not affect Ψ. Thus, for a superconducting loop, the phase change when traversing the entire loop must be an integer multiple of 2π in order to maintain the single-valued nature of the wavefunction. This results in the magnetic flux threading a superconducting loop to be quantized by the magnetic flux quantum ($\Phi_0 = h/2e$).

Fig. 2.9a shows a schematic of a DC SQUID, with each junction represented by an RCSJ. The SQUID operates as follows: a dc current greater than twice the critical current of each junction, $2I_0$, is supplied to the SQUID, dividing the current between the two branches that contain the junctions. In the absence of a magnetic field threading the loop, the current is evenly distributed between the branches. However, when an external magnetic field is applied to the loop, a screening current is induced around the loop to

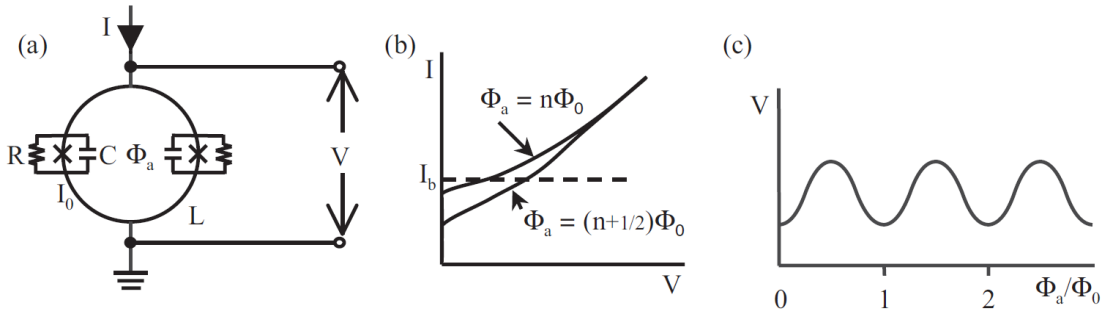


Figure 2.9: (a) Schematic of a dc SQUID in the RCSJ model. (b) I-V characteristic at integer and half-integer values of applied magnetic flux threading the SQUID loop. The bias current, I_b, is greater than twice the critical current of each junction, $2I_0$. (c) The output voltage across the SQUID as a function of magnetic flux. Adapted from [34].

counteract the applied magnetic flux, reducing it back to zero. This induced screening current supplements the applied current through one junction and opposes the current in the other junction. When the current passing through one junction exceeds the critical current, I_0, a voltage develops across that junction and consequently across the entire SQUID loop. When the applied magnetic flux exceeds half a flux quantum, $\Phi_0/2$, instead of screening the flux, it becomes energetically favorable to allow one flux quantum in the loop. As a result, the screening current changes direction to adjust the net flux in the loop to one flux quantum. This behavior continues as the applied magnetic flux is increased, with a periodicity of one flux quantum, Φ_0.

Fig. 2.9b shows the SQUID I-V characteristic for both half and integer values of Φ_0 threading the loop. As the applied magnetic flux increases, the I-V curve oscillates continuously between these two extremes shown in Fig. 2.9b. For a given bias current $I_b > 2I_0$, the voltage across the SQUID oscillates with applied magnetic flux, also with a periodicity of one flux quantum, Φ_0. An example of a $V - \Phi$ curve is shown in Fig. 2.9c.

2.5.3 SQUID amplifiers

In a conventional design of a SQUID, as used in Chapter 6, a square geometry is employed for the loop. It consists of a large "washer" connected to a small counter-electrode through two Josephson junctions, as depicted in Fig. 2.10. Typically, thin films of niobium (Nb) are used for both the washer and the counter-electrode. Additionally, aluminum oxide (Al_2O_x) is commonly employed as the insulating barrier to create Nb-Al_2O_x-Nb junctions. The junctions are also resistively shunted to produce a non-hysteretic I-V characteristic.

In a SQUID amplifier, a signal is applied to an input coil that is inductively coupled to the SQUID washer. The input coil converts electric current into magnetic flux, and the SQUID functions as a current-to-voltage transducer. The input coil is inductively coupled to the SQUID loop with a mutual inductance $M = \alpha\sqrt{L_{\rm in}L_{\rm sq}}$, where α represents a geometry-dependent coupling constant, and $L_{\rm in}$ and $L_{\rm sq}$ denote the inductance of the input coil and SQUID washer, respectively. The mutual inductance determines how much flux a given current through the input coil produces.

In order to utilize the SQUID as a practical amplifier, it must be biased appropriately to maximize the output voltage swing and linearize the flux-to-voltage relationship. The maximum slope of the $V - \Phi$ relation, $\frac{\partial V}{\partial \Phi}$, occurs when a static flux of $(2n-1)\frac{\Phi_0}{4}$ is supplied to the SQUID, where n is an integer. This flux bias is achieved by passing a dc current through a feedback coil coupled to the SQUID. To maintain this operating point for changes in applied flux from the input coil, a flux locked loop (FLL) circuit is employed. The FLL circuit involves a feedback circuit that keeps the flux through the SQUID constant by adjusting the current through the feedback coil. The FLL increases the dynamic range for linear operation to several thousand flux quanta.

Microstrip SQUID amplifier (MSA)

In the typical operation of a SQUID amplifier, the input signal is applied across the two ends of an input coil that is tightly coupled to the SQUID loop, as shown in Fig. 2.10. To achieve good coupling, the input coil is usually lithographically patterned directly above the SQUID, separated only by a thin insulating layer. However, when operating at frequencies

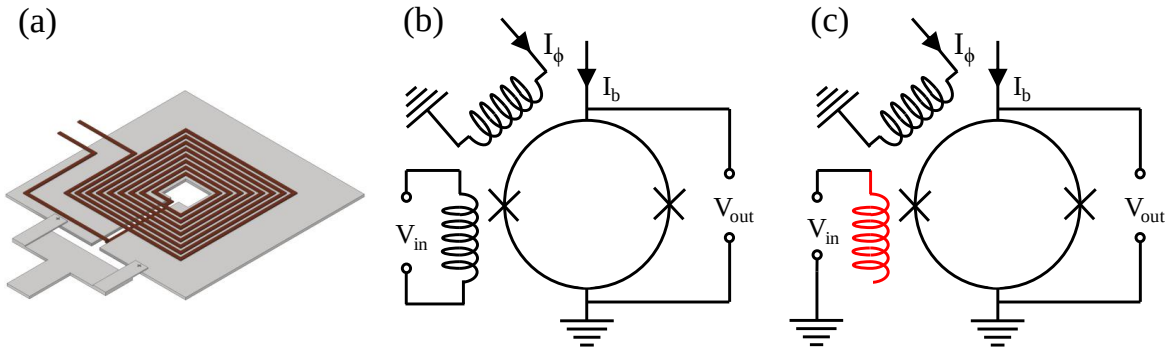


Figure 2.10: (a) Diagram of typical SQUID (adapted from Ref. [35]). The square washer and counter-electrode are shown in gray, connected by two Josephson junctions represented by the cross-indents. The input coil is depicted by the copper color and is patterned above the square washer. (b) Electrical schematic of a conventional SQUID amplifier. The input signal is coupled to both ends of the input coil. The additional coil carrying current I_ϕ is the feedback coil. (b) Electrical schematic of a microstrip SQUID amplifier (MSA). The input signal is coupled to one end of the coil and the SQUID washer. The other end of the coil is left open.

exceeding tens of megahertz, the parasitic capacitance between the input coil and the SQUID washer can lead to a substantial reduction in the device's gain. This issue can be overcome by coupling the input signal between one end of the input coil and the SQUID washer. In this configuration, the input coil now acts as a transmission line resonator. When the input coil is driven at a frequency close to the $\lambda/2$ standing wave resonance of the microstrip, the current is enhanced proportionally to quality factor Q of the microstrip [36]. This leads to an increased gain at the resonance frequency while maintaining a low-level of noise. A SQUID operated in this configuration is known as a *microstrip SQUID amplifier* (MSA), first reported in Ref. [37]. Fig. 2.10b shows the electrical configuration of an MSA.

One drawback of an MSA is that they can only operate in an open-loop configuration. This limitation arises from their higher-frequency operation, which prevents the use of the FLL scheme outlined earlier to increase the dynamic range. Due to technical constraints, the utilization of FLL is restricted to frequencies up to a few megahertz [38]. Nevertheless,

the noise temperature of MSAs has been demonstrated to be very low when cooled, primarily limited by the thermal noise produced by the shunt resistors. In Ref. [39], the authors demonstrated that an MSA cooled to 20 mK achieved a noise temperature of 50 mK at 520 MHz, within a factor of two of the quantum limit and over an order of magnitude lower than the best semiconductor amplifiers.

Chapter 3

Experimental methods

3.1 Introduction

This chapter serves a dual purpose. First, we provide a concise overview of the architecture and operational principles of the devices employed in our experimental work. Second, we elaborate on the characteristics and specifications of the cryostat utilized for conducting these experiments.

3.2 2D devices

Charge carriers can be confined within a 2D layer of a semiconductor through band gap engineering. These 2D devices can then be fabricated to take the form of Hall bar geometries, narrow one-dimensional constrictions, or zero-dimensional quantum dot structures. This section focuses on presenting the techniques employed to fabricate these 2D devices.

3.2.1 Heterojunctions and quantum wells

A heterostructure is simply a semiconductor arrangement where the chemical composition varies with position. A single heterojunction represents the most basic form of a

heterostructure, consisting of an interface between two dissimilar semiconductors. Heterostructures are typically grown using the molecular-beam epitaxy (MBE) technique, allowing for precise control over the thickness and chemical composition of each atomic layer. Heterostructures serve as the fundamental building blocks for advanced semiconductor devices. Within a heterojunction interface or a thin layer of material in a double heterojunction (also known as a quantum well), a conductive two-dimensional layer, such as a two-dimensional electron gas (2DEG) or a two-dimensional hole gas (2DHG), can be formed. The confinement of this 2D gas to a narrow region (approximately on the order of tens of nanometers) creates discrete energy level subbands along the growth direction. Typically, for charge carrier densities around 1×10^{15} m^{-2}, only the lowest subband is occupied, allowing the system to be effectively treated as two-dimensional. However, in wide quantum well structures (approximately 30 - 50 nm), the second subband is considerably lower in energy and can become populated even at low densities, around 1×10^{15} m^{-2}.

The gallium-arsenide/aluminum-gallium-arsenide (GaAs/AlGaAs) material system is the most studied III-V heterostructure. A typical GaAs/AlGaAs heterojunction is formed by combining GaAs and $Al_xGa_{1-x}As$. In the second layer, Al replaces some fraction of the Ga in the lattice (typically $x \approx 0.3$ - 0.5). The crystal lattices of GaAs and AlGaAs are similar, which produces structures with little strain and minimal defects. Consequently, confined electrons or holes move through the crystal lattice encountering very few scattering sites. This low level of scattering and disorder results in high mobility structures.

The formation of the 2D electron or hole gas in heterostructures arises from two mechanisms. The semiconductor materials that make up the single or double heterojunctions have different band gaps. Consequently, the conduction and valence band across a heterojunction develop step-like profiles and establish a common Fermi energy. The difference in band gaps alone does not form a 2D gas. The second crucial ingredient is an electrostatic potential that causes the conduction or valence band to bend appropriately at the heterojunction. To form a two-dimensional electron gas (2DEG), the conduction band is bent downwards to dip below the Fermi level. Alternatively, to form a two-dimensional hole gas (2DHG), the valence band is bent above the Fermi level. The electrostatic potential to bend the band structure is achieved by modulation doping or by gating the heterostructure.

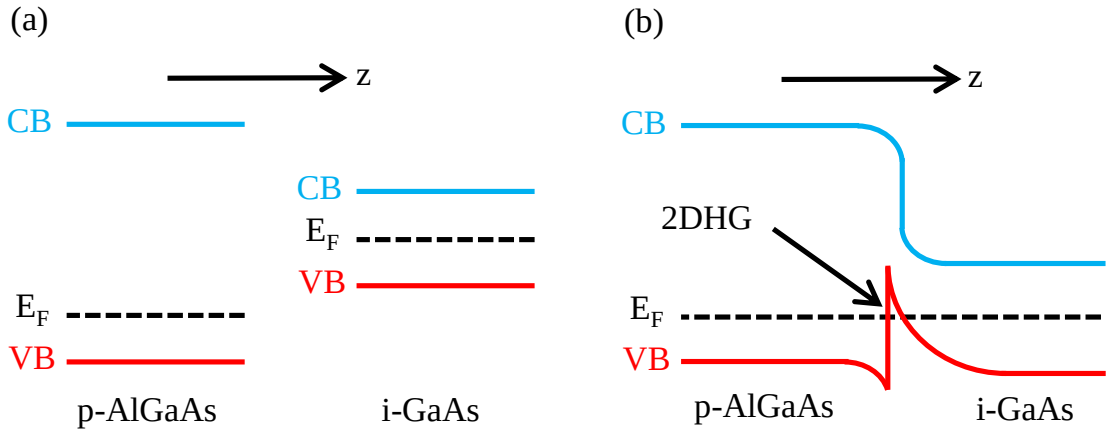


Figure 3.1: Modulation-doped example. (a) Energy band diagrams of the p-doped AlGaAs layer (p-AlGaAs) and intrinsic GaAs layer (i-GaAs) before contact. (b) Alignment of the energy bands and Fermi level after contact, illustrating the formation of a 2DHG at the heterojunction interface.

3.2.2 Modulation-doped devices

The standard method for creating an electrostatic potential involves introducing dopants into the material system, a technique known as modulation doping [40]. In modulation doping, during the wafer growth via MBE, a thin dopant layer is incorporated near the heterojunction. To form a 2DEG in a GaAs/AlGaAs heterojunction, an n-type dopant like silicon is introduced into the AlGaAs layer, replacing some of the Ga or Al atoms. As a result, some electrons from the n-type doping migrate into the GaAs layer, leaving positively charged ions in the n-AlGaAs layer. These positive ions cause a bending of the conduction band, while the free electrons accumulate to form the 2DEG. Alternatively, to create a 2DHG in a GaAs/AlGaAs heterojunction, a p-type dopant such as carbon is added to the AlGaAs layer. This leads to the migration of some holes from the p-type doping into the GaAs layer, leaving behind negatively charged ions. The negative ions induce a bending of the valence band, while the free holes accumulate to form the 2DHG. As an example, Fig. 3.1a shows the energy bands and Fermi level of a physically separated p-doped AlGaAs layer and intrinsic GaAs layer. Upon the contact of these two materials, the alignment of energy levels produces a 2DHG at the GaAs/AlGaAs interface, as depicted

in Fig. 3.1b. Modulation-doped structures can be readily fabricated with ohmic contacts to establish electrical connections with the 2D gas. As a standard technique, metal is deposited atop the heterostructure and then annealed at high temperatures, causing the metal to diffuse down to make contact with the 2D gas [41].

3.2.3 Dopant-free induced devices

An alternative approach to modulation doping involves the application of an external electric field along the growth direction of the heterostructure to modify the band structure and induce a 2D gas. This external electric field can be generated by applying a voltage to a metallic electrode or gate positioned on top of the heterostructure. To prevent leakage currents, a suitable dielectric material is initially deposited beneath the gate. Together, the gate and the 2D gas function as a parallel plate capacitor. This specific type of device is commonly referred to as a Heterostructure-Insulator-Gate Field Effect Transistor (HIGFET). Fig. 3.2a shows a schematic of a top-gated GaAs/AlGaAs HIGFET, representative of the devices investigated in this work. Fig. 3.2b depicts the energy band diagram of the heterostructure in its insulating state when no voltage is applied to the top-gate. To create a 2DHG, a negative voltage is applied to the gate, causing the energy bands and Fermi level to bend accordingly. With a sufficiently negative voltage, the Fermi level becomes pinned below the valence band, resulting in the formation of a 2DHG at the AlGaAs/GaAs interface, as illustrated in Fig. 3.2c.

Unlike modulation-doped devices, dopant-free devices do not conduct unless a voltage is applied to the gate. Because the gate only induces a 2D gas directly beneath it, the fabrication of ohmic contacts for dopant-free devices is considerably more complicated. One approach, employed for the devices investigated in this work, involves recessing the ohmic contact into the material by etching a portion of the heterostructure and subsequently depositing the ohmic material directly at the heterojunction. This process allows for lateral diffusion of the material in addition to the downward diffusion. More comprehensive details on the fabrication of ohmic contacts in dopant-free devices can be found in Refs. [42, 43, 44].

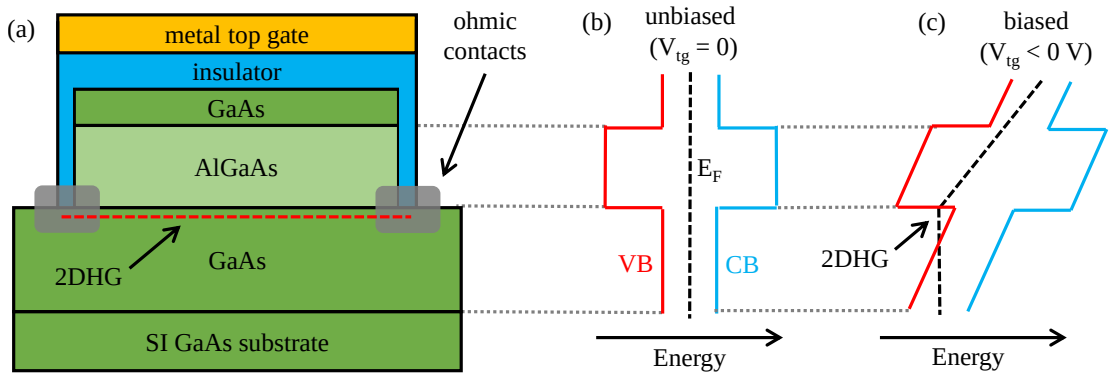


Figure 3.2: (a) Schematic of HIGFET structure. (b) Energy band diagrams when the device is unbiased. The Fermi level is midway between the conduction and valence band and the device is insulating. (c) When a negative voltage is applied to the top-gate, the Fermi level moves below the valence band resulting in a 2DHG layer at the heterojunction interface.

While dopant-free devices require more extensive and complex fabrication processes compared to their modulation-doped counterparts, they offer several advantages. In modulation-doped devices, the presence of remote-ionized donors from intentional dopants can lead to scattering through Coulomb interactions, limiting the mobility of the 2D gas [45]. In contrast, dopant-free structures have their mobility primarily limited by unintentional background impurities introduced during MBE growth. The reduced disorder in dopant-free devices allows for the study of 2D gases at lower carrier densities [46]. At these lower carrier densities, electron-electron (2DEG) or hole-hole (2DHG) interactions become more pronounced, facilitating the investigation of phenomena like Wigner crystallization [47, 48].

In modulation-doped devices, the charge carrier type (electrons or holes) is fixed during heterostructure growth using n-type or p-type dopants. However, dopant-free devices can be configured as ambipolar, enabling the simultaneous study of both electron and hole charge carriers in the same device [49]. Ambipolar operation in 2D gases is valuable for fabricating lateral p-n junction devices, which are useful in quantum optoelectronic applications [50]. Additionally, dopant-free devices can create much shallower 2D gases, making them suitable for quantum dot spin qubits [51]. The absence of dopants has also

been demonstrated to reduce telegraph (charge) noise in quantum dots [52].

In Chapters 4 and 5, we investigate GaAs/AlGaAs heterojunctions in a HIGFET geometry. These devices were fabricated into Hall bars for magnetotransport experiments. In Chapter 6, we utilize an n-type modulation-doped GaAs/AlGaAs heterojunction fabricated into a lateral quantum dot device.

3.3 Cryostat and experiment components

3.3.1 Dilution refrigerator

The cooling mechanism of the dilution refrigerator relies on the phase separation of a ^{3}He-^{4}He mixture in the mixing chamber. At temperatures below 0.87 K, the mixture undergoes phase separation into two distinct phases: a ^{3}He rich phase and a ^{3}He dilute phase. As the temperature approaches absolute zero, the ^{3}He rich phase becomes increasingly pure, while the ^{4}He rich phase maintains a constant ^{3}He concentration of 6.6 % at saturated vapor pressure, even when reaching 0 K. Leveraging this residual ^{3}He concentration in the ^{4}He rich phase is essential for achieving such low temperatures. The ^{3}He rich phase has a lower density and will float on top of the ^{3}He dilute phase. To facilitate the cooling process, ^{3}He from the concentrated phase is transferred across the phase boundary into the ^{3}He dilute phase. In practice, this is accomplished by pumping on the ^{3}He dilute side, reducing the temperature to approximately 0.7 K. At this temperature, the vapor pressure of ^{3}He becomes about 1000 times higher than that of ^{4}He. As a result, a significant portion of ^{3}He is drawn out from the dilute phase, disrupting its desired equilibrium concentration of 6.6 %. This forces ^{3}He to cross the phase boundary and enter the dilute phase in order to reestablish equilibrium, leading to a positive change in entropy. For this to occur, energy must be absorbed from the environment, resulting in an overall decrease in the system's temperature.

3.3.2 Shasta cryostat

The experimental work presented in this thesis was conducted using a customized High Precision Devices Shasta cryostat (model 106). Fig. 3.3 shows the schematic of the modified Shasta cryostat. This cryostat was equipped with a Cryomech (model PT410) dual-stage pulse tube refrigerator (PTR). The first stage of the PTR maintained a nominal temperature of 60 K, while the second stage maintained a temperature of 2.8 K. In the original, unmodified cryostat configuration, the second stage of the PTR was used for pre-cooling an adiabatic demagnetization refrigerator (ADR). However, in the modified cryostat setup, we removed the ADR stage and replaced it with an Oxford 200 dilution unit. The dilution fridge has a base temperature of approximately 40 mK. One particularly notable and advantageous feature of this cryostat is its dry operation. In recent years, the acquisition of liquid helium for wet-style dilution fridges has become both costly and unpredictable. In our dry-style dilution fridge, only inexpensive and readily available liquid nitrogen is required for a charcoal cold trap within the room.

In a wet-style dilution fridge, pre-cooling of the ^{3}He-^{4}He mixture is accomplished using a ^{4}He bath and a 1 K pot condenser. However, in a dry-style dilution fridge, this pre-cooling is achieved by connecting the incoming return line to the cold stages of the PTR. The ^{3}He-^{4}He mixture enters the cryostat at the 300 K plate with copper tubing, reaching a copper gasket seal located within the main vacuum space. Stainless steel tubing connects this fitting to the PTR's first stage. From there, the gas passes through a charcoal trap designed to freeze out contaminants. This trap connects to tubing coiled around the PTR's second stage regenerator. Subsequently, the gas flows through a small copper-nickel capillary wound around a copper block mounted on the PTR second stage before entering the custom-made main flow impedance and the Oxford 200 Dilution unit.

On the output side of the dilution unit, the still's pumping orifice connects to a stainless steel pipe, which is thermally anchored with clamps to the PTR's first and second cold stages. A radiation baffle at the PTR first stage serves to block 300 K radiation from reaching the still. To accommodate thermal expansion and contraction stresses, a flexible bellows is positioned between the PTR first stage and the 300 K plate. At the top of the cryostat, the output of the still pipe is connected to a double-gimbal metal bellows, which

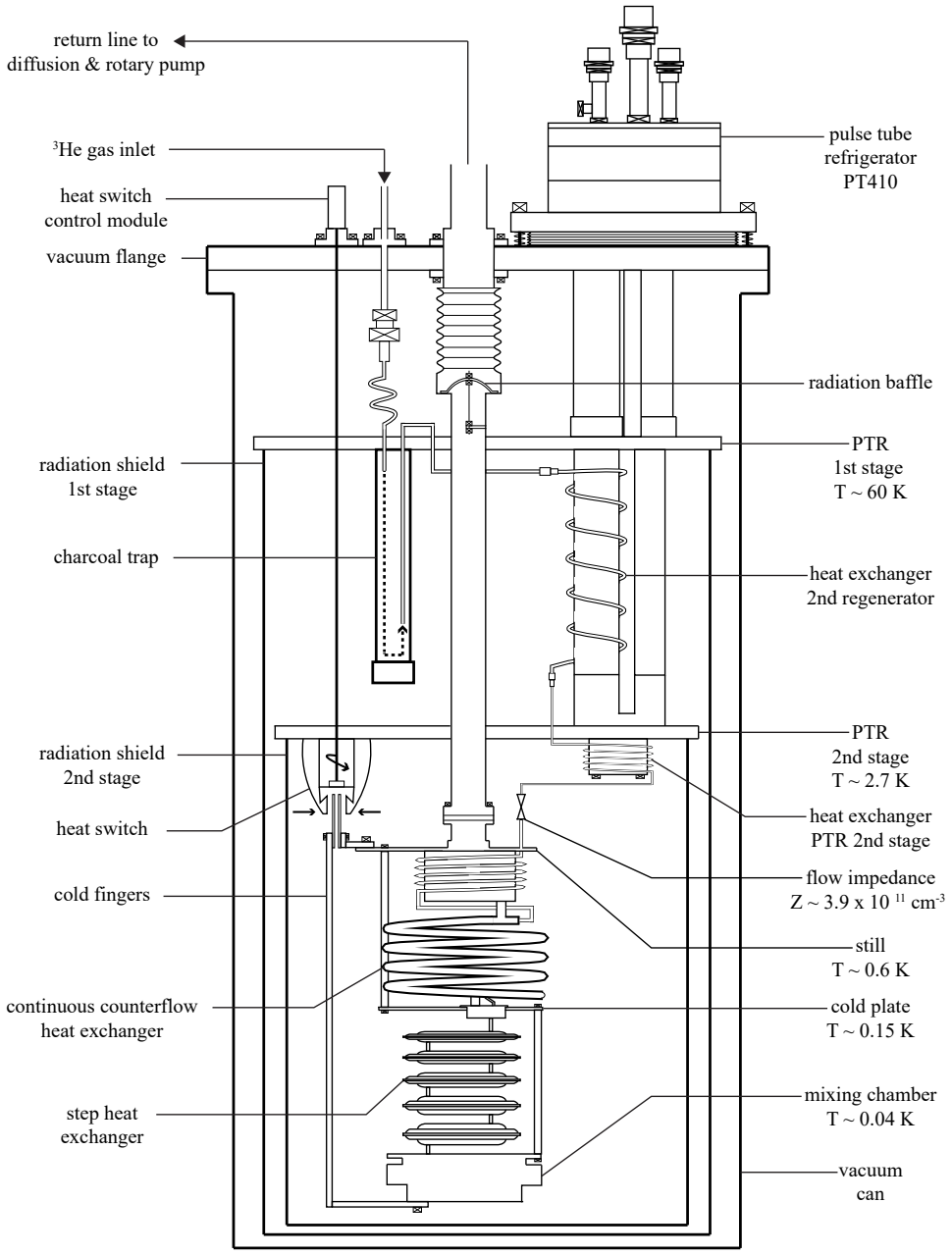


Figure 3.3: Schematic of the modified Shasta 106 cryostat, outlining the various cold stages, heat exchangers, and the Oxford 200 dilution unit.

was designed by Dr. David Pomaranski following the guidelines outlined in Ref. [53]. This gimbal system is specifically engineered to minimize vibrations transmitted to the cryostat from the pumping line due to the building and/or mechanical pumps. The still pumping line is connected to the gas-handling system via a 10-foot-long, 8" diameter PVC pipe. The pumping system is comprised of an oil vapor booster diffusion pump (Edwards, model 9B3) for achieving a low still pressure, backed by a mechanical rotary pump (Alcatel, model 402723). For more information regarding the cryostat modification, additional details can be found in Ref. [54].

3.3.3 Superconducting magnet

To conduct the magnetotransport measurements in Chapters 4 and 5, we installed a superconducting solenoid (magnet) on the second stage of the PTR. This magnet was purchased from Cryomagnetics and can generate a 9 T magnetic field within the central bore when supplied with 47.1 amps of current. We constructed thick copper cables for the room, and installed high-temperature superconducting leads (obtained from High Precision Devices) between the first and second stages of the PTR. These superconducting leads enable high-current operation for the magnet while introducing minimal heat load to the PTR's second stage. We observed that after the installation of the superconducting leads, the base temperature of the PTR's second stage increased by approximately 50 mK. Given the approximate cooling power of the second stage of the PTR is $\sim$ 1 mW/mK, this corresponds to a heat load of approximately 50 mW. This heat load was acceptable for operation of the dilution fridge, as the condensation of the ^{3}He/^{4}He mixture critically depends on maintaining the base temperature of the PTR's second stage. Fig. 3.4a shows a photo of the magnet installed in the cryostat next to the Oxford 200 dilution unit.

3.3.4 Sample cell and electrical filtering

Low-frequency twisted-pair wiring runs from a hermetic feedthrough located at the top of the cryostat to the mixing chamber, where the sample cell is mounted. For the segment of the wire that runs from room temperature to the PTR second stage at 2.8 K, we use

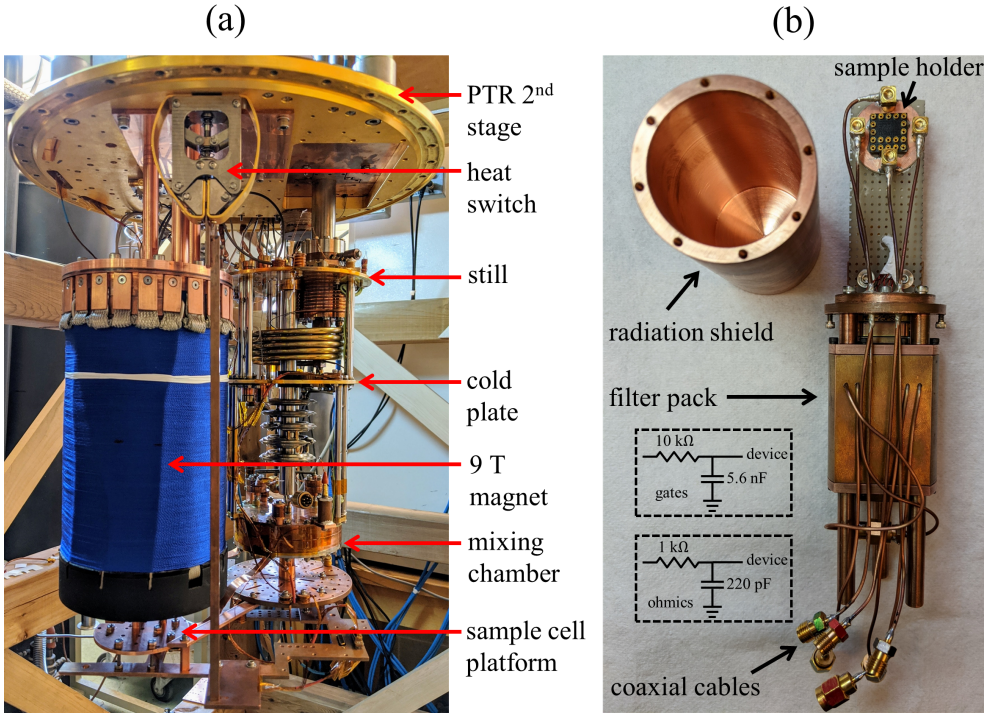


Figure 3.4: (a) Photo of the 2.8 K cold space within the cryostat and (b) sample cell used for measurements.

manganin wire. Beyond the PTR second stage, superconducting wire (copper-nickel clad with a niobium-titanium core) with poor thermal conductivity is used down to the mixing chamber. All the wiring is heat sunk at each successive cold stage by wrapping it around copper posts and securing it in place with GE varnish.

Measurements conducted at ultra-low temperatures are highly susceptible to external noise from the surrounding environment. In all experiments in this work, the sample was probed using electrical connections originating from room temperature electronics. Although shielding and the use of a twisted pair configuration help mitigate noise pickup from the wiring within the room and the cryostat, there will inevitably be some residual electrical noise that affects the sample. To first attenuate high-frequency noise, we implemented low-pass pi filters (Spectrum Control, model E, 800 kHz cutoff), which consist of inline inductors with capacitors grounded on either side, at the cryostat feedthroughs.

The sample cell used for experiments was constructed from copper and adapted based on a design by Dr. Jeffrey Mason. Fig. 3.4b shows a photo of the sample cell. This cell connects to low-frequency wiring on the fridge through a 25-pin micro-D connector, while high-frequency connections use UT-47 copper coaxial cables. The sample holder was designed by the NRC group, featuring a 19-pin socket and a high-frequency-compatible laminate printed circuit board (PCB, Rogers, TMM6). The sample holder was mounted on a standard PCB to provide structural support to the copper cold finger. Devices were GE varnished to the compatible chip carrier and plugged into the sample holder. A copper shield surrounds the device to shield it from 2.8 K radiation emanating from the PTR second stage.

To further reduce noise before reaching the sample, a compact single-pole RC-type filter was designed and constructed, as shown in Fig. 3.4b. For dc lines designated for metallic gates on the device that do not source current, we used 10 kΩ resistors and 5.6 nF discoidal capacitors (NPO dielectric, Spectrum Control), resulting in a cutoff frequency of 2.8 kHz. Meanwhile, for dc lines designated for current-carrying ohmic contacts, we increased the cutoff frequency to prevent heating effects and/or capacitive loading effects when using a current preamplifier. Therefore, the ohmic line filtering consisted of 1 kΩ resistors and 220 pF discoidal capacitors, producing a cutoff frequency of 720 kHz. To minimize the parasitic capacitance of the resistors, each resistor was securely mounted inside a hole in the copper block, where the hole's diameter was only slightly larger than that of the resistor. The resistors were thermally connected to the copper block using GE varnish.

Chapter 4

Spin-orbit splitting in dopant-free GaAs/AlGaAs two-dimensional hole gases

This chapter is adapted from: **N. A. Cockton**, F. Sfigakis, S. R. Harrigan, J. Baugh, Z. R. Wasilewski, S. A Studenikin, D. G. Austing, M. Korkusinski, G. Nichols, Z. Merino, A. Shetty, M. C. Tam, L. A. Tracy, J. L. Reno, T. Hargett, J. B. Kycia. Spin-orbit splitting in dopant-free GaAs/AlGaAs two-dimensional hole gases. Manuscript in preparation.

4.1 Introduction

The majority of research on low-dimensional semiconductor structures has focused on two-dimensional electron gases (2DEGs) within modulation-doped GaAs/AlGaAs heterostructures. The presence of dopants in modulation-doped devices can result in undesirable side effects, including reduced mobility, random telegraph noise, and poor reproducibility [55]. Alternatively, these issues can be mitigated by using devices fabricated from dopant-free GaAs/AlGaAs heterostructures, where the 2DEG is induced by a biased top-gate, operating analogously to enhancement-mode MOSFETs. Furthermore, in the context of quantum

devices, the promising properties of two-dimensional hole gases (2DHGs) in GaAs-based devices may provide significant advantages over their 2DEG counterparts, including reduced susceptibility to spin decoherence due to hyperfine interactions and strong spin-orbit interactions that enable electrical control of spin. In this chapter, we investigate 2DHGs created from dopant-free GaAs/AlGaAs heterostructures with the aim of enhancing device performance and developing a deeper understanding of the physics underlying future hole-spin-based quantum devices.

While dopant-free devices offer numerous advantages over their modulation-doped counterparts, one potential challenge with dopant-free devices is the possible induction of additional conduction channels within the system. The desired 2DHG is typically generated at the specified GaAs/AlGaAs interface, but unintended conduction may occur at a different interface in the heterostructure. It is critical to eliminate these parallel conducting channels to maintain precise electrostatic control over the targeted 2DHG of interest. Furthermore, while the tunable carrier density is an attractive feature in gated dopant-free devices, gate hysteresis could be another issue of concern. In this chapter, we study parallel conduction and gate hysteresis in our devices, resulting in fabrication improvements for future devices.

The spintronic properties of GaAs-based 2DHGs are of current interest for future quantum devices. Spin splitting in 2DHGs arises from either inversion asymmetry via spin-orbit interaction or an applied magnetic field via the Zeeman interaction. In this chapter, we will investigate both of these phenomena. We employ a Fourier transform technique to examine the Rashba spin-orbit splitting and effective masses of heavy-holes in our GaAs 2DHGs. We leverage our dopant-free 2DHGs, which enable us to attain higher mobilities (up to 70 m^2/Vs) compared to previous studies (7.7 m^2/Vs [56] and 65 m^2/Vs [57]). Notably, our devices demonstrate one of the largest spin-orbit splittings observed in GaAs 2DHGs. From analysis of the Zeeman spin splitting, we estimate the out-of-plane g factor and also gain insight of the heavy-hole character at higher magnetic fields in the quantum Hall regime.

4.2 Literature review

In this section, we will review previous experimental work characterizing spin-orbit splitting in 2DHGs and the methods employed to quantify the effective masses.

4.2.1 Spin-orbit splitting in 2DHGs

The first demonstration of Rashba spin-orbit interaction (SOI) induced spin splitting in a 2DHG was by Stormer *et al.* in 1983 [58]. They investigated magnetotransport in a GaAs/AlGaAs 2DHG heterojunction sample, which revealed a beating pattern in the Shubnikov-de Haas (SdH) oscillations, indicating the existence of two oscillation frequencies. The authors attributed these two frequencies to arise from two distinct Fermi surfaces resulting from the spin splitting.

Eisenstein *et al.* [59] expanded upon this study by comparing the SdH oscillations of a 2DHG in two different confinement potentials: a single heterojunction sample with a triangular well and a symmetric (square) quantum well. In the SdH oscillations of the single heterojunction, a distinct beating pattern was evident, whereas the square well only exhibited evidence of conventional Zeeman splitting. The frequencies of the oscillations were extracted to estimate the ratio of the spin-split subband populations p_+/p_-. In the case of the single heterojunction, p_+/p_- was found to be 2.44, while for the square well, it was 0.98. In the square well, the evenly spin-split populations are due to Zeeman splitting. However, in the heterojunction sample with an asymmetric confinement potential, spin-orbit splitting resulted in different populations for the two spin states. Additionally, the ratio p_+/p_- in the heterojunction sample was found to be independent of the perpendicular magnetic field, indicating that the spin degeneracy was already lifted even at B = 0.

In the samples described above, the electric fields responsible for the asymmetric confinement potential were determined by heterostructure composition (intentional doping) and were therefore fixed. However, the confinement potential can be electrically tuned in devices where the electric field is supplied by an external gate. This was first demonstrated by Wieck *et al.* in a (100) Si MOSFET 2DHG [60], where the strength of the spin-orbit splitting was tuned by adjusting the gate voltage, which also changed the hole density. A

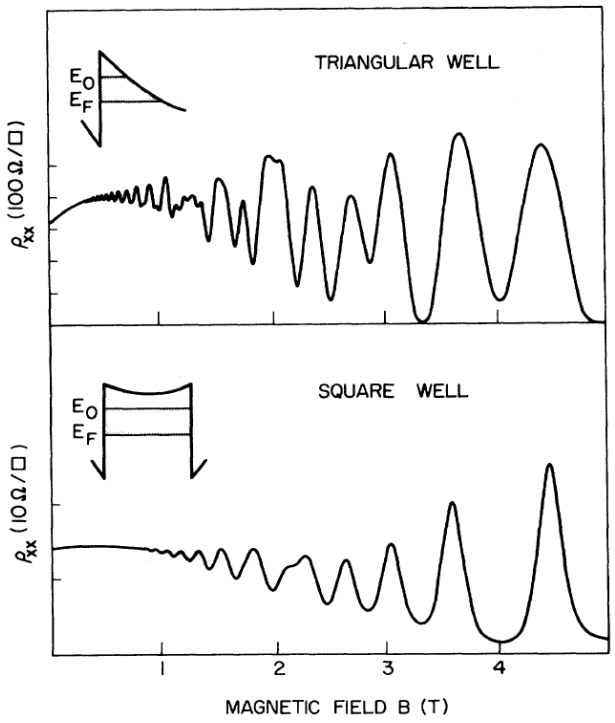


Figure 4.1: Shubnikov-de Haas (SdH) oscillations for single heterojunction sample with a triangular well (top panel) and for a symmetric square well (bottom panel). A clear beating pattern is observed for the single heterojunction sample while the square well sample shows no beating pattern. Adapted from Ref. [59] with permission.

similar experiment was later carried out by Lu *et al.* for a (311) GaAs/AlGaAs 2DHG heterojunction [61]. In both reports, the authors found that the spin-orbit splitting increased with hole density. However, in the single gated devices used in these two experiments, changing the gate voltage also resulted in changes to the hole density, thus inextricably linking the confinement potential asymmetry and carrier density.

Subsequently, double-gated devices were fabricated with a top- and back-gate. This enabled the investigation of the spin-orbit splitting strength at a constant density, and separation of the effects of the confinement potential from density. This was first demonstrated by Papadakis *et al.* with a top- and back-gated (311) GaAs quantum well (QW) [62]. In this setup, the QW's asymmetry, and consequently the electric field ϵ_z across the

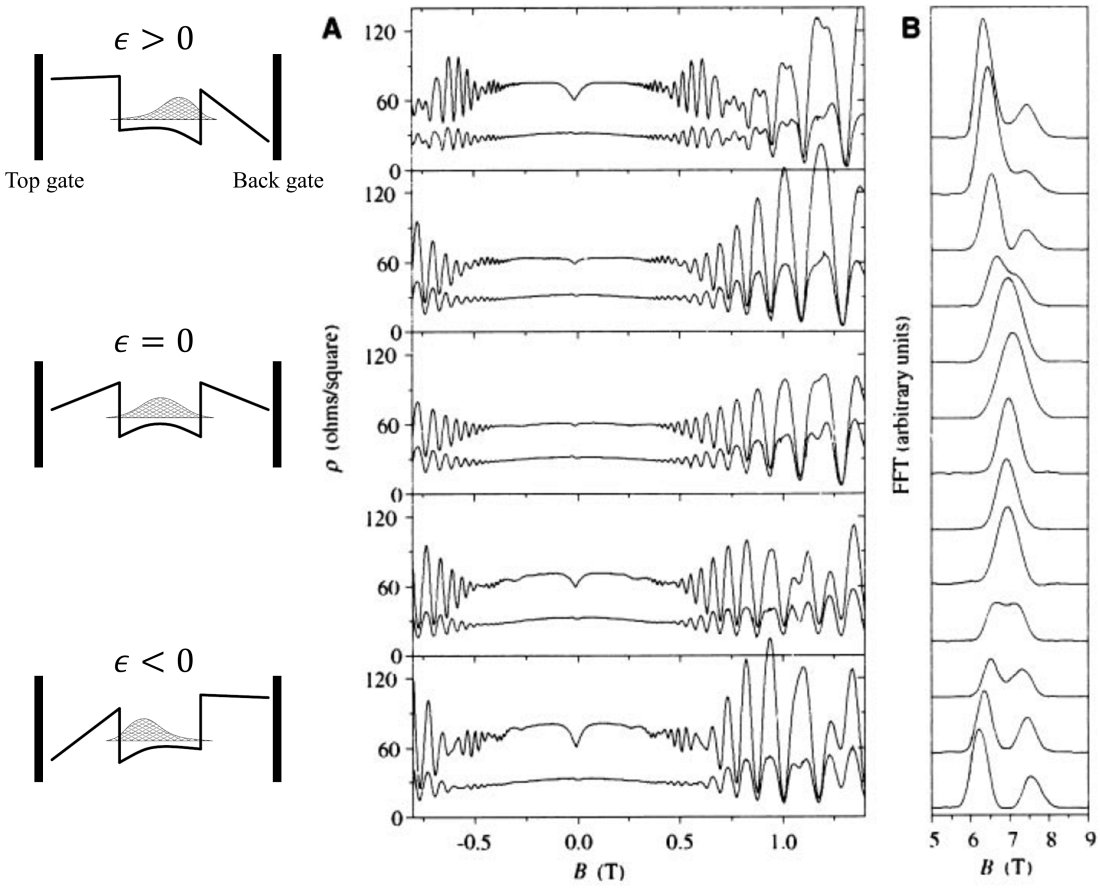


Figure 4.2: The diagrams on the left (taken from [22]) indicate the shape of the quantum well (QW) based on the confinement potential. Front and back gates are used to adjust the net electric field ϵ across the QW from positive, through zero, to negative. (a) SdH oscillations for a (311) GaAs 2DHG QW at a fixed hole density of $p_{2d} = 3.3 \times 10^{15}$ m^{-2} for two crystal directions [top trace $(01\bar{1})$ and bottom trace $(\bar{2}33)$]. (b) Fast Fourier transform of the SdH oscillations. When the QW is asymmetric ($|\epsilon| > 0$), beating occurs and two peaks are resolved. When the QW is symmetric ($\epsilon = 0$), there is no beating and only one peak is resolved. Adapted from Ref. [62] with permission.

heterostructure, could be adjusted from positive to zero and to negative values, all while maintaining a constant density of $p_{2d} = 3.3 \times 10^{15}$ m^{-2} (see left panel of Fig. 4.2). In Fig. 4.2, panel (a) shows the SdH oscillations, while panel (b) displays the corresponding frequencies obtained using a Fourier transform (FT). When the QW is asymmetric ($|\epsilon_z| > 0$), the SdH oscillations exhibit a beating pattern and two distinct frequency components are resolved in the FT. The difference in frequency between these FT peaks increases with ϵ_z, serving as a measure of the strength of the spin-orbit splitting. In contrast, when the QW is symmetric ($|\epsilon_z| = 0$), the SdH oscillations show no beating, and only one frequency component is present. Thus, this experiment demonstrates that spin-orbit splitting can be electrically tuned on or off by altering the shape of the confinement potential, independent of density.

4.2.2 Effective masses in 2DHGs

In a 2DHG of an asymmetric quantum well (QW), the beating pattern in the SdH oscillations complicates the determination of the effective mass. The spin-orbit splitting results in the heavy-hole (HH) band splitting into two subbands, HH- and HH+, with effective masses m_1 and m_2, respectively. At low magnetic fields, only the lighter effective mass m_1 is typically observable and can be extracted using the standard technique of analyzing the resistivity amplitude decay $\Delta\rho_{xx}/\rho_{xx}$ of SdH oscillations as a function of temperature [63, 64]. The heavier effective mass m_2 can then be inferred by assuming a parabolic dispersion, leading to $m_2/m_1 = p_2/p_1$ as used in Ref. [59], or $m_2/m_1 = \tau_2/\tau_1$ as in Ref. [65]. However, the valence bands cannot be accurately approximated by parabolic dispersion relations. Furthermore, the evaluation of effective masses from cyclotron resonance experiments is also problematic. Most experiments either report a single value for the HH band [66, 67, 68, 69] or measure two values at high magnetic fields, making it challenging to relate them to values near B = 0 [70].

Habib *et al.* were the first to deduce the HH effective masses in transport measurements without assuming parabolic dispersion curves for HH- and HH+ [56] (see Fig. 4.3). They conducted magnetotransport measurements in a (100) GaAs/AlGaAs 2DHG heterojunction and applied a Fourier transform to the SdH oscillations in 1/B. The individual spec-

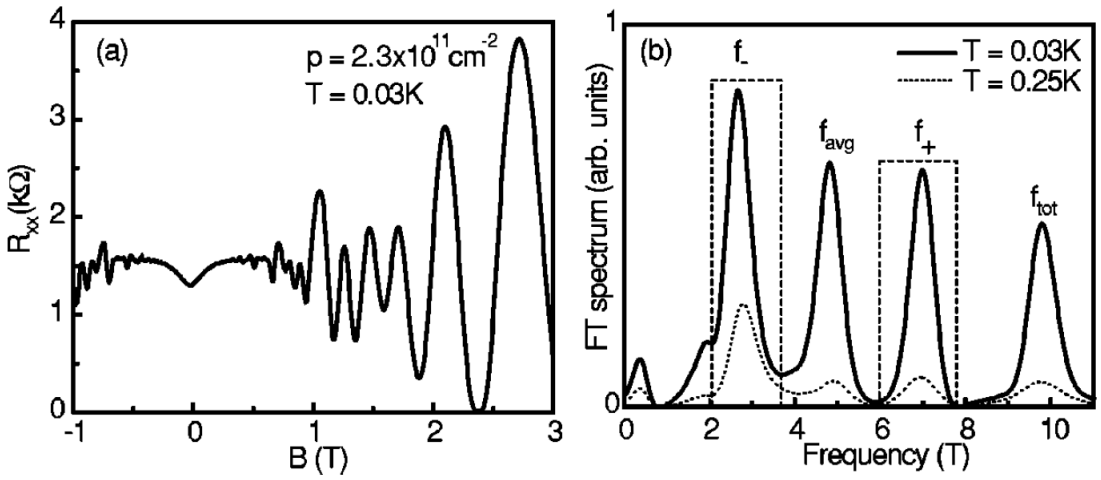


Figure 4.3: (a) Shubnikov-de Haas (SdH) oscillations of a (100) GaAs/AlGaAs 2DHG heterojunction, showing a beating pattern. (b) Fourier spectrum of the oscillations at T = 0.03 K and 0.25 K. Dashed boxes show the square windows used to isolate the two frequencies f_+ and f_- for the effective mass analysis. Adapted from Ref. [56] with permission.

tral components for HH- and HH+ were then isolated using finite-width square-window filters, as depicted in Fig. 4.3b. Once a peak is isolated in Fourier space, the inverse Fourier transform reveals the corresponding SdH oscillations. The effective masses were subsequently extracted using the standard technique of analyzing the resistivity amplitude decay $\Delta\rho_{xx}/\rho_{xx}$ of SdH oscillations of the isolated HH- and HH+ as a function of temperature. However, this technique cannot be applied when there is a small separation between successive peaks (small SO splitting). To address this limitation, Nichele *et al.* extracted the effective masses by simply analyzing the temperature decay of the individual peaks for HH- and HH+ in Fourier space [57]. This method is suitable for situations with limited SO splitting and was employed in this study to estimate the effective masses of heavy holes (HH) in our dopant-free GaAs 2DHGs

4.3 Experimental methods

4.3.1 Measurement setup

Magnetotransport measurements were conducted in a dilution refrigerator with a base temperature of $\sim$ 40 mK, equipped with a 9 T magnet (see Chapter 3 for details). The Hall bar was probed in a constant current mode using the measurement circuit depicted in Fig. 4.4. To prevent Joule heating, currents of less than 3 nA were employed. Two Stanford Research Systems (SRS, model SR830) lock-in amplifiers (LIAs) were employed to simultaneously measure the longitudinal voltage drop (ΔV_{xx}, LIA-1) and transverse voltage drop (ΔV_{xy}, LIA-2) of the Hall bar. These two LIAs were synchronized at a frequency of 17 Hz. The sine output from LIA-1 was connected to a 100:1 voltage divider and then through a 10 MΩ current-limiting resistor to the source contact of the Hall bar, while the drain contact was electrically grounded. The DC voltage for the top-gate was supplied with an IOtech digital-to-analog converter (DAC, model DAC488HR/4).

To reduce the noise level in the Shubnikov-de Haas oscillations (ΔV_{xx}) when using weak excitation currents of $\sim$ 1 nA, we utilized a low-noise differential preamplifier. The amplifier design was described by Scandurra *et al.* in Ref. [71], and was constructed by Dr. David Pomaranski. The amplifier featured a voltage gain of 100$\times$ and an equivalent input voltage noise of 1.2 nV/$\sqrt{Hz}$ at 10 Hz and 1 nV/$\sqrt{Hz}$ at 1 kHz. By comparison, the SR830 LIA alone typically has an input voltage noise of 6 nV/$\sqrt{Hz}$ at 1 kHz. Since measuring ΔV_{xx} and ΔV_{xy} simultaneously required sharing one of the Hall bar contacts (see Fig. 4.4), the noise from LIA-2 measuring ΔV_{xy} would increase the noise at the preamplifier input measuring ΔV_{xx}, with the noise adding in quadrature. Consequently, to fully benefit from the lower noise of the preamplifier, we often exclusively measured ΔV_{xx} to attain a lower noise.

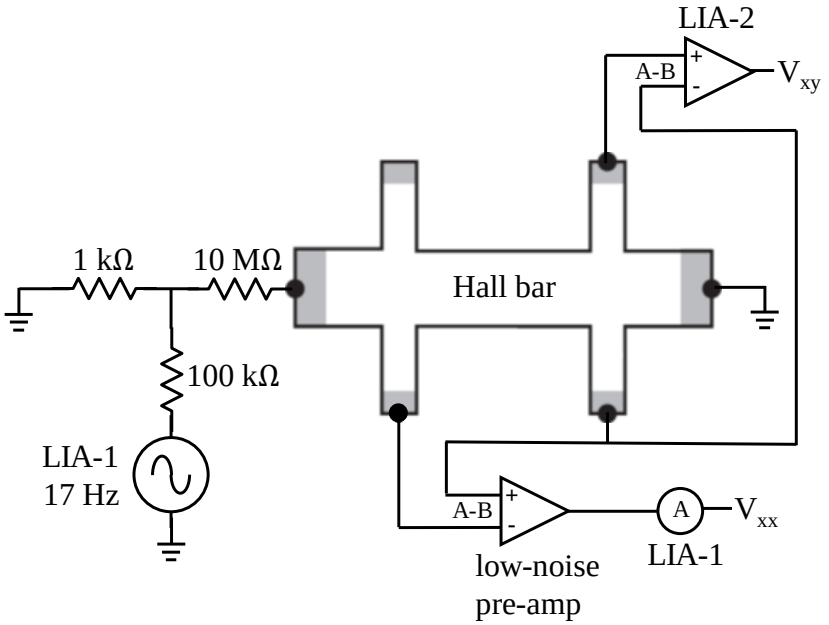


Figure 4.4: Schematic of the circuit used for the measurements of the Shubnikov-de Haas oscillations and Hall voltages. A SR830 lock-in amplifier produced an alternating current through the Hall bar and the longitudinal (ΔV_{xx}) and transverse (ΔV_{xy}) voltages were measured. The longitudinal voltage was measured using a custom-built low-noise differential voltage preamplifier. See text for details.

4.3.2 Wafers and sample fabrication

Five GaAs/AlGaAs heterostructures were analyzed in this work, all of which were grown using molecular beam epitaxy (MBE). Fig. 4.5 presents the MBE layer structure and the AlGaAs composition for each of these wafers. Wafer VB1137 was grown at Sandia National Laboratories, whereas the remaining four wafers were grown at the University of Waterloo by Prof. Zbig Wasilewski's group (led by Dr. Man Chun Alan Tam). All of the heterostructures were grown on semi-insulating (SI) GaAs (100) substrates without any doping. Some wafers, namely VB1137, G372, and G373, were grown with a smoothing superlattice in the buffer layer, while others, G265 and G522, employed low-temperature (LT) GaAs instead. The superlattice buffer was comprised of alternating GaAs and AlGaAs layers, used to clean the MBE chamber and suppress structural defects during growth.

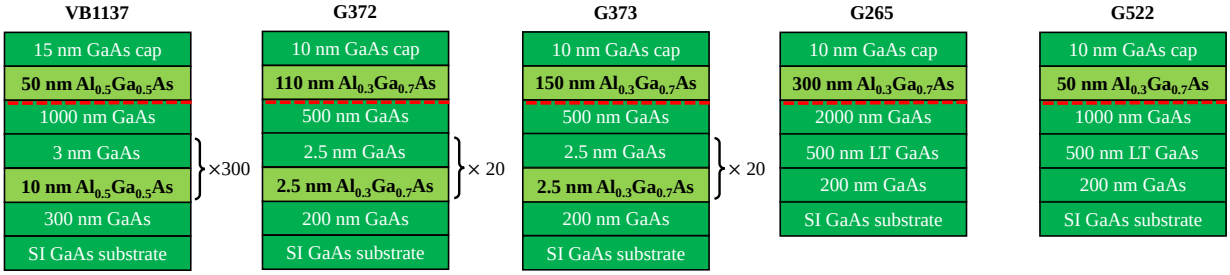


Figure 4.5: Layer structure of the five GaAs/AlGaAs heterostructures characterized (not to scale). The red dashed line indicates the location of the induced 2DHG.

Single-gated Hall bars were fabricated on all wafers at the University of Waterloo by Prof. Jonathan Baugh's group. The Hall bar channel was oriented in the high-mobility crystal direction $[1\bar{1}0]$ and had dimensions of 300 μm in length and 50 μm in width. In the case of the G522 wafer, additional narrow Hall bars with a 15 μm wide channel were also fabricated. Consequently, samples from the G522 wafer are designated as G522-50 (with a 50 μm wide Hall bar) and G522-15-1, G522-15-2 (two identical 15 μm wide Hall bars). The fabrication details of the recessed ohmic contacts can be found in Refs. [43, 49, 42]. The p-type ohmic contacts were created through the deposition of an AuBe alloy followed by annealing. A 300 nm layer of SiO_2 was deposited on top of the heterostructure using plasma-enhanced chemical vapor deposition (PECVD). Above this gate dielectric, a patterned Ti/Au top-gate was deposited, which overlapped with the ohmic contacts and the Hall bar channel. By utilizing the field effect generated by the insulated top-gate, a 2DHG was induced (accumulation mode) at the GaAs/AlGaAs interface, located $60-310$ nm below the GaAs/SiO_2 interface. Typical ohmic contact resistances were measured from a combination of two- and four-terminal measurements and were found to be less than 800 Ω at B = 0, and $5-7$ kΩ at B = 5 T.

4.3.3 2DHG density and gate hysteresis

When the top-gate voltage V_g is zero, the dopant-free Hall bars do not conduct. For all Hall bars reported here with 300 nm of SiO_2, $V_g < -1$ V is necessary to induce a 2DHG. Typically, when -5 V $< V_g <$ -3 V, the hole density can be linearly tuned within the range of

$0.75 < p_{2d} < 2.5 \times 10^{15}$ m^{-2}. When -3 V $< V_g <$ -1.5 V, the resistances of the ohmic contacts become very large ($\gtrsim 10\ k\Omega$), making it challenging to obtain accurate measurements of the Hall bar voltages in this range. Typically, when $V_g = V_0 < -5$ V, the voltage-density relationship $p_{2d}(V_g)$ shifts irreversibly towards more negative top-gate voltages for a given cooldown, by $\Delta V = V_0 + 5$ V. By cycling the sample to room temperature for several hours with all contacts grounded, the original $p_{2d}(V_g)$ can be recovered in a subsequent cooldown. The mechanism behind the observed top-gate voltage shift ΔV is attributed to the trapping of charges at the GaAs-SiO_2 interface at the top of the heterostructure. These charge traps become populated when holes from the 2DHG tunnel through the AlGaAs barrier while $V_g < -5$ V. These charge traps generate an opposing electric field that screens the field from the top-gate. Factors influencing the value of V_0 include the thickness and aluminum composition of the AlGaAs barrier, the thickness of the gate dielectric, and the permittivity of the dielectric material.

For small magnetic fields (< 0.5 T), the Hall resistance r_{xy} exhibits a linear relationship with the magnetic field B, in accordance with the classical Hall effect. To determine the hole density p_{2d} of our 2DHGs, we used the slope of $r_{xy}(B)$ between 0.1 T and 0.2 T and the following relation: $slope = 1/(e \cdot p_{2d})$, where e is the elementary charge. Measurement of the slope, rather than measuring r_{xy} at a single B-field value, eliminates any offsets that may occur in r_{xy} at $B = 0$. Fig. 4.6a shows p_{2d} as a function of top-gate voltage V_g for two samples, G522-50 and VB1137. As expected, the density-voltage profile is linear. The slope of this profile reflects the dielectric strength and thickness, primarily influenced by the 300 nm of SiO_2, while the x-intercept represents the turn-on voltage required to induce the 2DHG. For sample VB1137, the turn-on voltage was approximately $V_g \sim -1.5$ V, and the density-voltage profile remained stable within the range of -5 V $< V_g < -3$ V. However, for sample G522-50, V_0 was approximately -4.5 V instead of -5 V, leading to a shift in the voltage-density curve of about $\Delta V \sim -0.5$. Consequently, the operational range of G522-50 was limited to -4.5 V $< V_g < -3$ V. Samples G372, G373, and G265 exhibited similar turn-on voltages to VB1137, ranging from approximately -1.0 V to -1.5 V, as depicted in Fig. 4.6b. The slightly shallower slope of G265 is attributed to the significantly thicker AlGaAs layer of 300 nm, compared to G373 and G372, which have layer thicknesses of less than 150 nm.

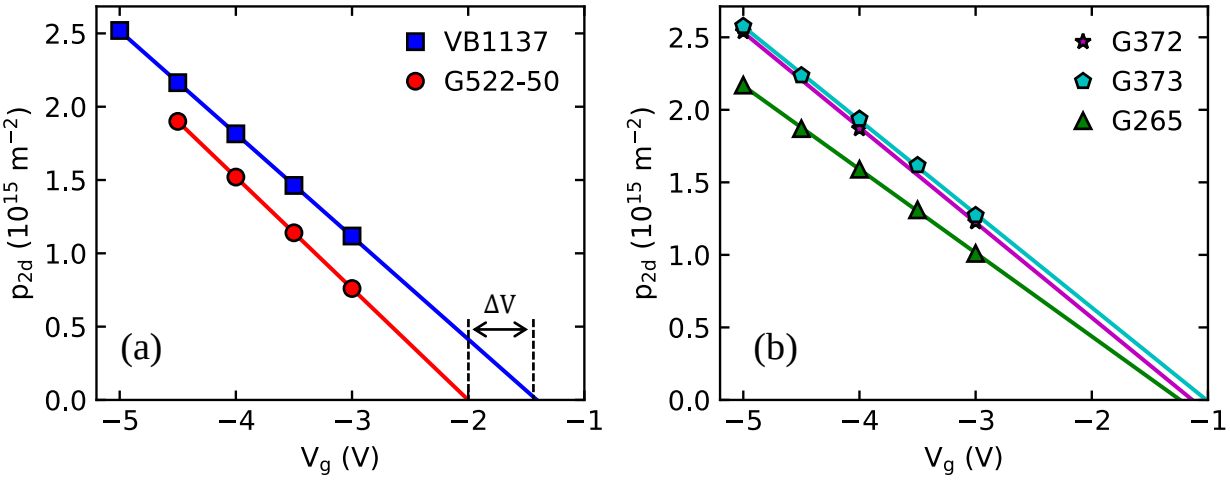


Figure 4.6: Hole density (p_{2d}) extracted from the Hall effect as a function of top-gate voltage (V_g) for (a) VB1137 and G522-50 and (b) G372, G373, and G265.

The thickness of the AlGaAs layer above the 2DHG was identical (50 nm) for both G522-50 and VB1137 (see Fig. 4.5). However, the aluminum content in the AlGaAs layer differed, with VB1137 containing 50% aluminum while G522-50 had only 30%. A higher aluminum content increases the AlGaAs barrier height, which likely inhibits holes in the 2DHG from populating charge traps at the GaAs-SiO_2 interface. Thus, this difference in aluminum content likely accounts for the reduced V_0 observed in G522-50 compared to VB1137. In samples G372, G373, and G265, the AlGaAs thickness exceeded 110 nm, preventing this issue from occurring. However, in the case of electrostatically defined structures with surface metallic gates (i.e., lateral quantum dot devices), it is advantageous to use a minimal AlGaAs thickness to achieve finer features in the 2DHG. Consequently, increasing the AlGaAs thickness to prevent this issue is typically undesirable. Instead, this observation highlights the importance of using 50% aluminum content in the AlGaAs layer to prevent gate hysteresis for top-gate voltages up to $V_g = -5$ V across devices with varying 2DHG depths. Additionally, this will also increase the upper limit of the top-gate voltage (V_0) and, consequently, increase the maximum achievable hole density.

4.3.4 Shubnikov-de Haas oscillations

In this section, we present the Shubnikov-de Haas (SdH) oscillations in a 2DHG, for the G522-50 Hall bar. Fig. 4.7a shows the longitudinal resistivity as a function of perpendicular magnetic field for T = 40 mK and $p_{2d} = 1.5 \times 10^{15}$ m^{-2}. The B-field was swept from 0.1 T to 1.5 T at a rate of 0.5 T/hour. The SdH oscillations show a beating pattern consistent with the spin-orbit splitting of the heavy-hole (HH) band. To reveal the individual HH- and HH+ populations, a Fourier transform (FT) of the SdH oscillations in 1/B is performed. The FT analysis employs standard techniques such as background subtraction, windowing and zero-padding (see Appendix A for details). For the FT to be valid, the analysis is limited to small magnetic fields where $\rho_{xx} \neq 0$. Fig. 4.7b shows the Fourier spectra of the SdH oscillations of the data in Fig. 4.7a. The frequency axis f can be directly converted into hole density p by $p = f \cdot e/h$. Several distinct peaks in the Fourier spectra can be resolved. The peak labeled $(p_1 + p_2)$ matches the Hall density p_{Hall}, which matches the sum of the individual peaks p_1 and p_2. The peak labeled $2p_1$ arises from the low B-field Zeeman splitting and is also a harmonic of p_1. The peak labeled $(p_1 + p_2)/2$ corresponds to the average of the peaks p_1 and p_2. This anomalous peak has been reported before [57, 72], and has been interpreted using non-adiabatic effects [73]. In Figs. 4.7a-e, four successive and distinct SdH regimes can be identified at different magnetic field ranges. The magnetic field values bounding these regimes vary with hole density p_{2d}, but occur in a successive order of appearance:

- Regime I, with a single SdH frequency (p_1)
- Regime II, with Zeeman splitting $(p_1; 2p_1)$
- Regime III, with spin-orbit splitting $(p_1; p_2)$
- Regime IV, with the quantum Hall effect onset

Regime I is most clearly illustrated in sample G265 within the magnetic field range of 0.07 T to 0.20 T (see Fig. 4.7c), where the first SdH oscillations become visible. Landau levels have formed and can be distinguished because their energy separation, $\hbar\omega_c = \hbar eB/m^*$,

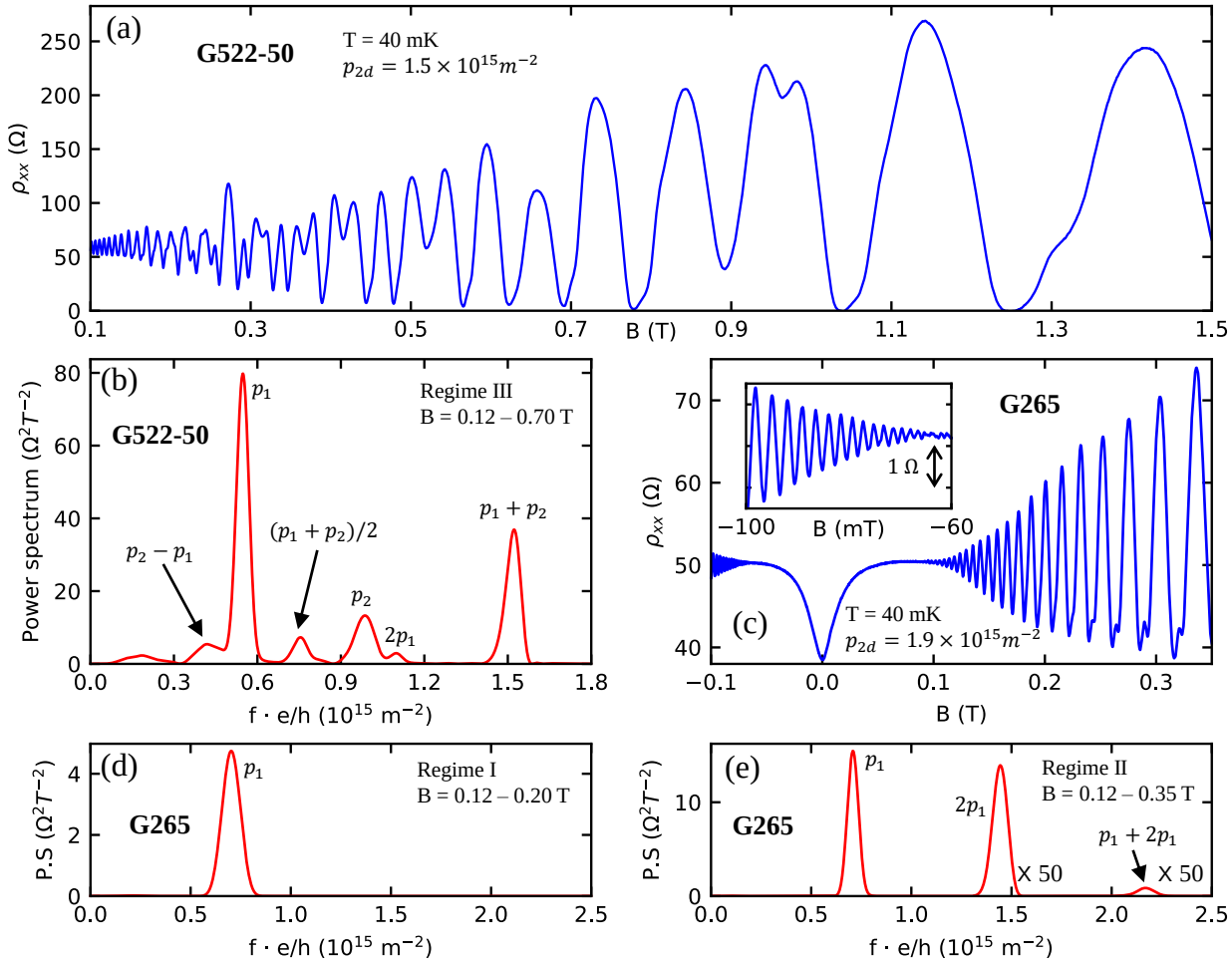


Figure 4.7: (a) Shubnikov-de Haas (SdH) oscillations at T = 40 mK and $p_{2d} = 1.5 \times 10^{15}$ m^{-2} for G522-50. (b) Corresponding Fourier transform of the SdH oscillations from panel (a). (c) SdH oscillations at low B-fields with inset providing a closer view of the same dataset for G-265. Power spectrum (P.S.) of the Fourier transform on the data in panel (c) illustrating (d) Regime I and (e) Regime II (see text).

exceeds the thermal energy k_BT. At very low temperatures (T < 50 mK) however, it is the mobility (i.e., disorder) that dictates the B-field onset of SdH oscillations. Disorder effectively reduces the Landau level energy separation. The full width at half maximum (FWHM) of a Lorentzian-shaped Landau level can be defined as 2Γ, where $\Gamma = \hbar/2\tau_q$ and τ_q is the quantum lifetime [64]. Consequently, SdH oscillations become apparent only when the temperature satisfies the condition $k_BT < (\hbar\omega_c - 2\Gamma)$. In all of our samples, the onset of SdH oscillations occurs near B $\sim$ 60 mT, a strong indication of high mobility and low disorder. The positive magnetoresistance observed for B < 0.1 T (see Fig.4.7c) has been interpreted with classical two-band transport [74, 75]. In our high-mobility, low-disorder samples, we do not observe any evidence of weak anti-localization (WAL) effects, which typically manifest as a small resistivity dip around zero magnetic field [19].

Significantly, only one SdH oscillation frequency p_1 is observed in Regime I; no other peaks are present in the Fourier spectrum from Fig. 4.7d. One possible explanation is that the energy splitting between the HH- and HH+ is too small to be resolved at this temperature. However, this same energy splitting is clearly resolved at higher magnetic field, so this explanation is unlikely to be correct. Recalling that the Landau level energy spacing has a direct dependence on effective mass, two sets of Landau levels might form, one set for each effective mass present in the 2DHG, m_1 and m_2. In this scenario, only one set of SdH oscillations is visible because $k_BT < (\frac{\hbar eB}{m_1} - 2\Gamma)$ for HH- whereas $k_BT > (\frac{\hbar eB}{m_2} - 2\Gamma)$ for HH+, i.e. the Landau level energy separation for the higher effective mass m_2 is too small to be resolved at this temperature. Stated differently, the HH-/HH+ spin-orbit splitting has already occurred even for B = 0, but the SdH oscillations associated with HH+ are simply not resolved at this temperature and magnetic field. At larger magnetic fields $B \gtrsim 0.3$ T, the Landau level energy spacing becomes sufficient to resolve the SdH oscillations from both m_1 (HH-) and m_2 (HH+).

Regime II is best illustrated in sample G265 within the magnetic field range of 0.20 T to 0.35 T (see Fig. 4.7c), where a second SdH oscillation frequency appears at $2p_1$ (see Fourier spectrum in Fig. 4.7e), twice the value of the SdH frequency observed in Regime I. This second set of SdH oscillations is consistent with an out-of-plane Zeeman splitting, $g^*_\perp \mu_B B$, where $g^*_\perp$ is the out-of-plane Landé g factor. For GaAs holes, $g^*_\perp = 7.2$ is theoretically predicted [22], while experimental studies have extracted values in the range

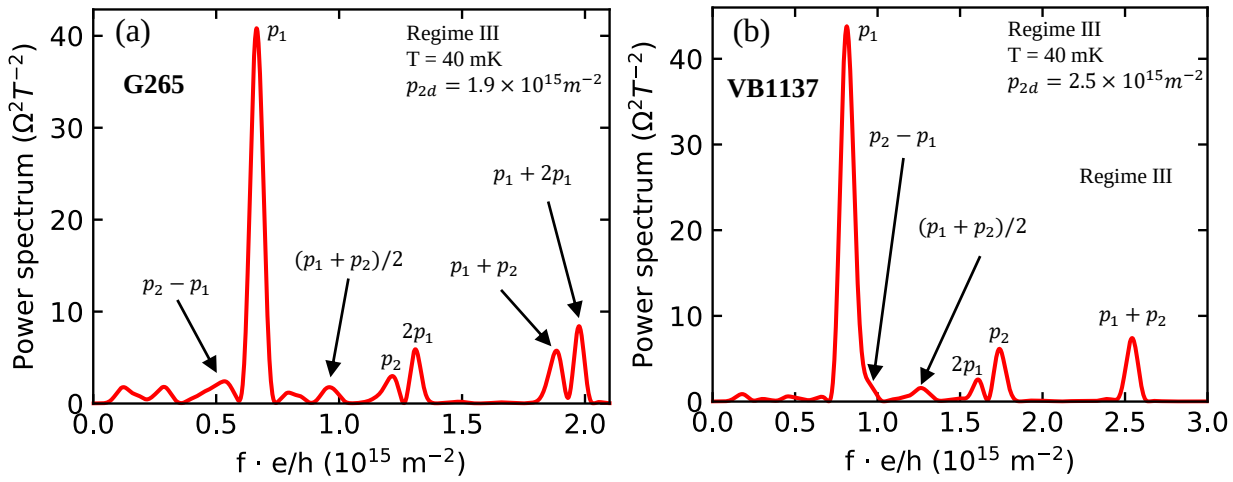


Figure 4.8: Fourier spectra of the SdH oscillations for samples (a) G265 and (b) VB1137 in Regime III.

of $g^*_\perp \sim 2-7$ [76, 77, 78, 79]. In Sec. 4.3.10, we will experimentally measure $g^*_\perp$. The onset of Zeeman spin-splitting occurs at similar B-field values observed in literature [80, 81], when $g^*_\perp \mu_B B > k_B T$. This transitory regime occurs briefly after the onset of the first SdH oscillations but before the onset of the complex SdH beating pattern. The small $(p_1 + 2p_1)$ peak observed in Fig. 4.7e is an artifact of the Fourier analysis, and does not correspond to any real SdH oscillations.

Regime III is best observed in sample G522-50 within the magnetic field range of 0.25 T to 0.75 T [see Fig.4.7a], where the SdH oscillations from HH+ become resolved, i.e., $k_B T < (\frac{\hbar e B}{m_2} - 2\Gamma)$. The SdH beating pattern now emerges, and p_2 appears in the Fourier spectrum for the first time [see Fig.4.7b]. Fig. 4.8 shows examples of the Fourier spectra in Regime III for samples G265 and VB1137.

The first three regimes can also be identified without the Fourier analysis by simply plotting the Landau level filling factor ν as a function of inverse magnetic field. Fig. 4.9a shows the SdH oscillations in 1/B for sample G522-50. The peaks in the SdH oscillations correspond to half-integer values of the Landau level filling factor ν. The filling factor index is determined for the SdH peaks for $B \gtrsim 1$ T in the quantum Hall regime by the corresponding Hall plateau. For each successive peak upon decreasing the B-field (increase

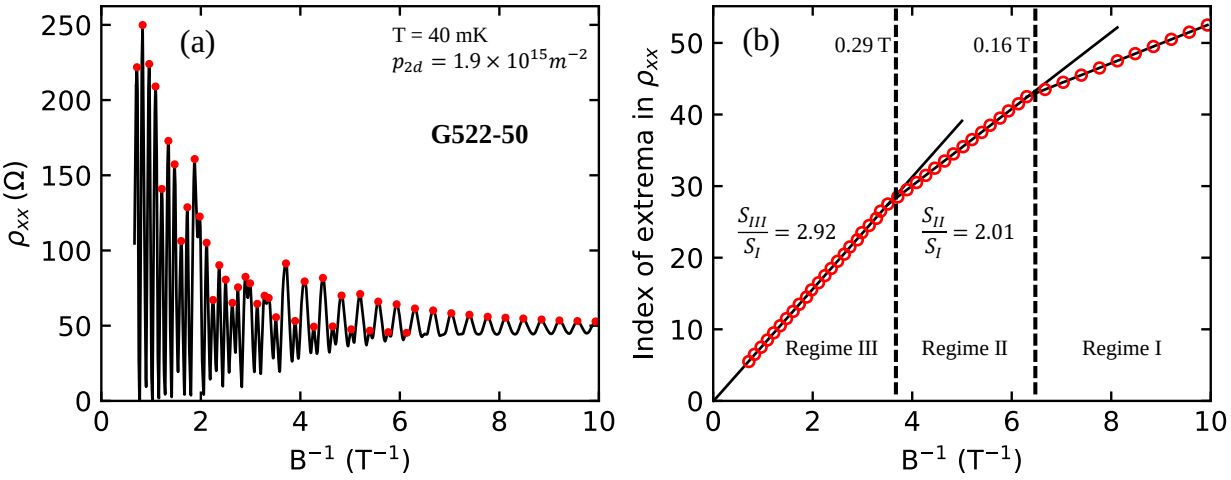


Figure 4.9: (a) SdH oscillations as a function of inverse magnetic field. (b) Index of extrema [red data points in panel (a)] of ρ_{xx} as a function of 1/B. The three regimes are clearly identified by changes in slope.

in 1/B), the Landau level index is incremented by a value of one. Fig. 4.9b shows the Landau level index as a function of 1/B for 0.1 T < B < 1.5 T. A linear trend is observed for each regime, and the slope of each line (S_I, S_{II}, S_{III}) can be directly converted into hole density p by $p = slope \cdot e/h$. For Regime I we obtain $p_1 = S_I \cdot e/h$ while for Regime II we obtain $2p_1 = S_{II} \cdot e/h$. From right to left in Fig. 4.9b, the change in slope at B = 0.16 T corresponds to the transition from Regime I to Regime II. For Regime III we obtain $p_1 + p_2 = p_{Hall} = S_{III} \cdot e/h$. Similarly, the change in slope at B = 0.29 T corresponds to the transition between Regime II to Regime III. It is noteworthy that Regime II was also discernible using this technique, albeit not explicitly identified, in one of the earliest publications in GaAs 2DHGs (see "triangular well" in Fig. 4.1 from Ref.[59]). This straightforward examination of the data clearly demonstrates that Regime II is real and not merely an artifact of the Fourier analysis.

Finally, Regime IV occurs for magnetic fields larger than $B \gtrsim 1$ T, when the SdH oscillation minima reach zero resistance ($\rho_{xx} = 0$). Due to $\rho_{xx} = 0$, Fourier analysis is not appropriate in this regime. Nevertheless, the SdH oscillations in Regime IV continue their periodicity from Regime III (see Fig. 4.9), reflecting the total hole density $p_1 + p_2 = p_{Hall}$.

4.3.5 Parallel conduction

Well-defined SdH oscillations at low temperatures were observed in all Hall bars. However, samples fabricated from wafers grown with a smoothing superlattice buffer (see VB1137, G372, G373 in Fig. 4.5) displayed evidence of parallel conduction. The most sensitive and universal sign for parallel conduction is the lifting of SdH oscillation minima above $\rho_{xx} = 0$ at high magnetic fields in the quantum Hall regime. This is best illustrated by comparing the high B-field data from samples G522-50 and VB1137. Fig. 4.10 shows ρ_{xx} and r_{xy} for the two samples with filling factors $\nu = 1 - 4$ labeled using the Hall plateaus. For the sample G522-50 with no superlattice buffer, the SdH minima first reach $\rho_{xx} = 0$ at B $\sim$ 1.5 T ($\nu \sim 6$) and this behaviour persists up to B = 9 T ($\nu = 1$). However, for the sample VB1137 with a superlattice buffer, the SdH minima never reach zero, with $\rho_{xx} \sim 5\ \Omega$ when B $= 1 - 2$ T ($\nu = 4 - 6$) and increasing to $\rho_{xx} \sim 60\ \Omega$ at B = 7 T ($\nu = 1$).

Another, less sensitive symptom of parallel conduction in a 2DHG is a mismatch between the total hole density extracted from the Hall effect and the 2DHG carrier density extracted from the FT analysis of SdH oscillations. In our single heterojunction 2DHGs, the HH-/HH+ spin-splitting causes two frequencies to appear in the FT of the SdH oscillations, yielding two separate carrier densities (FT frequencies), p_1 and p_2. The sum of the two HH density components equals the total 2DHG carrier density, $p_1 + p_2$. Ideally, $p_1 + p_2$ should be equal to the Hall density, $p_1 + p_2 = p_{Hall}$, as shown in Fig. 4.11a and 4.11b for G265 and G522-50, respectively. On the other hand, Fig. 4.11c shows that $p_1 + p_2 \neq p_{Hall}$ for G372, where the difference amounts to at least 20% of the 2DHG density. The difference between the Hall and SdH densities is also at least 10% for G373 (Fig. 4.11d), but is at most 1% for VB1137 (Fig. 4.11e). The most likely culprit for the observed parallel conduction is the low-density population of one or more of the $2.5 - 3$ nm wide GaAs quantum wells nearest the intended 2DHG, contained in the smoothing GaAs/AlGaAs superlattice of wafers G372, G373, and VB1137. We note that the hole density of the parallel conducting channel does not appear to change with top-gate voltage once the intended 2DHG populates. This is precisely the same behaviour observed in hole bilayers with two 2DHGs located in two different quantum wells, with the lower 2DHG not responding to a surface gate once the upper 2DHG populates [82]. The very

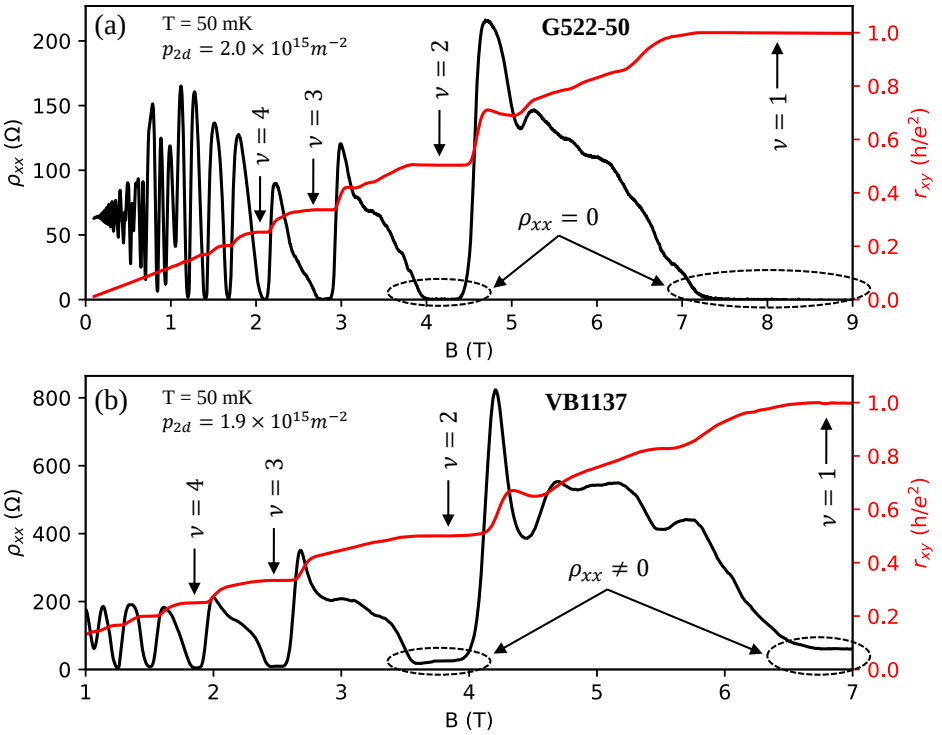


Figure 4.10: (a) ρ_{xx} (black, left y-axis) and r_{xy} (red, right y-axis) as a function of B-field measured for the G522-50 Hall bar (no superlattice buffer) showing no evidence of parallel conduction. (b) Comparable dataset to panel (a) but for the VB1137 Hall bar (with a superlattice buffer), demonstrating the lifting of SdH minima at high B-field, indicative of parallel conduction.

small difference between the Hall and SdH densities in wafer VB1137 is consistent with its larger AlGaAs barrier and 50% aluminum content (10 nm of $Al_{0.5}Ga_{0.5}As$) between the intended 2DHG and the nearest narrow GaAs quantum well in the smoothing superlattice, relative to G372 and G373 (2.5 nm of $Al_{0.3}Ga_{0.3}As$). Hence, to prevent unwanted parallel conduction, future devices should not incorporate a superlattice buffer layer during MBE growth. Removing the superlattice buffer has the potential to reduce the 2DHG mobility, as the primary purpose of the superlattice buffer is to clean the MBE chamber and mitigate structural defects during growth. Nevertheless, prioritizing the elimination of parallel conduction takes precedence over the 2DHG mobility.

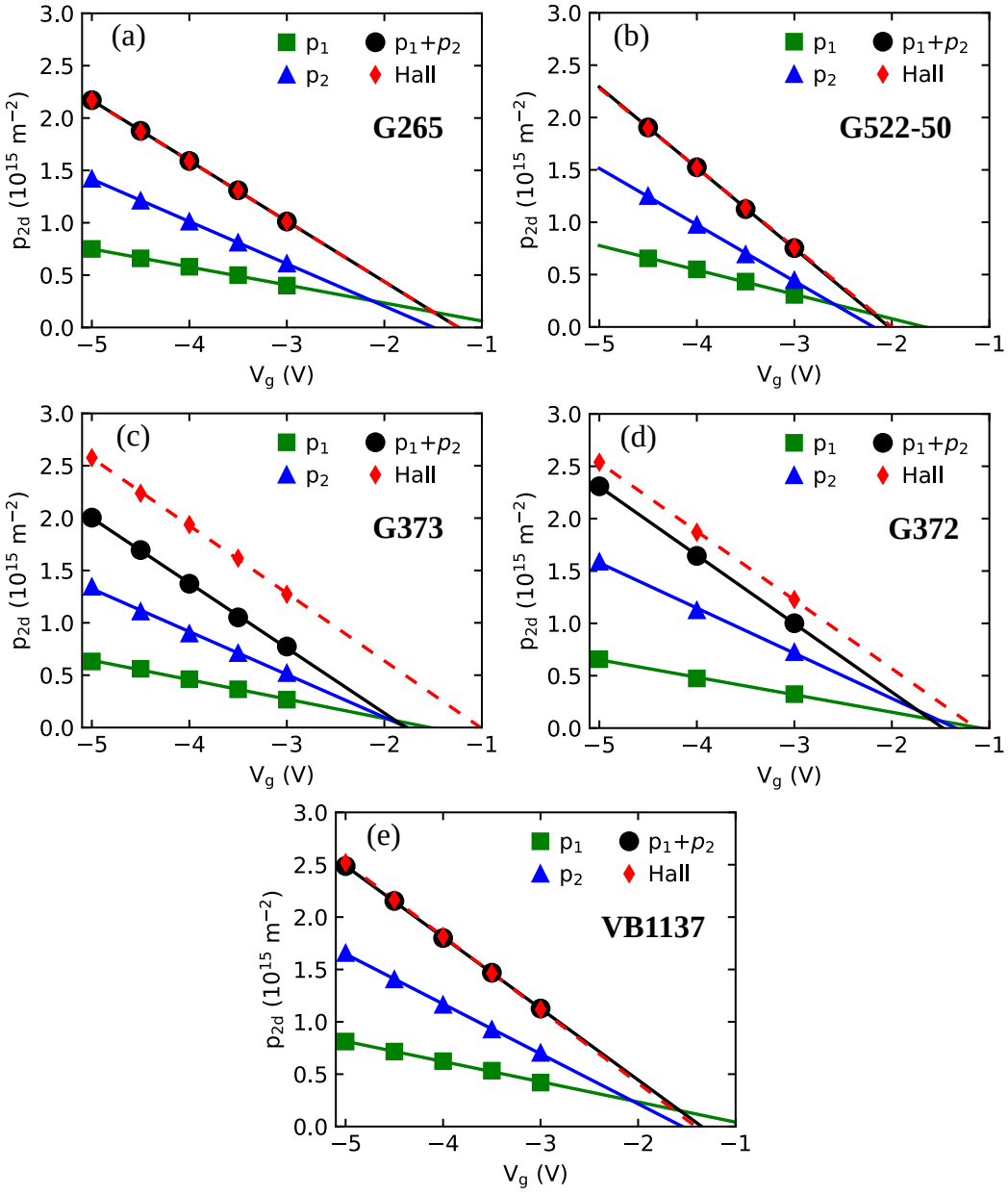


Figure 4.11: Comparison between hole densities extracted from the Hall effect and the SdH oscillations for all samples. (a) G265 and (b) G522-50 without a superlattice where $p_1 + p_2 = p_{Hall}$ (no parallel conduction). (c) G372, (d) G373, and (e) VB1137 with a superlattice where $p_1 + p_2 \neq p_{Hall}$ (parallel conduction).

4.3.6 2DHG Mobility

The mobility μ of our 2DHG can be calculated using the relation: $\mu = 1/(e \cdot p_{2d} \cdot \rho_{xx})$, where e is the elementary charge, p_{2d} is the hole density, and ρ_{xx} is the longitudinal resistivity. The extraction of the mobility in our GaAs 2DHGs at low temperatures (T $\approx$ 50 mK) is non-trivial. In 2DEGs, the mobility is typically evaluated for using the value of ρ_{xx} at small ($B \leq 0.1$ T) or zero magnetic field. However in our 2DHGs, at zero magnetic field, recall that a dip in ρ_{xx} (positive magnetoresistance) occurs (see Fig. 4.7c) which is attributed to classical two-band transport [19]. The temperature sensitivity of the $\rho_{xx}(B = 0)$ value is considerably higher than that of the desired background resistivity, as outlined in Appendix B.3. Consequently, using the value of $\rho_{xx}(B = 0)$ for our 2DHG could overestimate the mobility. Additionally, the onset of the SdH oscillations in our low-disorder 2DHGs occurs at B $\approx$ 60 mT (see Fig.4.7c inset). The combination of these effects makes it difficult to accurately extract the mobility at a single value of magnetic field. Therefore, we extract the mobility in our 2DHGs by estimating the background resistivity (ρ_0) from a sweep of $\rho_{xx}(B)$ in the range of 50 mT to 150 mT.

Fig. 4.12 shows the mobility μ of the 2DHG as a function of hole density for all samples, except for G372 and G373, which exhibited significant parallel conduction. In all cases, as the hole density increases, the mobility initially rises, reaches a peak value, and subsequently decreases. Sample G522-50 had the highest mobility, reaching a peak value of $\mu = 69\ m^2/V \cdot s$ at $p_{2d} = 1.5 \times 10^{15}$ m^{-2}. At low density, the mobility is limited by scattering from non-intentional background impurities, whereas it is limited by interface roughness scattering at higher densities [31, 18]. While higher mobilities up to $\sim 580\ m^2/V \cdot s$ have been demonstrated in modulation-doped GaAs 2DHGs [83, 84, 85], our dopant-free devices suffer much less from Landau level broadening [86] and can go to much lower carrier densities [46]. Recently, a dopant-free GaAs/AlGaAs quantum well achieved a maximum 2DHG mobility of $\mu = 150\ m^2/V \cdot s$ [80].

Here we also present mobility data for the two narrow width Hall bars made from the G522 wafer (G522-15-1 and G522-15-2) with $w = 15$ μm. The mobility of the 15 μm samples is approximately 30% less compared to the 50 μm sample (G522-50) from the same wafer. While this reduction in mobility could be simply attributed to variability in the

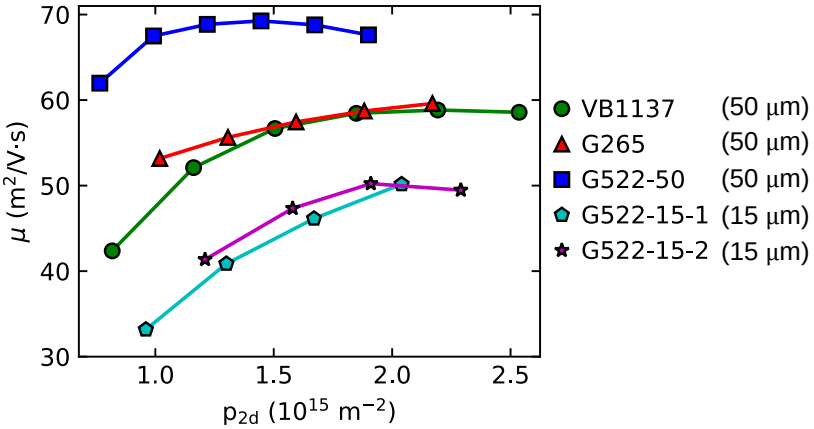


Figure 4.12: 2DHG mobility for all samples except for G372 and G373 which had significant parallel conduction.

wafer, it is also consistent with the boundary scattering effect that occurs in narrow Hall bars [87]. When the elastic mean-free path ℓ for a long Hall bar ($L > \ell$) becomes comparable to the Hall bar width w, boundary scattering with the sample edge becomes significant and reduces the mobility. For the Hall bars with mobility in the range $\mu \sim (40 - 70)\, m^2/V \cdot s$, the estimated hole mean-free path is $\ell_h \sim 3{-}5\ \mu$m, calculated using $\ell = \mu\hbar k_F/e$, where the Fermi wavevector is given by $k_F = \sqrt{2\pi p_{2d}}$. In the 50 μm sample, the mean-free path is an order of magnitude less than the Hall bar width and the boundary scattering is negligible. However, in the 15 μm samples, the mean-free path is only $\sim 5\times$ smaller, and therefore the reduced mobility is consistent with boundary scattering.

4.3.7 HH-/HH+ effective masses

For a system with only a single electric subband occupied, the effective mass is typically extracted by analyzing the resistivity amplitude decay $\Delta\rho_{xx}/\rho_{xx}$ of the SdH oscillations as a function of temperature [63], which can be fit to the following expression [30]

$$\frac{\Delta\rho_{xx}}{\rho_{xx}} = 2\,\exp\left(-\frac{\pi}{\omega_c\tau_q}\right)\frac{2\pi^2 k_B T/\hbar\omega_c}{\sinh(2\pi^2 k_B T/\hbar\omega_c)} \tag{4.1}$$

However, due to the complex beating of the SdH oscillations at low magnetic fields in our

asymmetric quantum wells, $\Delta\rho_{xx}$ cannot be simply normalized by a thermal dampening factor. Instead, we employed a technique pioneered in Refs. [56, 57]. This technique involves applying a Fourier transform (FT) to the SdH oscillations in 1/B and then fitting the individual FT peak heights of p_1 (HH-) and p_2 (HH+) as functions of temperature using Eq. 4.1. The SdH oscillations for a given temperature and B-field range can thus be individually re-constructed for m_1 and m_2. The background resistivity ρ_0 and spin-orbit split subband densities p_1, p_2 are directly obtained from the experimental data, while m^* and τ_q are fitting parameters. The Fourier analysis employs standard techniques such as windowing and zero-padding. These manipulations are valid as long as the same procedure is applied to the calculated resistivities as well. This method is robust in that it does not require any assumption regarding the form of the HH bandstructure.

Fig. 4.13a shows the temperature-dependence of the SdH oscillations for the G522-50 sample, ranging from 40 mK to 200 mK. The temperature-dependent data was collected in 10 mK increments from 40 mK to 100 mK and 25 mK increments from 125 mK to 200 mK. The G522-50 sample was selected for the effective mass analysis because it had the highest mobility of all samples and therefore had the largest FT amplitudes for p_1 and p_2. Fig. 4.13b shows the temperature-dependence of the p_1 and p_2 FT peaks within the magnetic field range of 0.12 T to 0.70 T for the SdH data set shown in panel (a). Fig. 4.13c shows the corresponding FT peak heights of p_1 and p_2 as a function of temperature, fitted to Eq. 4.1. Our analysis yields the following: $m_1 = (0.333 \pm 0.003)\, m_e$ and $\tau_1 = (13.72 \pm 0.09)$ ps for HH-, and $m_2 = (0.69 \pm 0.01)\, m_e$ and $\tau_2 = (20.0 \pm 0.9)$ ps for HH+. The error bars reported reflect the statistical errors of the fits. For Lorentzian-shaped Landau levels with a FWHM of 2Γ, where $\Gamma = \hbar/2\tau_q$, we calculate $\Gamma_1 \approx 24\, \mu eV$ and $\Gamma_2 \approx 16\, \mu eV$.

Due to thermal broadening when T $\gtrsim$ 0.1 K, the FT peak p_2 disappears, while p_1 only disappears for T $\gtrsim$ 0.2 K. This observation is consistent with m_2 being nearly twice as large as m_1, a characteristic that directly influences the visibility of the SdH oscillations through the cyclotron energy $\hbar\omega_c = \hbar eB/m^*$. For T $\gtrsim$ 0.2 K the SdH beating pattern is thermally smeared out, and only one SdH frequency, p_1, is observable in the Fourier spectrum. However, the disappearance of p_2 in the Fourier spectrum does not imply the vanishing of the spin-orbit splitting Δ_{HH}; rather, it means that the SdH oscillations can no longer resolve this splitting.

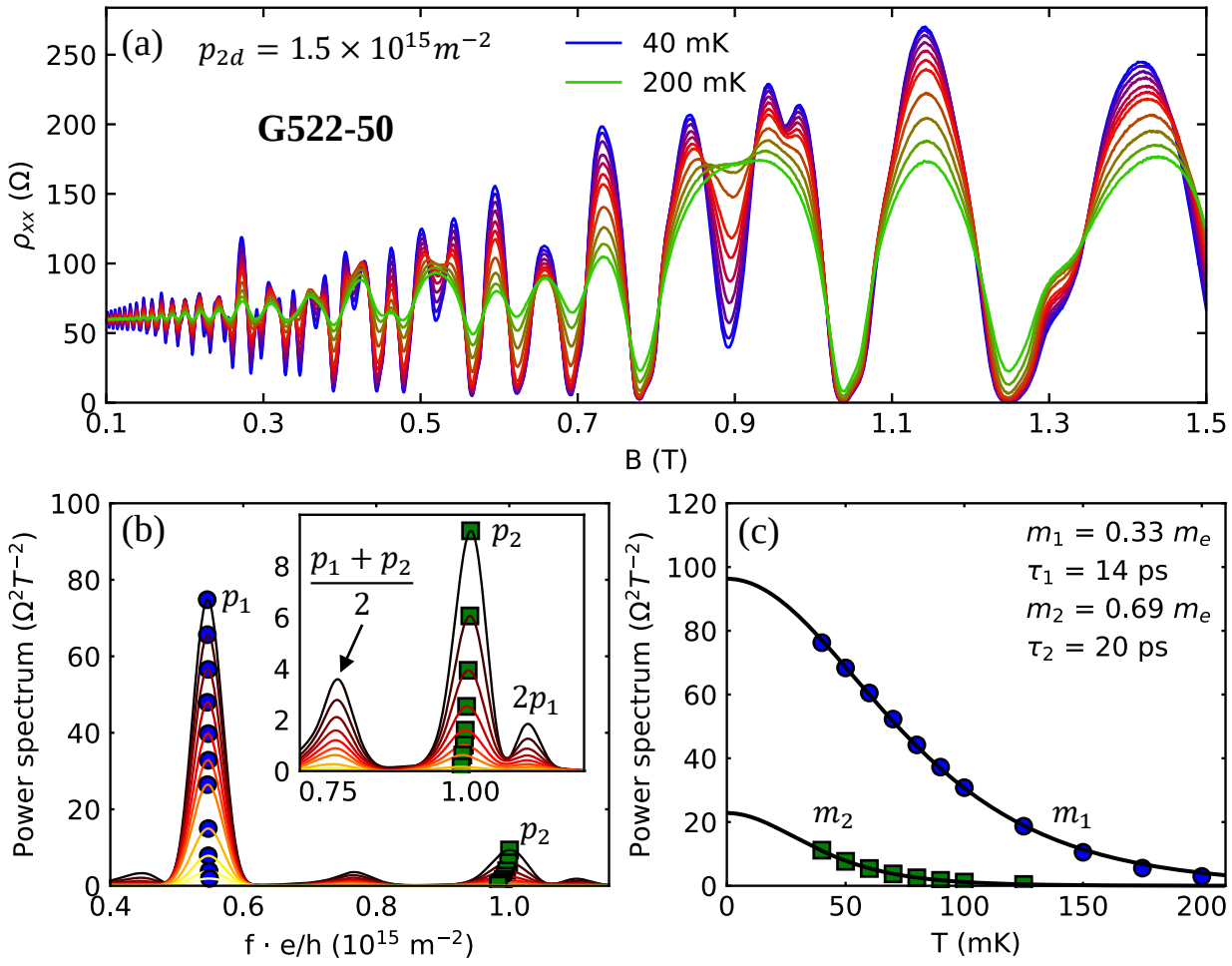


Figure 4.13: (a) Temperature-dependence of the SdH oscillations at $p_{2d} = 1.5 \times 10^{15}$ m^{-2} using $I_{ac} = 1$ nA excitation. The temperature data was collected in two different ranges: 40 mK to 100 mK in 10 mK increments, and 125 mK to 200 mK in 25 mK increments. (b) Temperature-dependence of the FT peaks p_1 and p_2 within the magnetic field range of 0.12 T to 0.70 T. (c) FT peak heights from panel (b) fitted to Eq. 4.1, using m^* and τ_q as fit parameters.

To ensure that the effective hole temperature was not saturating and skewing results, the analysis in Fig. 4.13 was also performed with the four lowest temperature points (40 mK, 50 mK, 60 mK, and 70 mK) of m_1 removed: the results of the fit were unchanged, indicating that the achieved hole temperature is close to that of the thermometer mounted on the mixing chamber of the dilution refrigerator. For consistency, the FT peaks $(p_1 + p_2)$ and $2p_1$ were also analyzed as fictitious masses and yielded the correct results of $(m_1 + m_2)$ and $2m_1$.

Hole density and B-field dependence of the effective masses

The same temperature-dependent Fourier analysis as in Fig. 4.13 was also performed over different ranges of magnetic field, and is shown in Fig. 4.14a and 4.14b. To produce these plots, the "start" of a B-sweep of SdH oscillations is always B = 0.12 T and the x-axis represents the "end" of the B sweep over which the SdH oscillations are Fourier-transformed. As mentioned previously, the FT analysis is not strictly valid once the SdH minima reach zero resistance in the strong quantum Hall regime. At $p_{2d} = 1.5 \times 10^{15}$ m^{-2} and T = 40 mK, the first instance where the SdH minima reached zero resistance occurred at B = 0.78 T, thereby limiting our Fourier analysis to magnetic fields below B < 0.75 T. The abrupt deviation in the trend observed for m_2 near B $\approx$ 0.78 T is likely due to artifacts resulting from the Fourier analysis.

Over the range where the FT analysis is valid (i.e., 0.1 < B < 0.75 T), Fig. 4.14a shows that both m_1 and m_2 are only very slightly increasing with magnetic field, in broad agreement with the modulation-doped 2DHGs from Ref. [57] but not with Ref. [56]. For B < 0.75 T, both quantum lifetimes τ_1 and τ_2 decrease almost linearly with magnetic field, indicating an increase in scattering due to transport becoming more localized.

Finally, the same temperature-dependent FT analysis was performed at four hole densities, shown in Fig. 4.14c and 4.14d (see Appendix B.1 for raw data and analysis). Over the measured density range of $p_{2d} = (0.7 - 1.9) \times 10^{15}$ m^{-2}, the HH- effective mass is constant with a value of $m_1 \sim 0.35\, m_e$ while the HH+ effective mass increases approximately linearly from $m_2 \sim (0.58 - 0.75)\, m_e$. Both observations are in broad agreement with the gated modulation-doped 2DHG in Ref. [57].

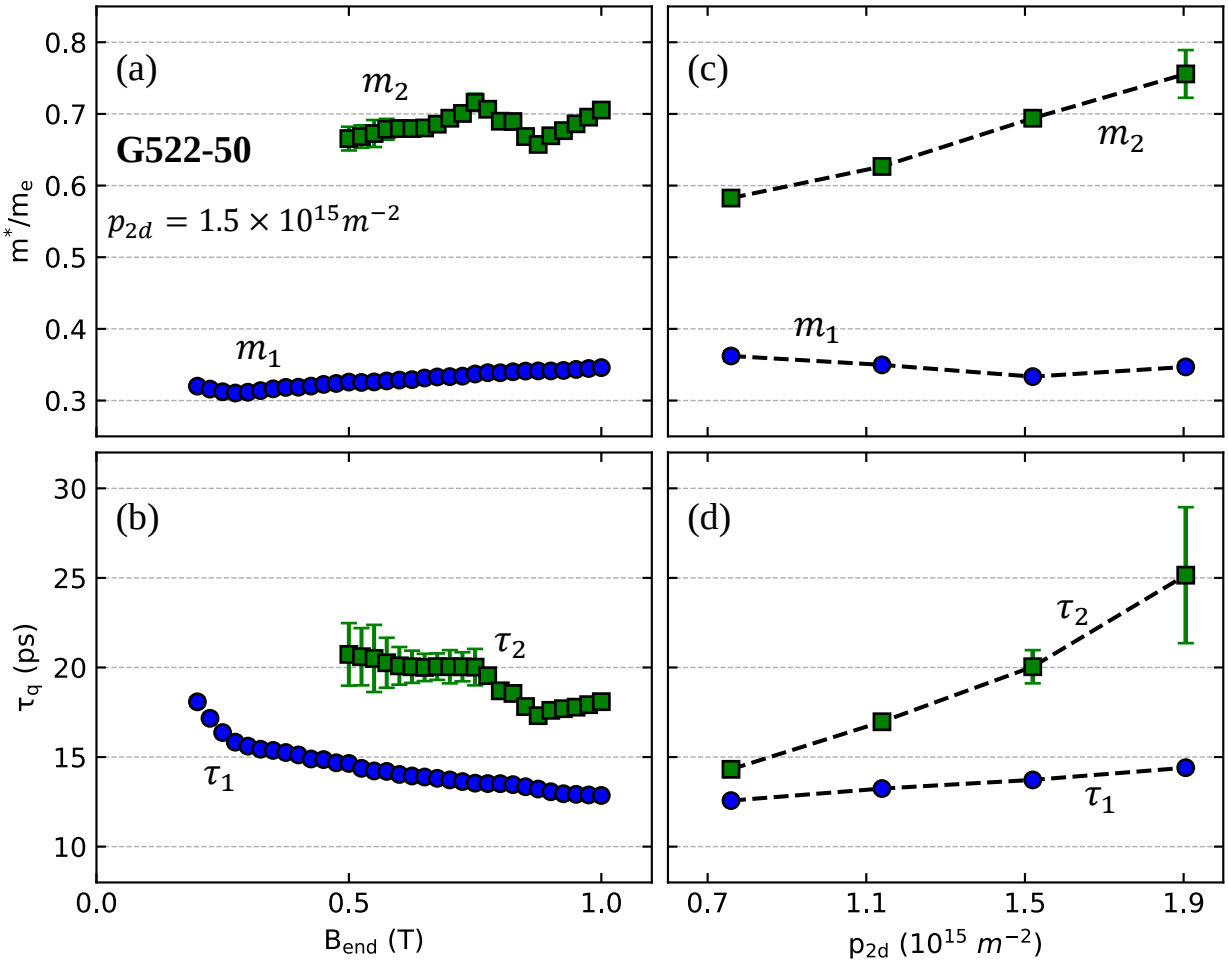


Figure 4.14: (a) Effective masses and (b) quantum scattering times analyzed over different magnetic field ranges at a constant hole density of $p_{2d} = 1.5 \times 10^{15}$ m^{-2}. (c) Effective masses and (d) quantum scattering times for different hole densities, using the SdH oscillations for $0.12 \leq$ B ≤ 0.7 T.

4.3.8 Spin-orbit splitting

The spin-orbit splitting Δ_{HH} between HH- and HH+ is primarily driven by SOI due to the structural inversion asymmetry (SIA) of the confining potential, also known as Rashba SOI. In GaAs 2DHGs, Rashba SOI has a k^3 dependence, and the approximate dispersion relation E_- (E_+) for HH- (HH+) is typically described by [22]

$$E_\pm(k_\parallel) = \frac{\hbar^2}{2\overline{m}^*}k_\parallel^2 \pm \alpha_{HH}k_\parallel^3 \tag{4.2}$$

where $\overline{m}^*$ is the average of the two HH effective masses m_1 and m_2, and α_{HH} is the Rashba parameter for HH in the valence band, which is given by [57]

$$\alpha_{HH} = \frac{\hbar^2}{2\overline{m}^*\sqrt{\pi}}\frac{p_2 - p_1}{p_2^{3/2} + p_1^{3/2}} \tag{4.3}$$

The energy difference between the spin-split HH subbands is then given by $\Delta_{HH} = 2\alpha_{HH}k_\parallel^3$. However, the Fermi wave vectors for the two HH subbands, k_1 and k_2, are different due to the unequal populations of p_1 and p_2, as calculated from the relation $k_i = \sqrt{4\pi p_i}$. Following the convention used in Refs. [57, 74], we adopt the smaller wave vector (k_1) as an estimate for the lower bound of the splitting. The Rashba coefficient and subband splitting were calculated as functions of density for the G522-50 sample and are shown in Fig. 4.15. The calculation of Δ_{HH} incorporated the density-dependent effective masses extracted in Sec. 4.3.7. In the accessible density range, $\Delta_{HH}(p_{2d})$ is linear, as expected for a k^3 dependence. In GaAs (100), linear behavior in $\Delta_{HH}(p_{2d})$ has also been observed in experiments at high densities [$p_{2d} = (1.5 - 3.0) \times 10^{15}$ m^{-2}] [57, 74] and low densities [$p_{2d} = (0.2 - 0.4) \times 10^{15}$ m^{-2}] [88].

The strength of the spin-orbit (SO) splitting can be parameterized by the population difference of the HH-/HH+ subbands normalized by the total hole density, expressed as $\Delta p/p = (p_2 - p_1)/(p_2 + p_1)$ [57]. Fig. 4.16a shows the density dependence of the SO splitting for all samples measured in this work, excluding G372 and G373 due to significant parallel conduction. The curves are very similar for all 50 μm wide Hall bars from wafers VB1137, G265, and G522, showing an increase in $\Delta p/p$ with increasing hole density induced by a more negative top-gate voltage. In our device architecture, a more negative top-gate voltage

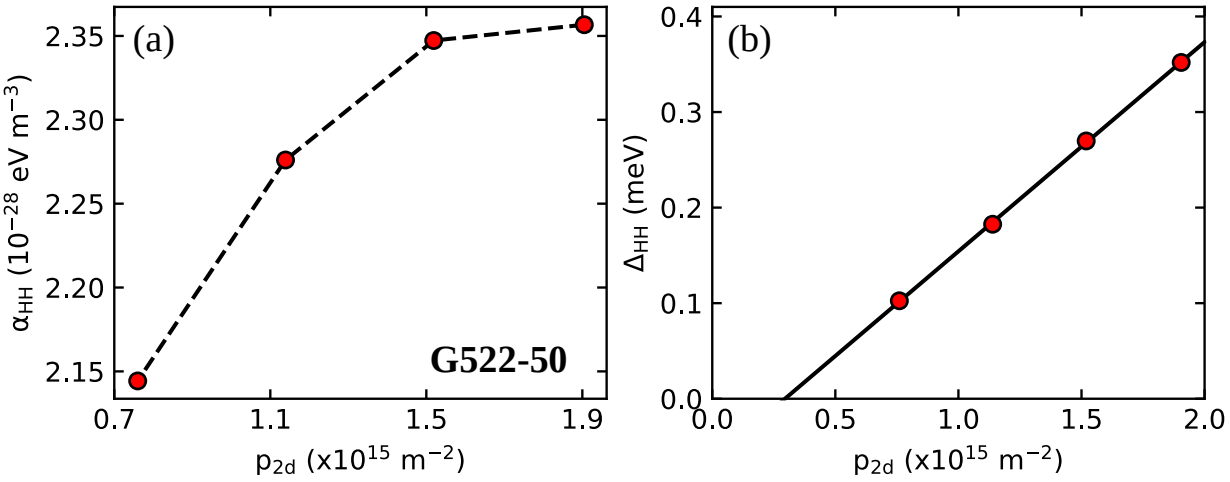


Figure 4.15: (a) Rashba coefficient as a function of hole density calculated using Eq. 4.3. Dashed line is a guide to the eye. (b) Corresponding energy gap Δ_{HH} between HH- and HH+ as a function of hole density. Solid line is a linear fit through the data.

results in a steeper confining potential for the 2DHG, resulting in stronger Rashba SOI. Indeed, the scaling of $\Delta p/p$ between the three samples is consistent with their individual potential profile. Sample VB1137, with the largest $\Delta p/p$, has the steepest 2DHG potential, due to its close proximity to the top-gate (50 nm AlGaAs) and the tallest AlGaAs barrier (50% Al content). Sample G265, with the smallest $\Delta p/p$, also has the weakest 2DHG potential from being the furthest away (300 nm AlGaAs) and shallow AlGaAs barrier (30% Al content). Sample G522 ranks between the other two samples, which is consistent with being close to the top-gate (50 nm AlGaAs) but having a shallow AlGaAs barrier (30% Al content).

The scaling and trends of $\Delta p/p$ is consistent for all 50 μm wide Hall bars. However, the 15 μm wide Hall bars (G522-15-1, G522-15-2) show the opposite trend at low density (less negative top-gate voltage), exhibiting an upturn in the splitting. This anomalous behavior is not yet understood but may be an artifact of the boundary scattering effect in narrow Hall bars, as discussed in Sec. 4.3.6 [87]. Further investigation of the SO splitting on Hall bars with varying widths would be valuable to understand the origin of this effect.

Fig. 4.16b presents a comparison of $\Delta p/p$ between the G522-50 sample and modulation-

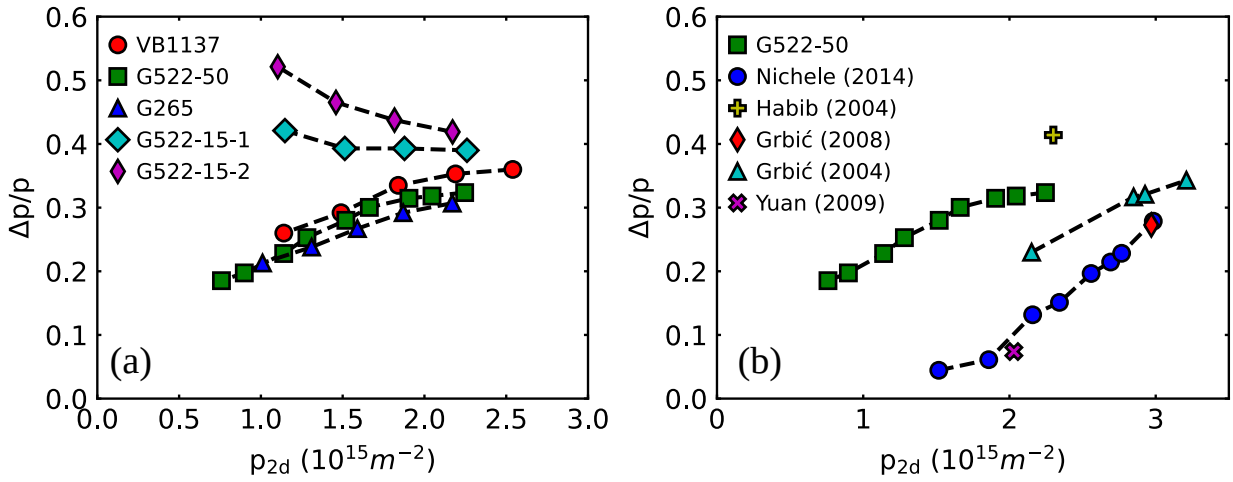


Figure 4.16: (a) SO splitting as a function of hole density for samples measured in this work. (b) Comparison of the SO splitting of G522-50 to other works in literature: Nichele *et al.* (2014) [57] [carbon doped 15 nm quantum well], Habib *et al.* (2004) [56] [beryllium doped single heterojunction], Grbić *et al.* (2008) [74] [carbon doped single heterojunction], Grbić *et al.* (2004) [65] [carbon doped single heterojunction], Yuan *et al.* (2009) [76] [carbon doped 15 nm quantum well].

doped samples from literature. The literature samples include both quantum wells and single heterojunctions, as indicated in the figure caption. In Nichele *et al.* (2014) [57] and Grbić *et al.* (2004) [65], the devices also featured a top-gate, allowing for the adjustment of the density and concomitantly the confining potential for the 2DHG. Factors influencing $\Delta p/p$ in modulation-doped samples include the thickness and concentration of the dopant layer, as well as the thickness of the spacer layer between the dopant layer and the 2DHG. These parameters vary among samples, accounting for the significant variation in $\Delta p/p$ for modulation-doped samples. In contrast, our 50 μm wide dopant-free samples exhibit consistent splitting between samples, with the variation aligning with the 2DHG potential profile as outlined above. Our devices, with the exception of Habib *et al.* (2004) [56], exhibit one of the largest SO splittings, with $\Delta p/p \approx 0.3$ at $p_{2d} = 2.0 \times 10^{15}$ m^{-2}.

4.3.9 Landau fan diagrams

In our gated devices, the hole density p_{2d} can be varied continuously with the top-gate voltage. This feature allows one to collect a high resolution data set of ρ_{xx} as a function of hole density and B-field. The hole density can be converted to an equivalent Fermi energy from the relation $E = p_{2d}\pi\hbar^2/m^*$. Fig. 4.17 shows the colormaps of $\Delta\rho_{xx}/\rho_0$ as a function of energy and B-field. Such colormaps are known in literature as "Landau fans". The effective mass was taken to be an average of the HH subbands ($\overline{m}^* \approx 0.5\ m_e$) and the energy is negative following standard convention for holes in the valence band. The observed energy range falls between -0.4 meV to -1 meV, corresponding to hole densities in the range of $p_{2d} \sim (1-2) \times 10^{15}$ m^{-2}. The low B-field colormap for G522-50 (see Fig. 4.17a) was generated by sweeping the top-gate voltage from -4.5 V to -3 V at a sweep rate of 10 mV/s and stepping the B-field from 0.1 T to 1.5 T in 2.5 mT increments. The high B-field colormap of G265 (see Fig. 4.17b) was generated by sweeping the top-gate voltage from -5 V to -3 V at a sweep rate of 20 mV/s and stepping the magnetic field from 8 T to 0.1 T in 5 mT increments.

Diagonal stripes of dark blue correspond to ρ_{xx} minima and can be assigned to integer filling factors ν with the corresponding Hall data. At low energy (low density), ν is lower for a given B-field, as expected according to $\nu = p_{2d}\hbar/eB$. Horizontal sections through the colormaps correspond to a typical plot of SdH oscillations, which were analyzed in detail via Fourier analysis in Sec. 4.3.4. All lines in the low B-field colormap in Fig. 4.17a appear to be straight and do not show any signs of curvature. However, in the high B-field colormap presented in Fig. 4.17b, fractional states are observed to emerge between $\nu = 1$ and $\nu = 2$. Additionally, the high B-field boundary of $\nu = 1$ starts to exhibit curvature at higher energy. The nature of this non-linearity is not understood. In a fan diagram of a Ge/SiGe 2DHG heterostructure at high energies, curvature was observed and attributed to the vanishing Zeeman splitting driven by SOI [89]. Fermi energies up to -18 meV were obtained, primarily due to the significantly lighter effective mass of holes in Ge/SiGe of $m^* \approx 0.06\ m_e$ [90].

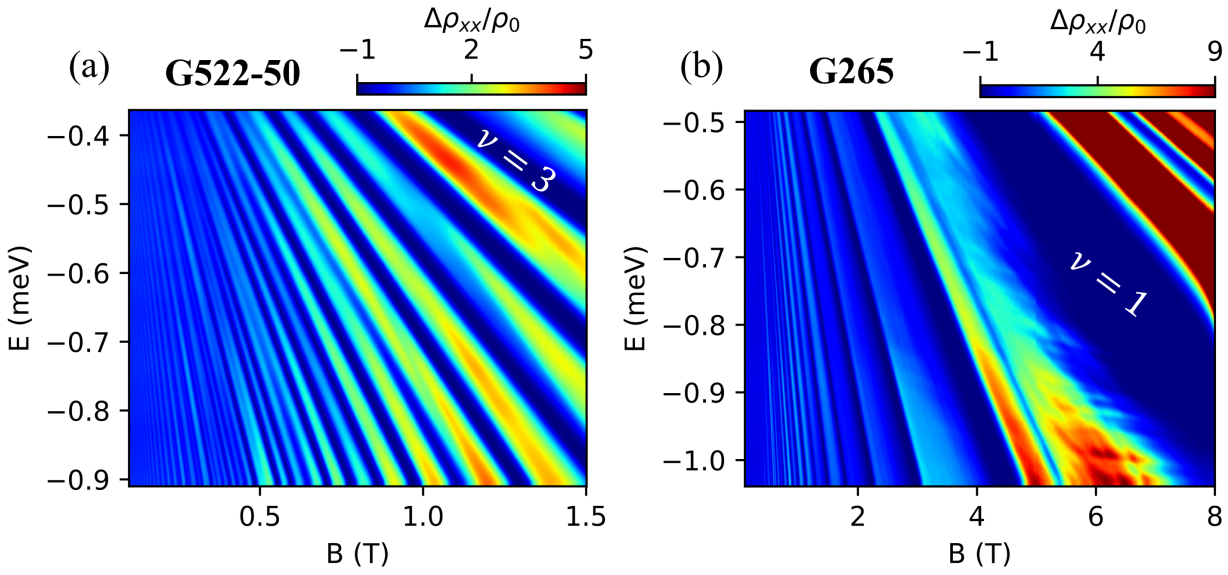


Figure 4.17: Landau fan diagrams at low B-field for (a) G522-50 and high B-field for (b) G265.

4.3.10 Thermal activation measurements

The Landé g factor is a fundamental parameter that governs the spin energy splitting in a magnetic field. In the case of GaAs 2DHGs, the g factor exhibits significant anisotropy, with theoretical predictions of $g^*_{\parallel} = 0$ and $g^*_{\perp} = 7.2$ [22]. Our focus is solely on the scenario where a magnetic field is applied perpendicular to the plane of the 2DHG. Here, we estimate the out-of-plane g factor ($g^*_{\perp}$) by examining the temperature-dependence of the SdH oscillations at small filling factors in the strong quantum Hall regime (Regime IV from Sec. 4.3.4).

In the limit of strong magnetic fields (B $\gtrsim$ 1 T) and low temperatures (T $\approx$ 50 mK), the cyclotron energy $\hbar\omega_c = \hbar eB/m$ and Zeeman energy ($g^*_{\perp}\mu_B B$) both significantly exceed the thermal energy ($k_B T$). This leads to well-separated Landau levels and results in $\rho_{xx} = 0$ at the SdH minima. At an odd-filling factor ρ_{xx} minimum, the Fermi level is midway between two spin-split Landau levels (N, $\uparrow$) and (N, $\downarrow$), where N is the Landau level index. Near equilibrium (small ac excitation current), the energy required to activate holes from the

Fermi level to extended states in the broadened Landau level (N, ↓) is equal to $E_{odd}/2$, where $E_{odd} = |g^*_\perp|\mu_B B - 2\Gamma$ [the energy gap between (N, ↑) and (N, ↓)] [64, 91]. Similarly, at an even-filling factor ρ_{xx} minimum, the Fermi level is midway between two Landau levels with different N and opposite spin (N, ↓) and (N+1, ↑). The activation energy required to populate extended states in the broadened Landau level (N+1, ↑) is $E_{even}/2$, where $E_{even} = \hbar\omega_c - |g^*_\perp|\mu_B B - 2\Gamma$ [the energy gap between (N, ↓) and (N+1, ↑)]. These activation energies can be extracted via the temperature-dependence of the ρ_{xx} minima, for odd- and even-filling factors separately, from an Arrhenius plot of $\rho_{xx} \sim \exp(E_{gap}/2k_B T)$.

Fig. 4.18a shows ρ_{xx} as a function of B-field for temperatures ranging from 50 mK to 650 mK. With the exception of the trace at 50 mK, the temperature-dependent data was gathered within the temperature range of 125 mK to 650 mK, in steps of 37.5 mK. The SdH minima corresponding to filling factors $\nu = 2 - 7$ all reach $\rho_{xx} = 0$ at T = 50 mK. However, at 650 mK, the minimum at $\nu = 2$ remains pronounced, while the minima for $\nu \geq 5$ disappear due to thermal broadening. It is noteworthy that in our GaAs 2DHG, we observe temperature-dependent behavior of the ρ_{xx} minima for both even and odd ν over the same temperature range. In similar measurements on 2DEGs [92, 93], to observe temperature-dependence at ρ_{xx} minima for even ν requires significantly higher temperatures (larger $k_B T$) than for odd ν. This is primarily a consequence of the much smaller effective mass in 2DEGs ($m^* = 0.067m_e$ for electrons in GaAs [94]), which leads to a much larger cyclotron energy gap compared to the Zeeman spin-split gap $\hbar\omega_c = \hbar eB/m^* \gg g^*_\perp \mu_B B$.

Fig. 4.18b shows the plots of $\ln[\rho_{xx}]$ as a function of 1/T for $\nu = 2 - 7$. For each filling factor, an appropriate temperature range is selected where the behaviour of $\ln[\rho_{xx}(1/T)]$ is linear. At $\nu = 2$, the ρ_{xx} minimum lifts from zero at $T \approx 0.35$ K ($1/\mathrm{T} \approx 2.9\ K^{-1}$), and has a linear trend with temperature up to the maximum temperature measured of T = 0.65 K ($1/\mathrm{T} \approx 1.5\ K^{-1}$). However, the ρ_{xx} minimum at $\nu = 7$ immediately lifts from zero at T = 0.125 K (1/T = 8), and has a linear trend only up to T ≈ 0.312 K ($1/\mathrm{T} \approx 3.2\ K^{-1}$), saturating at higher temperatures. A linear fit was applied to the data at each filling factor and E_{gap} was extracted. Fig. 4.18c shows the values of E_{gap} plotted as a function of magnetic field (at the B-field values where the ρ_{xx} minima are located), which will be used to estimate the absolute value of the out-of-plane g factor $|g^*_\perp|$.

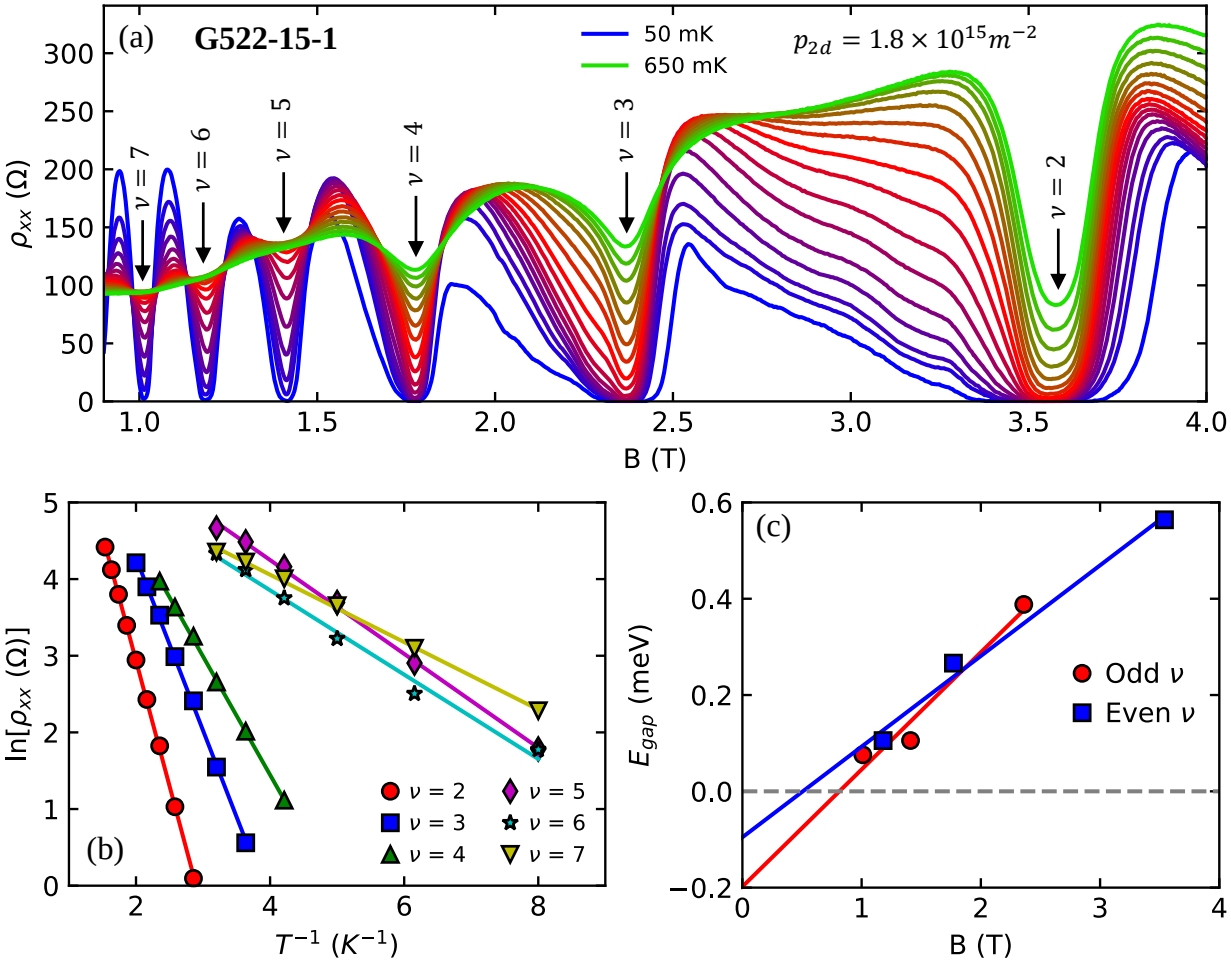


Figure 4.18: (a) Temperature-dependence of ρ_{xx} as a function of B-field for p_{2d} = 1.8 $\times 10^{15}$ m^{-2} using I_{ac} = 3 nA excitation. Excluding the B-field sweep at T = 50 mK, the temperature-dependence was collected over the range 125 mK to 650 mK in increments of 37.5 mK. (b) Arrhenius plot of ln[ρ_{xx}] as a function of 1/T for the data in panel (a) at the SdH minima $\nu = 2, 3, 4, 5, 6$, and 7. Linear fits are applied to each filling factor. (c) E_{gap} as a function of B-field determined from the linear fits in panel (b). Solid lines in red (odd ν) and blue (even ν) are linear fits.

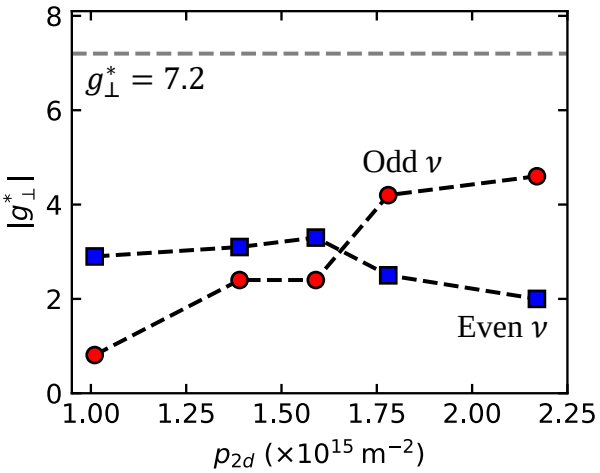
In magnetotransport measurements on 2DEGs, the value of $g^*_\perp$ extracted from odd-filling factors is known to be enhanced due to many-body electron-electron exchange interactions [93, 91, 64]. We could also expect similar hole-hole exchange interactions in our 2DHG that could lead to enhanced values of $g^*_\perp$. Thus, we will consider the value of $g^*_\perp$ extracted from even- and odd-filling factors separately. We will begin by analyzing data in Fig. 4.18c at odd-filling factors $\nu = 3, 5$, and 7. Using the slope extracted from a linear fit to $E_{odd} = |g^*_\perp|\mu_B B - 2\Gamma$, we find $|g^*_{o\perp}| = 4.2 \pm 0.9$, where the subscript o is to emphasize that the g factor is appropriate for an odd-filling factor that may be subject enhancement by many-body hole-hole exchange interactions. The error bar reflects the uncertainty in the slope of the linear fit, for which there are three data points. This value is consistent with those reported in literature for GaAs holes, $g^*_\perp \sim 2 - 7$ [76, 77, 78, 79], but lower than the bare theoretical value of $g^*_\perp = 7.2$ from Ref. [22]. Reduced values of $g^*_\perp$ (e.g., $g^*_\perp \sim 2.5$ in Ref. [95]) were reported from optical spectra of excitons and was attributed to light-hole–heavy-hole (LH-HH) mixing [96, 97].

Additionally, we can estimate the g factor using the even-filling factor data at $\nu = 2, 4$, and 6 in Fig. 4.18c. Recall that for even filling factors, the corresponding energy gap being probed is $E_{even} = \hbar\omega_c - |g^*_\perp|\mu_B B - 2\Gamma$, and therefore to estimate $g^*_\perp$ requires the cyclotron energy $\hbar\omega_c = \hbar eB/m^*$ and a value for the effective mass. At small B-fields (B $\lesssim$ 1 T) in our GaAs 2DHG, we have two effective masses, m_1 (HH-) and m_2 (HH+), derived from two distinct sets of Landau levels. The periodicity of the SdH oscillations at large B-fields in the quantum Hall regime reflects the total density from the sum of p_1 (HH-) and p_2 (HH+), which matches the Hall density p_{Hall} (see Sec. 4.3.4). However, due to the limited number of SdH oscillations at high B-field (periodic in 1/B), we cannot determine the individual populations of HH+/HH-. Thus, it is not clear if a single value for the effective mass would be appropriate, or, what value of m_1 or m_2 to use in the quantum Hall regime for this analysis. In the low B-field SdH analysis, we observe evidence of Zeeman spin splitting of the Landau levels from HH- with $m_1 \sim 0.35\, m_e$ (Regime II with $2p_1$ from Sec. 4.3.4) but find no evidence for spin splitting of HH+ with $m_2 = (0.58 - 0.75)\, m_e$. Nevertheless, we can use the values of m_1 and m_2 obtained in Sec. 4.3.7 to calculate the resulting $g^*_{e\perp}$, where the subscript e is to emphasize that the g factor is appropriate for an even-filling factor.

Using the values $m_2 = (0.58, 0.63)m_e$ from HH+ obtained for the smallest hole densities $p_{2d} = (0.7, 1.1) \times 10^{15}$ m^{-2}, we calculate $|g^*_{e\perp}| \sim (0.2, 0)$ using the slope extracted from a linear fit to $E_{even} = \hbar\omega_c - |g_\perp|\mu_B B - 2\Gamma$. A value of $|g^*_{e\perp}| \sim 0$ implies that the energy gap measured in the experiment, E_{even}, is equal to the cyclotron energy gap (i.e., $E_{even} \sim \hbar\omega_c = \hbar eB/m_2$), indicating no Zeeman spin splitting. This contradicts the relatively high value obtained for the odd-filling factor, $|g_{o\perp}| = 4.2$, and the large predicted value of $|g_\perp| = 7.2$ [22]. For the values $m_2 = (0.69, 0.75)\, m_e$ from HH+ obtained for the largest hole densities $p_{2d} = (1.5, 1.9) \times 10^{15}$ m^{-2}, the cyclotron energy is smaller than the energy gap measured in the experiment (i.e., $\hbar eB/m_2 < E_{even}$), and this lacks a meaningful physical interpretation. Thus, this strongly suggests that the Landau levels in the quantum Hall regime do not reflect that of HH+ with $m_2 = (0.58 - 0.75)\, m_e$. If we instead use the value $m_1 \approx 0.35\, m_e$ for HH-, we calculate $|g^*_{e\perp}| = 2.5 \pm 0.4$. This value is consistent with reports in literature for GaAs holes, $g^*_\perp \sim 2 - 7$ [76, 77, 78, 79]. Therefore, the HH character at high B-field in the quantum Hall regime appears to reflect the Landau levels for HH- (m_1), not HH+ (m_2). A Zeeman splitting of HH- (m_1) is also consistent with the low B-field SdH analysis (Regime II with $2p_1$ from Sec. 4.3.4).

One can also employ the thermal activation analysis to provide a rough estimate of the Landau level broadening Γ, by analyzing the zero B-field (y-axis) intercepts of Fig. 4.18c [92]. From the intercepts, Γ falls within the range $\sim 50 - 100$ μeV, which is comparable to the values obtained in Sec. 4.3.7 ($15 - 20$ μeV) for the G522-50 sample. We stress that the effective mass analysis for determining Γ is more robust, while the estimation method employed here is not so well established.

The same temperature-dependent g factor analysis presented in Fig. 4.18 was repeated at five hole densities over the range $p_{2d} = (1.0 - 2.2) \times 10^{15}$ m^{-2}. Fig.4.19 shows the g factors extracted from odd- and even-filling factor data (see Appendix B.2 for E_{gap} Vs B data used to obtain other $|g^*_\perp|$ values). $|g^*_{e\perp}|$ varies between $2.0 - 3.3$ in the measured range, but no clear trend is observed. However, $|g^*_{o\perp}|$ shows a strong density-dependence, increasing from $0.8 - 4.6$ over the measured density range. The estimated uncertainty in these values is ± 0.4, determined from the uncertainties in the slopes. In 2DEG systems, it is well established that the g factor increases at lower densities due to the increasing importance of electron-electron exchange interactions [98, 91, 77]. In contrast for our 2DHG, $|g^*_o|$



p_{2d} ($\times 10^{15} m^{-2}$)	$\lvert g^*_{e\perp}\rvert$	$\lvert g^*_{o\perp}\rvert$
2.2	2.0	4.6
1.8	2.5	4.2
1.6	3.3	2.4
1.4	3.1	2.4
1.0	2.9	0.8

Figure 4.19: Values of the g factor extracted for even- and odd-filling factor data at five hole densities over the range $p_{2d} = (1.0-2.2) \times 10^{15}$ m^{-2}. For the even-filling factor analysis, $m^* = m_1 = 0.35\, m_e$ was used. The predicted value of $g^*_\perp = 7.2$ [22] is indicated by the dashed gray line.

decreases at lower densities, which may suggest a lack of exchange enhancement in our 2DHG. Further evidence for this in GaAs 2DHGs has been reported in Refs. [99, 77]. However, the behaviour of decreasing $|g^*_o|$ with decreasing density is not yet understood.

4.4 Conclusions and future work

In summary, we have conducted magnetotransport measurements on Hall bar devices that were fabricated within dopant-free GaAs/AlGaAs 2DHG heterostructures. We evaluated five different wafers, all grown by MBE, which exhibited variations in 2DHG depths, aluminum composition, and the presence or absence of a smoothing superlattice buffer. We have established that the aluminum content and/or the thickness of the AlGaAs layer influence charge trapping and gate hysteresis in our devices. As a result of this work, it is recommended to use an AlGaAs composition with an aluminum content of 50% to prevent gate hysteresis within the designed operational voltage range ($V_g \leq -5$ V) for future devices. Additionally, we have determined that the smoothing superlattice buffer layer is

responsible for the undesired parallel conduction in our devices. The most likely cause of the parallel conduction is the low-density population of one or more of the $2.5-3$ nm wide GaAs quantum wells closest to the intended 2DHG, contained within the GaAs/AlGaAs superlattice. Thus, for future wafers, it is advisable to grow them without a superlattice buffer to eliminate parallel conduction in these devices.

By leveraging our low-disorder dopant-free 2DHGs, four successive and distinct SdH regimes can be identified at different magnetic field ranges, in order of appearance:

- Regime I, with a single SdH frequency (p_1)
- Regime II, with Zeeman splitting ($p_1; 2p_1$)
- Regime III, with spin-orbit splitting ($p_1; p_2$)
- Regime IV, with the quantum Hall effect onset

The first three regimes are clearly identifiable from a Fourier transform of the SdH oscillations in 1/B. These regimes are also evident without the Fourier analysis by simply plotting the Landau level filling factor ν as a function of 1/B. The latter verifies that Regime II is indeed real and not merely an artifact of the Fourier analysis. The average 2DHG mobility for all samples was approximately $\mu \sim 50\, m^2/V \cdot s$, with G522-50 exhibiting the highest mobility, reaching a peak value of $\mu = 69\, m^2/V \cdot s$ at $p_{2d} = 1.5 \times 10^{15}$ m^{-2}.

We extracted the effective masses of the spin-orbit split heavy hole (HH) band, extending the results to lower hole densities than those reported in modulation-doped samples in literature. Over the density range of $p_{2d} = (0.7 - 1.9) \times 10^{15}$ m^{-2}, the HH- effective mass is constant with a value of $m_1 \sim 0.35\, m_e$ while the HH+ effective mass increases approximately linearly from $m_2 \sim (0.58 - 0.75)\, m_e$. This increase is attributed to the SOI-induced nonparabolicities in the valence band. These observations are in broad agreement with the gated modulation-doped 2DHG in Ref. [57]. Based on the extracted quantum lifetimes of $\tau_q \sim (14 - 20)$ ps, we estimate the Landau level broadening to be on the order of $\Gamma \sim 20\, \mu eV$. This minimal broadening allowed us to extract the HH-/HH+ effective masses at the lowest hole densities.

We calculated the HH splitting in our GaAs 2DHG arising from Rashba SOI with a k^3 dependence. Over the density range of $p_{2d} = (0.7 - 1.9) \times 10^{15}$ m^{-2}, we estimated a lower bound for the HH splitting to be within the range of $\Delta_{HH} \sim (0.10 - 0.35)$ meV. The strength of the spin-orbit (SO) splitting can be parameterized by the population difference of the HH-/HH+ subbands normalized by the 2DHG density, expressed as $\Delta p/p = (p_2 - p_1)/(p_2 + p_1)$. Our dopant-free devices demonstrate one of the largest SOI driven HH+/HH- spin splittings in literature for a GaAs 2DHG, with $\Delta p/p \approx 0.3$ at $p_{2d} = 2.0 \times 10^{15}$ m^{-2}.

We estimated the out-of-plane g factor via thermal-activation measurements at both odd- and even-filling factors. Over the density range of $p_{2d} = (1.0 - 2.2) \times 10^{15}$ m^{-2}, the g factor representing even-filling minima was nearly constant $|g^*_{e\perp}| \sim 2.8$, while analysis of the odd-filling minima reveals a strong density-dependence, increasing from $|g^*_{o\perp}| \sim 0.8 - 4.6$. The analysis of the data at even-filling factor minima suggests that the high magnetic field regime predominantly reflects the Landau levels for HH- with an effective mass of $m_1 \sim 0.35\, m_e$, rather than HH+ with $m_2 \sim (0.58 - 0.75)\, m_e$.

In terms of future work, Hall bars could be fabricated with two separate accumulation gates, one for the ohmic contacts and another for the Hall bar itself. This configuration would allow for the investigation of lower hole densities where interactions are more pronounced, facilitating the study of phenomena such as Wigner crystallization and/or weak anti-localization (WAL). The latter can be utilized an additional technique to probe the SOI strength. Additionally, in devices made with 50% aluminum content in the AlGaAs layer, repeating the effective mass analysis at higher hole densities would provide additional insight into the shape of the valence band and SOI strength.

Chapter 5

Quantum Hall breakdown and nonlinear phenomena in a dopant-free GaAs/AlGaAs two-dimensional hole gas

This chapter is adapted from: **N. A. Cockton**, D. G. Austing, F. Sfigakis, S. R. Harrigan, J. Baugh, Z. R. Wasilewski, S. A Studenikin, M. Korkusinski, M. C. Tam, J. B. Kycia. Quantum Hall breakdown and nonlinear phenomena in dopant-free GaAs/AlGaAs two-dimensional hole gases. Manuscript in preparation.

5.1 Introduction

In Chapter 4, we investigated the magnetotransport properties of GaAs/AlGaAs 2DHGs Hall bars using small currents in the linear response regime. The use of small currents was critical in preventing Joule heating of the 2DHG, enabling low-temperature measurements of the SdH oscillations and the quantum Hall effect (QHE). The QHE was characterized by plateaus in the transverse (Hall) resistance, at values of $r_{xy} = h/\nu e^2$, accompanied by a

vanishing longitudinal resistivity $\rho_{xx} \sim 0$). In several measurements in Chapter 4, elevated temperatures caused gradual deviations in ρ_{xx} from the zero-temperature limit.

In this chapter, we explore the nonlinear magnetotransport properties of a GaAs/AlGaAs 2DHG Hall bar subjected to an additional dc current. At small magnetic fields, the current induces heating effects, while at large magnetic fields, the current gives rise to nonlinear behavior, including the breakdown of the quantum Hall effect. In contrast to elevated temperatures causing gradual deviations in ρ_{xx}, current-induced quantum Hall breakdown typically results in ρ_{xx} abruptly lifting from zero by several orders of magnitude above a critical current threshold (I_c). Above I_c, the response is nonlinear. While quantum Hall breakdown has been investigated since the discovery of the QHE, there is still no complete consensus on the mechanism.

An understanding of quantum Hall breakdown was initially motivated by metrology. In January 1990, the global resistance standard became the Von Klitzing constant, given by $\mathrm{R_K} = e^2/h \approx 25.8$ kΩ, based on the QHE. For high-precision standard measurements, the current should be as high as possible but should not exceed the critical current I_c, beyond which dissipative current flows. Breakdown and other nonlinear phenomena have regained interest recently as a tool for studying fundamental physics. Some examples of the nonlinear magnetotransport phenomena accessible in 2D systems include: Hall field-induced resistance oscillations [100], phase inversion of SdH oscillations [64, 101, 102], hysteresis near odd integer filling factors arising from dynamic nuclear polarization via the interaction of electron and nuclear spins through the hyperfine interaction [103, 104], and electric instability resulting in resistance fluctuations and negative differential resistance [105, 106, 107, 108].

The exploration of the aforementioned phenomena has primarily been carried out in 2DEGs, motivating us to investigate such behavior in our 2DHG. In this chapter, we explore a wide variety of nonlinear phenomena with holes, contrasting our results with those obtained for more widely studied electron systems. Additionally, we aim to gain a further fundamental understanding of our GaAs/AlGaAs 2DHG system, complementing the results obtained from Chapter 4.

5.2 Literature review

In this section, we will present previous experimental work on quantum Hall breakdown, including proposals to explain the underlying mechanism. We will also describe recent work on breakdown that inspired the measurements in this thesis. For additional information on breakdown, refer to the review by Nachtwei [109].

5.2.1 History of quantum Hall breakdown

The first instance of quantum Hall breakdown was reported by Ebert *et al.* [110] in 1983, three years after Klaus von Klitzing discovered the quantum Hall effect [111]. The authors investigated the current-voltage characteristics of a Hall bar within a GaAs/AlGaAs 2DEG at a filling factor $\nu = 2$. Fig. 5.1 shows the longitudinal electric field $E_x \propto V_{xx}$ plotted against the sheet current density $J_x = I/w$ (bottom x-axis) and the transverse (Hall) electric field $E_y = V_{xy}/w = Ir_{xy}/w$ (top x-axis), where $r_{xy} = h/\nu e^2$ is the quantized Hall resistance for a particular filling factor ν. It is important to highlight that the Hall resistance r_{xy} does not significantly deviate from its quantized value even when dissipation is observed in V_{xx}, a point that will be further emphasized below. In Fig. 5.1, breakdown is associated with a sharp jump in E_x at a sheet current density of $j_x \sim 0.56A/m$. Initially, the solid line in Fig. 5.1 might suggest an abrupt breakdown. However, upon zooming in on E_x by 50,000$\times$ (dashed line), a more gradual pre-breakdown increase becomes apparent before the sudden increase.

As mentioned above, the behaviour of r_{xy} near breakdown is typically very subtle in comparison to r_{xx}. Thus, the hallmark feature of breakdown is associated with the collapse of the dissipationless $r_{xx} \sim 0$ state. For example, Komiyama *et al.* [113] measured only a 1.6% deviation in r_{xy} for a Hall electric field twice that of breakdown at $\nu = 4$. Similarly, Iizuka *et al.* [114] measured a deviation of $\Delta R_H/R_H \sim -8ppm$ at breakdown, also for $\nu = 4$. Therefore the assumption of a constant Hall resistance $r_{xy} = h/\nu e^2$ in the calculation of the Hall electric field E_y is reasonably valid. However, for magnetic fields above and below the integer plateau ν, a small deviation in the Hall resistance is typically observed. The work by Kuchar *et al.* [112] highlights this behaviour. Fig. 5.2

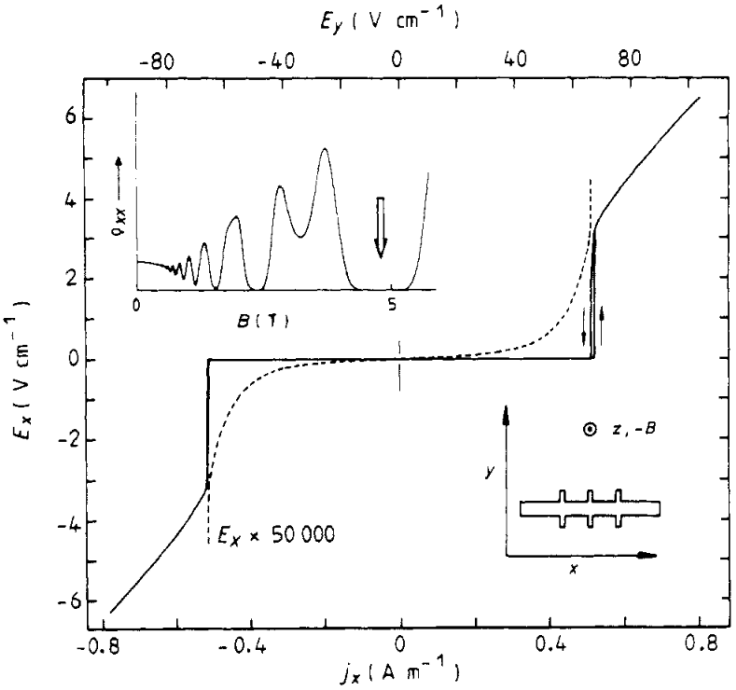


Figure 5.1: Breakdown voltage-current characteristic for filling factor $\nu = 2$ measured at a temperature of 1.4 K. The upper inset shows the SdH oscillations and $\nu = 2$ at B = 4.7 T. The lower inset shows the device geometry consisting of a 380 μm wide Hall bar. The solid line (zoomed out) shows the abrupt increase in E_x for $j_x \sim 0.56A/m$ while the dashed line (50,000× zoomed in) reveals breakdown is actually more gentle. Adapted from Ref. [110] with permission.

shows various traces of V_{xx} and V_{xy} at different magnetic fields above and below the $\nu = 2$ plateau. In V_{xx}, breakdown is observed at a critical current of $I_c \sim 0.7$ mA at the center of the $\nu = 2$ plateau (B = 4.4 T). For V_{xy} at $B = 4.4$ T, a linear dependence is observed above and below the critical current, consistent with the classical Hall effect. However, above (below) the center of the $\nu = 2$ plateau, an increase (decrease) in V_{xy} from the expected value is measured for a current greater than the critical current. This same behaviour was reproduced in more recent work in Ref. [92].

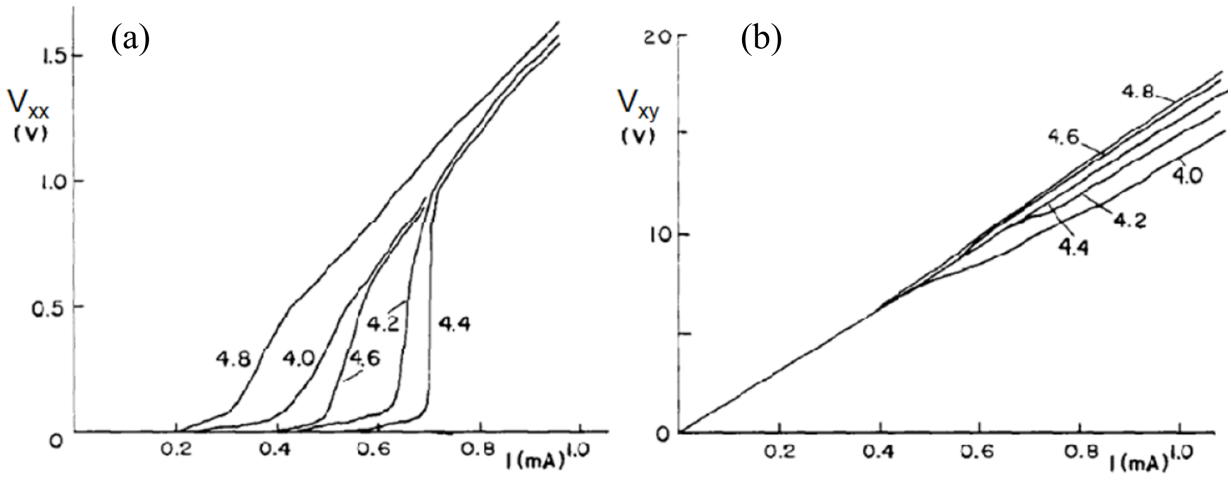


Figure 5.2: (a) Longitudinal voltage drop V_{xx} and (b) transverse (Hall) voltage drop as a function of dc current. Adapted from Ref. [112] with permission.

In the review by Jeckelmann and Jeanneret [115], they approximately demonstrate that the critical current decreases linearly as the magnetic field moves away from the center of an integer plateau. Figure 5.3a illustrates this behavior at filling factor $\nu = 2$, forming a triangular-shaped region where the QHE remains stable. However, in more recent works described later in Sec. 5.2.3, it is noted that the stable regions do not have straight edges; instead, they may exhibit curved boundaries, especially in samples with very high mobility.

Jeckelmann and Jeanneret also provide a compilation of data from various authors, illustrating the critical Hall electric field $E_c = hI_c/\nu e^2 w$ and its dependence on B-field for GaAs Hall bar devices at different electrons densities. Fig. 5.3b shows the results for even-filling factors $\nu = 2$ and $\nu = 4$. The straight lines on the log-log plot with a slope of 3/2 closely match the data, suggesting that E_c is approximately proportional to $B^{3/2}$. It is worth noting that Kawaji [117] also found an approximate $E_c \propto B^{3/2}$ relationship for odd-filling factors in a GaAs 2DEG. However, later on in Ref. [119], a further compilation of the E_c dependence on B-field was examined. The authors concluded that a linear B dependence fit is nearly equivalent to a $B^{3/2}$ fit [119]. In more recent work in Refs. [91, 120], the authors also reported a linear B dependence.

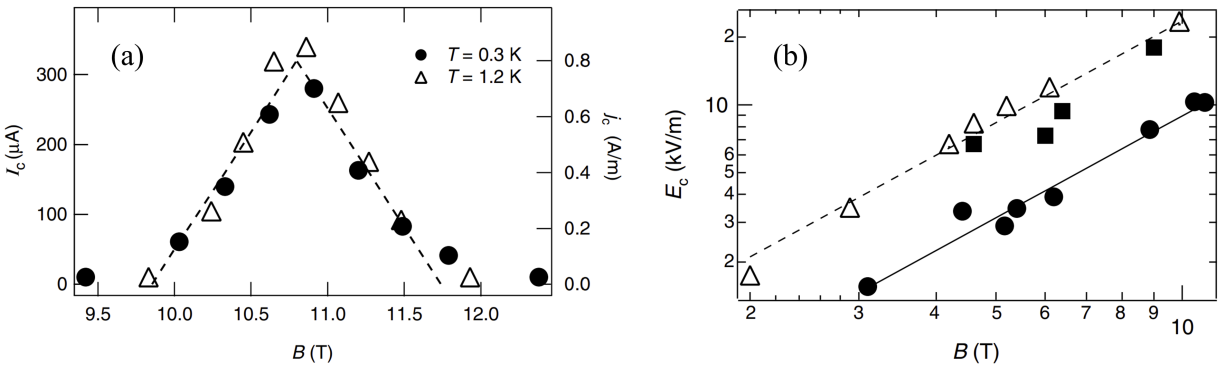


Figure 5.3: (a) Critical current I_c as a function of magnetic field in the vicinity $\nu = 2$ plateau at two (data from Jeckelmann *et al.* [116]). (b) Critical Hall electric field E_c as a function of magnetic field compiled from several authors. • Jeckelmann *et al.* [116], normal 400 μm Hall bars. △ Kawaji *et al.* [117], Hall bars with 600 μm long constriction in the middle (butterfly-type). ■ Ebert *et al.* [118], normal 380 μm wide Hall bars. The lines on the log-log plot have a slope of 3/2. Adapted from Ref. [115] with permission.

Multi-step transitions near breakdown

The behaviour of V_{xx} near breakdown is not always abrupt at the critical current I_c, but can be gentle with a pre-breakdown increase in V_{xx}. Additionally, several studies have reported multi-step transitions near breakdown [110, 121, 122, 123, 124, 125, 126, 127] by either sweeping the magnetic field at large currents or by sweeping the current at fixed magnetic field. Fig. 5.4 shows an example of such jumps in ΔE_x (or equivalently ΔV_x) for temperatures $T \leq 5.87$ K while sweeping the current in Ref. [110]. Explanations for this particular behaviour include a novel type of quantization in narrow constrictions [128, 126], the population of one or more Landau levels above the equilibrium Fermi energy [121, 124, 125], or simply macroscopic inhomogeneities within the Hall bar [127, 129].

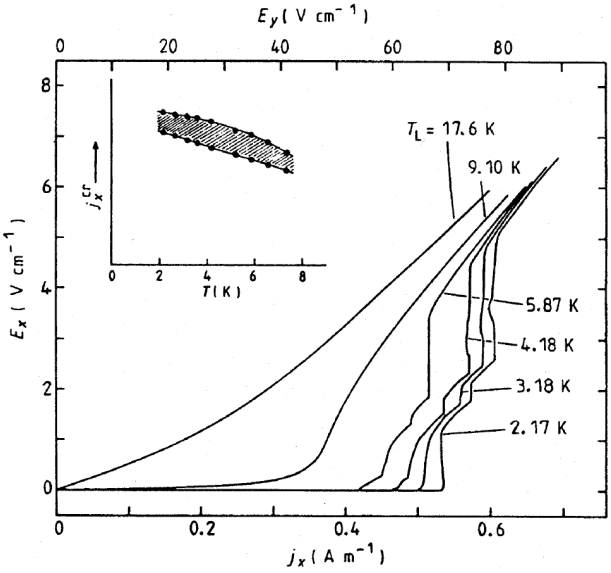


Figure 5.4: Current-voltage characteristics for $\nu = 2$ (B = 6 T) of a Hall bar at different lattice temperatures T_L. Several multi-step transitions are visible for $T_L \leq 5.87$ K. Adapted from Ref. [110] with permission.

Breakdown in a 2DHG

The reports outlined above studied breakdown in 2DEGs. To our knowledge, the only report of breakdown in a 2DHG is by Eaves *et al.* in 2000 [130]. They report breakdown in a modulation doped GaAs/AlGaAs 2DHG Hall bar ($w = 200$ μm) for filling factors $\nu = 1$ and $\nu = 2$, as shown in Fig. 5.5. The values of I_c obtained are $I_c \sim 9.3$ μA (~ 8.5 μA) for $\nu = 1$ ($\nu = 2$) at 4.2 T (2.1 T) for $p_{2d} = 1.0 \times 10^{15}$ m^{-2}. Thus, J_c and E_c are, respectively, ~ 0.046 A/m and ~ 2 kV/m (~ 0.042 A/m and ~ 0.55 kV/m) at $\nu = 1$ ($\nu = 2$). For even-filling factor $\nu = 2$, J_c and E_c are approximately an order of magnitude less than that reported in GaAs/AlGaAs 2DEGs.

The authors also report multi-step transitions and hysteretic behaviour in the voltage-current curves upon sweeping the magnetic field up and down near the filling factors $\nu = 1, 2$, as shown in figure 5.5. They interpret the steps and hysteresis phenomena in terms of an electronic hydrodynamic model. In Refs. [131, 130, 106, 105, 132], quantum Hall

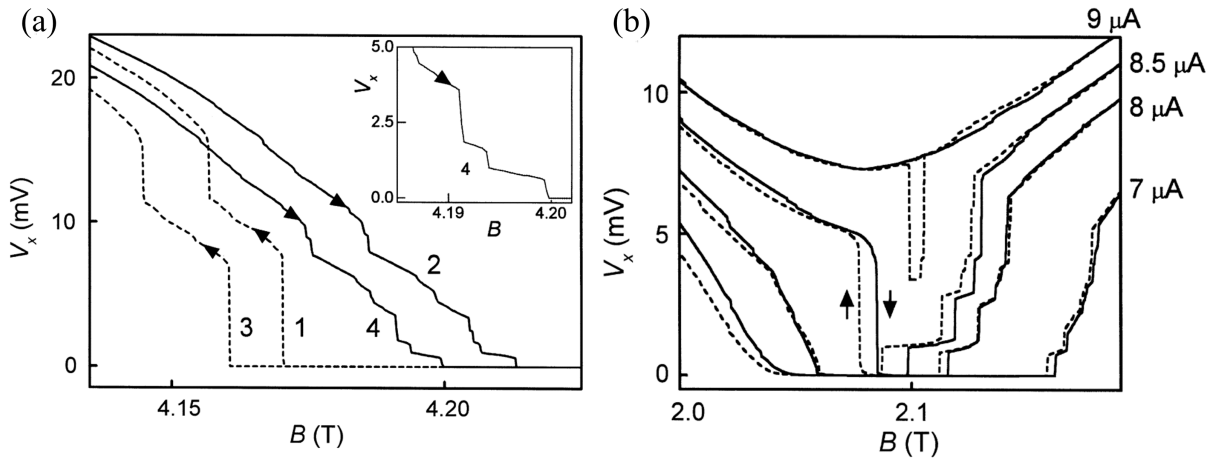


Figure 5.5: Breakdown in a 2DHG at T = 300 mK, highlighting hysteretic behaviour. (a) Breakdown at $\nu = 1$, measured at a fixed current of I = 9.2 μA. The numbers refer to the order of the sweeps and the arrows indicate the direction of the B-field sweep. (b) Breakdown at $\nu = 2$, measured for various constant currents. Solid (dotted) lines are sweeps up (down). Adapted from Ref. [130] with permission.

breakdown has been described analogously to classical fluid dynamics (hydrodynamics). Specifically, the electron flow in the quantum Hall regime at low current resembles classical laminar flow of a fluid in a pipe. However, when the critical current is reached, the dissipationless electron flow along the Hall bar breaks down. Similarly, when the critical volume flow rate is reached, this marks the transition between laminar and turbulent flow, the latter of which is associated with classical irregular fluctuations and eddies. Hysteresis and sporadic noise have been observed at the laminar-to-turbulent transition, hence the analogy between the step-like features and hysteresis observed for quantum Hall breakdown in Fig. 5.5. In Sec. 5.2.4, we will discuss other mechanisms for hysteresis.

5.2.2 Mechanisms of breakdown

Several mechanisms have been put forward to explain quantum Hall breakdown. Early proposals included quasielastic inter-Landau level scattering (QUILLS) [128], electron heating [113], Cherenkov-like acoustic phonon emission [133], and the formation of a compressible conduction filament [134]. These models generate various predictions that might distinguish them, such as the magnetic field dependence of the critical Hall electric field. However, the none of these models satisfactorily explained the data available. In particular, the predicted values of the critical Hall electric field were typically at least an order of magnitude larger than experimental values. Furthermore, some of the predictions from the models are dependent on details such as the particular nature of scattering or phonon emission, higher order tunneling processes, or Landau level broadening resulting from the Hall electric field [117].

Bootstrap electron heating model

In 2000, in an effort to reconcile the disparities between theoretical models and experiments, Komiyama and Kawaguchi developed a model that extended their previous electron heating model [113] and the QUILLS model introduced by Eaves and Sheard [128]. Here, we outline their model, referred to as *bootstrap electron heating* (BSEH) [135]. The basis for the BSEH model is that, regardless of the microscopic mechanisms that may induce breakdown, significant heating of the electron system must accompany breakdown.

We will now outline the relevant aspects of the BESH model. First, consider the equilibrium situation where a small dc current is applied to the Hall bar, along the x-direction, with the system in a stable dissipationless state $r_{xx} \sim 0$. The non-zero current will create a Hall electric field E_H along the width (y-direction) of the Hall bar. This Hall electric field tilts the Landau levels n and the Fermi level ϵ_F in the y-direction, $U(y) = -eE_y y$, as illustrated in Fig. 5.6a.

Fluctuations in the energy distribution at the Fermi level result in electrons being excited into higher Landau levels. Under non-zero electric fields, this excitation may occur through a Zener-type tunneling process (labeled **ZT** in Fig. 5.6a). Alternatively, for non-

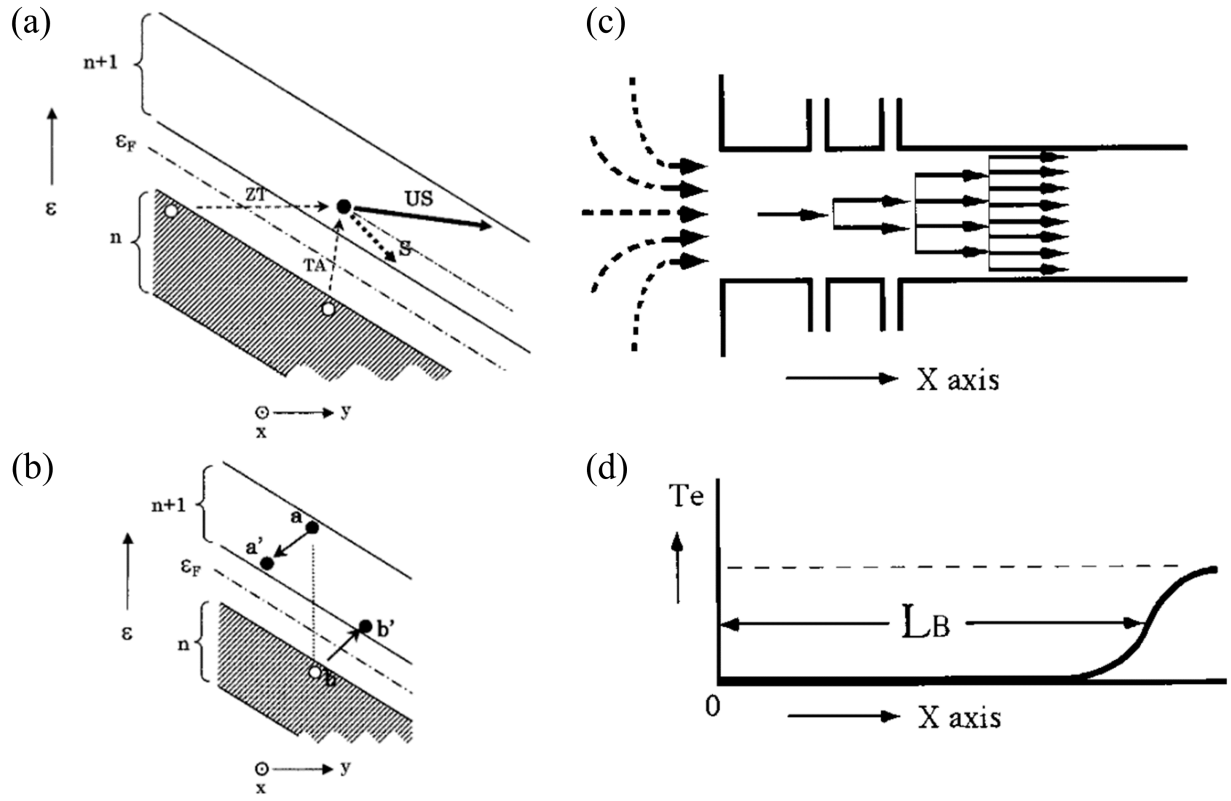


Figure 5.6: Bootstrap electron heating (BSEH) model. (a) Schematic of trajectories for electrons to be excited to a higher Landau level via Zener tunneling (ZA) or thermal activation (TA). An excited electron can lose kinetic energy (S, system is stable) or gain kinetic energy (US, system becomes thermally unstable). (b) Impact ionization process generating electron-hole pairs. (c) Illustration of carrier avalanche multiplication process. (d) Exponential increase in electron temperature T_e resulting from carriers traversing the breakdown length L_B after avalanche multiplication. Adapted from Ref. [135] with permission.

zero temperature, a thermal excitation process (labeled **TA** in Fig. 5.6a) is also possible. The combination of these excitations generates a finite density of excited, non-equilibrium carriers capable of initiating breakdown. These carriers can lose kinetic energy through acoustic phonon emission or gain kinetic energy due to scattering events. The ratio of energy gained to energy lost per carrier determines whether breakdown is triggered.

When the Hall electric field is below the critical Hall electric field $E_H < E_c$, excited carriers, on average, lose kinetic energy at a faster rate than they gain (labeled **S** in Fig. 5.6a), and they become reabsorbed into the Fermi sea through recombination. In this scenario, the quantum Hall state remains stable. Conversely, for $E_H > E_c$, excited carriers, on average, gain kinetic energy at a faster rate than they lose (labeled **US** in Fig. 5.6a). The high density of excited carriers can collide with cold carriers in the Fermi sea of a lower energy Landau level, leading to carrier avalanche multiplication through impact ionization. This results in an exponential increase in excited carriers, causing a sudden rise in electron temperature, and the system transitions from equilibrium to a dissipative state. The avalanche multiplication occurs over a macroscopic length scale, L_B (Fig. 5.6b), dependent on the sample mobility.

While the BSEH model is generally the most widely cited among the breakdown community, the predicted breakdown Hall electric fields still exceed those experimentally measured (see Fig. 6 in Ref. [135]). Additionally, it is subject to assumptions about the energy-relaxation mechanism.

5.2.3 Breakdown phase diagrams

Experimental studies on quantum Hall breakdown in the literature have traditionally concentrated on limited data sets, specifically a small number of $V_{xx} - I$ traces near integer filling factors. In this section, we examine two recent reports in the literature that distinctively provide comprehensive measurements of breakdown. These studies served as the motivation for the experimental work presented in this chapter.

In 2012, Studenikin *et al.* [64] conducted a study on non-linear transport in two distinct modulation-doped 2DEG systems: an InGaAs/InP quantum well (QW) structure and a

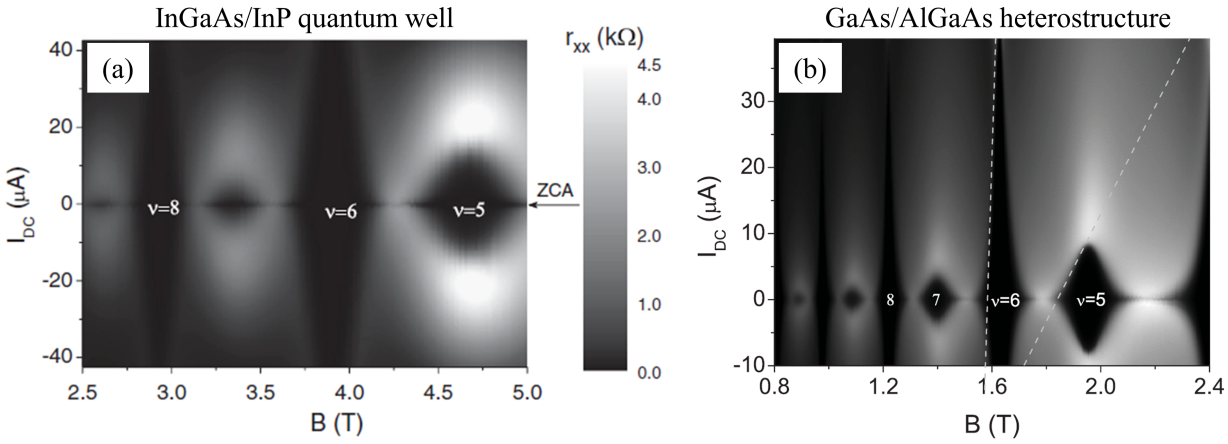


Figure 5.7: Grayscale maps of r_{xx} for (a) InGaAs/InP quantum well and (b) high mobility GaAs/AlGaAs heterostructure. Adapted from Ref. [64] with permission.

high-mobility GaAs/AlGaAs heterostructure. The authors measured non-linear effects of the longitudinal differential resistance r_{xx} as a function of dc current and perpendicular magnetic field. Distinct from previous works in literature, comprehensive measurements of r_{xx} are presented in a map or "phase diagram" by successively sweeping the current and stepping the magnetic field. Fig. 5.7 shows the maps in the quantum Hall regime up to filling factor $\nu = 5$ for the two material systems studied.

The maps reveal diamond-shaped structures (dark regions) where the quantum Hall state is stable, and dissipationless current flows. Outside these diamond-shaped regions or away from integer filling factors (white regions), dissipative current flows. The width of the diamonds in magnetic field is inversely proportional to the carrier mobility, explaining the narrow-width diamonds observed for the higher mobility GaAs/AlGaAs heterostructure. While the width of the diamonds in current is related to energy, a direct conversion is non-trivial. However, the diamond size generally increases with the magnetic field, albeit for even- and odd-filling factor diamonds separately. For both material systems, the width of the diamonds in current for odd-filling factors is significantly less than for even-filling factors. The authors note that this behavior aligns with the two energy scales of the spin-resolved Landau levels, namely the cyclotron energy gap ($\hbar\omega_c = \hbar eB/m^*$) for even-filling and the Zeeman spin splitting ($|g|\mu_B B$) for odd-filling. In both cases, the energy

grows linearly with the magnetic field, leading to larger diamonds at higher magnetic fields, consistent with the observations in Fig. 5.7.

In 2018, Victor *et al.* [91] generated similar maps, also utilizing a InGaAs/InP QW 2DEG structure. Colormaps of r_{xx} were obtained for large sheet current densities, up to ~ 1 A/m, and strong magnetic fields up to 9 T, reaching filling factor $\nu = 1$. Fig. 5.8 illustrates a colormap collected by sweeping the current and stepping the magnetic field at a electron density of $n_{2d} = 1.9 \times 10^{15} m^{-2}$. Similar to Ref. [64], the size of the diamonds alternates between even- and odd-filling factors in accordance with relevant energy gaps.

For their analysis, the authors consider Zener-type tunneling transitions between tilted Landau levels across the Hall bar arising from the Hall electric field when a large dc current is applied. This Zener-type tunneling mechanism was outlined in Sec. 5.2.2, which is also known in literature as quasi-elastic inter-Landau-level scattering [128, 135]. Within this model, for odd-filling factors, we anticipate that the maximum width in current of the $(2N+1)$th diamond (N = 0, 1, 2, ... for $\nu = 1, 3, 5$) reflects the transition (N, $\uparrow$) $\rightarrow$ (N, $\downarrow$), wherein the spin is flipped (via hyperfine or spin-orbit coupling [104]), but the Landau level index N is conserved. This transition has energy $|g|\mu_B B$. For even-filling factors, the maximum width in current of the $(2N+2)$th diamond (N = 0, 1, 2, ... for $\nu = 2, 4, 6$) could reflect the transition (N, $\downarrow$) $\rightarrow$ (N+1, $\downarrow$), where the spin is conserved but the Landau level index N is increased. However, it is more likely to reflect the smaller energy transition (N, $\downarrow$) $\rightarrow$ (N+1, $\uparrow$), where the spin is also flipped. This transition has energy $\hbar\omega_c - |g|\mu_B B$. In Fig. 5.8, white guide lines are drawn at the bounding tips for even- (odd-) filling factors to reflect the growth in the cyclotron energy (Zeeman energy) with increasing B-field.

Fig. 5.8a-g illustrate the alignment of spin-resolved Landau energy levels corresponding to the features marked in the colormap. The extended states of each level are represented as rectangular bars, with blue (white) indicating filled (empty) states. The left (right) ladder of levels is filled up to the chemical potential μ_L (μ_R). Here, L and R denote two physical coordinates along the y-axis of the Hall bar, defined such that $\mu_L \geq \mu_R$ so that transitions occur from the left ladder to the right ladder for both current polarities.

At $\nu = 2$, the chemical potential is midway between (0, $\downarrow$) and (1, $\uparrow$). At the tips of the $\nu = 2$ diamond, breakdown occurs when the fully filled (0, $\downarrow$) state at L aligns with the

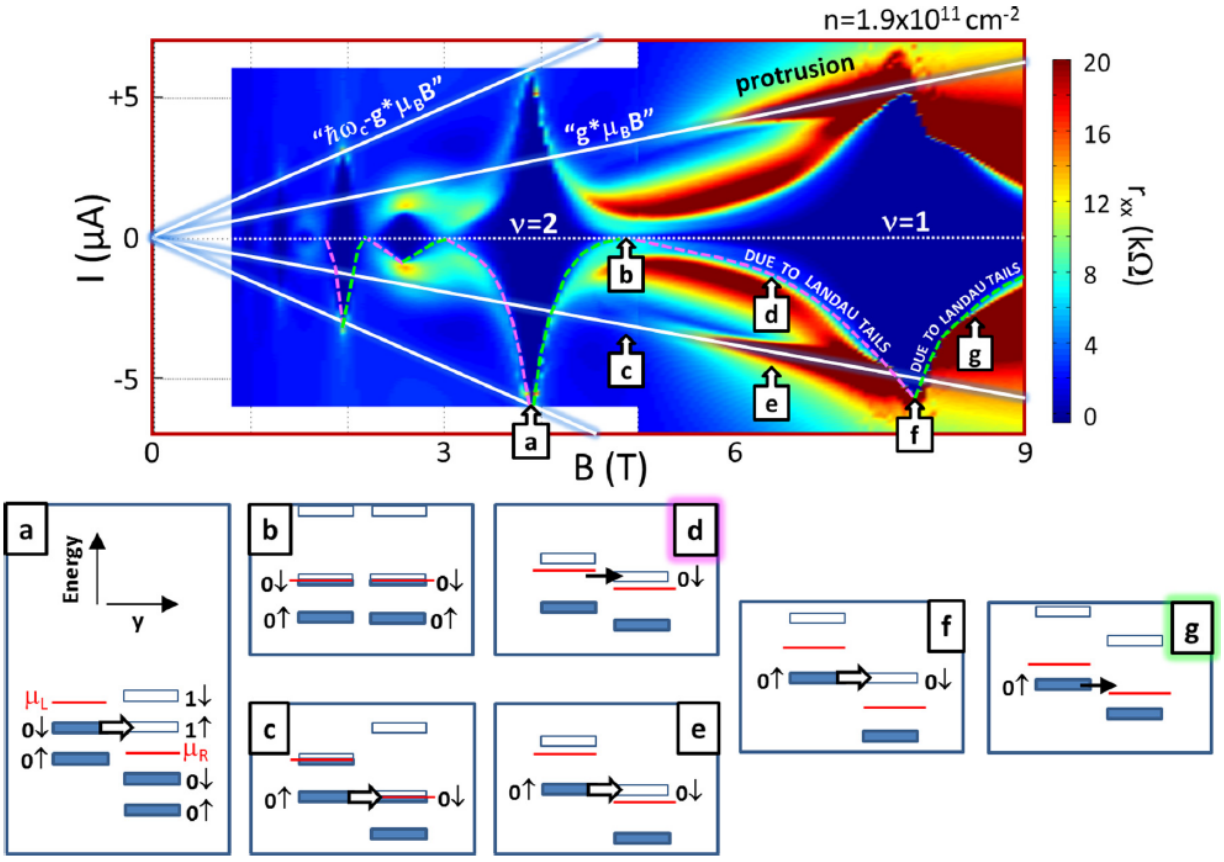


Figure 5.8: Colormap of r_{xx} for a InGaAs/InP QW 2DEG structure. White guide lines intersect the tips of even- (odd-) filling factor diamonds which principally reflect the growth in the cyclotron energy (Zeeman energy splitting) with B-field. Schematics (a)-(g) illustrate the alignment of Landau levels for for various points on the colormap. Adapted from Ref. [91] with permission.

empty (1, ↑) state at R (depicted in Fig. 5.8a), enabling an inter-Landau-level transition with a spin flip. Likewise, at $\nu = 1$, the chemical potential is midway between (0, ↑) and (0, ↓). At the tips of the $\nu = 1$ diamond, breakdown occurs when the fully filled (0, ↑) state at L aligns with the empty (0, ↓) state at R (illustrated in Fig. 5.8f), enabling a transition between the spin-split subband level of the $N = 0$ Landau level. Several other schematics are shown for various points on the colormap.

From Fig. 5.8, the authors estimate that $I_c \sim 6\ \mu$A ($\sim 5\ \mu$A) from the tips of the $\nu = 2$ ($\nu = 1$) transport diamonds at 3.9 T (7.8 T) for $n = 1.9 \times 10^{15}$ m^{-2}. Correspondingly, J_c and E_c are 0.4 A/m and 5.2 kV/m (0.33 A/m and 8.6 kV/m), respectively. These values are comparable to those reported for GaAs/AlGaAs 2DEG heterostructures compiled in Refs. [117, 115], with E_c typically in the range of 2-6 kV/m at 4 T ($\sim$ 6 kV/m at 8 T) for even-filling (odd-filling) factors. These values serve as a useful reference, which we will compare to later for the transport diamonds we measure in our GaAs 2DHG.

Within the framework of the simple Zener-type tunneling model, the authors estimate the characteristic length scale δ associated with the separation of points L and R. They assume uniform tilt of the Landau levels across the Hall bar. From the colormap in Fig. 5.8, the authors estimate $E_c \sim 5.2$ kV/m at $\nu = 2$ (B = 3.9 T). For a pure Zener-type tunneling mechanism shown in Fig. 5.8, one should expect $E_c \sim \Delta/e\delta$ where $\Delta = \hbar\omega_c - |g^*|\mu_B B$ is evaluated at 3.9 T with appropriate values of $m^* = 0.047m_e$ and $|g^*| = 4.8$ for the InGaAs/InP QW system. Consequently, a value for the characteristic length scale $\delta \sim \Delta/eE_c \sim (8.5\,mV)/(5.2\,kV/m) = 1.6\ \mu$m is calculated. This value is reasonable in that it is much less than the width of the Hall bar $\delta \ll w = 15\ \mu$m; one should not expect direct tunneling from one side of the Hall bar to the other. The authors note that δ should be on the same length scale as the spatial extent of the wavefunction for electrons in the Landau levels [117]. This is comparable to the magnetic length $\ell_B = 25.6nm/\sqrt{B}$, with B in units of Tesla. For $B = 3.9$ T, $\ell_B \sim 13\,nm \ll \delta$. Therefore, the experimental values of E_c are roughly two orders of magnitude smaller than anticipated based on a pure Zener-type tunneling model.

Multiple colormaps were collected at various carrier densities within the range $n_{2d} = 1.6 - 3.9 \times 10^{15} m^{-2}$ by using the persistent photo-conductivity effect through controlled illumination with a red-light-emitting diode. The comprehensive data compiled various

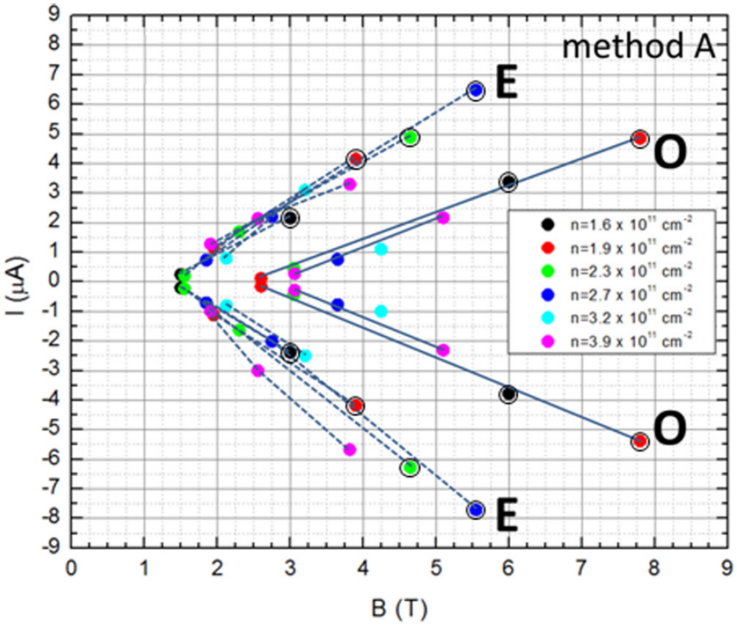


Figure 5.9: Critical currents I_c as a function of B-field for the InGaAs/InP QW 2DEG structure. Two distinct lines are observed for even (E) and odd (O) filling factor. Adapted from Ref. [91] with permission.

electron densities enabled the authors to analyze the critical current I_c dependence on filling factor and magnetic field. Fig. 5.9 shows I_c as a function of B-field, collected at six electron densities. The value of the critical current I_c is taken to be where r_{xx} exceeded a 10 Ω threshold. A linear dependence with B-field is observed for I_c, with two distinct lines obtained for even (E) and odd (O) filling factors.

5.2.4 Hysteresis near breakdown

Hysteresis has been attributed to changes in the degree of electron spin polarization [136, 137] or the polarization of nuclear spins in the substrate material via hyperfine interactions [103, 104]. The latter is particularly relevant for spin qubits made from gate-defined lateral quantum dots, where hyperfine interactions lead to decoherence. The hyperfine coupling of holes is estimated to be an order of magnitude weaker than that of electrons within the same

material system [11], which could have significant benefits for quantum dot spin qubits. In this section, we present how quantum Hall breakdown can induce the polarization of nuclear spins in a GaAs 2DEG, as observed by hysteresis in the voltage-current curves.

Hyperfine interaction in semiconductors

In type III-V semiconductors that possess non-zero nuclear spin, such as GaAs, electron spins in the quantum well are coupled to nuclear spins in the GaAs substrate through the contact hyperfine interaction. Each Ga and As nucleus has I = 3/2 nuclear spin, which couples to the S = 1/2 electron spin in the quantum well. The contact hyperfine interaction is described by the Hamiltonian [138]

$$H_{HF} = A\mathbf{I}\cdot\mathbf{S} = \frac{1}{2}A[I_+S_- + I_-S_+] + AI_zS_z \tag{5.1}$$

where A is the hyperfine coupling constant, which is proportional to overlap between the nucleus and the electron wave function, squared. The first term in brackets is responsible for the flip-flop interaction between the electron spin and a nuclear spin. The second term reflects that a finite nuclear-spin polarization will manifest as an effective magnetic field B_N, that acts on the electron spin. This effective magnetic field is proportional to the root mean square (RMS) average nuclear polarization $\langle I_z\rangle$, and is known as the Overhauser field, given by $B_N = A\langle I_z\rangle/g^*\mu_B$. For the GaAs material system, $B_N \sim 5$ T when all the constituent nuclear spins are fully polarized.

As a consequence of the hyperfine interaction, electron spins in a GaAs quantum well have rapid decoherence due to the coupling with the nuclear spin bath [139, 140]. The s-orbital symmetry of the electron spin wavefunction gives rise to a large contact hyperfine coupling strength. In contrast, the p-orbital character of holes suggests that their wavefunction vanishes at the nucleus, significantly suppressing the contact hyperfine coupling, leaving only the much weaker dipole-dipole hyperfine interaction [141, 11]. Thus, hole spins in GaAs have demonstrated an order of magnitude weaker hyperfine interactions [11]. This motivated our investigation in Sec.5.3.9, where we look for evidence of hyperfine interactions between the hole spins and spin-3/2 nuclei of the GaAs substrate.

Electrical polarization of nuclear spins

In 2007, Kawamura *et al.* demonstrated an electrical method to polarize nuclear spins utilizing quantum Hall breakdown[103]. In the breakdown regime at odd-integer filling factors, electrons are excited to the higher Landau levels with opposite spin polarity. The spin flipping process dynamically polarizes nuclear spins through the hyperfine interaction. The net polarization of the nuclear spins was found to reduce the spin-split energy gap between Landau levels, accelerating breakdown and causing hysteresis in the voltage-current curves. By probing the sample with nuclear magnetic resonance (NMR), dynamic nuclear polarization (DNP) was confirmed.

The details of the DNP scheme for a 2DEG system in a GaAs/AlGaAs heterostructure are as follows. When the Fermi energy lies between two spin-split Landau levels, the lower level is fully occupied with spin-up electrons (N, $\uparrow$) while the higher energy spin-down (N, $\downarrow$) level is empty. A current injected into the Hall bar tilts the Landau levels from the Hall electric field, as shown schematically in Fig. 5.10a. Above the critical Hall electric field, breakdown occurs and electrons from the lower energy level (spin-up) state are excited to the higher energy level (spin-down) state. As outlined in Sec.5.2.2, Zener-type tunneling (ZT) and/or impact excitation (IE) processes are possible for populating the higher energy Landau level. In both processes, the electron spin is flipped which will induce a counter spin-flop process of the nuclear spin via the hyperfine interaction. Consecutive flip-flop events can polarize the nuclear spins along the direction of the external magnetic field, creating an effective and opposing Overhauser field, due to the negative g factor ($g^* = -0.44$ electrons in GaAs). The opposing field reduces the Zeeman energy splitting $|g^*|\mu_B B - A\langle I_z\rangle$. Fig. 5.10a shows, schematically, the voltage-current curves being shifted to a lower value on the down sweep direction (red, $\langle I_z\rangle > 0$) versus the up sweep direction when there is negligible nuclear polarization (blue, $\langle I_z\rangle \sim 0$). Thus, DNP is expected to cause hysteresis in the $V_{xx} - I$ curve when sweeping the current up and down.

Kawamura *et al.* performed measurements at 20 mK on a Hall bar fabricated in a 2DEG GaAs/AlGaAs heterostructure. Fig. 5.10b shows the voltage-current curves taken by sweeping the current between -2.5 μA to +2.5 μA, at a sweep rate of 0.012 $\mu A/s$, near filling factors $\nu = 2, 3, 4$. For the even filling factor traces at $\nu = 2.15$, V_{xx} for the

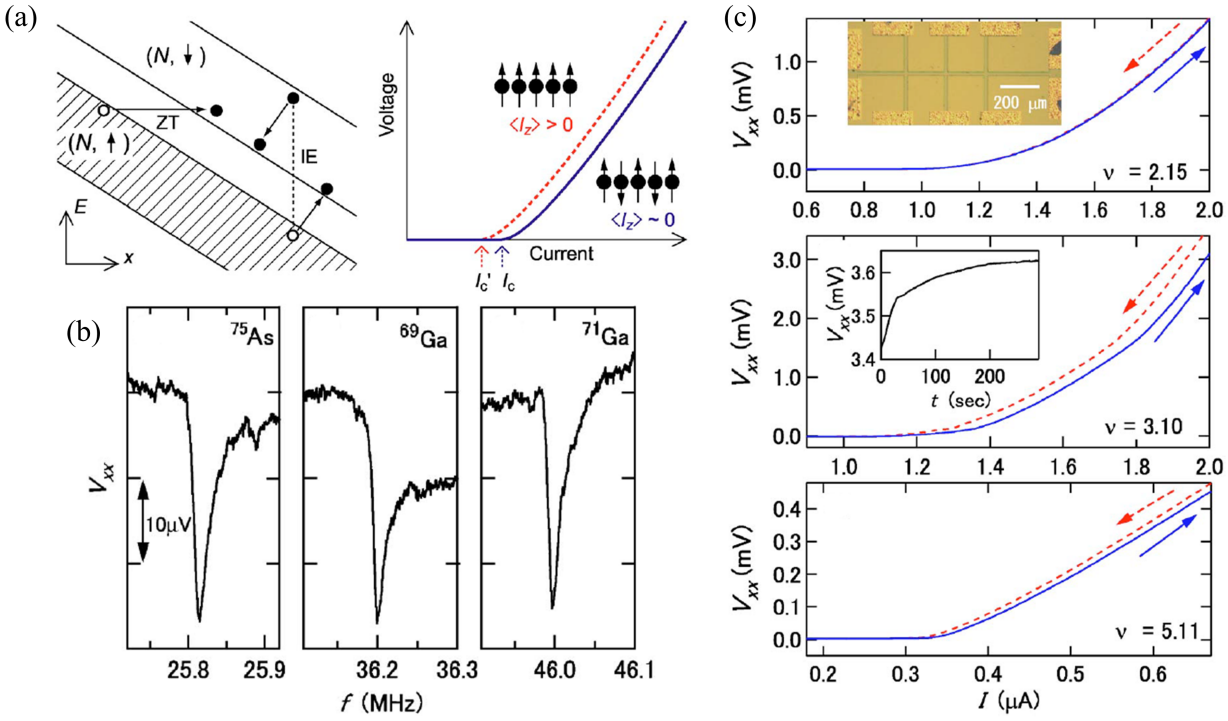


Figure 5.10: Electrical polarization of nuclear spins near breakdown. (a, left) Schematic of tilted, spin-split Landau levels in a breakdown regime at an odd-integer filling factor. (a, right) Expected $V_{xx} - I$ curves for $\langle I_z \rangle \sim 0$ (solid blue) and $\langle I_z \rangle > 0$ (dotted red). (b) Measured $V_{xx} - I$ curves for sweeping the current in positive (solid blue) and negative (dotted red) directions for $\nu = 2.15, 3.10, 5.11$. (b, upper inset) Micrograph of Hall bar device. (b, middle inset) Time evolution of V_{xx} when the current is changed from I = 0.0 to 2.0 μA for t = 0. (c) NMR spectra for ^{75}As, ^{69}Ga, ^{71}Ga detected by measuring changes in V_{xx}. Adapted from Ref. [103] with permission.

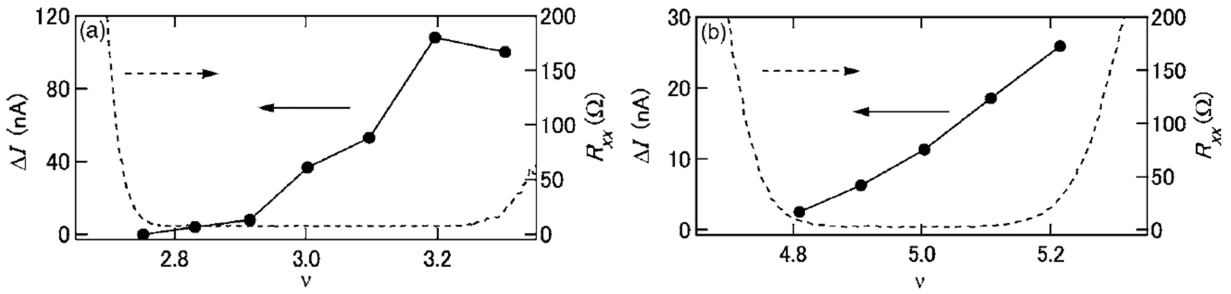


Figure 5.11: Shift of $V_{xx} - I$ curves between the up and down current sweeps at $V_{xx} = 2$ mV as a function of filling factor ν, for (a) $\nu = 3$ and (b) $\nu = 5$. Adapted from Ref. [103] with permission.

positive and negative sweep directions match; there is no hysteresis. However for the odd filling factor traces shown for $\nu = 3.10$ and $\nu = 5.11$, hysteresis is observed with the down sweep curve being shifted to a lower current. Note that the hysteresis is more pronounced at $\nu = 3.10$ (higher B-field, lower filling factor) than for $\nu = 5.11$. The shift in current ΔI at $V_{xx} = 2$ mV increases monotonically with increasing filling factor ν, as shown in Fig. 5.11. In other words, the hysteresis is most prominent on the lower B-field side of odd integer filling factors when the Fermi energy is located closer to the upper Landau subband. Additionally, the time evolution of V_{xx} was measured at $\nu = 3.10$ when the current was changed from 0.0 μA to 2.0 μA at t = 0 (Fig. 5.10 (b, middle inset)). A relaxation time of $\sim$ 300 s for V_{xx} was observed, consistent with a typical time scale for nuclear spin relaxation.

To validate the DNP model for hysteresis, NMR measurements were performed by using a single-turn coil around the device to produce a radio-frequency (rf) magnetic field. The rf magnetic field was applied parallel to the 2DEG for a current above the critical current I_c, I = 2.0 μA, after V_{xx} had completely saturated for $\nu = 3.10$. The rf frequency was swept while monitoring V_{xx}, as shown in Fig. 5.10d. Dips in V_{xx} occurred at the expected NMR resonance frequencies for the ^{75}As, ^{69}Ga, and ^{71}Ga isotopes. The resonance dips correspond to nuclear spin depolarization.

5.3 Experimental methods

5.3.1 Sample details

The Hall bar device for measurements in this chapter was fabricated from the G522 wafer, outlined in Chapter 4. Recall, the G522 wafer had no smoothing superlattice buffer and therefore did not show any features of parallel conduction. The G522-50 Hall bar measured in Chapter 4 was fabricated with a width $w = 50$ μm, which is not optimal for investigating quantum Hall breakdown. For breakdown measurements, the physical width w of the Hall bar should be carefully considered. As outlined in Sec. 5.2, the critical current I_c required for quantum Hall breakdown scales proportionally with the Hall bar width w. For 2DEGs up to 9 T, electron sheet current densities up to $J_c = I_c/w \sim 1$ A/m are required to reach the breakdown regime for the smallest filling factors $\nu = 1, 2$. For a 50 μm wide Hall bar, this would require a current of I = 50 μA to reach a sheet density of J = 1 A/m. Without using an additional power amplifier, voltage sources in the lab can typically supply up to 10 V, which combined with an appropriate 1-10 MΩ resistor can produce currents in the range of 1-10 μA. Thus, Hall bars for investigating quantum Hall breakdown should be fabricated with widths $w \sim 10$ μm such that $I_c < 10$ μA and no additional voltage amplification is required.

Consequently, for the nonlinear measurements presented in this chapter, we used the narrow width G522-15-1 Hall bar (W = 15 μm) fabricated from the G522 wafer. The length of G522-15-1 was kept the same as the other samples evaluated in Chapter 4 at L = 300 μm, resulting in a length-to-width ratio L/W = 20. The hole density for G522-15-1 could be adjusted using the top-gate voltage within the range of $1 - 2 \times 10^{15}$ m^{-2}, leading to corresponding variations in mobility, with values ranging from 33 - 50 $m^2/V \cdot s$ (see Fig. 4.12). Magnetotransport measurements were performed a dilution refrigerator with a 9 T magnet.

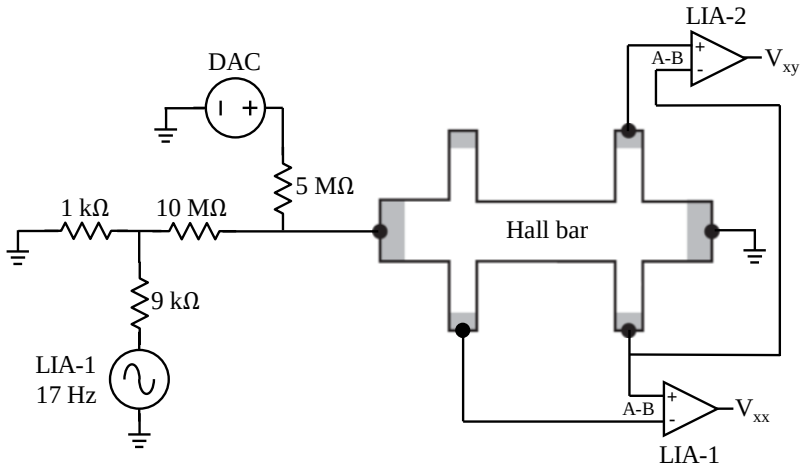


Figure 5.12: Schematic of the AC+DC circuit setup used for the nonlinear measurements to monitor the SdH and Hall voltages concomitantly. A SR380 lock-in amplifier (LIA) generates a small ($\leq$ 5 nA) AC current through the Hall bar while a DAC produces a larger (up to $\pm$ 2 μA) DC current.

5.3.2 AC+DC measurement setup

For the nonlinear transport measurements, we employed an AC+DC setup depicted in Fig. 5.12, which was adapted from Refs. [64, 91]. This circuit configuration allowed us to conduct measurements in a low-noise environment, achieved by utilizing a lock-in amplifier. Similar to the setup used in Chapter 4, two SR830 lock-in amplifiers (LIAs) are used to simultaneously measure the longitudinal voltage drop (ΔV_{xx}, LIA-1) and transverse voltage drop (ΔV_{xy}, LIA-2) of the Hall bar. These two LIAs were synchronized to operate at a frequency of 17 Hz. The sine output from LIA-1 was connected to a 10:1 voltage divider and subsequently passed through a 10 MΩ current-limiting resistor to generate a small ($\leq$ 5 nA) AC current applied to the source contact of the Hall bar, while drain contact was electrically grounded. This AC current was combined with a DC current, generated from the output of a DAC (IOtech DAC488HR/4), connected to a 5 MΩ current-limiting resistor. The LIAs only measure the respective voltage drop of the AC (17 Hz) component. The $\pm$ 10 V output of the DAC resulted in a DC current ranging up to $\pm$ 2μA, which was suitable for inducing quantum Hall breakdown in our devices.

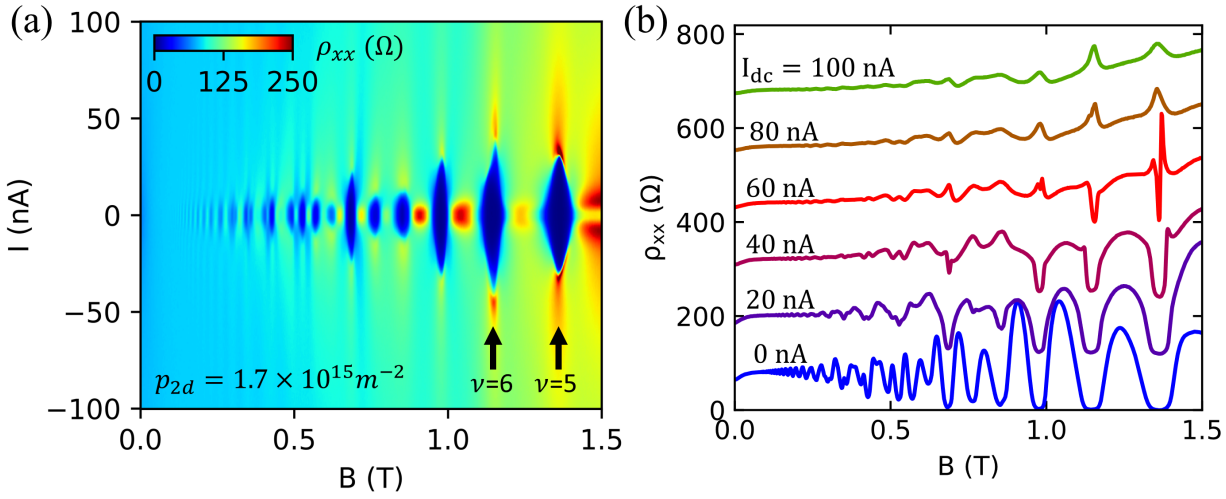


Figure 5.13: (a) Colormap of ρ_{xx} up to $\nu = 5$ at $p_{2d} = 1.7 \times 10^{15}$ m^{-2}. (b) Horizontal traces from panel (a). Curves for $I_{dc} \geq 20$ nA are shifted vertically by 120 Ω for clarity.

5.3.3 SdH phase inversion

In this section, we present SdH oscillations for the Hall bar driven with an additional dc current, using the AC+DC measurement technique. We begin by exploring the nonlinear behaviour at small magnetic fields in the large filling factor regime. Fig. 5.13a shows colormaps of ρ_{xx} as a function of dc current and perpendicular magnetic field, at a temperature of 50 mK. The measurement used a source-drain AC current of 1 nA at a modulation frequency of 17 Hz and time constant of 300 ms. The differential resistance $r_{xx} = dV_{xx}/dI$ is directly measured with a lock-in amplifier and converted to resistivity ρ_{xx}. To generate the colormap, ρ_{xx} is measured when sweeping the current from $0 \rightarrow +100$ nA, $0 \rightarrow -100$ nA at a rate of 1 nA/s and stepping the magnetic field from $0.1 \rightarrow 1.5$ T in increments of 2 mT. The current was swept in two segments, as opposed to a continuous sweep like $-I \rightarrow +I$, to mitigate asymmetry in the colormap caused by the integration time (lock-in time constant) of the measurement.

The dark blue (red) regions in the colormap identify the ρ_{xx} minima (maxima). For $B > 1.1$ T, the dark blue diamond shaped regions labeled as filling factors $\nu = 5, 6$ are the so-called transport diamonds discussed in Sec. 5.2.3. At large B-fields, the Landau levels

are sufficiently separated such that Zeeman spin-split minima are resolved and the SdH minima reach zero resistance. The high-current tips of these diamonds reflect the critical currents I_c. From Fig. 5.13a, we estimate that $I_c \sim 17$ nA (~ 10 nA) for the $\nu = 5$ ($\nu = 6$) diamonds at 1.35 T (1.15 T). We will return to discussing the transport diamonds in the strong quantum Hall regime in Sec. 5.3.5. For now, we will instead focus on the blue regions for $\nu > 6$ for magnetic fields $B < 1$ T. At small B-fields, the Landau levels are insufficiently separated such that the SdH minima do not reach zero, even for $I_{dc} = 0$. The width in current of the blue regions does not grow monotonically with increasing B-field. This behaviour most likely reflects the complex beating pattern of the SdH oscillations from the two effective masses and Zeeman spin splitting observed in Chapter 4.

Horizontal cuts at positive current polarity through the colormap are shown in Fig. 5.13b. For zero current, the familiar SdH oscillations from Chapter 4 are recovered. The SdH oscillations at non-zero current exhibit two notable features. Firstly at small currents, the SdH oscillation amplitude decreases with increasing current, similar to increasing temperature. In Sec. 5.3.4, we examine this effect to estimate the current-induced Joule heating of the 2DHG. Secondly, at larger currents, an inversion of the SdH oscillation extrema occurs. The SdH minima (maxima) develop into maxima (minima) at high current. This is most clearly observed in Fig. 5.13 for high B-fields and currents.

Several experimental works have documented the SdH phase inversion effect in high mobility 2DEG systems [64, 91, 142, 101, 120, 143, 144], as well as in a low mobility graphene sample [102]. The theoretical discussions on this phenomenon can be found in Refs. [145, 146]. In electron systems, the phase inversion effect can be explained by an electron heating model using the following relation [64]

$$r_{xx} = R_{xx} + I_{dc}\frac{\partial R_{xx}}{\partial T_e}\frac{\partial T_e}{\partial I} \tag{5.2}$$

where r_{xx} is differential resistance, R_{xx} is the magnetoresistance given by the Ando formula (Eq. 4.1), and T_e is the electron temperature. The second (differential) term in Eq. 5.2 gives rise to a π phase shift of the SdH oscillations that dominates at larger I_{dc}. T_e will always grow with increasing current and therefore the term $\partial T_e/\partial I$ is always positive. However, R_{xx} with increasing T_e can either decrease, for a maxima in r_{xx}, or increase for

a minima in r_{xx}. Stated differently, the term $\partial R_{xx}/\partial T_e$ is positive (negative) for an r_{xx} minima (maxima) at low current.

As outlined in Sec. 5.2, only a limited number of reports in literature have studied breakdown and other nonlinear phenomena in holes, with electron systems being more widely investigated. We note that for small B-fields, other reports on nonlinear behaviour in 2DHG systems have studied Hall field-induced resistance oscillations (HIRO) [147, 148] in addition to microwave-induced resistance oscillations (MIRO) [149]. To our knowledge, we are the first to report the phase inversion effect for a 2DHG system.

5.3.4 Current-induced heating of 2DHG

In this section, we quantitatively examine the empirical relationship between the hole temperature T_h and the applied dc current I_{dc} at small currents, prior to the onset of the SdH phase inversion phenomenon. Fig. 5.14a shows the SdH oscillations collected at fridge temperatures in the range of 50 mK to 300 mK, obtained by slowly sweeping the magnetic field (0.5 T/hour) and measuring ρ_{xx} using a source-drain AC current of 0.3 nA. Applying a Fourier transform (FT) to the SdH oscillations in 1/B over the magnetic field range of 0.1 T to 1.0 T for the SdH data set shown in panel (a), we obtain the familiar spectra of the SOI split subbands p_1 and p_2, as shown in the inset of Fig. 5.14b. The p_1 peak exhibits the largest FT amplitude, primarily attributed to its smaller effective mass ($m_1 \sim 0.35\, m_e$, $m_2 \sim 0.66\, m_e$). As a result, the FT peak height of p_1 is more suitable as an effective thermometer of the holes compared to p_2. Consequently, we employed the peak height of the p_1 subband as a measure of the hole temperature T_h.

We begin by calibrating the hole temperature T_h with the fridge temperature T_0. Following the effective mass analysis in Sec. 4.3.7 of Chapter 4, the peak height of the p_1 subband was fitted as a function of temperature to the Ando equation [30]

$$\frac{\Delta\rho_{xx}}{\rho_{xx}} = 2\,\exp\left(-\frac{\pi}{\omega_c\tau_q}\right)\frac{2\pi^2 k_B T/\hbar\omega_c}{\sinh(2\pi^2 k_B T/\hbar\omega_c)} \tag{5.3}$$

with the effective mass m_1 and quantum lifetime τ_{q1} as the two fitting parameters. The fit was first applied over the entire temperature range ($50 - 300$ mK), which yielded $m_1 =$

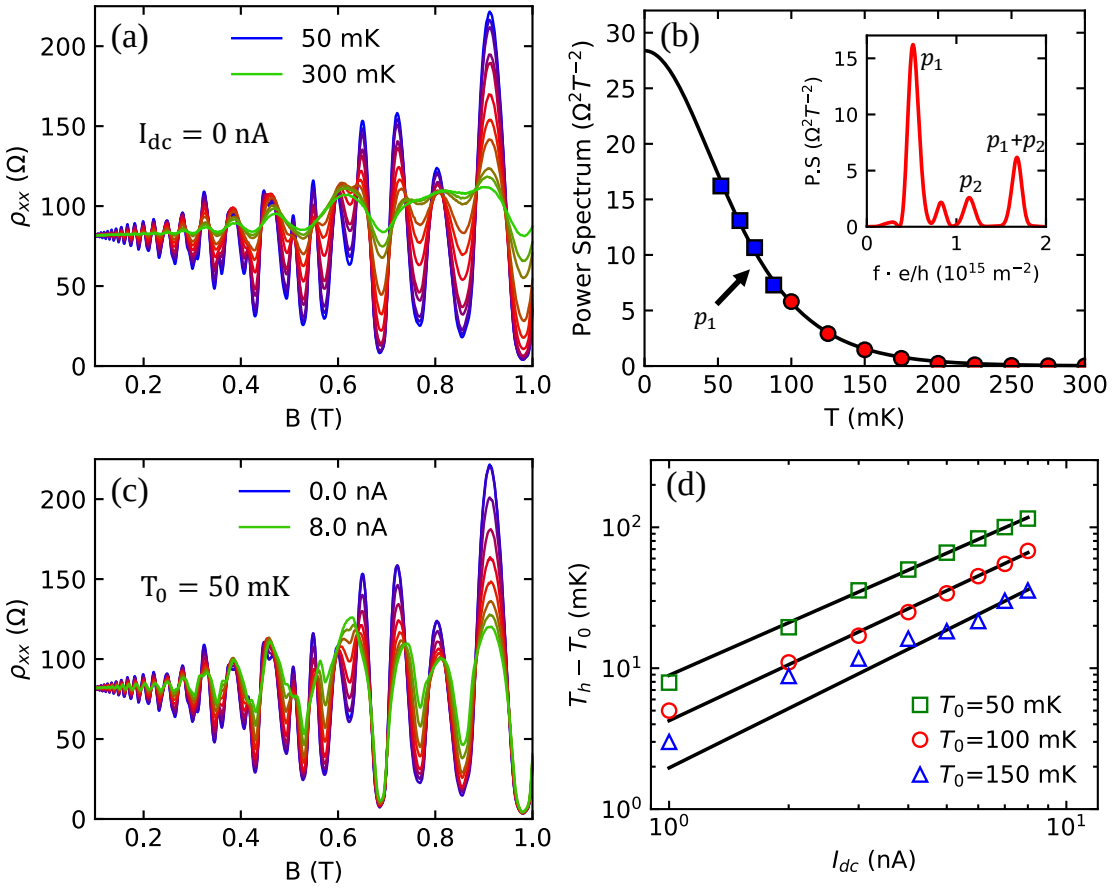


Figure 5.14: (a) Temperature-dependence of the SdH oscillations at $p_{2d} = 1.7 \times 10^{15}$ m^{-2} using $I_{ac} = 0.3$ nA excitation. The temperature data was collected in two different ranges: from 50 mK to 100 mK in 12.5 mK increments, and from 125 mK to 300 mK in 25 mK increments. (b) Power spectrum peak height of the p_1 subband as a function of temperature. The solid line is a fit to the high temperature (red) data points. The low temperature (blue) data points ($\leq$ 87.5 mK) are excluded from the fit. Inset: Fourier spectrum at $T_0 = 50$ mK. (c) SdH oscillations as a function of dc current from 0 nA to 8 nA in 1 nA increments at $T_0 = 50$ mK. (d) Power law fit (solid lines) for three different fridge temperatures: 50 mK, 100 mK, and 150 mK.

(0.352 ± 0.004) m_e and τ_{q1} = (11.92 ± 0.08) ps. At dilution fridge temperatures below approximately 100 mK, the hole temperature often starts deviating from the fridge temperature due to electrical noise or an insufficient thermal link between the sample and the cold finger (mixing chamber). To ensure the lowest temperature data points were not skewing the fit, the same fit was applied but excluded the lowest temperature points below 100 mK (blue squares), as shown in Fig. 5.14b. The high-temperature fit yielded m_1 = (0.355 ± 0.007) m_e and τ_{q1} = (12.0 ± 0.2) ps. The small variation in fitted parameters observed between the fits in the two different temperature ranges falls within the statistical errors of the fit. Thus, as a result of this analysis we can conclude that the hole temperature T_h under equilibrium conditions follows the fridge temperature down to $T_0 = 50$ mK.

Fig. 5.14c shows the SdH oscillations collected at $T_0 = 50$ mK for different I_{dc} values up to 8 nA. Above 8 nA, SdH phase inversion occurs, precluding further analysis. The SdH oscillations at different I_{dc} are Fourier transformed following the same procedure for the temperature-dependent analysis in Fig. 5.14b. The p_1 FT peak amplitudes are extracted at the different values of I_{dc}, and the corresponding hole temperatures T_h are extracted from the calibration curve (solid line) in Fig. 5.14b.

Fig. 5.14d plots the difference in hole temperature T_h and fridge temperature T_0, represented as $\Delta T_h = T_h - T_0$, as a function of I_{dc} conducted at three different fridge temperatures of 50 mK [data in panel (c)], 100 mK, and 150 mK. The data was fitted to a power-law relation, $\Delta T_h = \alpha I_{dc}^{\beta}$, where T_0 is in mK, I_{dc} in nA, and α and β are fitting parameters. The resulting fits are represented as solid lines on the log-log plot in Fig. 5.14. For the three datasets conducted at $T_0 = 50$ mK, $T_0 = 100$ mK, and $T_0 = 150$ mK, the best fit values obtained for α (β) are 8.8 mK/nA (1.2), 4.2 mK/nA (1.3), and 1.7 mK/nA (1.4), respectively. With a nominal value of $\beta \sim 1.3$, the empirical relation $\Delta T_h \propto I_{dc}^{1.3}$ can be reformulated to examine the heat dissipated by the 2DHG as a function of I_{dc}. Recall that the electrical power dissipated from Joule heating is proportional to $P \propto R_0 I_{dc}^2$. Consequently, the power dissipated by the 2DHG is proportional to the ~ 1.5 power of the hole temperature, expressed as $P \propto (T_h - T_0)^{1.5}$.

Reports of electron heating measurements of 2DEGs in materials systems including GaAs/AlGaAs [144], InGaAs/InP [64], and InSb/AlInSb [120], have all demonstrated $\Delta T_e \propto I_{dc}^{2/3}$, or equivalently $P \propto (T_e - T_0)^3$. These measurements employed currents

up to $I_{dc} \sim 10$s μA, and covered a wide range of temperatures ($T \sim 0.015 - 1.5$ K) and electron mobilities ($\mu \sim 16 - 2000\, m^2/V \cdot s$). It is worth mentioning that in an unconventional graphene sample with much lower mobility ($\mu \sim 0.8\, m^2/V \cdot s$), a linear dependence of electron temperature with I_{dc} was reported [102].

The empirical results obtained here suggest a higher sensitivity of the hole temperature to current-induced Joule heating compared to electrons in similar material systems. However, it is important to emphasize that, in contrast to similar measurements in electrons reported above, the data presented here for holes is conducted over a significantly restricted temperature and current range. The temperature range is constrained by the disappearance of the SdH oscillations above $T_0 \sim 200$ mK, while the current range is limited due to the early onset of phase inversion occurring at very small currents of $I_{dc} \sim 10$ nA.

5.3.5 Breakdown at integer filling factors

In this section, we present the measurements of quantum Hall breakdown at high magnetic fields in the strong quantum Hall regime. We begin by presenting conventional plots of ρ_{xx} and r_{xy} in the linear response regime, followed by the introduction of phase diagrams illustrating quantum Hall breakdown.

High B-field magnetoresistance of 2DHG

Fig. 5.15 shows ρ_{xx} and r_{xy} as a function of magnetic field measured at $T_0 = 50$ mK. The longitudinal (SdH) resistivity is represented in black on the left y-axis, while the transverse (Hall) resistivity is shown in red on the right y-axis. The Hall resistance has been normalized by the resistance quantum $R_k = h/e^2$. An AC current of 5 nA at a modulation frequency of 11 Hz was applied between the source and drain contacts on the Hall bar, and the magnetic field was swept at a rate of 2 T/hour. Fig. 5.15a is measured for an intermediate top-gate voltage $V_g = -3.5$ V corresponding to $p_{2d} = 1.3 \times 10^{15}$ m^{-2} and Fig. 5.15b is measured at the maximum top-gate voltage $V_g = -4.5$ V corresponding to $p_{2d} = 2.0 \times 10^{15}$ m^{-2}. The SdH oscillations reach zero up to the maximum B-field (9 T), indicating no parallel conduction. At $p_{2d} = 2.0 \times 10^{15}$ m^{-2}, the $\nu = 2/3$ fractional

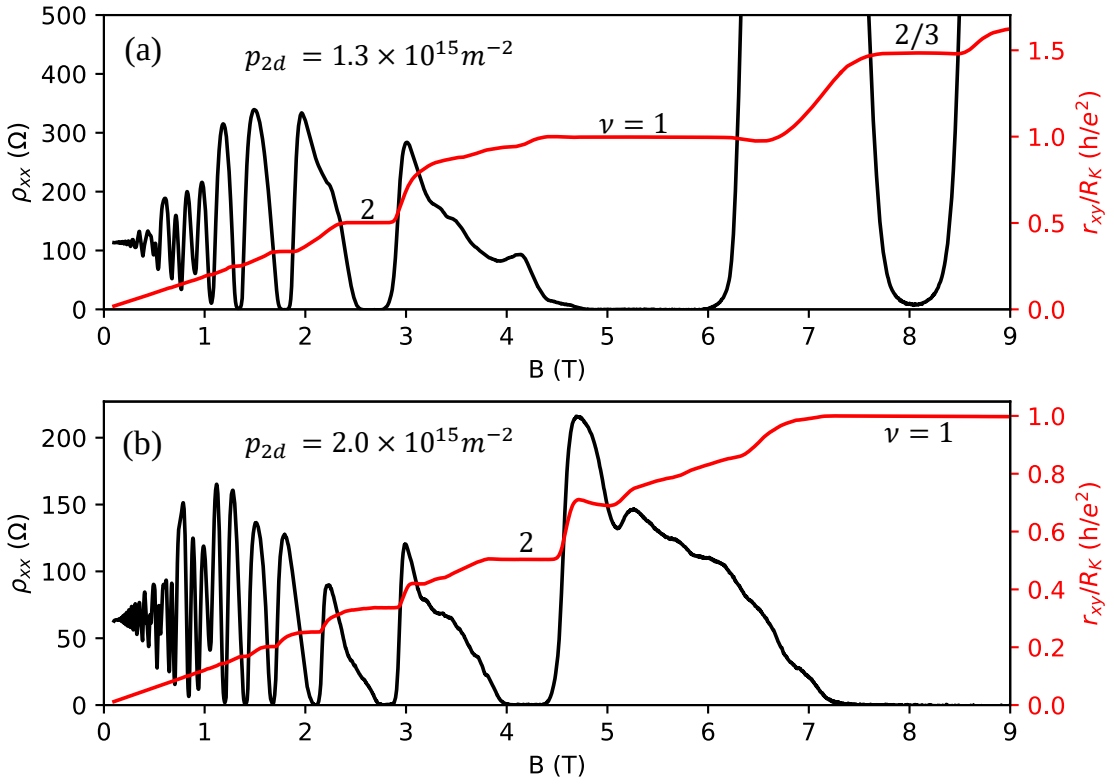


Figure 5.15: Magnetoresistance of the 2DHG measured in the linear response regime at $T_0 = 50$ mK. ρ_{xx} (black) and r_{xy} (red) for (a) $p_{2d} = 1.3 \times 10^{15}$ m^{-2} and (b) $p_{2d} = 2.0 \times 10^{15}$ m^{-2}.

quantum Hall state is just resolved at $\sim$ 8 T, along with emergence of other fractional states between $\nu = 1 - 2$. The presence of fractional states is an indication of low disorder and a high-quality MBE growth.

Breakdown phase diagrams

Here, we present the breakdown phase diagrams or colormaps for the 2DHG. Fig. 5.16 shows the colormaps of ρ_{xx} and r_{xy}, measured concomitantly, as a function of dc current and perpendicular magnetic field. Two sets of colormaps at low and high magnetic fields are provided to emphasize specific features. The colormaps for low (high) B-field are generated

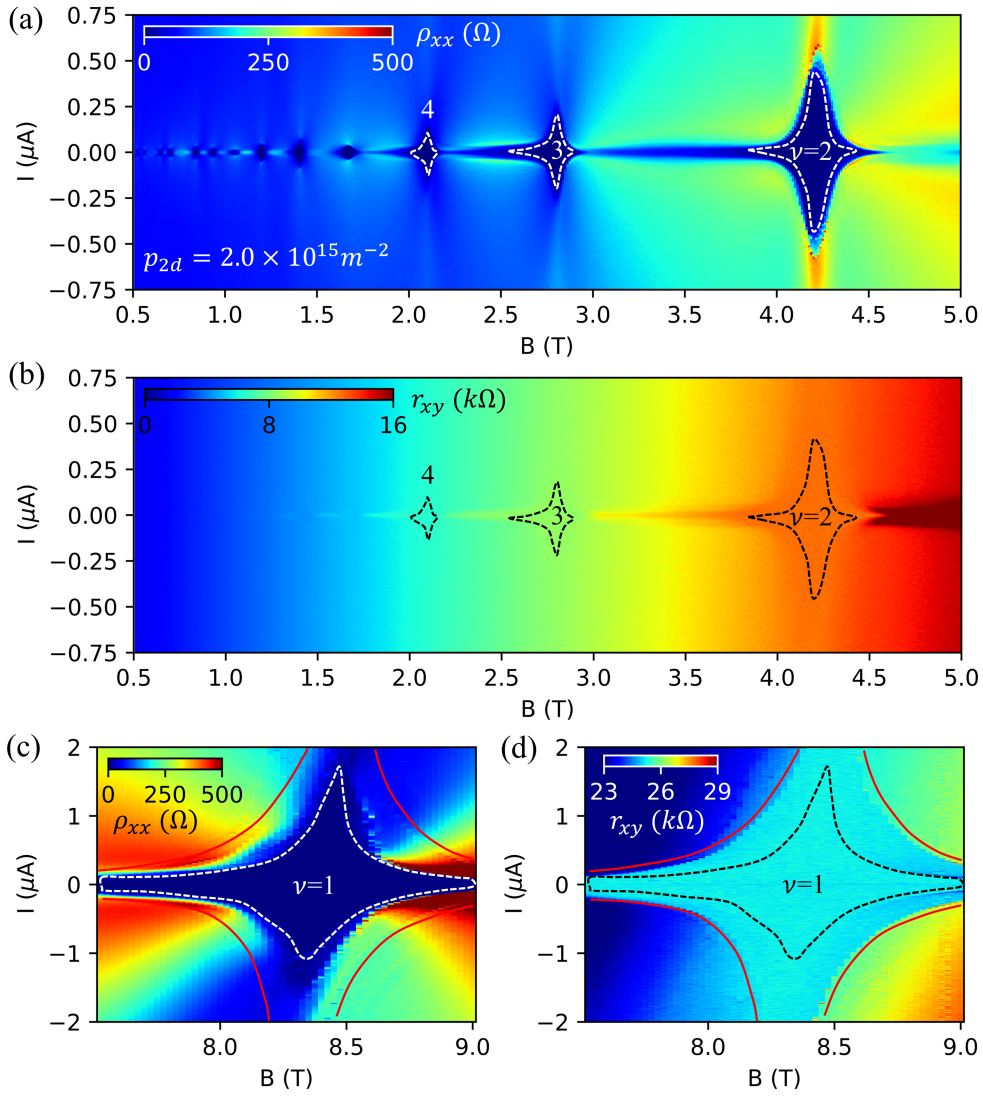


Figure 5.16: Colormaps measured at $p_{2d} = 2.0 \times 10^{15}$ m^{-2} and 50 mK. (a) Colormap of ρ_{xx}. White dashed lines outline the transport diamonds for integer filling factors $\nu = 2, 3, 4$ where $\rho_{xx} \sim 0$. (b) Colormap of r_{xy} with the diamonds in panel (a) outlined by black dashed lines. Within these diamonds, $r_{xy} = h/\nu e^2$ is quantized. (c) ρ_{xx} for $\nu = 1$ and (d) r_{xy} for $\nu = 1$. The white dashed lines outline the transport diamond while the solid red lines highlight the deviation in r_{xy} from its quantized value.

using the AC+DC technique by measuring the differential resistances when sweeping the current from $0 \rightarrow +0.75$ $(+2)$ μA, $0 \rightarrow -0.75$ (-2) μA at a rate of 5 nA/s and stepping the magnetic field from 5 (9) $\rightarrow$ 0.5 (7.5) T in increments of 12.5 mT (25 mT). The measurement used a source-drain AC current of 5 nA at a modulation frequency of 17 Hz and time constant of 100 ms. Similar to the measurement of the low B-field colormap in Sec. 5.3.3, the current was swept in two segments to mitigate asymmetry due to the integration time (lock-in time constant) of the measurement. The colormap shown in Fig. 5.16 was collected over approximately 2.5 days.

We note the following regarding the colormaps shown in Fig. 5.16. A horizontal cut through the maps at zero dc current would give the traditional plot of ρ_{xx} with B-field, as shown in Fig. 5.15b. The dark blue regions in the colormaps of ρ_{xx} correspond to where $\rho_{xx} \sim 0$ and outline the transport diamonds. These transport diamonds are associated with specific integer filling factors, determined by the value of r_{xy} within the same region in the current-magnetic field (I-B) plane. The diamonds corresponding to $\nu = 2, 3, 4$ are clearly visible and outlined in Fig. 5.16a. The much larger $\nu = 1$ diamond at higher B-field is presented separately in Fig. 5.16c.

An outline of the transport diamonds in the maps of ρ_{xx} (white dashed lines) is depicted in the maps of r_{xy} (black dashed lines). Within the diamonds in r_{xy}, the resistance is quantized according to $r_{xy} = h/\nu e^2$. r_{xy} does not deviate from its quantized value at the center of the diamonds, up to the maximum current measured. Away from the center of the diamonds and above the current required for breakdown in ρ_{xx}, r_{xy} deviates from its quantized value. This is most evident in Fig. 5.16d for the $\nu = 1$ filling factor diamond, where the black dashed line shows the breakdown in ρ_{xx} and the solid red line at a larger current highlights the deviation in r_{xy} from its quantized value. On the low (high) B-field side of the $\nu = 1$ diamond, r_{xy} deviates to lower (higher) resistance. These observations are consistent with those reported 2DEGs in Refs. [112, 92].

We will now outline qualitative features of the transport diamonds in ρ_{xx}

1. The width of the diamonds in B-field are sharp due to the relatively high mobility ($\mu \sim 50m^2/V \cdot s$) of the 2DHG. Recall that for the integer quantum Hall effect, the width of the resistance minimums $\rho_{xx} = 0$ and Hall plateaus $r_{xy} = h/\nu e^2$ in magnetic field is inversely proportional to the mobility.

2. Breakdown at the tip of the $\nu = 1$ diamond is very gentle compared to $\nu = 2$ diamond. Interestingly, the opposite behaviour is observed in Ref. [91] for a InGaAs/InP QW 2DEG.

3. For the $\nu = 1$ diamond, the breakdown current at the diamond tip is larger for positive currents and smaller for negative currents. This asymmetry is a consequence of the local hole density of the Hall bar being affected as a result of the large dc current and large sample resistance at high B-field. When $\rho_{xx} \sim 500\,\Omega$ this corresponds to $r_{xx} \sim 10\,k\Omega$. For $I_{dc} \sim 1\ \mu$A, this corresponds to a $V = IR \sim 10$ mV shift on the source contact on the Hall bar. This reduces or enhances (depending on the current polarity) the electric field from the top-gate used to accumulate holes in the 2DHG.

4. In contrast to the colormaps in Refs. [91, 64] for InGaAs/InP and GaAs/AlGaAs 2DEGs, for $\nu = 1 - 4$ we do not observe an even- and odd-filling factor dependence on the size (width in current) of the transport diamonds.

Zener tunneling model of transport diamonds

Here we examine the transport diamonds within the framework of the Zener tunneling model outlined in Sec. 5.2.3. Recall that in Ref. [91], focusing on an InGaAs/InP 2DEG Hall bar, the authors observed that the size of even-filling factor diamonds (in current) were larger than their odd-filling factor counterparts. This was attributed to the width of the diamonds predominately reflecting the energy $\hbar eB/m^* - g^*_\perp \mu_B B$ for even-filling factor factors or $g^*_\perp \mu_B B$ for odd-filling factors.

In our GaAs/AlGaAs 2DHG, we do not observe an even- and odd-filling factor dependence on the width of the transport diamonds. This is clearly illustrated in Fig. 5.17,

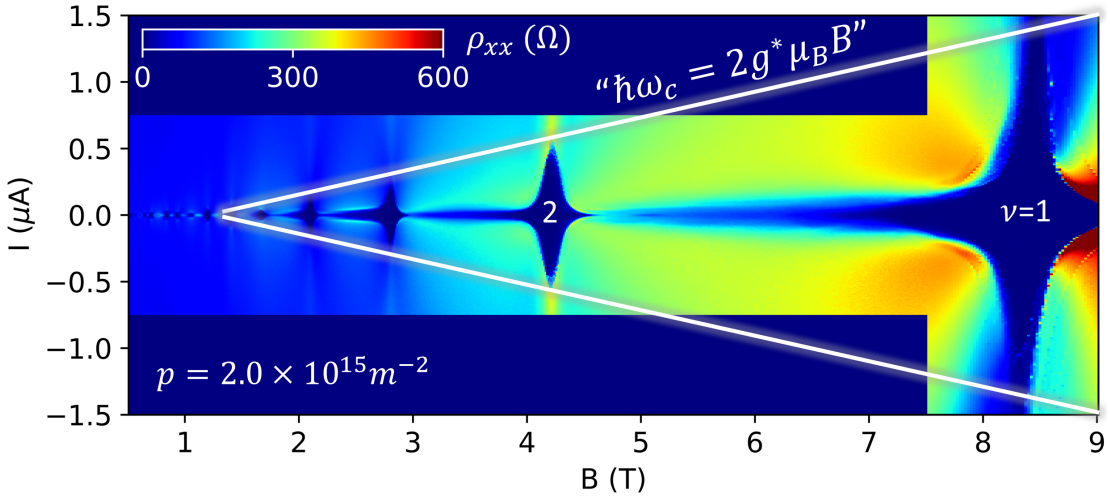


Figure 5.17: Colormap of ρ_{xx} for $p_{2d} = 2.0 \times 10^{15}$ m^{-2}. White lines intersect the tips of the transport diamonds and reflect the growth in the cyclotron energy and Zeeman energy with B-field.

where a single line intersects the tips of both even- and odd-filling factor diamonds. Such behaviour implies that the cyclotron energy is approximately twice as large as the the Zeeman energy ($\hbar\omega_c = \hbar eB/m^* \approx 2g^*\mu_B B$). We can corroborate this result by calculating the two energy gaps, utilizing the values for the effective mass m^* and g factor g^* extracted in Chapter 4. Recall from Sec. 4.3.10 that the Landau levels of our GaAs/AlGaAs 2DHG in quantum Hall regime primarily reflect that of HH- with $m^* \sim 0.35\, m_e$. Using this value, the cyclotron energy (/T) is $\hbar e/m^* \sim 0.33$ meV/T. Furthermore, the nominal value of g^* from Sec. 4.3.10 was estimated to be $g^* \sim 2.8$, yielding a Zeeman energy (/T) of $g^*\mu_B \sim 0.16$ meV/T. Thus, from these calculations, we also find the cyclotron energy to be nearly twice the Zeeman energy (i.e., $0.33/0.16 \sim 2$). In these calculations we have neglected Landau level broadening Γ. However, from the measurements in Chapter 4, we estimate the broadening to be on the order of $\Gamma \sim 20\,\mu$eV, over an order of magnitude smaller than the calculated cyclotron and Zeeman energies in a one Tesla magnetic field. These results demonstrate that the ratio of the sizes of even- and odd-filling factor diamonds can serve as a tool for estimating the ratio of cyclotron and Zeeman energy gaps, thereby providing information about the effective mass and g factor.

For Zener-type tunneling transitions to occur, we can estimate the characteristic length scale δ between two points L and R across the Hall bar. This analysis follows from Ref. [91], where we assume the Landau levels are tilted uniformly across the Hall bar. We will examine breakdown at $\nu = 2$ (B = 4.2 T) where we estimated $E_c \sim 0.34$ kV/m. The length scale for pure Zener tunneling can be estimated from $\delta \sim \Delta/eE_c$ where $\Delta = \hbar\omega_c - |g_e^*|\mu_B B$ is evaluated at 4.2 T with values $0.35m_e$ and 2.8 for m^* and $|g_e^*|$, respectively. We calculate $\Delta \sim 0.71$ meV and $\delta \sim 2.1$ μm (i.e., 0.71/0.34). This is very similar to the value of 1.6 μm obtained in Ref. [91] for an InGaAs/InP 2DEG system. These values are two orders of magnitude larger than what would be expected from the spatial extent of the wavefunction of electrons or holes in the Landau levels, which is dictated by the magnetic length $\ell_B = 25.6nm/\sqrt{B}$, with B in units of Tesla. For $B \sim 4$ T, $\ell_B \sim 13$ nm $\ll \delta$.

Breakdown current density and Hall electric field at $\nu = 1, 2$

In Sec. 5.2, we outlined two methods for quantifying breakdown: the critical current density $J_c = I_c/w$ and the critical Hall electric field $E_c = hI_c/\nu e^2 w$. While a precise definition of the critical breakdown current I_c will be provided in Sec. 5.3.7, here we present initial estimates for these parameters based on the colormap in Fig. 5.17a. When the $\nu = 1$ ($\nu = 2$) transport diamond is at its widest, we observe breakdown currents of $I_c \sim 1.2$ μA (~ 0.4 μA) at 8.4 T (4.2 T) for $p_{2d} = 2.0 \times 10^{15}$ m^{-2}. Consequently, J_c and E_c are ~ 0.08 A/m and ~ 2.1 kV/m (~ 0.027 A/m and ~ 0.34 kV/m) at $\nu = 1$ ($\nu = 2$). In the calculations for J_c and E_c, we used the nominal width of the Hall bar (15 μm).

To contextualize these values, we can compare them to those reported in other Hall bar samples in literature. In the case of a similar GaAs/AlGaAs 2DHG in Ref. [130], albeit modulation-doped and for $p_{2d} = 1.0 \times 10^{15}$ m^{-2}, the values obtained for $\nu = 1, 2$ are very similar with our results here, differing by less than a factor of two. In modulation-doped GaAs/AlGaAs 2DEGs compiled in Refs. [117, 115], we infer E_c values in the range $2 - 6$ kV/m at 4 T (~ 6 kV/m at 8 T) for even-filling (odd-filling) factors. The value $E_c \sim 0.34$ kV/m obtained for even-filling factor $\nu = 2$ at 4.2 T in our 2DHG is approximately an order of magnitude lower than that found in 2DEGs (i.e., 4/0.34 $\sim$ 12). Interestingly, an order of magnitude is also consistent with the difference in energy $\hbar\omega_c - |g^*|\mu_B B$,

accounting for the different values of effective mass and g factor in GaAs/AlGaAs for electrons ($m^* = 0.067\, m_e$ [94] and $|g^*| = 0.44$ [22], $\hbar\omega_c - |g^*|\mu_B B \sim 1.70$ meV/T) and holes ($m^* = 0.35\, m_e$ and $|g^*| \sim 2.8$, $\hbar\omega_c - |g^*|\mu_B B \sim 0.17$ meV/T).

The value $E_c \sim 2.1$ kV/m obtained for odd-filling factor $\nu = 1$ in our 2DHG is approximately 3× smaller compared 2DEGs (i.e., $6/2.1 \sim 3$). Recall that odd-filling factors reflect the energy $|g^*|\mu_B B$, determined by $|g^*|$. Initially, the smaller E_c for holes is not consistent with a larger value of $|g^*|$ compared to electrons. However, g factors at odd-filling factors in 2DEGs are known to be significantly enhanced in magnetotransport measurements due to many-body electron-electron exchange interactions [93, 91, 64]. For example, in Ref. [150], a GaAs/AlGaAs 2DEG reported an enhanced value of $|g^*| \sim 12$ at $\nu = 3$. In our analysis of the odd-ν g factor for the 2DHG in Sec. 4.3.10, we did not find evidence for exchange enhancement. However, the g factor exhibited variation with density, with a value of $|g^*| \sim 4.4$ at $p_{2d} \sim 2.0 \times 10^{15}$ m^{-2}. Thus, the $\sim 3\times$ smaller value of E_c at odd-filling factor could be attributed to the difference in the g factor between electrons and hole in GaAs/AlGaAs (i.e., $12/4.4 \sim 2.7$).

Selected vertical traces through the colormap

In Fig. 5.18, we analyze the $\rho_{xx} - I$ and $r_{xy} - I$ traces by taking vertical cuts through the $\nu = 1, 2$ diamonds in the colormaps of Fig. 5.16. The traces plotted in red correspond to the widest section of the diamonds, located at the center of the integer filling factor. For the ρ_{xx} traces, the width of the resistance minima, where $\rho_{xx} \sim 0$, becomes narrower away from the diamond center. On the high magnetic field side of the $\nu = 1$ diamond, breakdown is abrupt, and ρ_{xx} jumps by approximately 5 kΩ near 9 T. However, at the center of the $\nu = 1$ diamond, breakdown is gradual, characterized by a small jump in ρ_{xx} (~ 100 Ω), and the resistivity gradually increases with increasing current.

In the case of the $\nu = 2$ diamond, breakdown is more symmetrical on the high and low magnetic field sides of the diamond. Similar to $\nu = 1$, breakdown is also gradual at the center of the $\nu = 2$ diamond, with ρ_{xx} initially jumping by approximately 80 Ω and gradually increasing with increasing current. Regarding the r_{xy} traces at the diamond center, the resistance remains constant at the quantized values h/e^2 and $h/2e^2$ for the

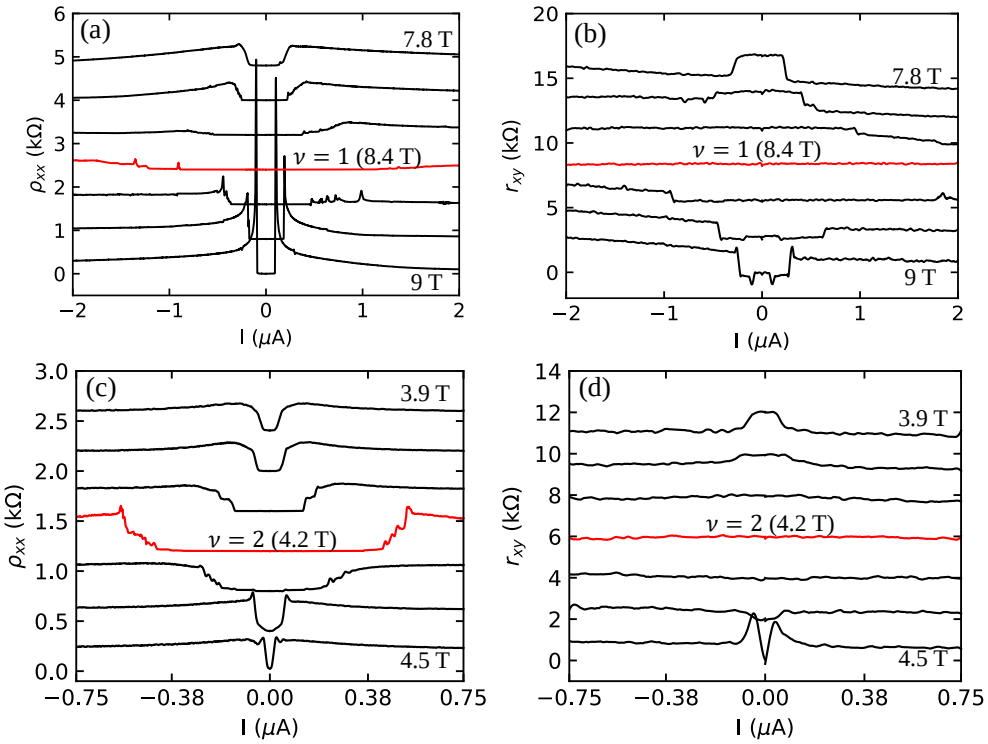


Figure 5.18: ρ_{xx}-I traces through (a) $\nu = 1$ (vertically shifted by 0.8 kΩ) and (c) $\nu = 2$ (vertically shifted by 0.4 kΩ). r_{xy}-I traces through (b) $\nu = 1$ (vertically shifted by 2.8 kΩ) and (d) $\nu = 2$ (vertically shifted by 2.0 kΩ).

$\nu = 1$ and $\nu = 2$ diamonds. On the low (high) magnetic field side of the diamonds, r_{xy} deviates to lower (higher) resistance, consistent with reports in Refs. [112, 92].

5.3.6 Progression of colormaps with hole density

Fig. 5.19 shows the colormaps of ρ_{xx} collected at four hole densities in the range $p_{2d} = 1 - 2 \times 10^{15}$ m^{-2} by adjusting the voltage on the top-gate. The colormaps for low (high) B-field are collected with a resolution of 12.5 mT (25 mT). For comparison between the maps, the current (y-scale) remains constant (± 1.5 μA), while the width of figures (magnetic field, x-axis) increases proportionally with the growing magnetic field range.

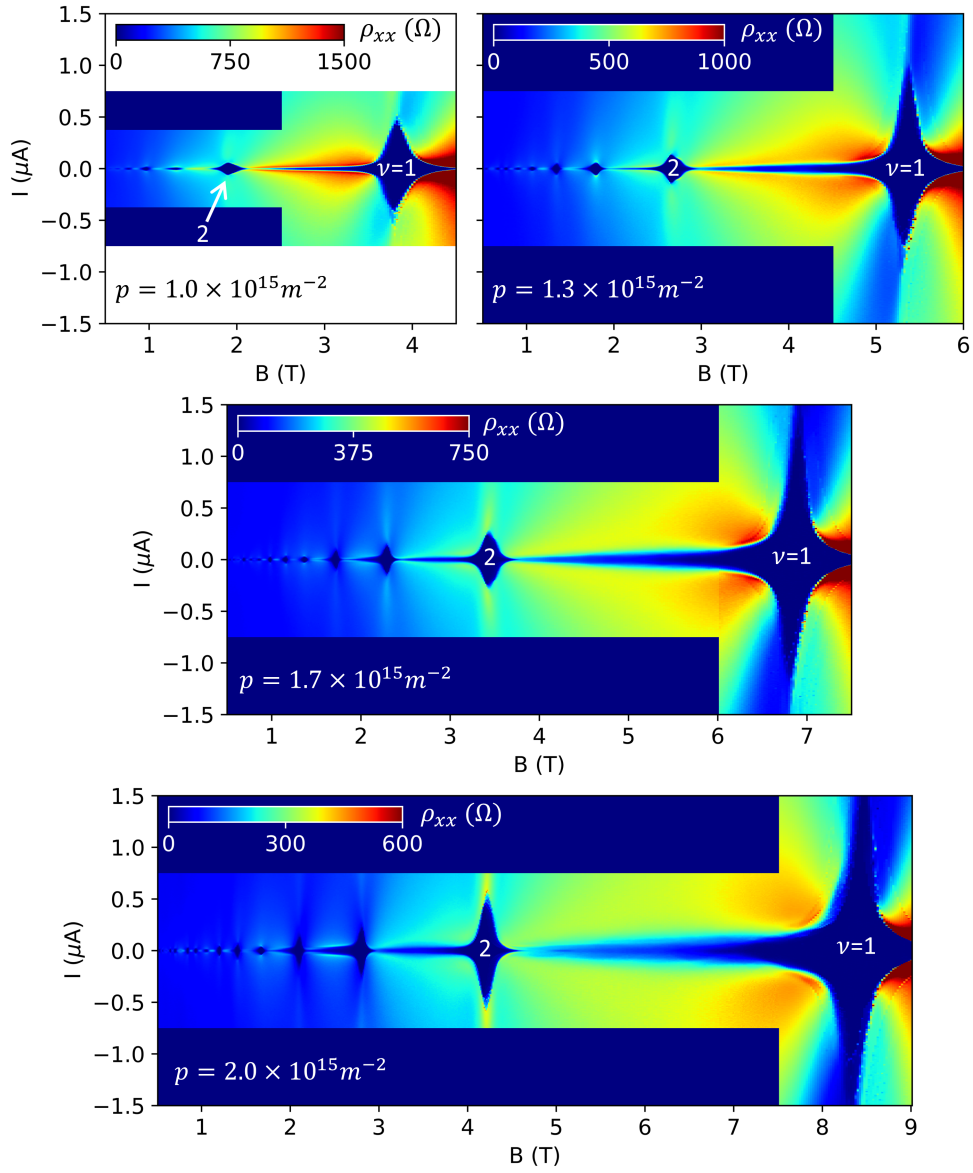


Figure 5.19: Colormaps of ρ_{xx} measured at $T_0 = 50$ mK and collected at four hole densities in the range $p_{2d} = 1.0 \times 10^{15}$ m^{-2} to $p_{2d} = 2.0 \times 10^{15}$ m^{-2} by systematically adjusting the voltage on the top-gate.

We observe the following trends with varying the hole density

1. For the smallest two-hole densities, $p_{2d} = 1 \times 10^{15}$ m^{-2} and $p_{2d} = 1.3 \times 10^{15}$ m^{-2}, only the transport diamonds corresponding to filling factors $\nu = 1, 2$ are clearly visible. For the largest two-carrier densities, $p_{2d} = 1.7 \times 10^{15}$ m^{-2} and $p_{2d} = 2 \times 10^{15}$ m^{-2}, filing factors $\nu = 1, 2, 3, 4$ are clearly visible.

2. With increasing hole density, all of the transport diamonds move to higher magnetic field, as expected, according to $\nu = p_{2d}\hbar/eB$. For instance, the center of the $\nu = 1$ diamond moves from ~ 4 T at $p_{2d} = 1 \times 10^{15}$ m^{-2} to ~ 8 T at $p_{2d} = 2 \times 10^{15}$ m^{-2}. Fortuitously, the $\nu = 1$ diamond is visible within the maximum range of magnetic field (9 T) at the maximum hole density ($p_{2d} = 2 \times 10^{15}$ m^{-2}).

3. With increasing hole density, the width in current of the transport diamonds increases. For instance, the breakdown current for the $\nu = 1$ diamond increases from ~ 0.5 μA at $p_{2d} = 1 \times 10^{15}$ m^{-2} to ~ 1.5 μA at $p_{2d} = 2 \times 10^{15}$ m^{-2}. The B-field dependence of the breakdown currents with hole density will be presented in Sec. 5.3.7.

4. In the B-field regions between diamonds for all hole densities, a narrow resistance minimum (dip) is observed near zero current. This phenomenon is known as the zero-current anomaly (ZCA) and will be discussed in Sec. 5.3.8.

5. With increasing hole density, breakdown at the tip of the $\nu = 1$ transport diamond becomes less abrupt (reduced contrast). The opposite behaviour is observed in a 2DEG system in Ref. [91], where the contrast for the $\nu = 1$ diamond is most prominent. The reason for this is unknown.

6. The diamonds for all hole densities seem to exhibit curved edges. In Ref. [64], it is observed that high filling factor diamonds ($\nu \geq 5$) have straight edges, whereas in Ref. [91], it is noted that the diamonds acquire curvature at higher magnetic fields as they become more well-developed.

Vertical traces through the transport diamonds

Here we present vertical traces through the ρ_{xx} colormaps at the center of the transport diamonds. We emphasize trends concerning filling factor for a constant hole density and hole density at a fixed filling factor. The traces are plotted with both a linear and logarithmic y-scale. In the logarithmic scale plots, a horizontal gray dashed line is included at $\rho_{xx} = 3\,\Omega$ to emphasize the noise level in ρ_{xx}. This will be important in Sec. 5.3.7 for the quantitative determination of the critical breakdown current I_c.

Trends at fixed hole density for different filling factors

Fig. 5.20 shows the ρ_{xx} traces for filling factors $\nu = 2 - 6$ for the hole densities $p_{2d} = 1.3 \times 10^{15}$ m^{-2} and $p_{2d} = 2 \times 10^{15}$ m^{-2}. We note the following trends and observations: i. The width of the ρ_{xx} minimum centered at zero current grows with decreasing filling factor, as also evident in the colormaps in Fig. 5.19. ii. In general, ρ_{xx} after breakdown sharply increases to a maximum value and steadily decreases with increasing current. However, this is not the case for $\nu = 3, 4$ at $p_{2d} = 2 \times 10^{15}$ m^{-2}, where breakdown is gradual and the ρ_{xx} monotonically climbs with increasing current. iii. With increasing filling factor, the value of ρ_{xx} at the maximum current decreases. iv. For filling factor $\nu = 2$, ρ_{xx} jumps several times after breakdown before reaching a stable value. These jumps disappear with increasing filling factor. v. At $p_{2d} = 1.3 \times 10^{15}$ m^{-2}, ρ_{xx} for filling factors $\nu = 5, 6$ does not reach zero (within the noise level). However, it still has a zero current "dip" in ρ_{xx}, which will be discussed in Sec. 5.3.8.

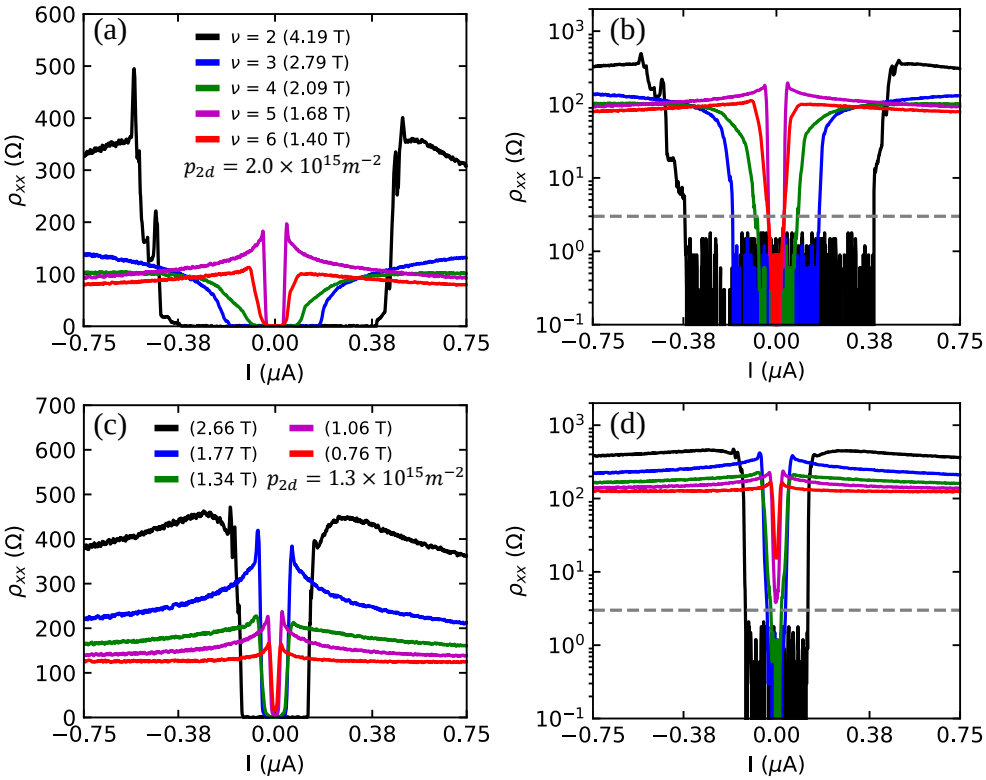


Figure 5.20: Vertical traces through the transport diamonds for $p_{2d} = 2.0 \times 10^{15}$ m^{-2} and $p_{2d} = 1.3 \times 10^{15}$ m^{-2}. Plotted with a linear y-scale (a, c) and log scale (b, d). The gray dashed line at $\rho_{xx} = 3\,\Omega$ in panels (b, d) serves to highlight the noise level in ρ_{xx}.

Trends at fixed filling factor for different hole density

Fig. 5.21 shows the ρ_{xx} traces for filling factors $\nu = 1$ and $\nu = 2$ for all four hole densities. We note the following trends and observations: i. The width of the ρ_{xx} minimum centered at zero current grows with increasing hole density, reflecting the increase in size of the transport diamonds in Fig. 5.19. ii. With increasing hole density, the value of ρ_{xx} at the maximum current for each hole density decreases. iii. Very clearly for the $\nu = 1$ traces, the behaviour of ρ_{xx} for positive and negative current is not symmetric. For example, the negative current traces for $\nu = 1$ exhibit several jumps in ρ_{xx} beyond breakdown compared to the positive current traces. As mentioned previously, this current asymmetry is

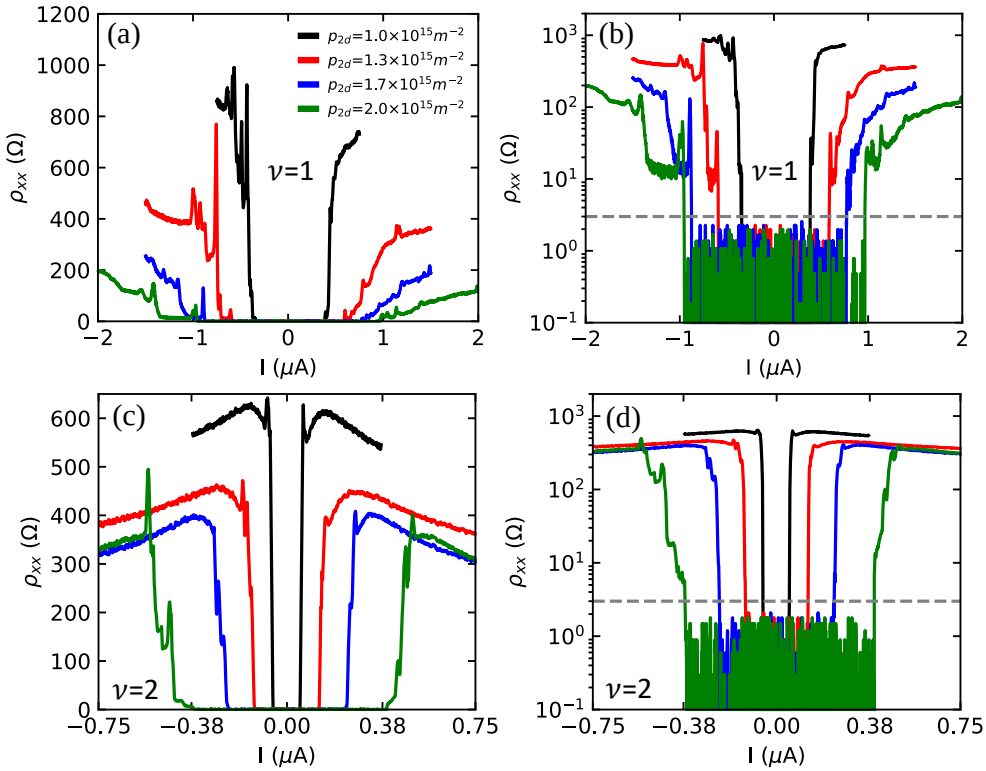


Figure 5.21: Vertical traces through the transport diamonds for filling factors $\nu = 1, 2$. Plotted with a linear y-scale (a, c) and log scale (b, d). The grey dashed line at $\rho_{xx} = 3\,\Omega$ in panels (b, d) serves to highlight the noise level in ρ_{xx}.

consistent with the local hole density of the Hall bar being affected by the large current and large resistance of the sample. iv. For the $\nu = 1$ traces, ρ_{xx} continues to grow beyond breakdown, while for the traces for $\nu = 2$, ρ_{xx} steadily decreases after reaching a peak value.

5.3.7 Magnetic field dependence of critical current

In this section, we present the magnetic field dependence of the critical breakdown currents I_c. Using the colormaps at different hole densities, we can extract the values of I_c at the transport diamond tips. In literature, two reasonable methods have been used to quantify I_c [91]. In method A, the value of I_c is taken to be when ρ_{xx} exceeds a small threshold. The threshold value is influenced by the noise level in ρ_{xx} data. In method B, I_c is given by the position of a maximum in ρ_{xx} that often occurs near the diamond tip. Note that this point corresponds to the steepest slope of V_{xx} with current. For our data, no clear maximum in ρ_{xx} is consistently observed over a wide range of filling factors and hole densities (see Sec. 5.3.6). Furthermore, for filling factor $\nu = 1$, several multi-peak features are observed. Thus, we only utilize method A for the extraction of I_c.

The noise level in ρ_{xx} was typically 1-2 Ω (see Sec. 5.3.6), and therefore the threshold value in method A for determining I_c was set to 3 Ω. For this analysis, only low-filling factor diamonds with $I_c > 0.05$ μA were considered. Specifically, $\nu = 1 - 4$ for $p_{2d} = 2.0 \times 10^{15}$ m^{-2} and $p_{2d} = 1.7 \times 10^{15}$ m^{-2}, and $\nu = 1 - 2$ for $p_{2d} = 1.3 \times 10^{15}$ m^{-2} and $p_{2d} = 1.0 \times 10^{15}$ m^{-2}. Fig. 5.22a shows the I_c values extracted for both current polarities using method A. The I_c values for even-filling factors (represented by ∘) and odd-filling factors (represent by △) more or less fall on a single straight line. The dashed lines for each polarity are least-squares linear fits through the data. The lines do not extrapolate to zero current at 0 T, but instead have a zero current intercept of ∼ 1.8 T. A finite zero current intercept is to be expected since a non-zero breakdown current requires the SdH minima to reach zero resistance, something that only occurs for $B \gtrsim 1$ T. In Fig. 5.22b, the I_c vs B data is presented with a logarithmic scale on the x-axis to accentuate lower magnetic field data. Fig. 5.22c shows the corresponding the critical electric field $E_c \propto I_c/\nu$ as a function of magnetic field, also plotted with a logarithmic scale on the x-axis in Fig. 5.22d. The dashed lines for each polarity are least-squares linear fits through the data.

In our data presented in Fig. 5.22a, a linear B dependence of I_c is suggested, with a common line for both even- and odd-filling factors. It is important to note that data for even-filling factors is available only up to $B \sim 4.2$ T ($\nu = 2$ at $p_{2d} = 2.0 \times 10^{15}$ m^{-2}), and thus obtaining more even-filling factor data for $B > 4.2$ T would be desirable. In

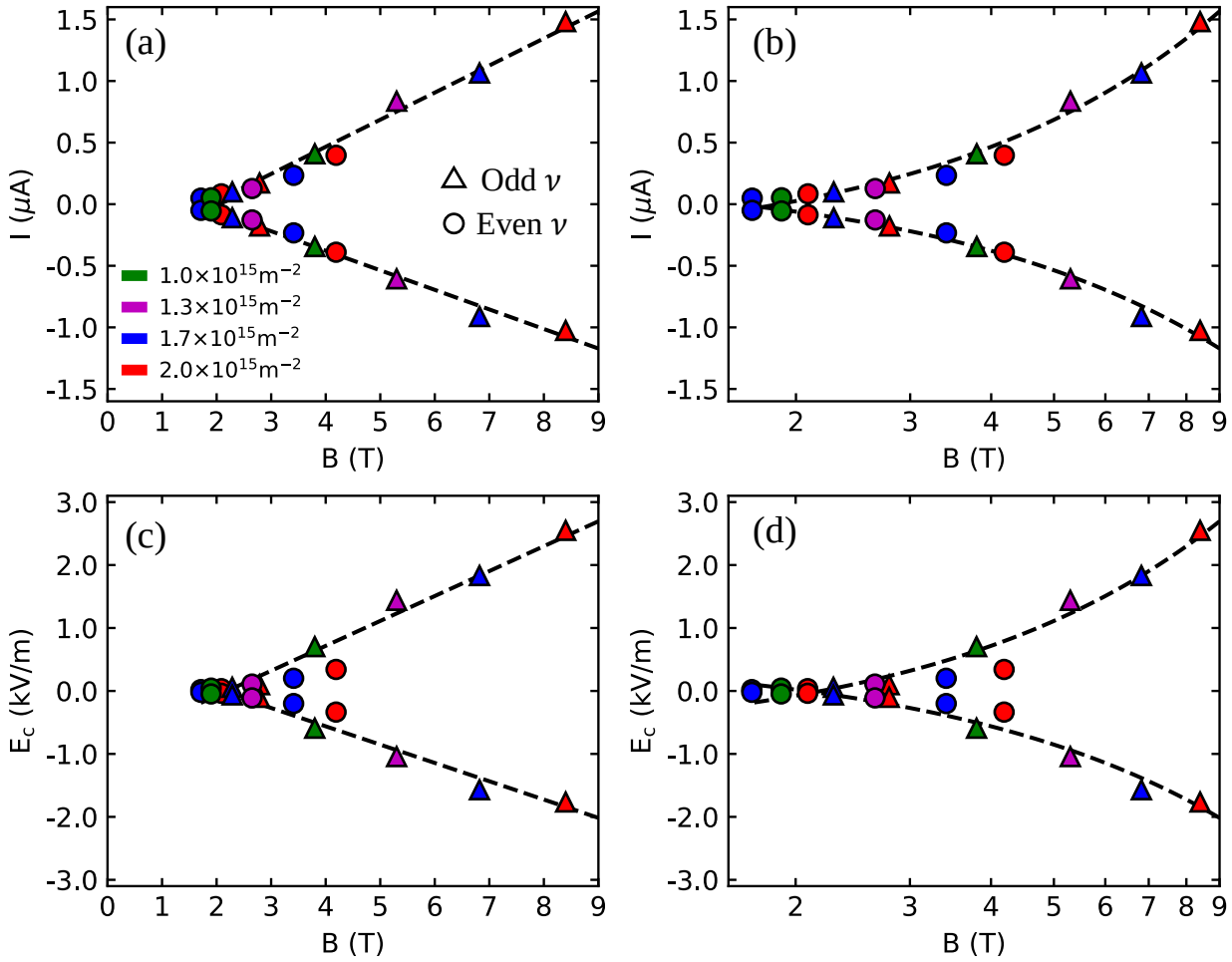


Figure 5.22: (a) Critical current I_c as a function of magnetic field B compiled for $\nu = 1-4$ for $p_{2d} = 2.0 \times 10^{15}$ m^{-2} and $p_{2d} = 1.7 \times 10^{15}$ m^{-2}, and $\nu = 1-2$ for $p_{2d} = 1.3 \times 10^{15}$ m^{-2} and $p_{2d} = 1.0 \times 10^{15}$ m^{-2}. Odd-filling factor values are represented by $\triangle$, while even-filling factor values are represented by $\circ$. (b) I_c vs B data plotted with a logarithmic scale on the x-axis to emphasize lower B-field data. (c) Critical electric field E_c as a function of magnetic field. (d) E_c data with a logarithmic scale on the x-axis. All plots include dashed lines representing a least-squares linear fit.

Ref. [91], where breakdown was also studied in a InGaAs/InP 2DEG for different electron densities, the authors similarly found a near linear B-field dependence of I_c. In contrast, they observed two separate lines for even- and odd-filling factors (see Fig. 5.9), reflecting the much larger cyclotron energy compared to the Zeeman energy gap ($\hbar\omega_c \gg g^*\mu_B B$) in that system. The authors also reported similar zero-current intercepts of $B \sim 1.5$ T for even-filling factor data and $B \sim 2.5$ T for odd-filling factor data.

In the breakdown of GaAs/AlGaAs 2DEGs, it was originally proposed that the critical Hall electric field E_c was proportional to $B^{3/2}$ [117, 115]. However, upon further evaluation in Ref. [119], the authors concluded that a linear B dependence fit of the compiled data to be just as good as a $B^{3/2}$ dependence fit. In the InGaAs/InP 2DEG system discussed in Ref. [91], the authors did not find a power-law dependence when examining I_c/ν ($E_c \propto I_c/\nu$). This is also true for our GaAs/AlGaAs 2DHG data, where a linear fit is a better representation of the data than a power-law relationship.

5.3.8 Zero current anomaly

In Sec. 5.3.6, it was noted that a "dip" in ρ_{xx} is observed near zero current for regions of B-field outside the transport diamonds. This "dip" is a signature of the zero-current anomaly effect (ZCA) which has be described in Refs. [64, 91] for InGaAs/InP 2DEG Hall bars. The ZCA can be observed over a wide range of B-fields except at integer filling factors when ρ_{xx} is zero. Fig. 5.23 shows traces of ρ_{xx} as a function of I_{dc} collected at $p_{2d} = 2.0 \times 10^{15}$ m^{-2} on the high B-field side of where the transport diamonds touch at zero current. The full width at half maximum (FWHM) at magnetic fields of 1.80 T, 2.29 T, 3.12 T, and 4.96 T, is determined to be 0.015 μA, 0.03 μA, 0.06 μA, and 0.14 μA, respectively. The growth of FWHM with increasing with B-field was not reported in Refs. [64, 91], instead only a nominal value was specified.

Following Ref. [91], we can convert the FWHM of the ZCA into an energy by correlating the width of the transport diamond to energy. We use the even-filling factor diamond $\nu = 2$ (B = 4.2 T) collected at $p_{2d} = 2.0 \times 10^{15}$ m^{-2} for this purpose. Recall that even-filling factor diamonds reflect the energy $\Delta = \hbar\omega_c - |g^*_\perp|\mu_B B$. Using the values $m^* = 0.35\, m_e$ and $|g^*_\perp| \sim 2.8$, we calculate $\Delta \sim 0.7$ meV to be equivalent to $I_c \sim 0.4\,\mu$A. From the near

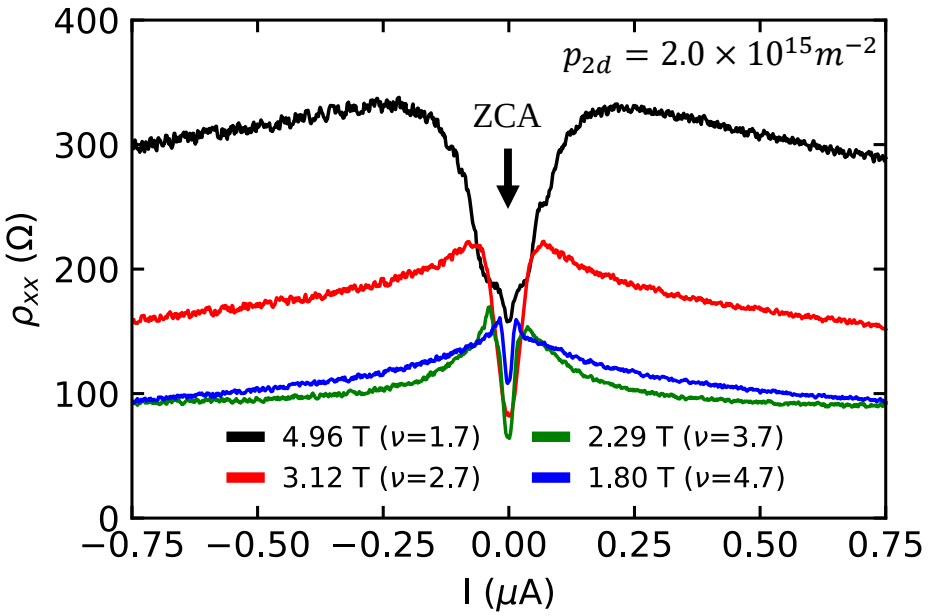


Figure 5.23: Selected traces of ρ_{xx} as a function of I_{dc} at four different magnetic fields between transport diamonds for $p_{2d} = 2.0 \times 10^{15}$ m^{-2}. The zero-current anomaly (ZCA) "dip" is labeled and present in all traces shown.

linear increase in width of even-filling factor transport diamonds with B-field, we estimate that the average FWHM of ~ 0.06 μA to be equivalent to an energy ~ 0.1 meV.

Studenikin *et al.* [64] outlined the characteristics of the ZCA for InGaAs/InP 2DEG Hall bars for B-fields up to ~ 5 T ($\nu \geq 5$). The ZCA FWHM was determined to be ~ 2.1 μA (~ 0.25 μA) for a 100 μm (10 μm) wide Hall bar, indicating the FWHM is proportional to the Hall bar width. Similarly, a FWHM of ~ 0.4 μA was estimated in Ref. [91] for a 15 μm wide Hall bar in a InGaAs/InP 2DEG. In our GaAs/AlGaAs 2DHG Hall bar of the same width (15 μm), we find the FWHM to be $\sim 7\times$ smaller (i.e., $0.4/0.06 \sim 7$).

To our knowledge, we are the first to report the ZCA for a 2DHG. The ZCA has been reported in InGaAs/InP and GaAs/AlGaAs material systems [64]. The origin of the ZCA is not understood and we are not aware of any theoretical investigations on this subject. In Ref. [64], it has been speculated to originate from a Coulomb gap in the single-particle density of states of interacting electrons in the presence of disorder and magnetic field.

5.3.9 Investigation of hysteresis near breakdown

In the preceding sections, we exclusively measured quantum Hall breakdown as the current swept from zero to a maximum for both current polarities. Essentially, we assumed that the behavior remained independent of the current sweep direction and, consequently, the system's history. As outlined in Sec. 5.2.4, we described how hysteretic behaviour near breakdown of odd-integer filling factors has been associated with dynamic nuclear polarization of nuclear spins in the substrate. In the context of a GaAs/AlGaAs 2DHG system, we anticipate a significant suppression of this behavior due to the p-orbital character of the hole wavefunction. Nonetheless, our objective is to experimentally verify this, or discern hysteresis originating from a different source.

Colormaps for studying hysteresis

Fig. 5.24a-d shows the colormaps of ρ_{xx} for filling factors $\nu = 1 - 4$ collected for both up and down current sweep directions. The measurement used the AC+DC technique with a source-drain ac current of 5 nA at a modulation frequency of 17 Hz and time constant of 100 ms. For each B-field, ρ_{xx} and r_{xy} (not shown) were collected in four separate current sweeps in the sequence $0 \rightarrow +dc \rightarrow 0 \rightarrow -dc \rightarrow 0$. The current was swept at a rate of 5 nA/s and the B-field was progressively lowered from the maximum value in steps of 25 mT.

Visually, the colormaps for up and down current sweep directions look identical. In Fig. 5.24e-f, the colormaps $\Delta\rho_{xx}$ are presented, obtained by subtracting ρ_{xx} collected during the down-sweep from that collected during the up-sweep ($\Delta\rho_{xx}(I) = \rho_{xx}^{\text{down}} - \rho_{xx}^{\text{up}}$). If the down- and up-sweep data were identical, $\Delta\rho_{xx}$ would be zero in the entire I-B plane (green in the colormap). Instead, we clearly observe red (blue) regions of hysteresis near the transport diamond edges which correspond to when $\Delta\rho_{xx}$ is positive (negative).

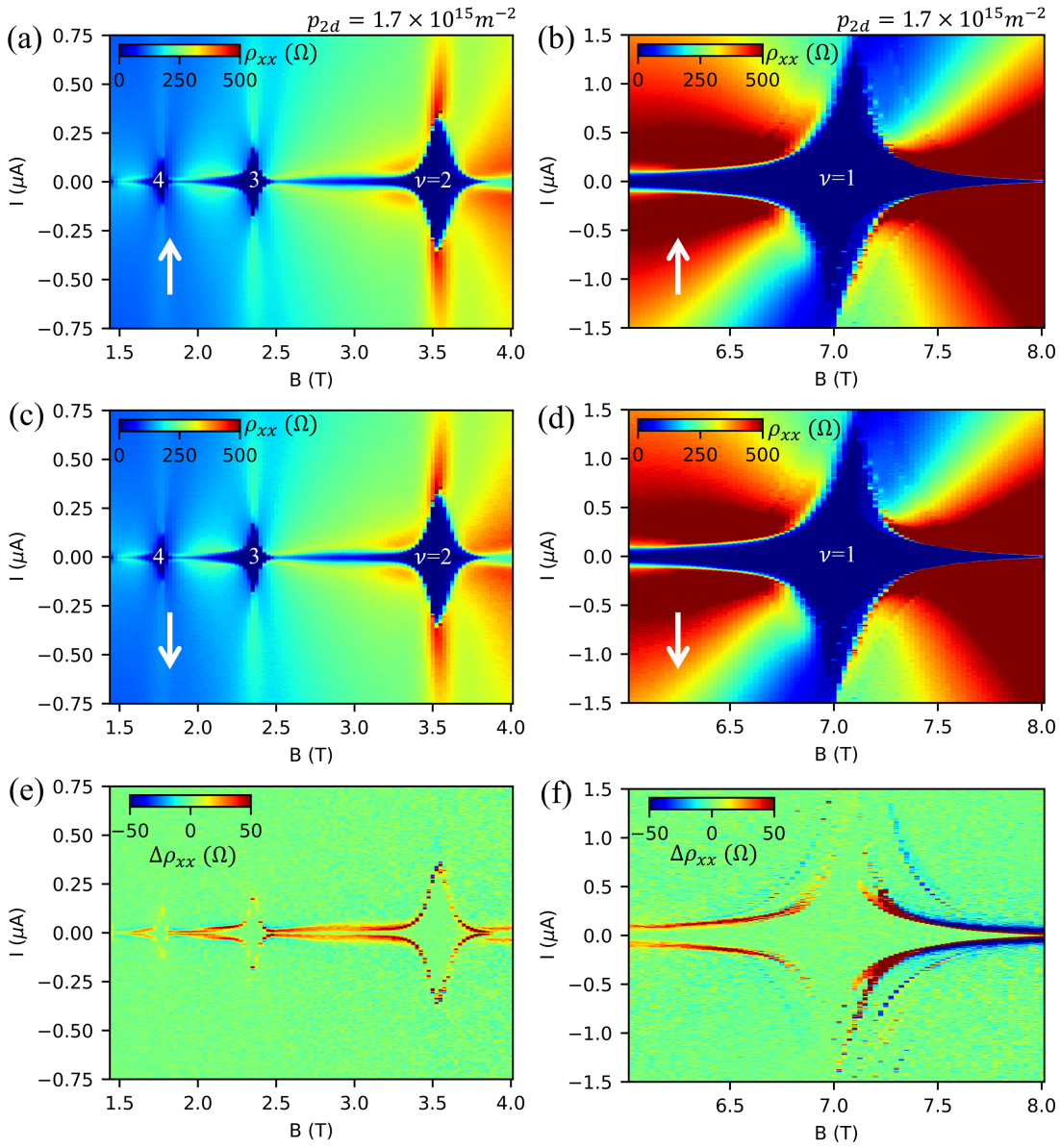


Figure 5.24: Colormaps of ρ_{xx} for up (a-b) and down (b-c) current sweep directions at $p_{2d} = 1.7 \times 10^{15}$ m^{-2}. (e-f) Colormaps of $\Delta\rho_{xx}$ obtained by subtracting ρ_{xx} taken on the up and down current sweep directions.

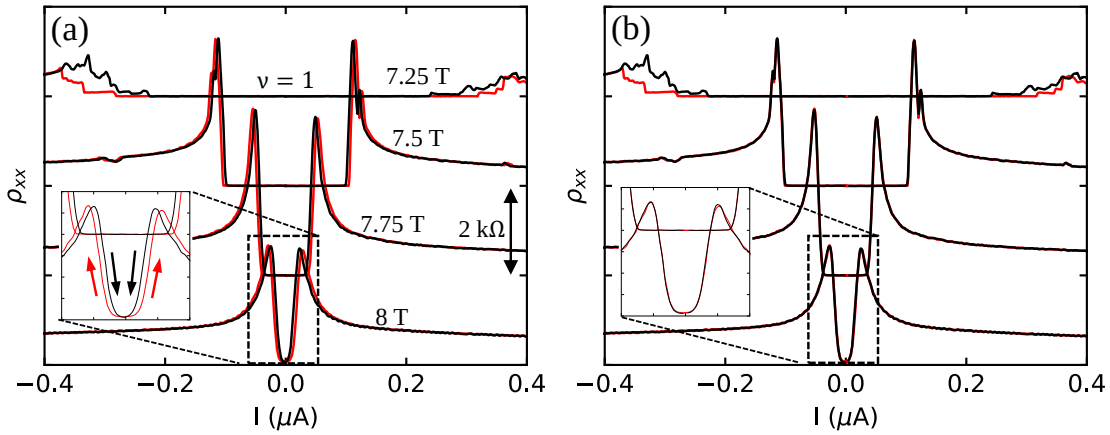


Figure 5.25: Removal of trivial hysteresis. (a) As measured up (red) and down (black) current sweep traces of ρ_{xx} for select B-fields. (b) The same current sweep traces after removal of trivial hysteresis. The traces are vertically offset for clarity.

Removal of trivial hysteresis

Before proceeding, we must identify and remove trivial hysteresis resulting from measurement transients when sweeping the current. The time constant of 100 ms on the lock-in amplifier, employed in the AC+DC measurement technique, introduces a small lag in the measurement of the differential resistance $r_{xx}(I_{dc})$ while sweeping the current. This lag leads to hysteresis between the up and down current sweep data. Fig. 5.25a shows example traces of ρ_{xx} taken from the colormaps in Fig. 5.24b, d. At first glance, it would appear hysteresis is present in all $\rho_{xx} - I$ traces near breakdown. However, upon closer inspection for traces 8-7.5 T, it becomes apparent that up-sweep traces (red) are shifted to higher current, while down-sweep traces (black) are shifted to lower current. This current shift is consistent with the lag caused by the 100 ms time constant. To correct for the lag, the up-sweep (down-sweep) traces are shifted lower (higher) current by $\sim$ 2.1 nA. The corrected traces are depicted in Fig. 5.25b, where hysteresis in traces at 8-7.5 T is eliminated, revealing only non-trivial hysteresis for B = 7.25 T. This non-trivial hysteresis is what we are interested in characterizing.

Non-trivial hysteresis colormaps

Fig. 5.26 shows the corrected colormaps of $\Delta\rho_{xx}$ and Δr_{xy} with trivial hysteresis removed. The hysteresis in the low B-field colormap ($\nu = 2 - 4$) of ρ_{xx} is now completely eliminated after the correction procedure. Concomitantly, no hysteresis is observed for r_{xy}. However, hysteresis is still observed in the high B-field $\Delta\rho_{xx}$ colormap near filling factor $\nu = 1$. The hysteresis is predominately located on the high B-field side of $\nu = 1$, albeit, a small amount is also located on the low B-field side for positive current polarity only. In the colormap of $\Delta\rho_{xx}$, positive $\Delta\rho_{xx}$ (red) hysteresis occurs near the critical breakdown current I_c where ρ_{xx} switches between a dissipative and non-dissipative state. Specifically, the traces of $\rho_{xx} - I$ near breakdown shift to a lower current on the down-sweep direction. Additionally, negative $\Delta\rho_{xx}$ (blue) hysteresis occurs in the same region of B-field but at a larger value of current. Furthermore, a small amount of hysteresis is observed in r_{xy} on the high B-field side of $\nu = 1$. Interestingly, the hysteresis in r_{xy} is in the same location of the I-B plane as the negative hysteresis in ρ_{xx} (indicated by arrows). The correlated hysteresis between ρ_{xx} and r_{xy} is an indication that the hole density is shifting from the large current bias (voltage) on the source contact of the Hall bar. As previously mentioned, the current polarity asymmetry of the $\nu = 1$ transport diamond is consistent with the local hole density of the 2DHG shifting from the large current bias. This bias effectively enhances or reduces (depending the current polarity) the local electric field used to accumulate holes. Hysteresis could be anticipated if the hole density shifts and does not precisely return to the initial value, possibly due to inhomogeneities in the Hall bar. While this explanation is plausible, we characterize the hysteresis further and identify whether it is consistent with other effects.

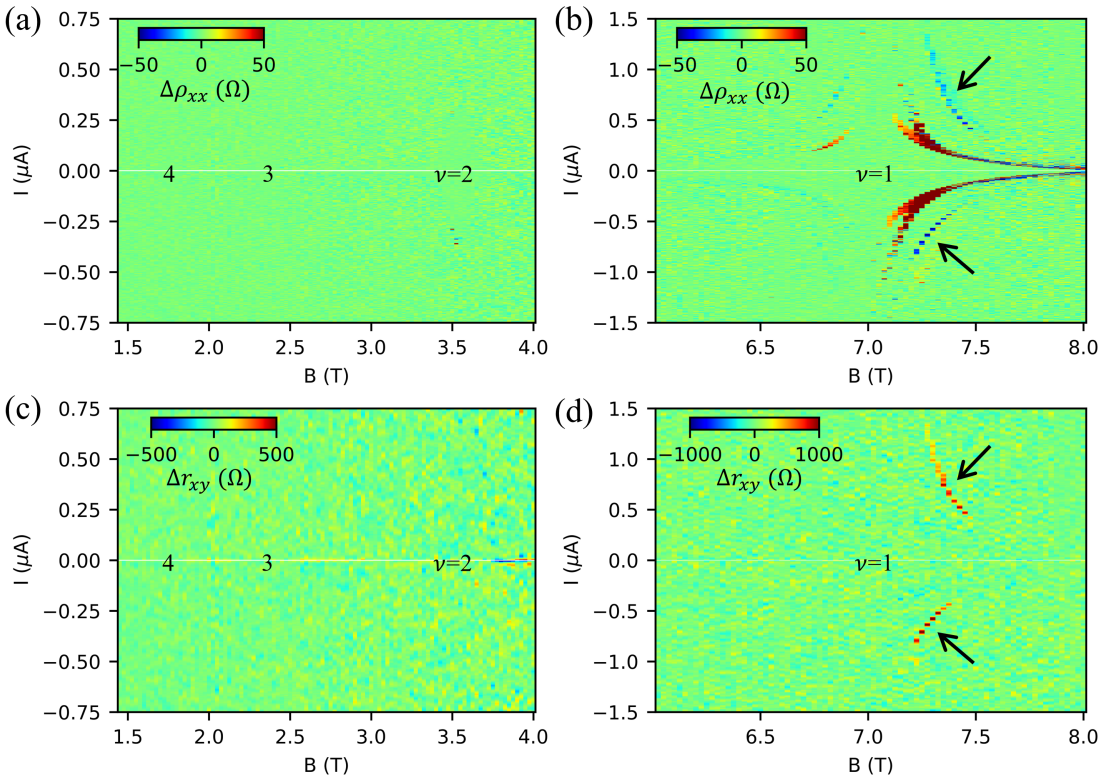


Figure 5.26: Corrected hysteresis colormaps. (a) $\Delta\rho_{xx}$ for $\nu = 2 - 4$. (b) $\Delta\rho_{xx}$ for $\nu = 1$. (c) Δr_{xy} for $\nu = 2 - 4$. (d) Δr_{xy} for $\nu = 1$.

Characterization of hysteresis near $\nu = 1$

Fig. 5.27a shows the up (red) and down (black) current sweep traces of $\rho_{xx} - I$ on the high B-field side of $\nu = 1$ at B = 7.25 T. The up and down traces have similar features, but below $\sim 0.5\,\mu$A, the down sweep traces are clearly shifted towards lower current. To highlight the location in B-field where the hysteresis is strongest, we can quantify the shift in critical current I_c near filling factor $\nu = 1$. Fig. 5.27b shows the shift in critical current ΔI as a function of filling factor (bottom x-axis) and B-field (top x-axis). Here we consider the current sweep traces for positive current polarity, where hysteresis is located on the left and right side of $\nu = 1$. On the low B-field side of $\nu = 1$, a maximum shift of $\Delta I \sim 50$ nA is recorded. At the center of $\nu = 1$, no hysteresis is observed and $\Delta I = 0$. On the high

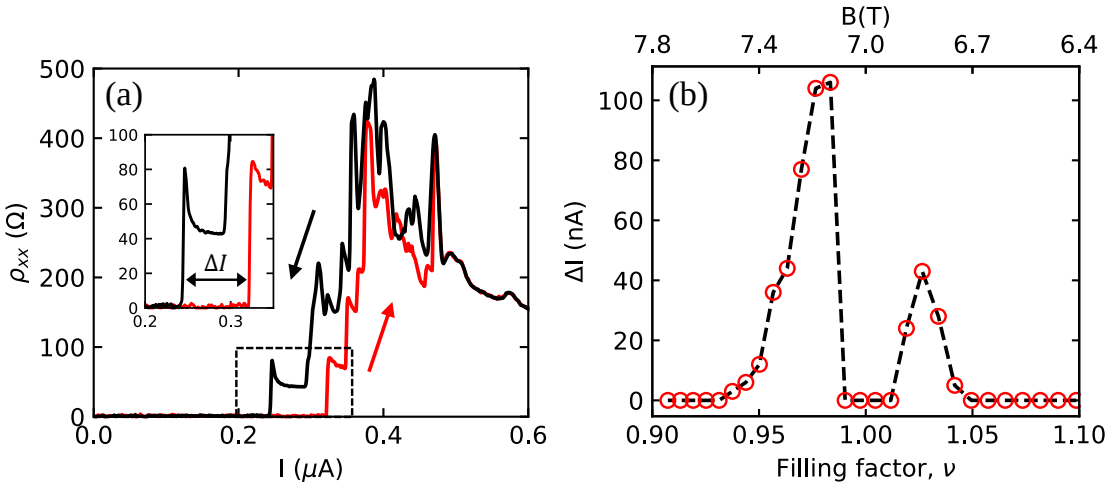


Figure 5.27: (a) Current sweep trace of ρ_{xx} on the high B-field side of the $\nu = 1$ transport diamond where the strongest hysteresis is observed. Inset: Zoomed in region highlighting the shift in critical current ΔI. (b) The shift in critical current as a function of filling factor ν (bottom x-axis) and B-field (top x-axis).

B-field side of $\nu = 1$, a maximum shift of $\Delta I \sim 100$ nA is recorded. Thus, the hysteresis is strongest, and only reproducible for both current polarities, on the high B-field (low ν) side of $\nu = 1$.

We now discuss whether the observed hysteresis is consistent with a picture of dynamic nuclear polarization (DNP), as outlined in Sec. 5.2.4. In the work of Kawamura *et al.* [103], the hysteresis linked to DNP had the following criteria

1. Pronounced hysteresis in the $V_{xx} - I$ curves was observed near odd-integer filling factors of $\nu = 1$, 3, and 5, and nearly absent for even-integer filling factors $\nu = 2$, 4, and 6.

2. The hysteresis was most prominent on the low B-field side (high ν side) of odd-integer filling factors.

3. The $V_{xx} - I$ curves shifted to smaller current on the down-sweep direction.

In the thesis of Victor Yu [92], hysteresis in a InGaAs/InP 2DEG system was studied extensively. They also sought to determine whether DNP could be generated from quantum Hall breakdown. While they did not definitively confirm a DNP picture with NMR as in Kawamura *et al.*, their results were in strong agreement with the criteria above. On the contrary, our results do not fit with a DNP picture. We observe no hysteresis near $\nu = 3$. We do observe hysteresis near $\nu = 1$, but it is most prominent on the high B-field side (low ν side). Additionally, the hysteresis on the low B-field (high ν side) side is only observed for positive current polarity. Thus, the only criterion that aligns with a DNP interpretation is the shift of $\rho_{xx} - I$ curves to smaller current on the down-sweep direction. However, this shift could be explained by various other effects [109], including the previously outlined shift in hole density.

Hysteresis near $\nu = 1$ with dc measurement techniques

To further explore the hysteretic behaviour and better compare the hysteresis to Kawamura *et al.*, we also studied hysteresis by employing dc measurement techniques. To be thorough, we employed two dc circuit configurations. In method DC1, the longitudinal voltage V_{xx} is measured by taking the difference between the single ended voltages on two potential probes V_A, V_B, located along the length of the Hall bar. The voltage on each potential probe is measured with respect to electrical ground of the cryostat and utilizes two separate multi-meters. Fig. 5.28a shows traces of $V_{xx} - I$ for the up (red) and down (black) sweep directions at B = 7.25 T. Hysteresis of the same character as the AC+DC technique is reproduced, with the down sweep trace of $V_{xx} - I$ also being shifted to lower current. Fig. 5.28b shows the comparison of the $V_{xx} - I$ and $\rho_{xx} - I$ up-sweep traces at B = 7.25 T. The results from the two methods are in excellent agreement. The trace of $\rho_{xx} - I$ collected from the AC+DC technique, which uses a lock-in amplifier, reflects the derivative dV_{xx}/dI of the $V_{xx} - I$ curves from the DC1 technique. Stated differently, the values of current where jumps occur in V_{xx} (steepest dV_{xx}/dI) precisely match the peaks in ρ_{xx}. Furthermore, the values of current where jumps (V_{xx}) and peaks (ρ_{xx}) occur were very reproducible in many scans collected at B = 7.25 T using the two methods.

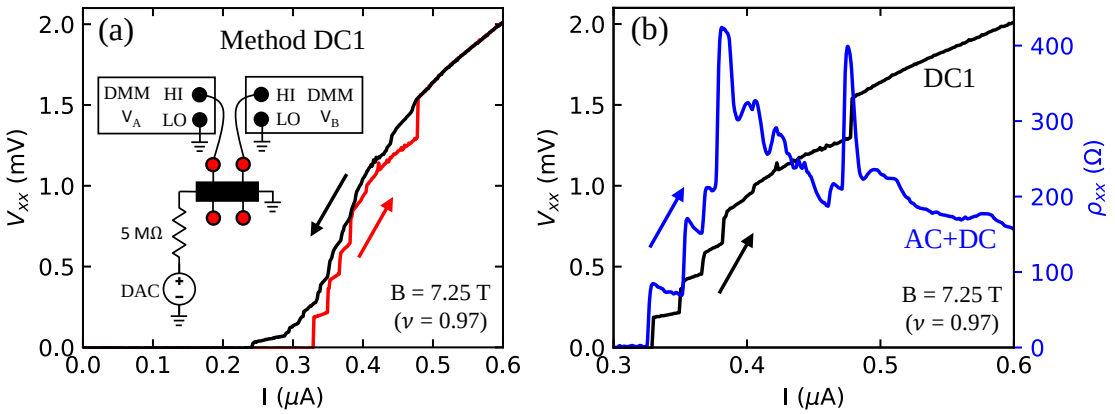


Figure 5.28: (a) Hysteresis measured with method DC1: The voltage on each V_{xx} probe with respect to electrical ground using two multi-meters. (b) Comparison between the hysteresis measured with the AC+DC technique (blue trace) and the DC1 technique (black trace).

Intriguingly, in Fig. 5.28a, distinct voltage jumps ΔV_x are evident during the up-sweep direction, separated by approximately 0.13-0.24 mV. Instances of such multi-step transitions have been documented in literature [109]. The jumps in V_{xx} may stem from transitions between Landau levels, resembling the Zener-type tunneling model outlined in Sec. 5.3.5. To investigate this hypothesis, we compare the voltage height of the breakdown steps to relevant energy scales, specifically the cyclotron and Zeeman spin-split energy gaps at B = 7.25 T. We calculate energies nearly an order of magnitude larger than ΔV_x, $\hbar\omega_c \sim 2.4$ meV and $g^*\mu_B B \sim 1.2$ meV, using 0.35 m_e and 2.8 for m^* and g^*, respectively. Consequently, the observed jumps are inconsistent with a pure Zener tunneling model.

For the second dc technique, method DC2, the differential voltage $V_{xx} = A - B$ between the two potential probes is measured directly using a single multi-meter. Fig. 5.29a shows traces of $V_{xx} - I$ for the up (red) and down (black) sweep directions at B = 7.25 T using method DC2. Unexpectedly, no clear hysteresis is observed. The breakdown current $I_c \sim 0.3$ μA and the magnitude V_{xx} are in agreement with method DC1. Upon closer inspection, we find that the voltage difference between the down and up sweeps $\Delta V_{xx} = V_{xx}^{down} - V_{xx}^{up}$ is significantly more noisy in the interval of current $0.25 - 0.5$ μA.

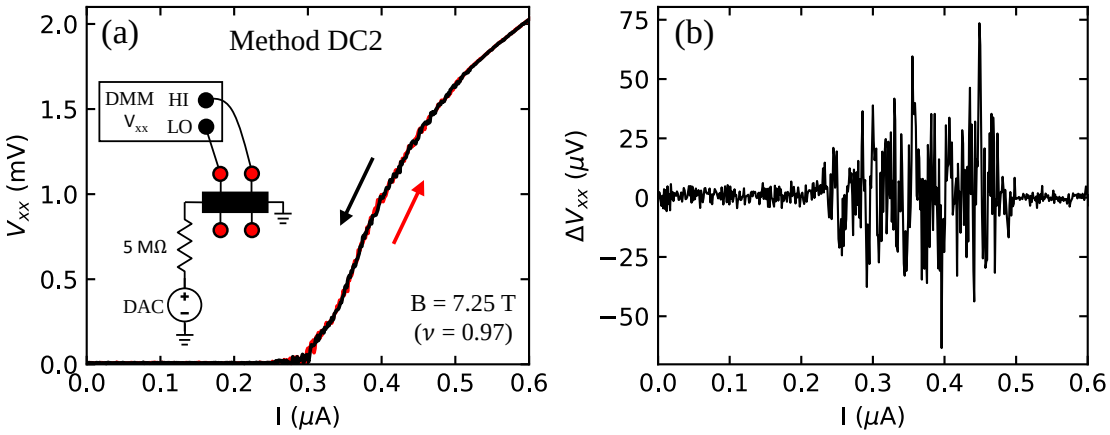


Figure 5.29: (a) Method DC2: The differential voltage measured between two probes along the length of the Hall bar, with a single multi-meter. (b) The difference between the up and down sweeps ΔV_{xx}.

Interestingly, this is the same interval of current is where hysteresis is observed in the AC+DC and DC1 measurement techniques. However, the noise is centered around zero, and thus, does not indicate any hysteresis. The discrepancy between the results of this measurement (DC2) and the AC+DC and DC1 techniques is not fully understood. In method DC1, which exhibited hysteresis, the voltages V_A, V_B are measured with respect to the electrical ground of the cryostat. One possibility is that the electrical ground is shifting, resulting in hysteresis. However, in the AC+DC technique, which also demonstrated hysteresis, a differential voltage $V_{xx} = A - B$ (with the electrical ground ignored) is measured using the lock-in amplifier in differential $A - B$ mode. Further measurements are needed to understand the discrepancy between the results obtained from this and previous measurement techniques.

We conclude this section with two points. Firstly, addressing the question posed at the beginning of this section: If hysteresis is generated from quantum Hall breakdown in our GaAs/AlGaAs 2DHG, is it consistent with dynamic nuclear polarization? Upon careful consideration of the work by Kawamura *et al.* [103], our observations do not fit with a picture that the hysteresis measured arises from dynamic nuclear polarization generated at breakdown. Secondly, the comprehensive investigation of hysteresis suggests that it may

stem from an experimental artifact, either due to a shift in the hole density of the 2DHG or a shift in the electrical ground of the measurement.

5.4 Conclusions and future work

In summary, we have conducted nonlinear magnetotransport measurements on a Hall bar device fabricated within a dopant-free GaAs/AlGaAs 2DHG heterostructure. For the first time in a 2DHG, we report the SdH phase inversion phenomenon. We explored the empirical relationship between the hole temperature T_h, and applied dc current I_{dc} through the Hall bar. We fitted the data to the form $\Delta T_h = T_h - T_0 \propto I_{dc}^{\beta}$, where T_0 is the fridge temperature and β is a fitting parameter. We found the dimensionless exponent to be $\beta \sim 1.3$ for our GaAs/AlGaAs 2DHG. In contrast, previous measurements conducted on similar 2DEG samples [144, 64, 120] report a lower value of $\beta \sim 2/3$. This suggests that the hole temperature exhibits greater sensitivity to current-induced Joule heating compared to the electron temperature in its 2DEG counterpart.

We have presented detailed maps of the differential resistance (ρ_{xx} and r_{xy}) over a wide range of sheet current density (up to ~ 0.1 A/m) and magnetic field (up to 9 T). These maps offered valuable insight into quantum Hall breakdown, specifically revealing transport diamonds at integer filling factors. By employing a Zener tunneling model for breakdown, we interpret the width of the diamonds (in current) as representing the energy $\hbar eB/m^* - g_{\perp}^* \mu_B B$ for even-filling factor diamonds or $g_{\perp}^* \mu_B B$ for odd-filling factor diamonds. In breakdown measurements of similar 2DEG samples, it's noteworthy that even-filling factor diamonds are larger than their odd-filling factor counterparts. This is attributed to the larger cyclotron energy, which is determined by the effective mass m^*, in comparison to the Zeeman energy gap, which is governed by the g factor ($g_{\perp}^*$). In contrast, in our 2DHG, we do not observe an even- and odd-filling factor dependence for the width of the transport diamonds. This implies that the cyclotron energy is approximately twice as large as the the Zeeman energy ($\hbar eB/m^* \approx 2g^* \mu_B B$), which is consistent based on values $m^* \sim 0.35 m_e$ and $g_{\perp}^* \sim 2.8$ extracted in Chapter 4. Additionally, the ratio of the critical electric field E_c in our GaAs/AlGaAs 2DHG, when compared to compiled data for GaAs/AlGaAs 2DEGs,

approximately reflects the difference in effective mass and g factor between the two carrier systems. Consequently, the sizes of even- and odd-filling factor diamonds can serve as a tool for probing the cyclotron and Zeeman energy gaps, thereby providing information about the effective mass and g factor.

We gained additional perspective by compiling maps at four different hole densities ranging from $p_{2d} = 1.0 - 2.0 \times 10^{15}$ m^{-2}. From these maps, we extracted the critical breakdown currents (I_c) and critical Hall electric fields ($E_c \propto I_c/\nu$) for filling factors in the range $\nu = 1 - 4$. Upon analyzing the magnetic field dependence in our GaAs/AlGaAs 2DHG, I_c and E_c both exhibit an approximate linear B-field dependence. A near-linear dependence of such parameters is also commonly observed in GaAs/AlGaAs 2DEGs [119] and was reported in Ref. [91] for a InGaAs/InP 2DEG.

For the first time in a 2DHG, we report the zero-current anomaly (ZCA) phenomenon. While the origin of ZCA remains unknown, we quantify its behavior. We observe the FWHM of the ZCA to increase with increasing magnetic field, behaviour not previosuly reported. We determine the average FWHM to be ~ 0.06 μA at B ~ 3.1 T. Using the width of an even-filling factor transport diamond $\nu = 2$, which principally reflects the energy $\Delta = \hbar\omega_c - g^*\mu_B B$, we estimate the FWHM of ~ 0.06 μA to be equivalent to an energy ~ 0.1 meV. Notably, the FWHM is $\sim 7\times$ smaller than that specified in Ref. [91] for a InGaAs/InP 2DEG Hall bar of identical width ($w = 15\,\mu$m).

Finally, we investigate hysteresis in the maps of differential resistance (ρ_{xx} and r_{xy}) observed when sweeping the current up and down. Our primary motivation for this investigation stems from a report on a GaAs/AlGaAs 2DEG [103], where hysteretic behaviour was validated (with NMR) to result from dynamic nuclear polarization (DNP) through the interplay of electron and nuclear spins via the hyperfine interaction. They observed hysteresis near odd-integer filling factors ($\nu = 1, 3, 5$), with the hysteresis being most prominent on the low B-field side (high ν side) of odd-integer filling factors. In our measurements in a GaAs/AlGaAs 2DHG, we only observe hysteresis in $\rho_{xx} - I$ near the $\nu = 1$ transport diamond. Furthermore, in contrast to Ref. [103], the hysteresis near $\nu = 1$ is most prominent on the high B-field side (low ν side). This suggests that the minor amount of hysteresis observed in our 2DHG is inconsistent with DNP. Additional measurements of hysteresis in $r_{xy} - I$ indicate a shift in the 2DHG density, which could explain the

hysteresis in $\rho_{xx} - I$. Alternatively, the inconsistent results when measuring hysteresis in $V_{xx} - I$ using two different DC measurement techniques suggest that the hysteresis could be attributed to a measurement artifact. In summary, the minimal and/or incorrect nature of hysteresis observed near $\nu = 1$, along with the lack of hysteresis at $\nu = 3$, suggests that the hyperfine coupling between hole and nuclear spins is indeed weaker compared to that between electron and nuclear spins.

In terms of future work, it would be of significant value to replicate these measurements using a single Hall bar device equipped with ambipolar (n- and p-type) ohmic contacts. This configuration would enable seamless switching between a 2DEG and a 2DHG, facilitating a direct one-to-one comparison. For instance, one could repeat the Joule heating via dc current experiment and verify the empirical value obtained in literature for GaAs/AlGaAs 2DEGs, $\beta \sim 2/3$, and for the 2DHG in this work, $\beta \sim 1.3$. Additionally, one could precisely compare the critical breakdown current I_c and electric field E_c between the electrons and holes. Finally, one could aim to reproduce the hysteresis behavior observed in a GaAs/AlGaAs 2DEG in Ref. [103]. This would support the evidence in this work that the near absence of hysteresis in a GaAs/AlGaAs 2DHG is consistent with a weaker hyperfine interaction between hole and nuclear spins.

Chapter 6

RF-QPC readout of lateral quantum dot device

6.1 Introduction

Quantum information processing promises the capability of solving a set of computational problems much faster than could be done on a classical computer, such as prime number factorization [151] and searching unstructured databases [152]. While classical computers operate by performing gate operations on classical bits of 0's and 1's, quantum computers utilize quantum bits or qubits to process information. The significant speed-up over classical computing for particular tasks is achieved by leveraging quantum phenomena, such as superposition, entanglement, and interference.

Numerous physical systems are currently under exploration for the implementation of quantum processors. These include trapped ions [153], superconducting circuits [154], and spins in semiconductors [7, 155], just to name a few. Each of these systems comes with its own set of advantages and disadvantages, particularly in terms of scalability and qubit gate fidelity. In this chapter, our primary focus is on the qubit architecture based on spins in semiconductor quantum dots. In a semiconductor quantum dot, electrons (or holes) are confined in all three spatial directions, creating a zero-dimensional system. These quantum

dots occupy a submicron region within the semiconductor, with sizes typically ranging from tens to hundreds of nanometers, depending on the specific material system. The strong confinement of these dots leads to single charges occupying discrete energy levels, similar to the electronic states found in real atoms. As a result, quantum dots are sometimes referred to as artificial atoms.

A critical aspect for any implementation of a quantum computer is the ability to quickly and accurately measure the states of the qubits, much faster than their coherence time. For spin qubits in a quantum dot device, the spin states can be correlated to different charge states via spin-to-charge conversion techniques, and therefore by subsequent measurement of the charge state, the spin state is determined [7]. The spin-to-charge mapping has been demonstrated by the difference in energy of the spin states [156] and by the difference in tunnel rates of the spin states to the reservoir [157]. The readout of the charge state, and thereby the qubit state, typically employs a nearby electric field sensor such as a quantum point contact (QPC) [158]. To increase the measurement fidelity and bandwidth, one can embed the QPC in a radio-frequency (rf) resonant circuit. This integrated sensor is known as a radio-frequency quantum point contact (RF-QPC). The primary focus of this chapter is to enhance the sensitivity of an RF-QPC charge detector.

6.2 Literature Review

In this section, we will introduce the lateral quantum dot device architecture and the QPC charge sensor. Subsequently, we will provide an overview of the working principle behind the RF-QPC and discuss the optimal design parameters for the rf circuit.

6.2.1 Lateral quantum dot devices

In this work, the quantum dots are formed within a 2DEG of a GaAs/AlGaAs heterostructure. Unlike the previous chapters where the 2DHG was induced using a global accumulation gate, in this case, the 2DEG is populated through modulation doping (n-doping) of the AlGaAs layer with Si. Fig. 6.1 shows a scanning electron microscopy (SEM) image

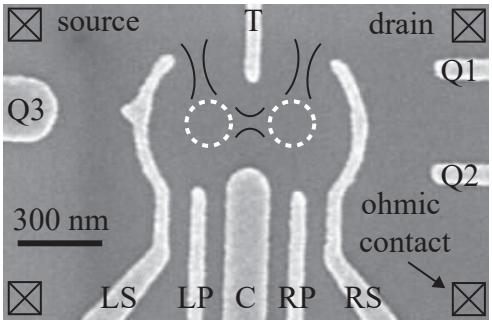


Figure 6.1: SEM image of the DQD device fabricated and designed by the NRC group. White dashed circles indicate the approximate locations of the quantum dots. Pairs of curved black lines highlight the constrictions within the 2DEG that are responsible for the dot-to-dot and dot-to-lead tunneling resistances. Ohmic contacts are labeled by ⊠. Figure adapted from Ref. [159].

of the double quantum dot (DQD) device utilized in this work, which was both designed and fabricated at the National Research Council Canada (NRC). Nine labeled TiAu gate electrodes (Q3, LS, LP, C, T, RP, RS, Q1, Q2), deposited on top of the heterostructure (approximately 90 nm above the 2DEG [159]), are employed to locally adjust the confining potential of the 1D constrictions and 0D quantum dots. These gates are patterned using electron beam lithography techniques. Additionally, ohmic contacts to the 2DEG are established to facilitate electrical transport measurements.

By applying negative voltages to the gates, the 2DEG directly underneath the gates can be depleted. Between pairs of gates, the electron density can be adjusted such that variable conductance narrow 1D constrictions can be formed. For gate voltages in the range -0.5 V to -1 V, two quantum dots can be formed at the approximate positions indicated by the white dashed circles in the SEM image. The electrostatic energy of the dots is primarily controlled by the side gates, RS and LS, but can be fined-tuned with the left and right plunger gates, LP and RP. The dot-to-lead tunnel coupling (resistance) is primarily controlled with gate T while the dot-to-dot coupling is adjusted with gate C. The gates Q1, Q2, and Q3 are used for charge detection of the quantum dot environment. A standard quantum point contact (QPC) can be formed on the left side of the device between gates

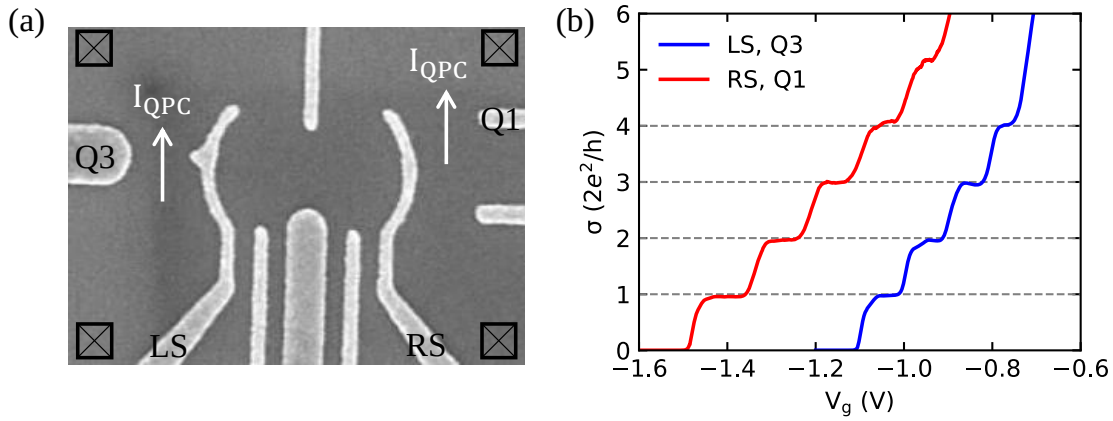


Figure 6.2: (a) SEM image of the DQD device. QPCs are formed on the left and right side of the device. (b) Conductance as a function of gate voltage for QPCs formed with gates on the left (LS, Q3) and right (RS, Q1) side of the device.

Q3 and LS, or, on the right side between gates Q1 and RS or Q2 and RS. Additionally, a sensor quantum dot (SQD) can be formed with gates Q1, Q2 and RS. The SQD may offer improved performance over the QPC but is significantly more difficult to operate [160].

6.2.2 QPC charge sensor

Fig. 6.2b shows the conductance as a function of gate voltage for QPCs formed between gates Q3, LS and Q1, RS. The voltage on the two gates for each QPC channel are swept symmetrically, denoted by a single label V_g. A voltage bias (200 μV) along the QPC channel generates a measured current I_{QPC}. With decreasing gate voltage, the 2DEG locally depletes under the gates and the conductance decreases. Upon further decreasing the voltage, a 1D channel develops and conductance plateaus occur at integer multiples of $2e^2$/h. The electrons in the 1D channel occupy discrete energy subbands, with each spin-degenerate subband contributing $2e^2$/h to the conductance of the channel. The first 4 conductance plateaus are clearly visible and closely match the expected quantized integer values. At large enough negative gate voltage, the conductance goes to zero, known as the pinch-off regime.

The conductance of the QPC between quantized plateaus is highly sensitive to variations in gate voltage and/or to changes in the electrostatic environment, including the number of electrons on the nearby quantum dots. The conductance of the QPC is most sensitive at a point halfway between the last plateau and pinch off, corresponding to $G_{QPC} = e^2/h$ or $R_{QPC} \approx 25.8$ kΩ. Therefore, for optimal operation of the QPC as a sensitive charge detector, the gate voltages should be configured such that $G_{QPC} \sim e^2/h$.

6.2.3 RF-QPC charge sensor

Charge sensing using a DC-QPC technique has a limited bandwidth of tens of kHz due to the QPC resistance and the capacitance of the fridge wiring to ground, creating a low-pass filter effect. Additionally, the charge sensitivity is limited by low-frequency 1/f noise and by the intrinsic noise of the current preamplifer, which is typically operated at room temperature to avoid dissipating heat into the sample [161]. To overcome these issues, an rf reflectometry technique can be employed where the QPC is embedded into an rf circuit with coaxial cables and cryogenic rf amplifiers, known as the radio-frequency quantum point contact (RF-QPC) [162, 163].

Using the same principle as the radio-frequency single electron transistor (RF-SET) [164], the RF-QPC indirectly probes the change in R_{QPC} by measuring the amplitude of a reflected signal from a resonant tank circuit. The tank circuit is responsible for transforming R_{QPC} down near the impedance of the transmission line $Z_0 = 50\ \Omega$ in a L-network configuration. Fig. 6.3a shows the L-network used in this work, consisting of an inductor L shunted by a capacitor C and R_{QPC}. For a given resonant frequency, impedance matching is achieved when the positive imaginary impedance of the inductor $j\omega L$, cancels the imaginary component of the shunted load $\mathrm{Im}(R_{QPC}||C) = -j\omega L$, leaving only $\mathrm{Re}(R_{QPC}||C) = Z_0$.

Matching network

This section outlines the general principle for designing a resonant tank circuit that transforms the impedance of R_{QPC} to match the 50 Ω of the transmission line at a particular

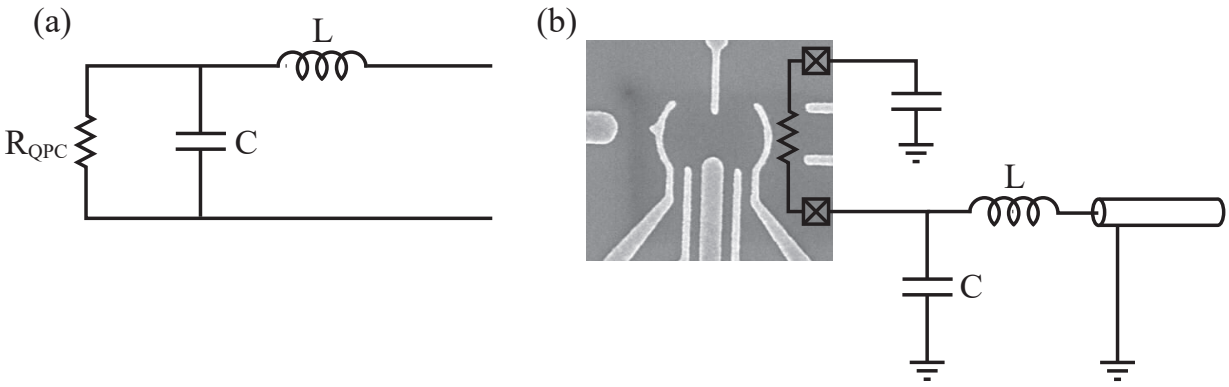


Figure 6.3: (a) LC matching network used to transform the QPC resistance to the line impedance (50 Ω). (b) Matching circuit implemented on the DQD device with the QPC charge detector. Figure adapted from Ref. [159].

frequency. The following derivations closely follow those described for the RF-SET in Refs. [165, 166] and RF-QPC in Ref. [159]. The input impedance of the circuit in Fig. 6.3a is given by

$$Z_{in}(\omega) = j\omega L + \frac{R_{QPC}}{j\omega C R_{QPC} + 1} \tag{6.1}$$

On resonance, the imaginary part of the impedance goes to zero, and we can solve for the angular resonance frequency

$$\omega_0 = \sqrt{\frac{1}{LC} - \frac{1}{(CR_{QPC})^2}}$$

Since R_{QPC} is large, we can ignore the second term and arrive at the familiar definition of resonance frequency

$$\omega_0 \approx \frac{1}{\sqrt{LC}} \tag{6.2}$$

On resonance, the impedance is real and equal to

$$Z_{in}(\omega = \omega_0) = \frac{L}{CR_{QPC}} \tag{6.3}$$

For $\omega = \omega_0 = 2\pi f_0$, the reactance of L and C are equal and one can define the characteristic impedance of the transformer

$$Z_T = \sqrt{\frac{L}{C}} = \omega_0 L = \frac{1}{\omega_0 C}$$

The input impedance can then be written as

$$Z_{in}(\omega = \omega_0) = \frac{Z_T^2}{R_{QPC}}$$

When this is matched to the line impedance, $Z_{in} = Z_0$, we obtain

$$Z_0 = \frac{Z_T^2}{R_{QPC}} \tag{6.4}$$

or equivalently

$$Z_T = \sqrt{Z_0 R_{QPC}} \tag{6.5}$$

In other words, Z_T for the matching condition is the geometric mean of the two loads. For designing an impedance matching network, one should choose a value of $R_{QPC} > h/e^2 \approx 25.8$ kΩ where the QPC is most sensitive the electrostatic environment of the dots, and appropriate values for L and C such that Eq. 6.5 is satisfied. An additional parameter to consider is the bandwidth of the readout. The bandwidth of the matching circuit is proportional to the resonance frequency and inversely proportional to the quality factor. Formally, the quality factor of a resonance is the ratio of the stored energy to the energy lost in a given cycle. The unloaded quality factor of just the LC circuit damped by Z_0 of the transmission line, is given by

$$Q = \frac{Z_T}{Z_0} \tag{6.6}$$

which on match (Eq. 6.4) produces

$$Q^2 = \frac{R_{QPC}}{Z_0} \tag{6.7}$$

which gives a bandwidth of $BW = \omega_0/2\pi Q$. The loaded quality factor, which is additionally damped by R_{QPC}, is given by

$$Q_L = \left(\frac{Z_0}{Z_T} + \frac{Z_T}{Z_0}\right) \tag{6.8}$$

RF-QPC sensitivity

The rf reflectometry technique is the foundation of the RF-QPC readout. In rf reflectometry, when an ac signal travels in a coaxial cable with characteristic impedance Z_0 and encounters a change in impedance Z, a fraction of the signal will be reflected back. In the context of the RF-QPC readout, the matching RLC circuit represents the change in impedance encountered at the end of the coaxial cable (see Fig. 6.3b). The amplitude of the reflected signal is $A_r = \Gamma A_{in}$, where A_{in} is the amplitude of the incoming signal and Γ is the reflection coefficient given by [167]

$$\Gamma = (Z_{in} - Z_0)/(Z_{in} + Z_0) \tag{6.9}$$

The input impedance on resonance $Z_{in}(\omega_0)$ is proportional to R_{QPC} from Eq. 6.3. The unique charge state of the quantum dot environment is mapped to distinct values of R_{QPC}, Z_{in}, and therefore Γ.

Optimizing the RF-QPC readout will decrease the required measurement time to resolve charge transitions within the quantum dot environment, which is crucial for achieving a single-shot readout essential for fault-tolerant quantum computing. Reducing the measurement time is equivalent to increasing the signal-to-noise ratio (SNR). In the RF-QPC readout, the signal represents the difference in reflected voltage between the two charge states, a and b, of the quantum dot environment [168]

$$SNR = \left|(\Gamma_a - \Gamma_b)\frac{v_0}{v_N}\right|^2 = |\Delta\Gamma|^2 \frac{P_0}{P_N} \tag{6.10}$$

where v_0 (P_0) and v_N (P_N) are the input and noise voltage (power), respectively, and $\Gamma_{a(b)}$ are the reflection coefficients corresponding to the two charge states. It is clear from Eq. 6.10 that enhancing the SNR involves maximizing $\Delta\Gamma$ for a given input power while also minimizing the noise power. In the RF circuit for the RF-QPC readout, the noise power includes contributions from thermal noise, instrumentation noise, and gate voltage noise. However, the noise is typically dominated by the RF amplifier stages [168]. Minimizing such amplifier noise will be discussed in the following Sec. 6.2.3.

With regard to enhancing the signal, the change in the reflection coefficient for small changes in ΔR_{QPC} is given by [168]

$$\Delta\Gamma = \frac{\partial\Gamma}{\partial R_{QPC}}\Delta R_{QPC} \tag{6.11}$$

Evaluating for the circuit in Fig. 6.3, we obtain

$$|\Delta\Gamma| = \frac{2Z_{in}Z_0}{(Z_{in}+Z_0)^2}\frac{\Delta R_{QPC}}{R_{QPC}} \tag{6.12}$$

The first ratio represents the circuit coupling, reaching its peak when the circuit is critically coupled, signifying that the input impedance (Z_{in}) matches with the characteristic impedance of the transmission line (Z_0). The second ratio, $\Delta R_{QPC}/R_{QPC}$, is maximal when the fractional changes in resistance are maximized. Consequently, the largest signal is obtained when the value of R_{QPC} is close to: (i) the matching condition and (ii) the point where the QPC is most sensitive to electric field.

A full expression for the charge sensitivity can be derived following the analysis developed by Roschier *et al.* for the RF-SET [161], which was extended by Dr. Jeffrey Mason for the RF-QPC [159]. In Eq. 6.10, the noise power P_N of the rf readout can be collectively characterized by an effective noise temperature $T_N = P_n/k_B B$, where B is the bandwidth (Hz) and k_B is the Boltzmann constant. This effective T_N coupled to a transmission line with an impedance Z_0 produces a Johnson noise such that Eq. 6.10 can be written as (in RMS units)

$$SNR = \left|\frac{\Delta\Gamma v_0}{\sqrt{4k_B T_N Z_0}}\right|^2 \tag{6.13}$$

Since $\Delta\Gamma$ is produced by changes in charge state δq, it can be converted into an effective RMS charge noise with units of $e/\sqrt{Hz}$

$$\Delta\Gamma = \sqrt{2}\Delta\Gamma_{RMS} = \frac{\partial|\Gamma|}{\partial q}\sqrt{2}\delta q_{RMS} \tag{6.14}$$

Substituting this relation into Eq. 6.13 and setting SNR = 1, we find

$$\delta q_{RMS} = \frac{\sqrt{2k_B T_N Z_0}}{v_0\frac{\partial|\Gamma|}{\partial q}} \tag{6.15}$$

The voltage amplitude of the incoming signal v_0 needs to be converted to a voltage across the QPC v_{QPC}. Away from the matching condition, only a fraction, K, of the incident signal power, $P_0 = v_0^2/2Z_0$, is dissipated by the QPC, $P_{QPC} = KP_0$. The power dissipated by the QPC is $P_{QPC} = v_{QPC}^2/2Z_0$, and we obtain the relation

$$v_0 = v_{QPC}\sqrt{\frac{Z_0}{R_{QPC}K}} \tag{6.16}$$

As a final step, one can expand $\partial|\Gamma|/\partial q$ to include the slope of the QPC resistance curve. Using chain rule we obtain

$$\frac{\partial|\Gamma|}{\partial q} = \frac{\partial|\Gamma|}{\partial R_{QPC}}\frac{\partial R_{QPC}}{\partial q} \tag{6.17}$$

Substituting Eqs. 6.16, 6.17 into Eq. 6.15, we arrive at the final expression for charge sensitivity

$$\delta q = \frac{\sqrt{2k_B T_N R_{QPC} K}}{v_{QPC}\frac{\partial|\Gamma|}{\partial R_{QPC}}\frac{\partial R_{QPC}}{\partial q}} \tag{6.18}$$

in RMS units of $e/\sqrt{Hz}$. For the largest charge sensitivity and thus smallest δq, one should minimize the system noise T_N and maximize the transfer functions in the denominator of Eq. 6.18 related to the circuit coupling ($\partial|\Gamma|/\partial R_{QPC}$) and the QPC resistance curve ($\partial R_{QPC}/\partial q$).

RF amplifier noise

In the RF-QPC readout, RF amplifiers are essential for increasing the signal to a level where it can be analyzed by digital electronics. However, in addition to amplifying the signal, each amplifier stage also contributes noise and thus degrades the SNR. The system noise, T_N, in Eq. 6.18, is typically dominated by the noise introduced from the amplifier chain. The performance of the first stage amplifier is particularly critical. To appreciate why this is true, consider the gain and noise at the output of a series of amplifiers cascaded together. Each amplifier stage has power gain G_i, and noise temperature T_{Ni}. Additionally, the transmission line loss L_i at the input of each amplifier decreases the signal and the noise, but also produces noise proportional to the magnitude of L_i and its physical temperature

T_i. For a perfectly impedance matched system, the total gain of the entire chain is given by

$$G_{tot} = \frac{G_1 G_2 G_3 ...}{L_1 L_2 L_3 ...} \tag{6.19}$$

and noise temperature is given by

$$T_N = [(L_1 - 1)T_1 + L_1 T_{N_1}] + \frac{L_1}{G_1}[(L_2 - 1)T_2 + L_2 T_{N_2}] + \frac{L_1 L_2}{G_1 G_2}[(L_3 - 1)T_3 + L_3 T_{N_3}] + ... \tag{6.20}$$

In a cryogenic environment and when the transmission line losses are small ($L_i < 2$), the first term in each square bracket can be neglected, producing

$$T_N \approx L_1 T_{N1} + \frac{L_1 L_2}{G_1} T_{N2} + \frac{L_1 L_2 L_3}{G_1 G_2} T_{N3} \ + \ ... \tag{6.21}$$

Since the gain for each amplifier is typically $G \sim$ 100-1000 (20-30 dB), it is clear from Eq. 6.21 that the overall noise is dominated by the first stage amplifier in the chain. Cryogenic semiconductor amplifiers that are mounted at the $2 - 4$ K stage of the refrigerator have a low noise temperature ($\sim$ 2 K) and high gain ($>$ 30 dB), and are commonly employed in quantum RF measurements. To further lower the noise level, one can employ superconducting amplifiers such as the Josephson parametric amplifier (JPA) [169] or a superconducting quantum interference device (SQUID) amplifier [170]. In Sec. 6.3.5, we characterize a SQUID amplifier and incorporate it into the RF-QPC readout.

6.3 Experimental Methods

In this section, we describe the design requirements and the basic characterization of the RF-QPC readout.

6.3.1 Matching network design

The matching network for the RF-QPC consists of an inductor, L, and a parasitic capacitance to ground, C_p. While the value for L is chosen and therefore is well-defined, C_p is not. Contributions to C_p likely include the stray capacitance to ground from the

inductor, device bond pad, and the interconnecting wire bonds. This capacitance should be minimized to increase $Z_T = \sqrt{L/C_p}$, and consequently increase $Q = Z_T/Z_0$. A larger Q will result in the reflection coefficient Γ being more sensitive to dampening from R_{QPC}, leading to a more sensitive readout.

A primary design goal for the tank circuit was to operate at a resonant frequency of approximately 145 MHz to be compatible with a microstrip SQUID amplifier (MSA) later on. The MSA, characterized in Sec. 6.3.5, offers much lower noise than than the typical cryogenic semiconductor rf amplifier employed, but with a bandwidth of only 12 MHz. The limited bandwidth required the resonance frequency of the tank circuit must be configured very precisely, which is challenging when C_p is not well-defined. However, the value of C_p can be estimated to be in the range of 0.4 - 1 pF based on the rf readout configured in a nearly identical device by previous group member Dr. Jeffrey Mason [159], and to those in literature [162, 163].

With the resonance frequency constrained to $f_0 = 145$ MHz and using a reasonable estimate for $C_p \approx 0.7$ pF, an estimate for the value of the inductance can be determined using

$$f_0 = \frac{1}{2\pi\sqrt{LC_p}} \tag{6.22}$$

for which we calculate $L \approx 1.8$ μH. Substituting these values into Eq. 6.5 corresponds to a matching condition at $R_{QPC} \approx 50$ kΩ. This is very reasonable considering optimal charge sensing values for R_{QPC} (steepest slope in dR_{QPC}/dV_g) in literature are in the range of $30 - 90$ kΩ ($G_{QPC} = 0.86 - 0.29\, e^2/h$) [159, 162, 163]. Similar to other RF-QPC readouts in literature, we opted to employ commercial (Coilcraft) copper wire wound chip inductors with a low-temperature compatible ceramic core, which come in a variety of discrete inductance values. However, the chip inductors are not perfect lumped elements, which becomes increasingly important for larger inductors. For a wire wound inductor, as the inductance increases so does the parasitic inter-coil capacitance due to the individual turns of the coil being close to one another. With increasing frequency, the impedance of this capacitance decreases until its magnitude equals that of the ideal inductance, creating a resonant tank circuit from the inductor alone. The frequency at which this occurs is known as the self-resonance frequency (SRF), which can also be calculated from Eq. 6.22,

where C_p is the parasitic inter-coil capacitance. At the SRF, the net impedance of the inductor becomes very large. Above the SRF, the inductor behaves like a capacitor, with the impedance being dominated by the inter-coil capacitance. Thus, the inductor only behaves ideally up to its SRF. Coincidentally, inductors with $L \sim 1.8$ μH typically have SRFs between 150 - 200 MHz (depending on the package size), slightly above the 145 MHz target frequency for the rf readout. To avoid the SRF of a single large inductor, we instead employed two smaller inductors in series, which achieves the large inductance needed but pushes the SRF to above 300 MHz. The final design used two inductors connected in series, a 1.2 μH (Coilcraft, model 1206CS-122, SRF = 380 MHz) and a 0.56 μH (Coilcraft, model 0805CS-561, SRF = 330 MHz), with a total inductance of 1.76 μH. The values for the inductance and SRF are nominal and come from the specification sheet provided by Coilcraft.

6.3.2 Matching network characterization

Fig. 6.4a shows the matching network connected between the input coax line and the QPC charge detector of the DQD device. To establish an rf ground, the top ohmic contact of the QPC is connected to ground with a 47 pF capacitor (NPO dielectric, American Technical Ceramics, P/N 116XEA470K100TT). At 143 MHz, this capacitor presents a 23 Ω impedance to ground. The RLC circuit is probed by applying an rf signal via the the input coax line in Fig. 6.4a and measuring the amplitude of the reflected signal. Fig. 6.4b shows the S_{11} scattering parameter as a function of frequency, measured with a vector network analyzer (Agilent E5071C). Several curves are shown for different values of R_{QPC}, formed with gates Q1 and RS. With increasing $R_{QPC} < 69$ $k\Omega$, a decrease in the reflected signal (dip in S_{11}) develops at $f_0 = 143$ MHz, corresponding to the situation where $Z_{in} > Z_0$. When $R_{QPC} = 69$ kΩ, the amplitude of the reflected signal reaches a minimum ($\sim$ -50 dB), corresponding to the matching condition $Z_{in} = Z_0 = 50$ Ω. Upon further increasing $R_{QPC} > 69$ kΩ, the amplitude of the reflected signal increases, corresponding to $Z_{in} < Z_0$.

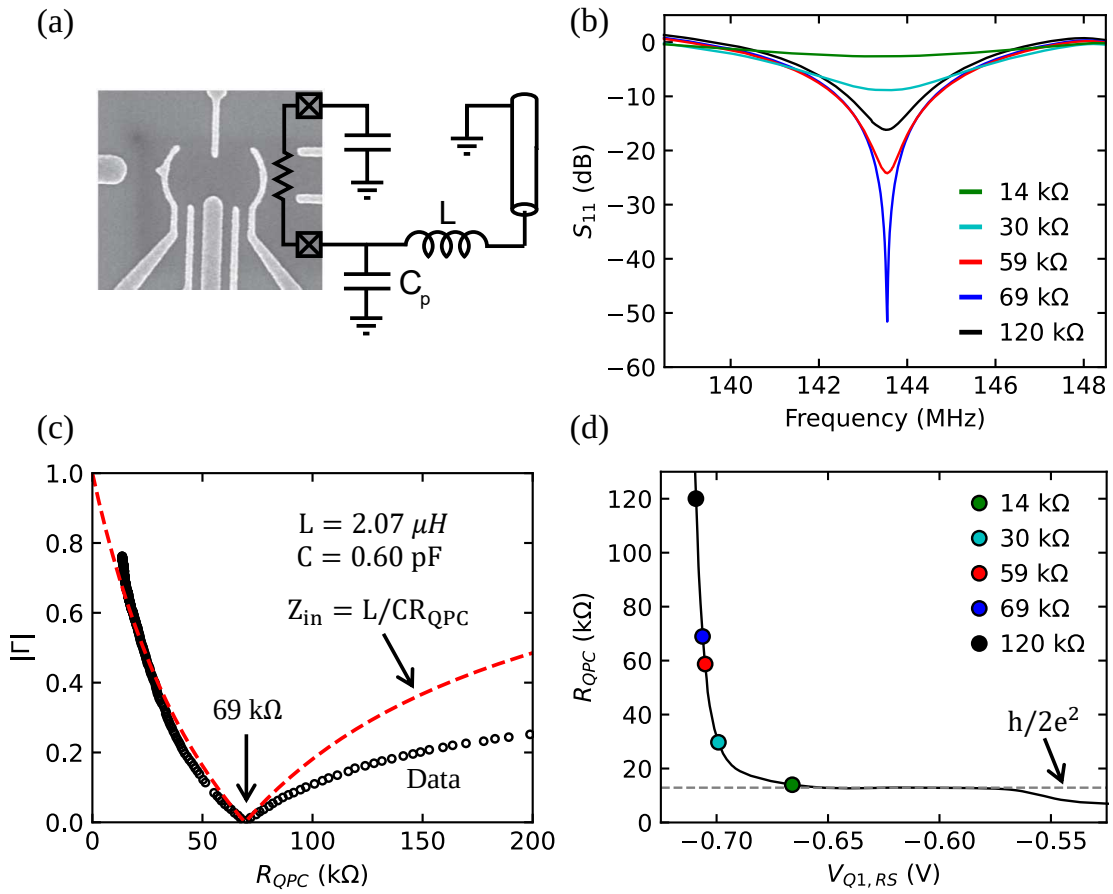


Figure 6.4: (a) Tank circuit configured on the DQD device. The capacitor on the top ohmic contact provides an rf ground. (b) S_{11} as a function of frequency for several values of R_{QPC}. (c) Reflection coefficient as a function of R_{QPC}, with data points represented by black circles and calculated indicated by a dashed red line). (d) R_{QPC} as a function of QPC gate voltage (Q1, RS).

The values of L and C_p in the context of the matching network can be determined from the equation for resonant frequency

$$LC_p = 1/(2\pi f_0)^2 \tag{6.23}$$

and from the impedance transformation on resonance

$$L/C_p = R_{QPC}Z_0 \tag{6.24}$$

where Eq. 6.24 is valid when $\Gamma \to 0$. Using the values $f_0 = 143$ MHz and $R_{QPC} = 69$ kΩ obtained from Fig. 6.4b, we calculate $L = 2.07$ μH and $C_p = 0.60$ pF.

The behaviour of the matching network can also be demonstrated by looking at the reflection coefficient Γ as a function of R_{QPC}. This is shown for S_{11} (143 MHz) in Fig. 6.4c, where the background away from resonance is used as a reference for which $\Gamma = 1$. The red dashed line is calculated with $Z_{in} = L/C_pR_{QPC}$, using the inductance and capacitance values for the matching network extracted above, $L = 2.07$ μH and $C_p = 0.60$ pF. Good agreement between the data and calculated $|\Gamma|$ is achieved for $R_{QPC} < 69$ kΩ, but at higher R_{QPC} the data clearly deviates to a lower value and does not approach 1, as would be expected. The smaller $|\Gamma|$ can be explained by rf power being dissipated into the matching network, instead of being fully reflected back to the source [159]. Similar behaviour is observed in RF-QPC readouts in literature that also use normal metal copper chip inductors, which are lossy [162, 163]. However, in Ref. [159] where a lithographic superconducting inductor was used, the expected $|\Gamma| \to 1$ at large R_{QPC} is achieved from the low losses of the superconducting coil. The matching condition corresponds to a minimum in $\Gamma(R_{QPC} = 69\,k\Omega)$, near where the gradient of $d|\Gamma|/dR_{QPC}$ is steep. Fortunately, this optimal R_{QPC} also corresponds to a steep slope in the QPC resistance curve (see Fig. 6.4d), which should produce a sensitive RF-QPC readout.

The inductance, parasitic capacitance, resonant frequency, and circuit bandwidth for this work and other RF-QPC readouts in literature are displayed in Table 6.1. In the work by Dr. Jeffrey Mason [159], a superconducting inductor was employed, while in this work, Reilly *et al.* [162], and Cassidy *et al.* [163], copper chip inductors were used.

	This work	J. Mason [159]	Reilly *et al.* [162]	Cassidy *et al.* [163]
L	2070 nH	255 nH	820 nH	490 nH
C_p	0.60 pF	0.36 pF	0.63 pF	0.47 pF
f_0	143 MHz	522 MHz	220 MHz	332 MHz
BW	4 MHz	15 MHz	8 MHz	21 MHz

Table 6.1: Comparison of the inductance, capacitance, resonance frequency, and bandwidth of several matching networks in literature and this work.

6.3.3 Readout circuit

Fig. 6.5 shows the RF-QPC reflectometry circuit configured on the dilution refrigerator. A signal generator (Agilent E8241A) is used to generate a 143 MHz carrier sine wave that is directed toward the device via semi-rigid coaxial cables. On both the input and output rf lines, copper is used at room temperature, copper-nickel (CuNi) down to the 2.8 K stage, superconducting niobium-titanium (NbTi) down to the mixing chamber, and finally copper to the device. On the input drive line, attenuators at the 2.8 K stage (20 dB) and the still plate (10 dB) absorb room temperature rf noise. At base temperature, the input signal is further attenuated by 40 dB from the directional coupler (Fairview Microwave, model MC3202-30) and sent to a homemade bias tee. The bias tee consists of a 1.2 μH conical inductor (Coilcraft, model BCS-122JL) and a 471 pF capacitor (NPO dielectric, American Technical Ceramics, 700A series). Finally, the output of the bias tee is connected to the DQD device containing the matching network and the QPC resistance.

When the QPC resistance is tuned such that $Z_{in} \neq Z_0$, a fraction of the carrier signal is reflected back through the bias tee and the directional coupler ($<$ 1 dB insertion loss), eventually reaching the cryogenic low-noise amplifier (LNA) mounted on the 2.8 K stage. The LNA (Cosmic Microwave Technology, model CITLF2) employs SiGe field effect transistors to achieve a noise temperature of 2.3 K and gain of 37 dB at 150 MHz. To reflect room temperature high frequency noise from feeding through the LNA, a 225 MHz cutoff low pass filter (Mini-circuits, model VLF-225+) is placed at the output of the LNA. The signal is further increased at room temperature by two amplifiers (Mini-circuits, model ZX60-P103LN+), each with a noise temperature of 35.4 K and gain of 25 dB at 143 MHz.

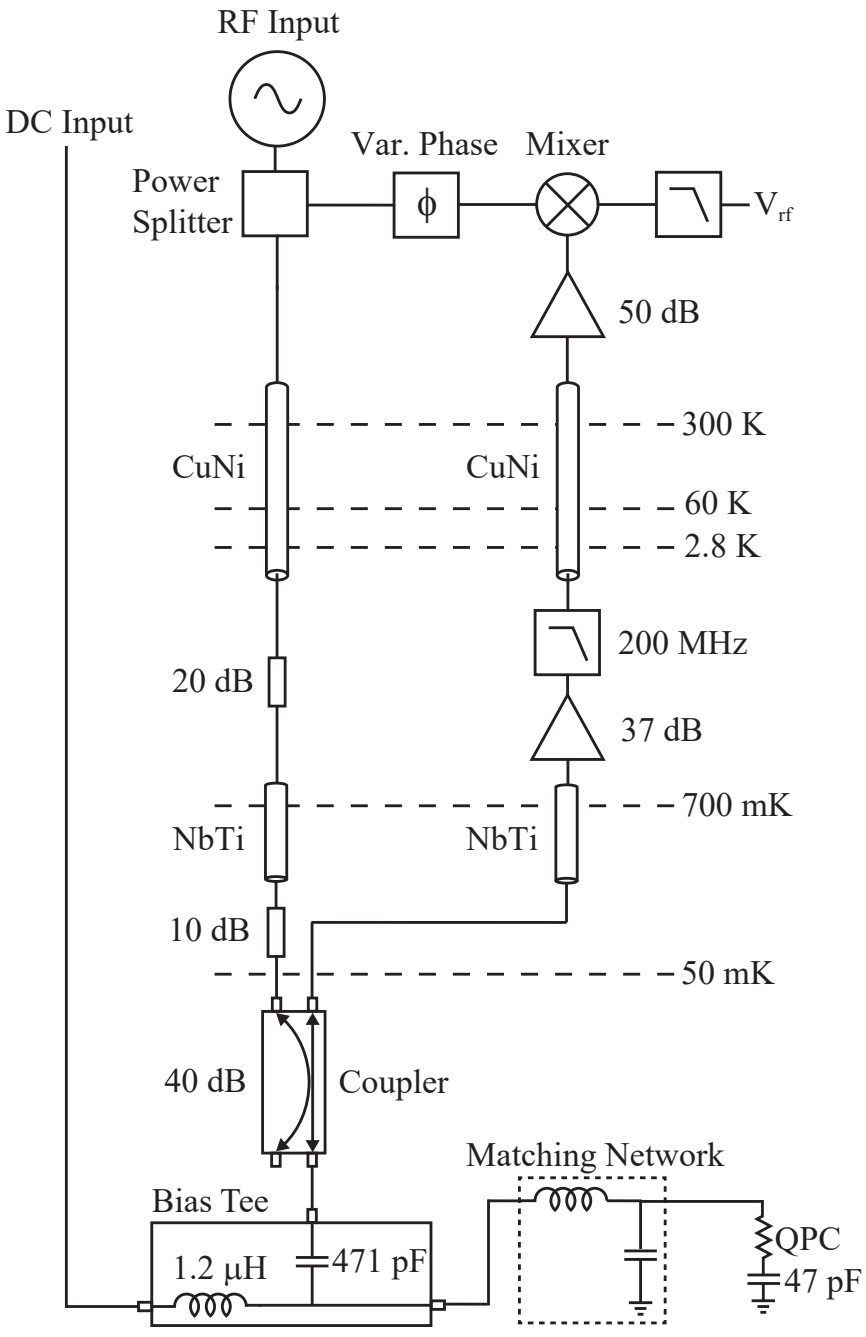


Figure 6.5: RF-QPC readout circuit configured on the dilution refrigerator. Figure modified from Ref. [159].

The reflected signal is demodulated with a homodyne detection scheme. At room temperature, the output signal from the Mini-Circuit amplifiers is connected to the radio-frequency (rf) input of a passive mixer (Macom, model M2BC). The original carrier signal is split with a power splitter (Mini-circuits, model ZFSC-2-5-S+), connected to a passive phase shifter (874-LA), and finally to the local-oscillator (LO) port of the mixer. The intermediate frequency (IF) port of the mixer produces a dc voltage V_{rf} proportional to the modulation depth of the carrier. The LO signal is adjusted to be in phase with the rf signal to produce a maximum signal amplitude.

6.3.4 Charge sensitivity measurements

In this section, we evaluate the charge sensitivity of the RF-QPC sensor by measuring single electron transitions in the double quantum dot (DQD) regime.

Double quantum dot regime

A single quantum dot is first established by measuring transport through the DQD structure, as shown in Fig. 6.6a. The single dot is tunnel coupled to the leads and strongly capacitively coupled to gate C. Tunnel barriers for the dot are formed by gates LS, T, and RS. When tuned appropriately to form a single quantum dot, the current through the DQD structure will exhibit Coulomb blockade peaks when decreasing the voltage on gate C. The other gates are held at constant (negative) voltages required to form the single dot. With a single quantum dot formed, the charge state can then be monitored by using charge detection with the QPC sensor formed by gates RS and Q1. The double quantum dot regime is realized by splitting the single dot, which is achieved by decreasing the voltage on the C gate. Each dot is tunnel coupled to a lead and the other dot and strongly capacitively coupled to a side gate, LS or RS, as shown in Fig. 6.6b. The C gate controls the tunnel barrier between the two quantum dots. Decreasing the voltage on the side gates expels electrons from the dots to the leads. Using the QPC sensor, the parameter space spanned by the voltages on gates LS and RS produce what is known as a stability diagram corresponding to stable charge configurations on the quantum dots.

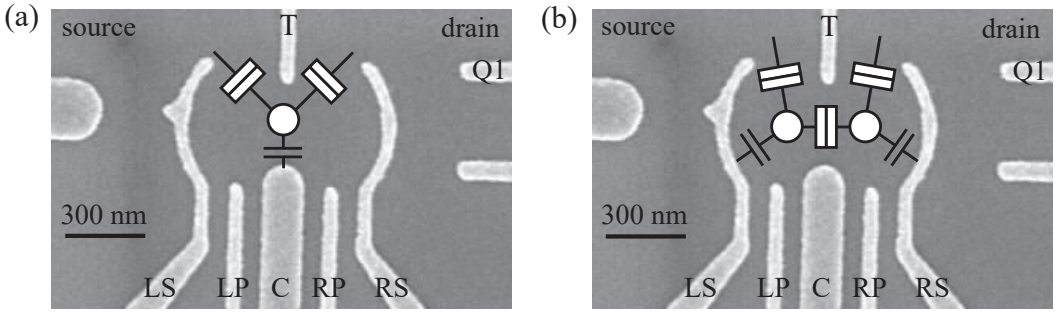


Figure 6.6: (a) Single quantum dot circuit superimposed on an SEM image of the device. (b) Double quantum dot (DQD) circuit superimposed on the device. Figures adapted from Ref. [159].

Fig. 6.7a shows an SEM image of the device and the circuit used to acquire the DQD stability diagram. The dashed white circles show the approximate locations of the two quantum dots. The QPC charge detector is formed on the right side of the device between gate Q1 and RS. The QPC is voltage biased with 200 μV created by a 0.2 V DAC output and a 1000:1 voltage divider as shown in Fig. 6.7a. The corresponding current is measured using a current to voltage preamplifier (Ithaco, model 1211). Fig. 6.7b shows R_{QPC} as a function of V_{Q1}. Between the last conductance plateau ($R_{QPC} = 12.9$ kΩ) and pinch-off, the slope is steep and the optimal sensitivity to electric field is determined to be when $R_{QPC} = 45$ kΩ (described in Sec. 6.8). At this working point (red circle in Fig. 6.7b), the nominal QPC current is 4.4 nA (for a 200 μV bias). An electron moving from the left to right dot, closer to the QPC, increases the electric field at the QPC and reduces I_{QPC}. Likewise, an electron moving from the right to left dot increases I_{QPC}. Expelling (adding) electrons via the leads increases (decreases) I_{QPC}.

The changes in I_{QPC} that reflect single charge transitions of the DQD charge state are typically small, on the order of ~ 100 pA. To better highlight the small changes in I_{QPC}, it is sometimes preferable to directly measure the derivative of I_{QPC} using a lock-in amplifier instead. This is accomplished by measuring the transconductance, dI_{QPC}/dV_{LP}, which only reveals changes in the DQD charge state [171]. This technique involves applying an oscillating voltage (2 $\mathrm{mV_{RMS}}$, 17 Hz) to gate LP in addition to the dc voltage (200

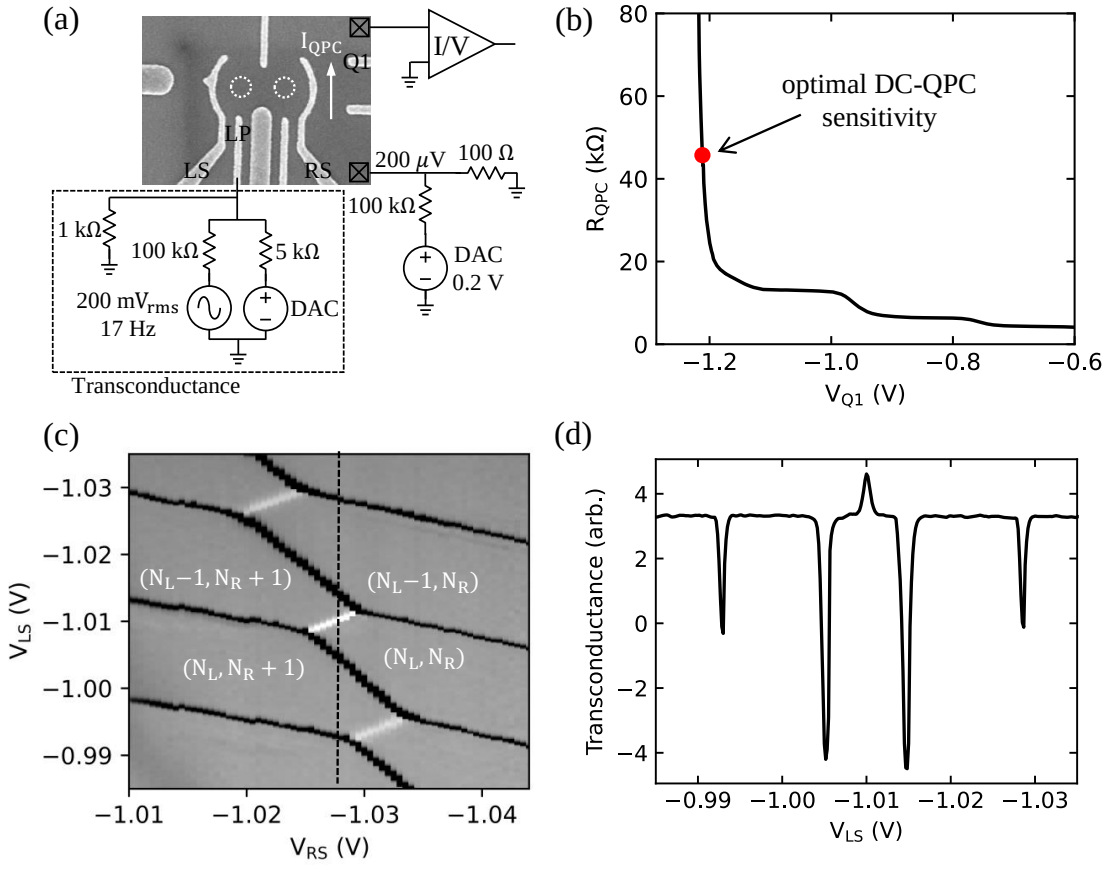


Figure 6.7: (a) DC-QPC readout configuration. The QPC is voltage biased (bottom right ohmic) and the resulting current is measured with a current pre-amplifier (top right ohmic). (b) QPC resistance as a function of V_{Q1} (operating point indicated by red circle). (c) DQD stability diagram acquired using the transconductance technique. (d) Vertical trace through (c).

μV) across the QPC. The dashed box in Fig. 6.7a shows the bias tee circuit connected to LP consisting of a 100:1 voltage divider for the ac signal (lock-in amplifier) for the transconductance technique, and a 5:1 voltage divider for the dc signal (DAC) used to supply a constant voltage to deplete the 2DEG. The oscillating electric field produced by gate LP results in a oscillation in R_{QPC} and thus I_{QPC}. The lock-in amplifier measures the ac (17 Hz) component from the output of the Ithaco current preamplifier, with a voltage proportional to the transconductance of the QPC.

Fig. 6.7c shows the DQD stability diagram, consisting of a grey scale plot of the QPC transconductance signal as a function of side gate voltages V_{LS} and V_{RS}. Stable charge configurations reflect the nearly constant background signal in grey, which are bounded by charge transition lines. Electrons are added to the dots from the leads as the side gate voltages are made progressively more positive. Such charge transitions are known as addition lines (black) and have negative slope in Fig. 6.7c. With two quantum dots, exchange of electrons can occur via inter-dot transitions. These are known as charge transfer lines (white) and have positive slope. Fig. 6.7d shows an example of the QPC transconductance signal taken along the vertical dashed line in 6.7c. A dip in the transconductance signal occurs for the charge addition lines while a peak occurs for a charge transfer line.

The device was tuned in the many-electron regime and the charge configurations on the dots (N_L, N_R) were not known. While the single electron regime could in principle be realized (see Ref. [159] in an identical device), it requires further tuning of the gate voltages and was not necessary for this work. Next, we evaluate the charge sensitivity of the QPC, first using a standard DC-QPC technique and then with the RF-QPC.

DC-QPC charge sensitivity

As mentioned previously, the QPC formed between gates Q1 and RS has the highest sensitivity when $g_{QPC} = 0.57\,e^2/h$ ($R_{QPC} = 45$ kΩ) (see Fig. 6.7b). The maximum electric field sensitivity of the QPC is determined by applying a low frequency (17 Hz, 2mV_{RMS}) to gate LP and measuring the output of the Ithaco current preamplifier (I/V) with a lock-in amplifier while sweeping V_{Q1}. The maximum lock-in amplifier response corresponds to the QPC resistance with the highest sensitivity. Fig. 6.8a shows the stability diagram in the

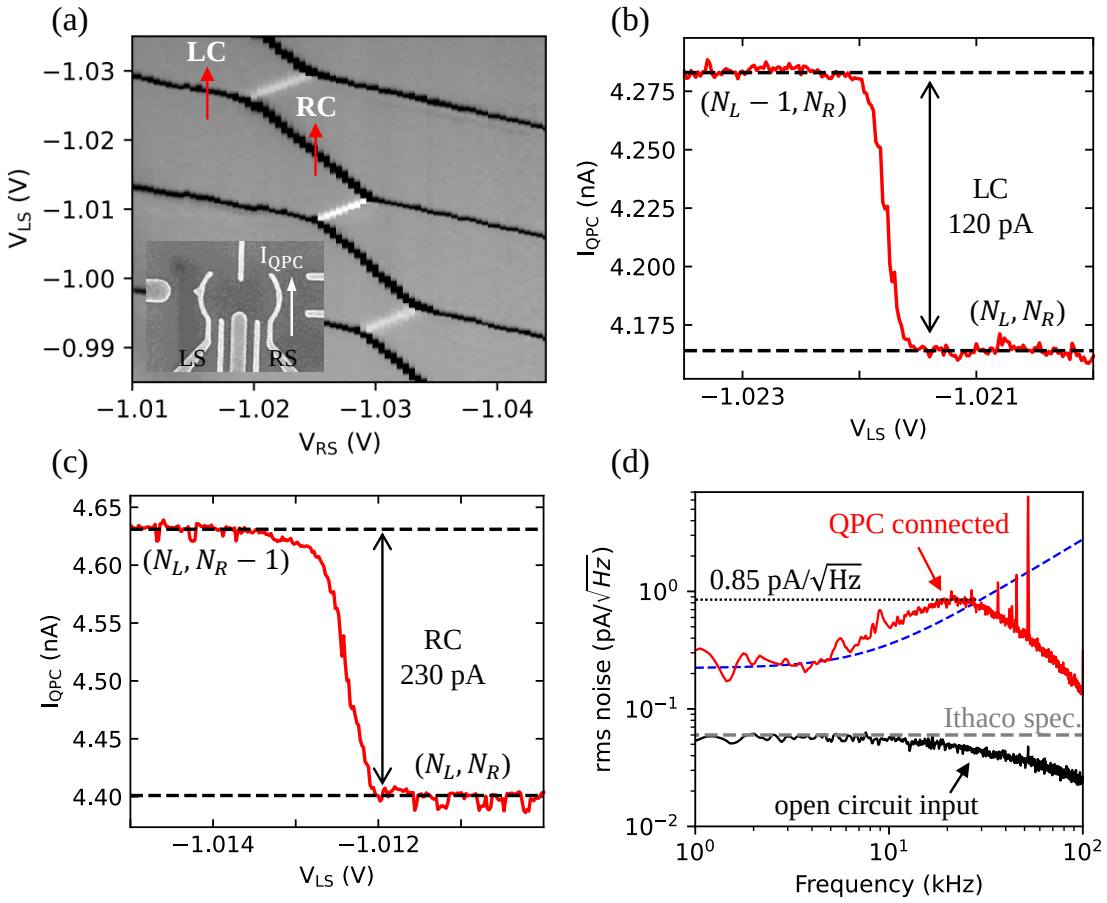


Figure 6.8: (a) Stability diagram highlighting traces for left charge (LC) and right charge (RC) transitions. (b) Vertical trace through (a) for the LC transition. (c) Vertical trace through (a) for the RC transition. (d) Current noise spectrum measured at the output of Ithaco current preamplifier with the input connected to the QPC (red trace) or open circuit (black trace). The dashed blue curve is the predicted noise calculated with Eq. 6.25, using $V_A = 10\,nV/\sqrt{Hz}$, $C_L = 440\,pF$, and $R_{QPC} = 45\,k\Omega$.

many-electron regime acquired using the transconductance technique. Sweeping V_{LS} more negative along the red vertical arrows at $V_{RS} \sim -1.015$ V ($V_{RS} \sim -1.025$), an electron is ejected from the left (right) dot. Fig. 6.8b and 6.8c shows the corresponding traces of I_{QPC}. Moving from right to left towards more negative values of V_{LS}, the ejected electron reduces the local electric field observed by the QPC and increases I_{QPC} by 120 pA and 230 pA for the left and right dot, respectively. The parasitic effect of sweeping V_{LS} on the QPC is compensated by making V_{Q1} more positive during the sweep, which maintains a nearly constant value of I_{QPC} during the sweep. The signal from the right dot, which is closer to the QPC channel, is nearly twice as coupled compared to the left dot (i.e., $230/120 \sim 1.9$). The change in I_{QPC} from the single electron transitions of 2.8 % (left) and 5.1 % (right) is slightly larger than the approximately 1 % change reported in Refs. [172, 159]. The increased coupling observed here may be attributed to the measurements being conducted in the many electron regime, as opposed to the single electron regime in Refs. [172, 159], resulting in a reduced spatial separation between the quantum dots and the QPC channel.

To evaluate the charge sensitivity, we quantified the noise spectrum of the measurement using an FFT dynamic signal analyzer (Agilent 35670A). Fig. 6.8d shows the current noise spectrum of the Ithaco current preamplifer, measured with (red) and without (black) the QPC connected. The Ithaco current preamplifier was configured to use battery power with a gain setting of 10^{-7} A/V and minimum rise time. Without the QPC connected, the measured noise floor of $I_A = 60$ fA/$\sqrt{Hz}$ and the 25 kHz bandwidth match the specification for the current preamplifier. When the QPC is connected, the system noise is clearly higher than the intrinsic noise of the preamplifier and is frequency dependent. The increased noise is primarily due to the current preamplifier input voltage noise, V_A, which produces a current noise to ground via R_{QPC} in parallel with the net capacitance of the dc lines and filters, C_L. The fridge wiring capacitance is unknown but the RC filters for the ohmic contacts has a total capacitance of 440 pF. The resulting current noise is given by [172]

$$I_{NA} = V_A(1 + j2\pi f R_{QPC} C_L)/R_{QPC} \tag{6.25}$$

The frequency dependence of the noise arises from the frequency dependent impedance of C_L. This produces the behaviour in the red trace of Fig. 6.8d, where I_{NA} increases with frequency up until the 25 kHz bandwidth of the preamplifier. While the filter capacitance

could be lowered to increase the sensitivity, the trade-off would be an increased electron temperature.

The charge sensitivity (in conventional units of e/$\sqrt{Hz}$) can be evaluated by dividing the current noise (pA/$\sqrt{Hz}$) by the current change ΔI_{QPC} for a single electron transition (pA/e). For an electron leaving the right dot (230 pA/e), the upper bound for the charge sensitivity ($f < 1$ kHz, $I_{NA} = 0.3pA/\sqrt{Hz}$) is $\delta q = 1.3 \times 10^{-3}$ e/$\sqrt{Hz}$, and the lower bound ($f = 20$ kHz, $I_{NA} = 0.9pA/\sqrt{Hz}$) is $\delta q = 3.9 \times 10^{-3}$ e/$\sqrt{Hz}$. Thus, the DC-QPC readout has a sensitivity on the order of 10^{-3} e/$\sqrt{Hz}$ when using a 200 μV (4.4 nA) QPC bias. This is consistent with other DC-QPC charge sensitivities in literature [159, 172].

RF-QPC charge sensitivity

The charge sensitivity measurement was repeated with the RF-QPC readout using the same charge transitions for the left and right quantum dots. The maximum sensitivity was determined by applying an oscillating voltage to LP (2 $\mathrm{mV_{RMS}}$, 17 Hz) and measuring the output of the readout circuit (rf mixer), V_{rf}, with a lock-in amplifier while sweeping V_{Q1}. The maximum lock-in amplifier response and thus highest sensitivity occurs at the value of V_{Q1} corresponding to $g_{QPC} = 0.44e^2/h$ ($R_{QPC} = 59$ kΩ). The working point is indicated in Fig. 6.9a for Γ and R_{QPC} (inset) and is consistent with what would be expected from the discussion in Sec. 6.2.3: near the matching condition for the resonant circuit and where the QPC is sensitive to electric field. A carrier power of $P_{rf} = -95$ dBm at the device was used for the following measurements.

Fig. 6.9b and 6.9b show the single charge transitions for the left and right quantum dot for the RF-QPC readout. Moving from right to left towards more negative values of V_{LS}, the ejected electron reduces the local electric field observed by the QPC and decreases V_{rf} by 260 μV and 475 μV for the left and right dot, respectively. The ratio of the coupling for the left and right dot, $475/260 \sim 1.8$, is similar to what was observed for the DC-QPC readout (~ 1.9).

Fig. 6.9d shows the voltage noise spectrum measured at the output of the rf readout circuit (mixer). The noise is constant at 0.6 μV/$\sqrt{Hz}$ over the measured range of $10 - 100$ kHz. The level of noise is proportional to the system noise but also the gain from the rf

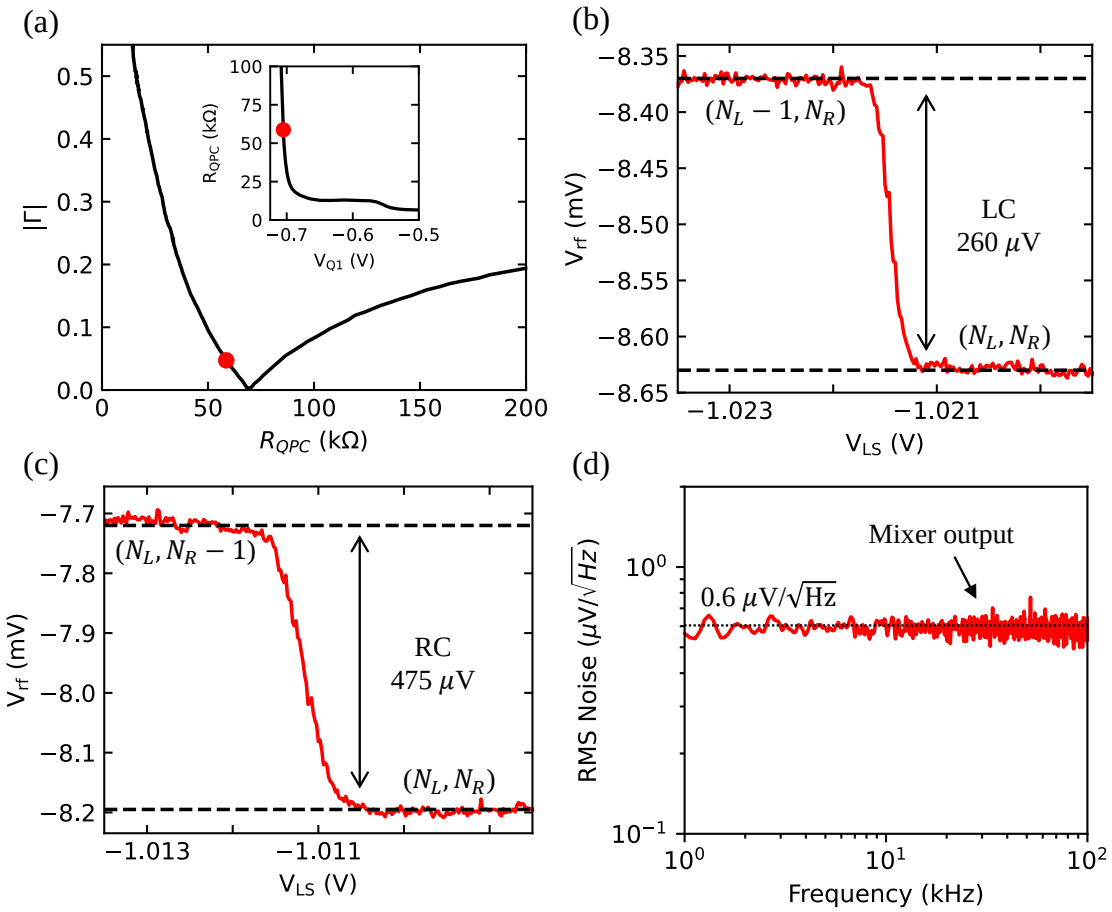


Figure 6.9: (a) $|\Gamma|$ as a function of R_{QPC} (red dot indicates operating point). Inset: R_{QPC} as a function of V_{Q1} (red dot indicates operating point). (b) V_{rf} for sweeping V_{LS} along the LC transition. (c) V_{rf} for sweeping V_{LS} along the RC transition. (d) Voltage noise spectrum measured at the output of the RF-QPC readout (mixer).

amplifiers in the readout circuit. For an electron leaving the right dot, the charge sensitivity of the RF-QPC readout is $\delta q = 1.3 \times 10^{-3}$ e/$\sqrt{Hz}$ (i.e., 0.6/475) when using a -95 dBm carrier signal.

Comparison to literature

In this section, we compare key parameters of the RF-QPC of this work and those of Dr. Jeffrey Mason [159], Reilly *et al.* [162], and Cassidy *et al.* [163]. Table 6.2 shows the charge sensitivity of each readout and provides relevant parameters related to the charge sensitivity. For convenience, the charge sensitivity expression derived in Sec. 6.2.3 is also shown here

$$\delta q = \frac{\sqrt{2k_B T_N R_{QPC} K}}{v_{QPC} \frac{\partial |\Gamma|}{\partial R_{QPC}} \frac{\partial R_{QPC}}{\partial q}} \tag{6.26}$$

For all works, the system noise temperature T_N was determined by measuring the shot noise as a function source-drain bias across the QPC (see Appendix. C for details). In all cases, T_N appears to be dominated by the first stage cryogenic semiconductor amplifier ($T_{amp} \sim 2 - 3$ K). The values of T_N are approximately twice that of the input noise of the cryogenic semiconductor amplifiers employed (T_{amp}), which is consistent with the reflection of the amplifier noise with the LCR circuit for the rf readout. The larger noise could also be due cables losses between the device and cryogenic amplifier.

In Refs. [162, 163] there is not enough information to generate the derivative $\partial|\Gamma|/\partial R_{QPC}$. The better sensitivity in Refs. [162, 163] is largely due to the higher carrier power (i.e., larger v_{QPC}). The near factor of two better coupling ($\partial R_{QPC}/\partial q$) in this work and Ref. [163] is attributed to working in the many-electron regime instead of the single-electron regime in Refs. [159, 162].

In this work, the carrier power dependence of the RF-QPC was linear until approximately -80 dBm (see Appendix C). Thus, we can evaluate the sensitivity improvement compared to a prior RF-QPC readout implemented in our group (Ref. [159]), independent of the carrier power p_{rf} and coupling $\partial R_{QPC}/\partial q$. A carrier power that is 10 $\times$ larger (i.e., $p_{rf} = -95$ dBm in this work compared to $p_{rf} = -85$ dBm in Ref. [159]) corresponds to a $\sqrt{10} \approx 3.16\times$ larger voltage across the QPC (v_{QPC}), resulting in a charge

	This work	J. Mason [159]	Reilly *et al.* [162]	Cassidy *et al.* [163]
R_{QPC} (kΩ)	59	70	86	25.8
$\partial R_{QPC}/\partial q$ (kΩ/e)	2.2	1	0.85	2
$\partial\|\Gamma\|/\partial R_{QPC}$ (μS)	7	2	-	-
P_{rf} (dBm)	-95	-85	-75	-73
T_N (K)	6.8	5.2	3.5	< 5.8
δq ($\times 10^{-3}$ $e/\sqrt{\text{Hz}}$)	1.3	2	1	0.2

Table 6.2: RF-QPC readout parameters and charge sensitivity compared to other works.

sensitivity of $\delta q \approx 0.4 \times 10^{-3}$ e/$\sqrt{Hz}$ (i.e., 1.3/3.16). With a 2.2 × better coupling (i.e., $\partial R_{QPC}/\partial q = 2.2$ kΩ/e in this work compared to $\partial R_{QPC}/\partial q = 1$ kΩ/e in Ref. [159]), the charge sensitivity in this work, if conducted in the single-electron regime with $p_{rf} = -85$ dBm, would be $\delta q \approx 0.9 \times 10^{-3}$ e/$\sqrt{Hz}$ (i.e., $0.4 \cdot 2.2$). Thus, the equivalent improvement in sensitivity compared to Ref. [159] is approximately 2.2 ×, which is close to the expected increase of $\sim 3\times$ if one considers the improvement of the RF-QPC operating point (i.e., $\partial|\Gamma|/\partial R_{QPC} = 7$ in this work compared to $\partial|\Gamma|/\partial R_{QPC} = 2$ in Ref. [159]) but slightly higher noise temperature (i.e., $T_N = 6.8$ K in this work compared to $T_N = 5.2$ K in Ref. [159]). Overall, the RF-QPC readout achieved an improved charge sensitivity compared to a previous readout configured within our group.

6.3.5 Microstrip SQUID amplifier

Motivated by the possibility of improved sensitivity, we sought to incorporate a microstrip SQUID amplifier (MSA) as the first amplification stage of the RF-QPC readout to reduce the system noise level. The MSA device was acquired from *ez-SQUID* [173]. The MSA consists of a square washer of niobium interrupted by two Josephson junctions. A 60 turn niobium input coil overlays the square washer, separated by a thin layer of SiO_2. Fig. 6.10a shows a diagram of the MSA. The niobium square washer of the SQUID is shown in gray and the Josephson junctions are represented by the cross indents. The input coil is shown overlaying the washer. The input signal is applied to one end of the input coil, leaving the other floating to create a microstrip resonator. The device was mounted to a coplanar

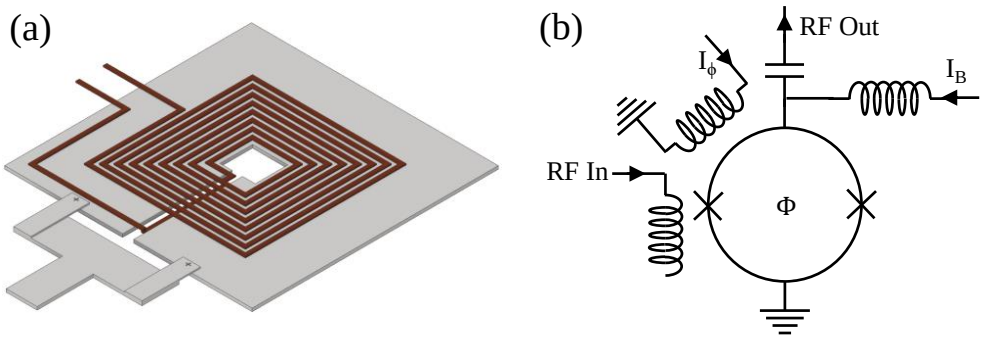


Figure 6.10: (a) Diagram of MSA (adapted from Ref.[35]). (b) Electrical schematic of MSA.

waveguide PCB board with coaxial connectors. Static magnetic flux to the SQUID loop is provided by a small custom-made wire-wound-coil, mounted directly underneath the device. A 3 dB attenuator was placed at the MSA output for impedance matching and to reduce noise feeding in from the cryogenic semiconductor amplifier. To magnetically shield the MSA, the assembly was enclosed in a superconducting niobium tube, followed by a larger Cryoperm shield that is wrapped with Metglas ribbon. To further reduce any static magnetic flux while cooling, a large μ-metal shield is used to enclose the outer vacuum can of the cryostat.

Fig. 6.10b shows the circuit diagram of the MSA. The MSA requires two adjustable dc bias currents. One is used to bias the SQUID above the critical current, I_B, which produces a voltage across the square washer. I_B was supplied to a bias tee (on the PCB board with the SQUID chip), consisting of a 2.35 μH conical inductor and a 12 nF capacitor (NPO dielectric). The other is a flux bias, I_ϕ, used to position the SQUID at the steepest point on its $V - \Phi$ curve. The dc currents are supplied with a homemade, battery-operated current source. Low-pass RC filters (R = 200 kΩ, C = 12 nF) mounted on the 2.8 K stage were used to electrically filter the dc lines used for the bias currents.

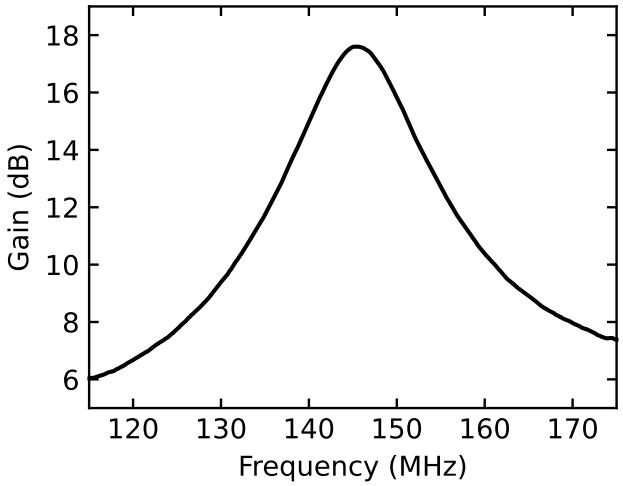


Figure 6.11: MSA gain (including a 3 dB attenuator on the output) as a function of frequency biased for maximum gain. Measured at T = 80 mK and a rf drive power of -130 dBm.

MSA gain and noise

The packaged MSA was mounted on the mixing chamber of the dilution fridge. At the time of these measurements, the base temperature of the fridge was limited to 80 mK. The device gain was determined by measuring the transmission (S_{21}) with a vector network analyzer. Fig. 6.11 shows the gain as a function of frequency for the MSA biased at $I_B = 4.6$ μA and the optimum flux bias. For weak drive signals (-130 dBm at the MSA input), the MSA had a maximum gain of 17.5 dB (including 3 dB attenuator on the output) at 145 MHz and a bandwidth of 12 MHz (Q $\sim$ 12).

Fig. 6.12a shows the rf circuit for characterizing the MSA. The noise level of the MSA was evaluated by using an amplifier chain, and comparing the signal-to-noise ratio (SNR) with and without the MSA in the measurement chain. Using a 145 MHz tone incident on the amplifier chain, the SNR was measured in two separate cooldowns. In the first cooldown, the MSA was bypassed with a short length of copper coax (red dashed line in Fig. 6.12a), and the signal was amplified by the cryogenic SiGe amplifier (model CITLF2) mounted on the 2.8 K stage, followed by two identical Mini-Circuit amplifiers (model ZX60-

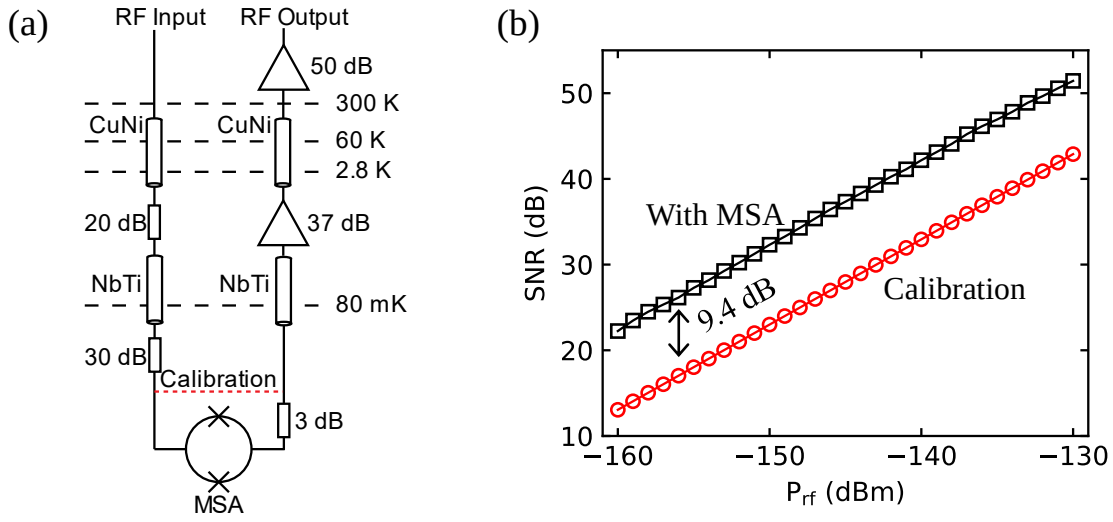


Figure 6.12: (a) RF circuit used to characterize the MSA. (b) SNR of 145 MHz tone with and without the MSA in the measurement chain. The resolution bandwidth of the spectrum analyzer is set to 100 Hz.

P103LN+) at room temperature. In the second cooldown, the MSA was connected and used as the first amplification stage.

The system noise of the three-stage amplifier chain without the MSA, T_{N1}, can be calculated using the following expression

$$T_{N1} = T_{Attn} + T_{SiGe} + \frac{T_{RT}}{G_{SiGe}} \tag{6.27}$$

Here we have neglected transmission line losses because the critical coaxial cables are predominately made from low-loss superconducting niobium titanium (NbTi) in addition to the rf losses being very small the working frequency of 145 MHz. The first stage, T_{Attn}, is the equivalent noise temperature at the output of the 30 dB attenuator. On the drive line, the 20 dB (30 dB) attenuator heat sunk to the 2.8 K stage (mixing chamber, 80 mK) absorbs thermal noise produced at higher temperature stages. The attenuators also add noise proportional to their loss L (linear power ratio) and physical temperature T_{phys}, according to $T_{out} = [(L-1)/L]T_{phys}$. For attenuators greater than 20 dB ($L > 100$), the contributed noise is more than 99 % of T_{phys}. Thus, the equivalent noise at the output of the

30 dB attenuator is simply the sum of the reduced thermal noise from higher temperature stages ($\sim$ 6 mK) and the physical temperature of the attenuator ($\sim$ 80 mK), giving T_{Attn} = 86 mK. The second stage is the cryogenic SiGe amplifier, which has a noise temperature of T_{SiGe} = 2.3 K and a gain of G_{SiGe} = 5012 (37 dB) at 145 MHz (from the specification sheet). The room temperature Mini-Circuit amplifiers are the third stage and have a noise temperature of T_{RT} = 35.5 K (from the specification sheet). Substituting these values into Eq. 6.27 gives T_{N1} = 2.4 K.

Fig. 6.12b shows the SNR measured with a spectrum analyzer as a function of rf power (at the input of the amplifier chain), with and without the MSA. The SNR increases linearly with rf power in both cases. Comparing the SNR of these two measurements yields a SNR increase of 9.4 dB with the MSA in the circuit. This SNR increase corresponds to a decrease in the system noise temperature by a factor of 8.7$\times$ (i.e., $10^{9.4/10} = 8.7$). Thus, the system noise of the four-stage amplifier chain with the MSA is $T_{N2} = 2.4/8.7 = 0.28$ K, and is given by the following expression

$$T_{N2} = T_{Attn} + T_{MSA} + \frac{T_{SiGe}}{G_{MSA}} + \frac{T_{RT}}{G_{MSA}G_{SiGe}} \tag{6.28}$$

The gain of the MSA, including the 3 dB attenuator on the output, is G_{MSA} = 56 (17.5 dB). Substituting this and the other values outlined above into Eq. 6.28, we estimate the noise of the MSA to be $T_{MSA} \approx 0.15$ K. The SNR-ratio technique for estimating the noise temperature is sensitive to impedance mismatches between components, and thus provides an upper bound for the noise temperature. Nonetheless, the system noise is significantly reduced with the MSA compared to a conventional cryogenic semiconductor amplifier alone. For instance, if we were to utilize the MSA as the primary (first stage) amplifier in the RF-QPC readout, the approximate 10 $\times$ reduction in T_N compared to the SiGe semiconductor amplifier would yield a $\sqrt{10} \sim 3.16\times$ improvement (see Eq. 6.18) in the charge sensitivity δq.

MSA power dependence

Fig. 6.13a shows the gain of the MSA as a function of frequency for different drive powers. At 145 MHz, the gain drops significantly for larger rf power. Fig. 6.13b shows the MSA

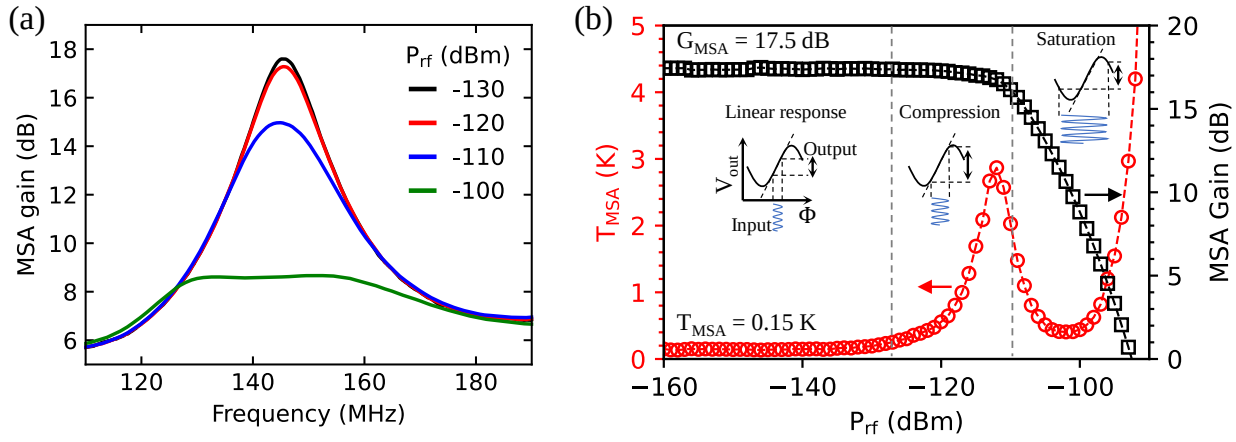


Figure 6.13: (a) MSA gain as a function of frequency for various rf input powers. (b) Gain and noise temperature at f = 145 MHz as a function of rf power. (insets) The three operating regimes highlighted on the flux-to-voltage ($V - \Phi$) curve.

gain and noise temperature as a function of drive power. The 1 dB compression point of the MSA occurs at -115 dBm, which is consistent with other MSAs in literature [174]. For larger powers, the MSA reaches saturation, corresponding to when the change in flux $\delta\Phi$ exceeds half a flux quantum ($\Phi_0/2$). The poor dynamic range is typical for an MSA and reflects the non-linearity of the $V - \Phi$ curve, as indicated by the insets in Fig. 6.13b. The noise temperature is determined using the SNR-ratio technique outlined above. Although the gain decreases when $P_{rf} \gtrsim -120$ dBm, the noise temperature starts to rise at an even lower power level of approximately ~ -130 dBm. This analysis underscores that to leverage the lower noise of the MSA, only extremely weak signals below -130 dBm can be applied.

6.3.6 Carrier nulling

To incorporate the MSA as the initial amplification stage in the RF-QPC readout, it is critical that the signal level at the MSA input remains low (< -130 dBm). In the RF-QPC readout, a fraction of carrier signal is always reflected by the matching circuit due to the impedance mismatch ($Z_{in} \neq Z_0$). The signal of interest is embedded within the

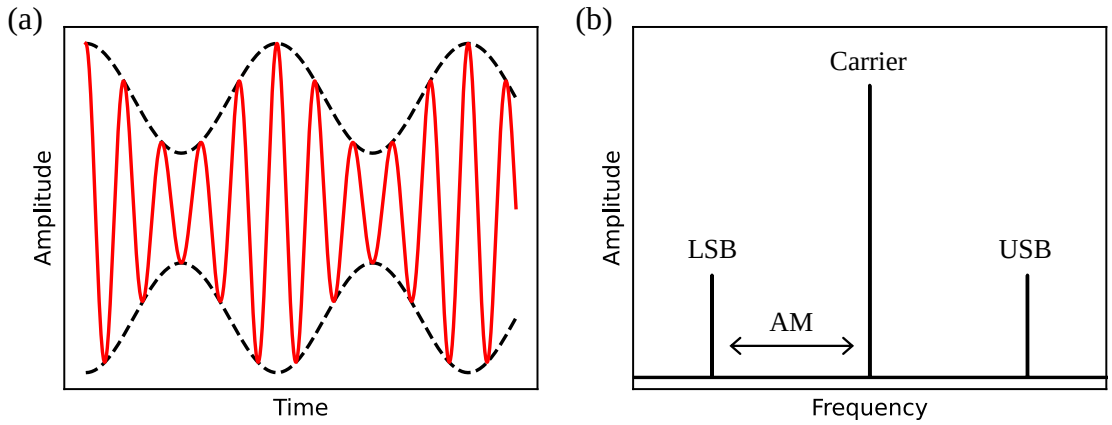


Figure 6.14: (a) Simulated amplitude modulation (AM) of carrier signal in the time domain. (b) Resulting frequency spectrum of the data in panel (a).

amplitude modulation, or envelope, of this reflected carrier signal. Fig. 6.14a illustrates a simulated example of carrier signal with frequency f_c, which is amplitude modulated at a frequency f_m in the time domain. In the frequency domain, this amplitude modulated carrier signal produces sidebands in the power spectrum at $f_c \pm f_m$. The signal above the carrier frequency is referred to as the upper sideband (USB), while the signal below the carrier frequency is known as the lower sideband (LSB). Fig. 6.14b depicts a simulated example of the power spectrum. In the homodyne detection technique employed for charge sensitivity measurements in Sec. 6.3.4, the power is extracted from both sidebands.

The power (in dBm) of the reflected carrier signal is directly proportional to Γ, as determined by the return loss. The return loss, representing the ratio of incident power to reflected power (in dB), is given by RL (dB) = -20log$_{10}|\Gamma|$. For the RF-QPC readout in this work, the maximum charge sensitivity (optimal working point) occurs when $\Gamma = 0.05$, resulting in RL = 26 dB. For a -95 dBm carrier power incident on the matching circuit (used in Sec. 6.3.4 for charge sensitivity measurements), the power of the reflected carrier, also serving as the input power to the first amplification stage, is approximately -121 dBm (i.e., -95 - 26 = -121). Here, we neglect cable and/or insertion losses. This power level exceeds the MSA's dynamic range of -130 dBm, thereby increasing the noise of the MSA. However, the power of the modulated signal is substantially lower. The modulated signal

level generated by the degeneracy of two charge states can be estimated using the following expression (see Sec. 6.2.3).

$$P_{mod} = |\Delta\Gamma|^2 P_{ref} \tag{6.29}$$

where P_{mod} and P_{ref} are the modulation and reflected power in watts, respectively, and $|\Delta\Gamma|$ denotes the change in reflection coefficient for the two charge states. From the charge sensitivity measurements in Sec. 6.3.4, a single charge transition corresponds to $|\Delta\Gamma| \sim 10^{-2}$ resulting in $|\Delta\Gamma|^2 \sim 10^{-4}$. Thus, the modulated signal level is approximately four decades smaller in power (40 dB) than the reflected carrier. In the example above, where the power of the reflected carrier is -121 dBm, a single charge transition yields a modulated signal level of ~ -161 dBm (i.e., -121 - 40 = -161). This power level is within the operational range for the MSA (see Fig. 6.13).

In summary, the power of the reflected carrier signal in the RF-QPC readout is too high for the MSA to operate within a linear response regime with low noise. However, the modulated signal is significantly smaller, allowing the MSA to maintain linearity and low noise performance. Consequently, for successful integration of the MSA into the RF-QPC readout, it is critical to diminish the carrier signal to a level below -130 dBm. One potential approach to achieve this reduction is through a nulling technique. This technique involves introducing a tone with identical amplitude and frequency as the carrier but with a 180-degree phase shift. This tone is injected after the signal's reflection from the matching circuit but before reaching the MSA input. The injected tone effectively cancels out the carrier signal while preserving the amplitude modulated signal, allowing it to pass through unaffected. However, one concern is the potential interaction between the reflected signal and the nulling signal. This interaction could potentially generate noise at the MSA input, thereby jeopardizing the viability of the nulling technique. Furthermore, it is unclear whether this nulling technique can be applied to larger carrier powers, and what the practical limitations of this technique might be.

Carrier nulling experiment with MSA

To investigate the feasibility of carrier nulling technique in the RF-QPC readout, we conducted an experiment solely focused on carrier suppression using the MSA, without involv-

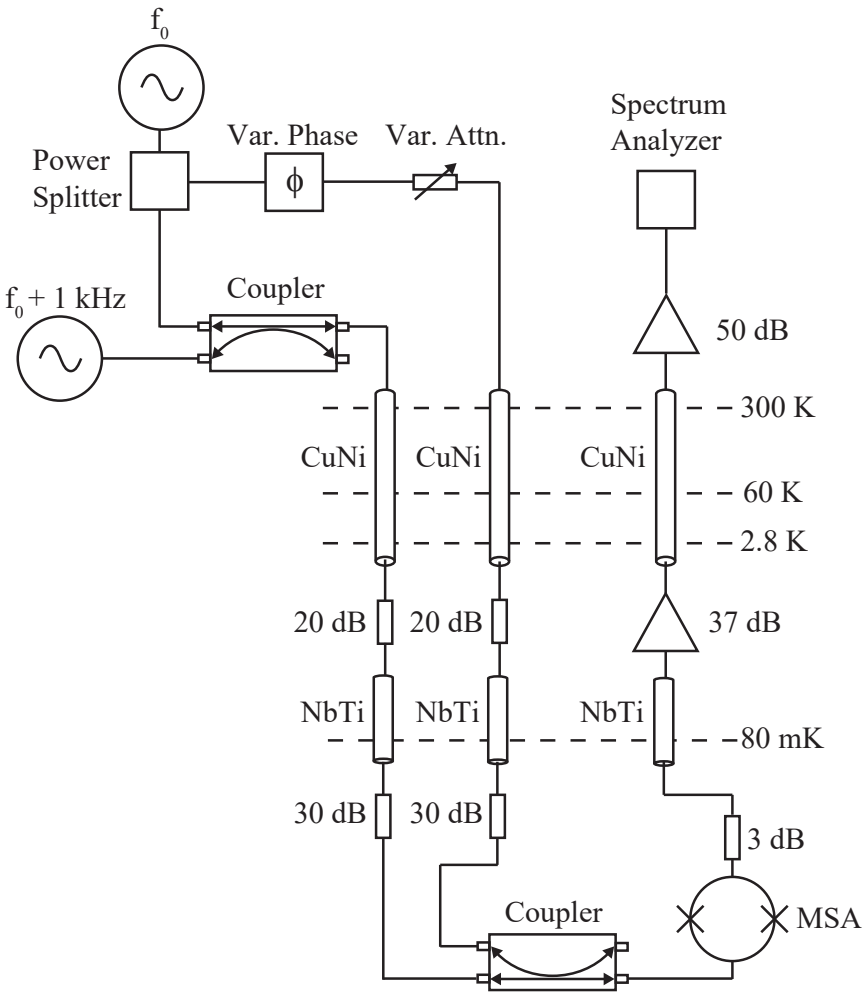


Figure 6.15: RF circuit for the carrier nulling experiment configured on the dilution refrigerator.

ing the RF-QPC itself. Fig. 6.15 shows the rf circuit for the nulling experiment. In this setup, a single signal generator is employed to produce a 145 MHz "carrier" and nulling tone, which is evenly divided using a power splitter. To monitor the gain of the MSA during nulling, a second signal generator is used to inject a small tone on the main drive line, offset in frequency from the carrier by 1 kHz. The "carrier" signal is combined with this small tone through a directional coupler at room temperature. The main drive and nulling line both feature 20 dB of attenuation at the 2.8 K stage and 30 dB at the mixing chamber (80 mK) before reaching a directional coupler, also mounted at the mixing chamber. The nulling line is connected to the coupled port of the directional coupler (with 30 dB attenuation), while the main drive is connected to the input port. The directional coupler is used to cancel-out (via destructive interference) the "carrier" and nulling signal before reaching the MSA input. The signal from the MSA is further amplified by the cryogenic SiGe amplifier (model CITLF2) followed by two identical Mini-Circuit amplifiers (model ZX60-P103LN+) at room temperature, and is connected to a spectrum analyzer to monitor the gain and noise level.

On the nulling line, we employed variable phase and attenuation mechanisms at room temperature. Phase adjustments were made using a passive adjustable-length line equipped with a custom-made mechanical turnbuckle-style fine adjustment. At 145 MHz, the corresponding wavelength is approximately 1.43 meters, considering the speed of light in a coaxial cable is $\sim 0.69 \times$ the speed of light in a vacuum, c. With our fine adjustment setup, we could achieve length increments of less than 1 mm, resulting in phase adjustments of approximately 0.25 degrees at 145 MHz. Additionally, we controlled attenuation by using a shorted, adjustable-length stub connected to the nulling line through a tee. By adjusting the length of this stub, we could modify the characteristic impedance of the transmission line away from 50 Ω. This adjustment effectively altered the amplitude of the nulled signal by fractions of a dB.

With the nulling line disconnected, Fig. 6.16a shows the output of the spectrum analyzer for three different carrier powers. The peak at f_0 corresponds to the reflected "carrier" signal, and the peak at $f_0 + 1$ kHz represents the modulated carrier, or the upper-sideband ("USB"). The amplitude of the USB was held constant at -150 dBm at the MSA input, while the carrier power was adjusted. As the carrier power is increased, the noise floor rises

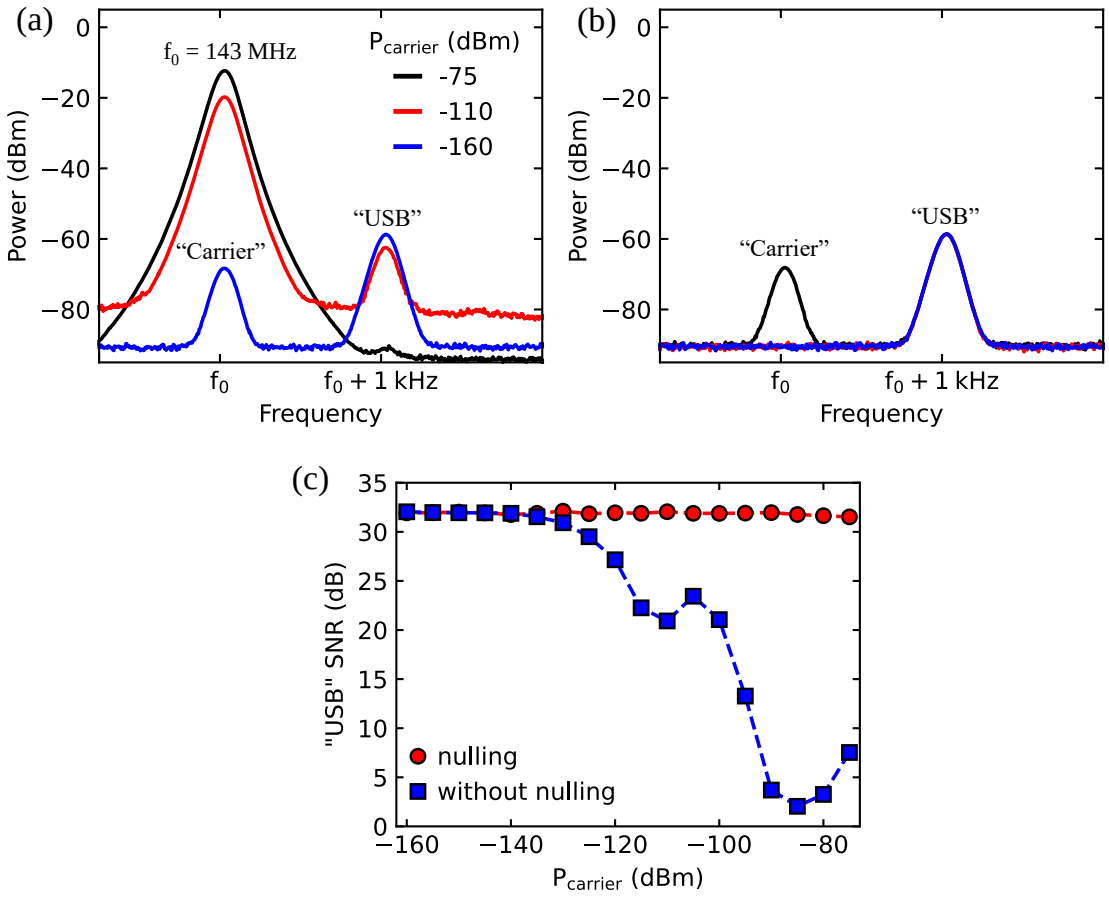


Figure 6.16: Carrier nulling experiment with the MSA. Output of the spectrum analyzer (a) without carrier nulling and (b) with nulling. (c) SNR of "USB" as a function of carrier power with and without nulling.

followed by the USB signal level decreasing into the noise floor, depicting what would happen if the MSA was merely integrated into the RF-QPC readout without carrier nulling. The same experiment was repeated with the nulling line connected and the attenuation and phase adjusted for maximal carrier suppression, as shown in Fig. 6.16b. The carrier signal was effectively suppressed below the noise floor for lower powers, with a small amount feeding through at the highest power. The noise floor and USB signal level remained constant for all powers. Fig. 6.16c shows the SNR of the USB as a function of carrier power with and without nulling. Without nulling, the SNR decreases for powers exceeding -130 dBm, consistent with the results in Sec. 6.3.5. In contrast, with the nulling technique, the SNR was maintained up to a carrier power of -75 dBm. These results demonstrate that the nulling technique can be implemented without introducing noise and is effective for powers up to -75 dBm, well exceeding the amplitude of a reflected carrier in a RF-QPC readout. It is noteworthy that the nulling technique with an MSA was recently demonstrated in the readout of a carbon nanotube single-electron transistor embedded in a nanomechanical resonator, as described in Ref. [175].

6.3.7 Integrating the MSA into RF-QPC readout

In this section, we will present the results of integrating the MSA into the RF-QPC readout. Fig. 6.17 shows the modified RF-QPC readout circuit, which now includes both the nulling circuit and MSA as the first-stage amplifier. The directional coupler located at the MSA input is employed for carrier nulling, while the other is utilized for the reflectometry scheme required for the RF-QPC readout. The significance of the highlighted transmission line in red and the "Attn/Filter" component will be discussed shortly.

As a first step, the MSA needs to be current biased with the appropriate critical current and the flux bias to position the SQUID at the steepest point on its $V - \Phi$ curve. With the MSA not current biased in the "off" state, the signal "feedthrough" in the frequency range of $100 - 200$ MHz is attenuated by approximately 20 dB. When the MSA is biased appropriately in the "on" state, a gain of 17.5 dB is achieved at 145 MHz. Thus, when tuning the MSA, a change in signal level of approximately 37.5 dB is expected near 145 MHz when the MSA is in the "on" state.

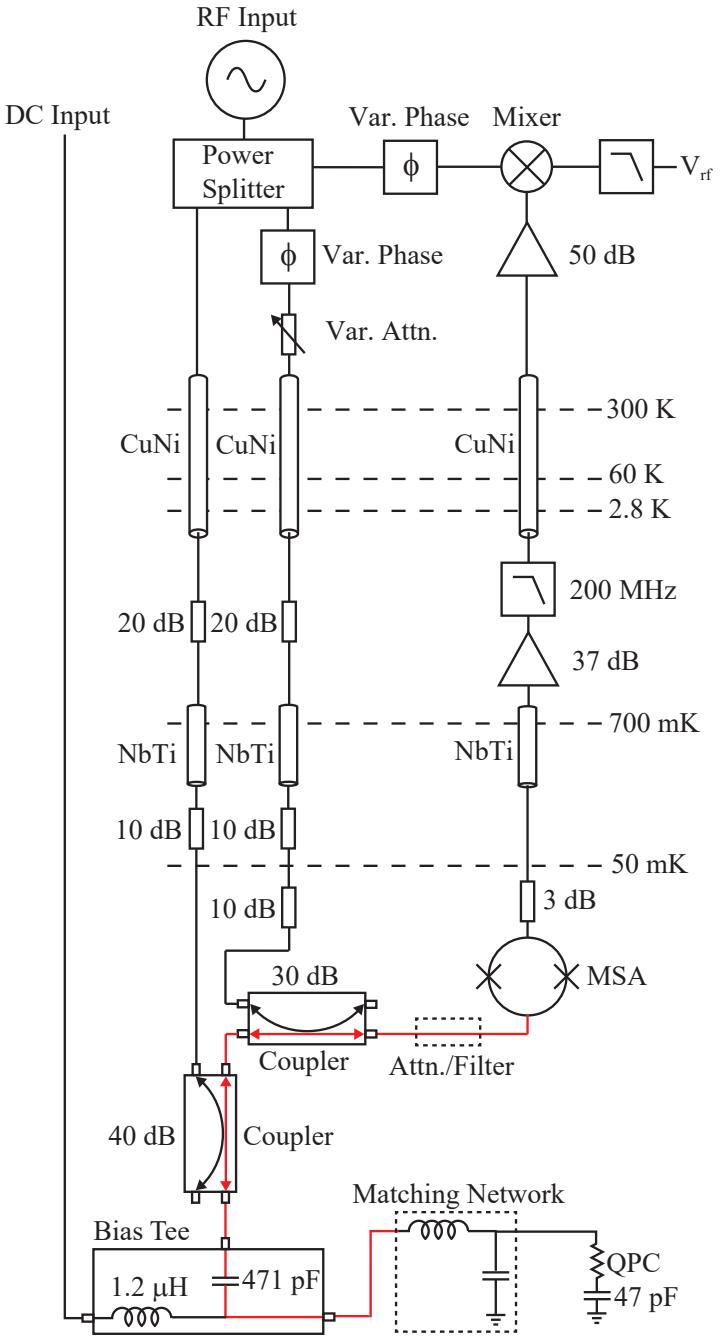


Figure 6.17: RF-QPC readout with the nulling circuit and MSA configured on the dilution refrigerator.

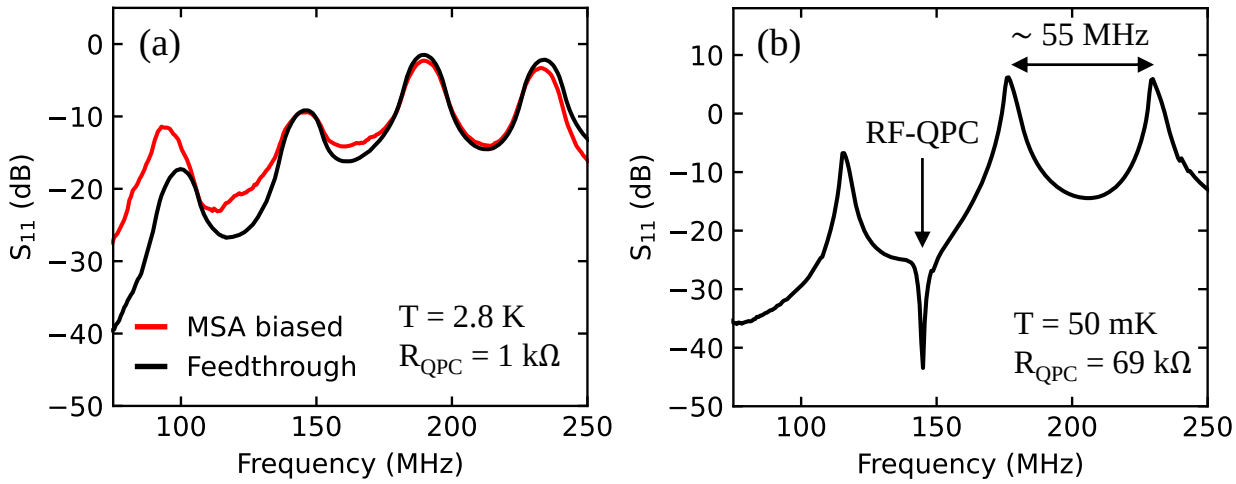


Figure 6.18: RF-QPC and MSA interaction. (a) S_{11} as a function of frequency measured at 2.8 K when the MSA is"off" (feedthrough, black trace) and "on" (current biased, red trace). (b) Same measurement in panel (a) but at 50 mK and $R_{QPC} = 69$ kΩ where $\Gamma \sim 0$ at 143 MHz.

While tuning the MSA, the gates on the quantum dot device used for the RF-QPC, specifically Q1, Q2, and RS, were set to negative voltages to deplete carriers beneath them. The QPC formed between Q1 and RS was set to $R_{QPC} = 1$ kΩ such that $\Gamma \sim 1$ at 143 MHz. Fig. 6.18a shows the S_{11} scattering parameter as a function of frequency measured with a network analyzer at 2.8 K. A signal power of -150 dBm at the device input (RLC matching circuit) was used such that reflected signals would not saturate the MSA. A large wave structure is clearly evident in the S_{11} versus frequency data, which is characteristic of a cable resonance (to be discussed in more detail shortly). The MSA was biased with the appropriate critical current ($I_c \sim 4.6$ μA) and the flux bias was adjusted while the output signal level was monitored. Unexpectedly, only a very small change (< 5 dB) in the output signal level was observed with the correct current bias I_B, and no change in response was observed when adjusting the flux bias I_ϕ. The same result was obtained when $R_{QPC} = 69$ kΩ such that $\Gamma \sim 0$ at 143 MHz. Fig. 6.18b shows the S_{11} versus frequency data with $R_{QPC} = 69$ kΩ at 50 mK showing the rf readout "dip" at 143 MHz.

After ruling out trivial explanations, such as issues with the MSA bias circuit, we hypothesized that the lack of response from the MSA might be due to the signal level at the input saturating the MSA. When the MSA becomes saturated, any adjustments to the flux bias have no impact on the output, consistent with our observations. To further investigate the poor performance of the MSA, we examined the wave structure in S_{11} as a function of frequency in Fig. 6.18. This structure was absent when the MSA was not included in the readout circuit. The periodic nature ($\Delta f \sim 55$ MHz) is characteristic of a cable resonance generated between two impedance mismatched components [174]. From independent measurements conducted in other experiments, we have established that Δf is inversely proportional to the length of the cable separating the two impedance-mismatched components. In this specific setup, it is likely that the cable resonance occurs between the RLC circuit and the MSA input, which are both broadband impedance mismatched. To confirm this hypothesis, we reduced the cable length in a subsequent cooldown, and as expected, the frequency spacing increased proportionally. This section of cable corresponds to the red section of the rf signal path depicted in Fig. 6.17.

To dampen the cable resonance and the resultant signal level at the input of the MSA, rf filters and attenuators were placed between the MSA and the RLC circuit during subsequent cooldowns (denoted as "Attn/Filter" in Fig. 6.17). An attempt was made to address cable resonance and high-frequency noise using a conventional inductor-capacitor (LC) low-pass filter (Mini-Circuits, model VLFX-225+ with a 350 MHz cutoff frequency); however, this did not result in any noticeable change in the MSA response. The conventional filter operates by being impedance mismatched (reflective) outside the passband, which might not effectively resolve the cable resonance issue. An alternative filter technology, known as a reflectionless filter, provides broadband impedance matching and functions by absorbing rf power outside the passband [176]. We acquired a commercial low-pass reflectionless filter (Mini-Circuits, model ZXLF-K221+ with a 370 MHz cutoff frequency), but it was tested and found to be incompatible at low temperatures. To address this issue, a custom-made reflectionless bandpass filter was constructed, following the design outlined in Ref. [176]. This custom filter has a narrow bandwidth of 50 MHz centered at 143 MHz (RF-QPC readout) and provided over 10 dB of attenuation outside the passband. Unfortunately, even with this custom filter, the MSA's lack of gain response remained unresolved.

Furthermore, a 3 dB attenuator was tested but also proved ineffective. As a proof of concept, a 10 dB attenuator was tested and the results are presented in Fig. 6.19. The observed change in signal level between the MSA's "off" state (feedthrough) and its "on" state (MSA biased) aligns precisely with the expected ~ 37.5 dB increase outlined above. This experiment serves as a clear demonstration that the MSA had been saturated in previous experiments, highlighting the necessity for further modifications for it to function within the rf readout circuit.

Although not experimentally evaluated, the sensitivity of the RF-QPC readout in this configuration (with a 10 dB attenuator at the MSA input) may surpass that of the cryogenic SiGe amplifier. The attenuator at the MSA input reduces the signal by 10 dB, but the noise contribution from the MSA would still be lower ($T_{MSA} \sim 150$ mK, as estimated in Sec. 6.3.5) compared to the cryogenic SiGe amplifier ($T_{SiGe} \sim 2.3$ K). Consequently, with the 10 dB attenuator at the MSA input, the effective noise temperature of the MSA would increase by a factor of 10×, resulting in $T_{eff} \sim 1.5$ K.

The 10 dB attenuator could also potentially eliminate the reflection of the input noise from the first-stage amplifier (which otherwise doubles the noise temperature in the rf readout). Thus, the input noise would solely be that of the MSA (not doubled). For example, if we were to employ the MSA (with a 10 dB attenuator at the input) as the primary (first stage) amplifier in the RF-QPC readout, the approximately 3 × reduction in T_N compared to the SiGe semiconductor amplifier (i.e., $2.3/1.5 \sim 1.5$, and a factor of 2× from the lack of reflected noise) would yield a $\sqrt{3} \sim 1.7\times$ improvement (see Eq. 6.18) in the charge sensitivity δq.

Moving forward, this work highlights the need for further research on addressing the challenges of integrating MSA into practical readout applications. The measurements clearly indicate that the input impedance of the MSA deviates significantly from 50 Ω, introducing cable resonances and noise in a reflectometry scheme, which saturate the MSA. In order to optimize the MSA's performance and extend it's practical usefulness, it is essential to develop techniques for impedance matching the MSA to 50 Ω. This problem has been emphasized and tackled in Refs. [177, 36, 178]. This is particularly challenging for an MSA, as the dynamic resistance of the SQUID is a complex nonlinear function of both the current and the flux bias. In a simplified model of the MSA, the input impedance

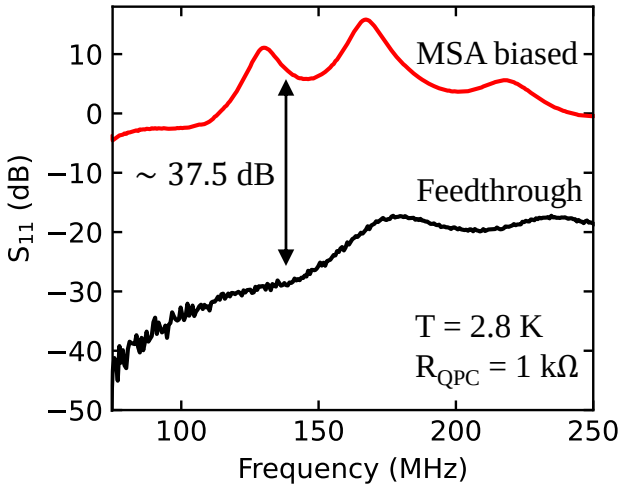


Figure 6.19: RF-QPC with the MSA and a 10 dB attenuator. S_{11} as a function of frequency measured at 2.8 K when the MSA "off" (feedthrough, black trace) and current biased (red trace). The signal level increases by $\sim$ 37.5 dB, as expected when the MSA is operational.

is directly proportional to the shunt resistance per junction R, and is scaled by the number of turns n, of the microstrip input coil: $z_i \approx n^2 R$ [36]. For the MSA utilized in this study, with $n = 60$ and $R \sim 5\,\Omega$, we expect $z_i \approx 18\ k\Omega$. This corresponds to an input return loss of $|S_{11}|^2$ of -0.05 dB, signifying that nearly all of the incident power is reflected. This is consistent with the large cable resonance observed with the MSA included in the RF-QPC readout circuit.

It's also worth noting that in a recent study by Schupp *et al.* [179], the authors demonstrated a dispersive (capacitive) readout of a quantum dot device using an MSA as the primary amplifier. In their study, the MSA had a gain of only 11.7 dB, which is smaller compared to the 20.5 dB gain (without the 3 dB attenuator on the output) of the MSA in this work. This nearly 10 dB reduction in gain resulted in a proportional increase in the dynamic range of their MSA. Additionally, they utilized a feedback capacitor between V_{in} and V_{out} of the MSA, with the intention of reducing the input impedance closer to 50 Ω. The combination of reduced gain and the feedback capacitor for impedance matching may explain why they were able to operate the MSA within their reflectometry circuit. However, they were also only able to achieve a noise temperature of $\sim$ 600 mK.

6.4 Conclusions and future work

In summary, we configured an RF-QPC readout at a low frequency of 143 MHz, precisely tuned to match a narrow bandwidth MSA. To overcome the self-resonance of a single large inductor needed for a low operating frequency, we utilized two inductors in series. This approach not only resolved the self-resonance problem but also allowed us to operate at a lower resonance frequency without resorting to increasing the capacitance C in the LC matching circuit, which degrades the readout sensitivity. Both transfer functions governing the RF-QPC readout sensitivity, namely $\partial R_{QPC}/\partial q$ and $\partial|\Gamma|/\partial R_{QPC}$, were optimized, resulting in an improved charge sensitivity compared to a previous readout configured within our group. This optimized setup achieved a charge sensitivity of $\delta q = 1.3 \times 10^{-3}$ e/$\sqrt{Hz}$ when using a -95 dBm carrier signal.

We characterized an MSA for use as the primary amplifier in the RF-QPC readout. For weak input signals, the MSA had a maximum gain of 17.5 dB (including 3 dB attenuator on the output) at 145 MHz and a bandwidth of 12 MHz. The reduced noise in the MSA, in comparison to our cryogenic semiconductor (SiGe) amplifier, resulted in a 9.4 dB improvement in the SNR when using a 145 MHz tone. This improvement corresponded to an MSA noise temperature of $T_{MSA} \sim 150$ mK, which is over an order of magnitude lower than that of the SiGe amplifier ($T_{SiGe} = 2.3$ K). The gain of the MSA was observed to degrade for input signal levels greater than -120 dBm, while the noise was found to increase for signal levels greater than -130 dBm. We conducted a successful proof-of-principle experiment to demonstrate how the limitations of the poor dynamic range of the MSA can be mitigated in a reflectometry scheme (RF-QPC readout) using a nulling technique. This technique did not introduce noise and was effectively demonstrated for powers up to -75 dBm, well exceeding the amplitude of a reflected carrier signal in a practical RF-QPC readout.

When we integrated the MSA into the RF-QPC readout, we encountered a significant issue: the MSA could not be biased to provide gain. This problem was attributed to the presence of a pronounced cable resonance between the MSA and the RLC circuit of the RF-QPC readout. This cable resonance indicated a substantial mismatch between the input impedance of the MSA and the line impedance (50 Ω), resulting in a signal level at the MSA input sufficient enough to saturate the MSA. In an attempt to resolve this issue,

we experimented with various commercial and custom-made filters at the MSA's input, but none of them proved successful. It was only when we employed an impractical 10 dB attenuation at the MSA input that the MSA became operational in the RF-QPC readout. Consequently, the integration of the MSA into the RF-QPC readout highlights the need for the MSA to be impedance-matched with the line impedance for proper functioning and, in turn, to enhance the sensitivity of the RF-QPC readout. For future work, it would be beneficial to characterize the input impedance of the MSA and develop strategies for matching it to the line impedance (50 Ω).

Chapter 7

Summary and future work

7.1 Summary

This thesis has presented magnetotransport measurements in 2DHGs within a dopant-free GaAs/AlGaAs material system, along with the setup of an RF-QPC readout in a double quantum dot device. These measurements have yielded several important conclusions, briefly outlined below.

In Chapter 4, we have established that the aluminum content of the AlGaAs layer influence charge trapping and gate hysteresis in our devices. Based on these findings, it is recommended to utilize an AlGaAs composition with an aluminum content of 50% to mitigate gate hysteresis in future devices. Furthermore, we have identified the smoothing superlattice buffer layer as the cause of undesired parallel conduction in our devices. Therefore, for future wafers, it is recommended to grow them without a superlattice buffer to eliminate parallel conduction in these devices. Leveraging our low-disorder dopant-free 2DHGs, four successive and distinct SdH regimes were identified at different magnetic field ranges, resulting from Rashba spin-orbit interaction (SOI) and Zeeman splitting within the Heavy-hole (HH) valence band. We extracted the effective masses of the HH- and HH+ subbands, extending the results to lower hole densities than those reported in modulation-doped samples in literature. Within the accessible density range, the HH- effective mass

remains constant, whereas the HH+ exhibits a strong density dependence due to the spin-orbit induced nonparabolicities in the valence band. Due to our device architecture, we demonstrate one of the largest observed spin-orbit-driven HH-/HH+ splittings in a GaAs 2DHG in literature. Our examination of the out-of-plane effective g factor suggests that at higher magnetic fields in the quantum Hall regime, the 2DHG population is predominantly described by Landau levels from HH- with a smaller effective mass.

In Chapter 5, we report the observation of the SdH phase inversion phenomenon in a 2DHG for the first time. We explored the empirical relationship between the hole temperature T_h, and applied dc current I_{dc} through the Hall bar. Our results suggest that the hole temperature exhibits a greater sensitivity to current-induced Joule heating compared to the electron temperature in its 2DEG counterpart. Detailed maps of the differential resistance (ρ_{xx} and r_{xy}) over a range of sheet current density and magnetic field revealed transport diamonds at integer filling factors. The absence of an even- and odd-filling factor dependence for the width of transport diamonds in our GaAs 2DHG implies the cyclotron energy to be approximately twice as large as the the Zeeman energy, which is consistent with the extracted effective mass and g factor values obtained in Chapter 4. Additionally, the ratio of the critical electric field (E_c) in our GaAs/AlGaAs 2DHG, when compared to compiled data for GaAs/AlGaAs 2DEGs, approximately reflects the difference in effective mass and g factor between the two carrier systems. By compiling maps at four holes densities, we find that critical breakdown current (I_c) and electric field (E_c) both exhibit an approximate linear B-field dependence, consistent with similar 2DEG samples. We report the observation of the zero-current anomaly (ZCA), also for the first time in a 2DHG. The limited and/or incorrect nature of hysteresis near breakdown suggests that the hyperfine coupling between hole and nuclear spins is indeed weaker compared to that between electron and nuclear spins.

In Chapter 6, we configured an RF-QPC readout charge detector at a low resonance frequency of 143 MHz, precisely tuned to match a narrow bandwidth microstrip SQUID amplifier (MSA). We addressed the self-resonance issue associated with a single large inductor required for a low operating frequency by employing two inductors in series. The designed operating point of the RF-QPC readout was successfully achieved, resulting in an improved charge sensitivity compared to a previous readout configured within our group.

We characterized the MSA for use as the primary amplifier in the RF-QPC readout. We estimated the noise temperature of the MSA to be over an order of magnitude lower than that of the cryogenic semiconductor amplifier used in the RF-QPC readout. We successfully demonstrated a carrier nulling technique that would mitigate the poor dynamic range of the MSA for use in reflectometry (RF-QPC) readout. Upon integrating the MSA into the RF-QPC readout, the MSA could not be biased to provide gain. The root cause of this issue was attributed to the impedance mismatch between the MSA and the line impedance (50 Ω). The combination of this factor along with the impedance mismatch of the RLC matching (tank) circuit in the RF-QPC readout likely results in the saturation of the MSA.

In summary, the first part of this thesis has outlined experimental studies on the characterization of p-type GaAs/AlGaAs Hall bar devices, required for development of novel devices based on hole spins. It provides valuable feedback to the fabrication team to improve their structures. It also provides valuable information based on the analysis of magnetotransport measurements about hole effective masses, SOI strength, effective g-factor, and the overall complex energy spectrum of holes. This knowledge is critical for designing quantum devices based on hole spins, including the development of hole spin qubits for quantum computing.

In the second part of this thesis, a high-speed and sensitive charge sensor was developed for a quantum dot device. The thorough characterization and analysis provides valuable information for the design and implementation of an optimized RF-QPC charge sensor. Furthermore, initial efforts were made to enhance the sensitivity of the RF-QPC readout by incorporating a superconducting-based microstrip SQUID amplifier.

7.2 Future work

Our findings suggest several potential avenues for further research, briefly outlined below.

Following Chapter 4, the effective mass analysis could be extended to higher hole densities in devices fabricated with with 50% aluminum content in the AlGaAs layer. This would further map-out the curvature of the HH-/HH+ subbands, providing further insight

into the hole density and electric-field dependence of the SOI-induced splitting. Additionally, the lower hole density regime could be explored in devices fabricated with two separate accumulation gates, one for the ohmic contacts and another for the Hall bar itself. This could facilitate the study of phenomena such as weak anti-localization (WAL), an alternative method for investigating the SOI strength.

Following Chapter 5, one could also extend the quantum Hall breakdown maps to higher hole densities in devices fabricated with with 50% aluminum content in the AlGaAs layer. This would assist in validating the linear B dependence of I_c and E_c up to larger magnetic fields. Additionally, one could replicate the many of the measurements using a single Hall bar device equipped with ambipolar (n- and p-type) ohmic contacts. This configuration would enable seamless switching between 2DEG and 2DHG, facilitating a direct one-to-one comparison.

Following Chapter 6, it is essential to investigate the input impedance of the MSA. One could analyze how the input impedance is influenced by the bias conditions and/or resonant frequency of the MSA. Subsequently, developing techniques to impedance match the MSA to the line impedance (50 Ω) would facilitate its successful integration into the RF-QPC readout.

References

[1] Aron Pinczuk and Sankar Das Sarma. *Perspectives in Quantum Hall Effects: Novel Quantum Liquids in Low-Dimensional Semiconductor Structures*. Wiley, 1997.

[2] MJ Manfra, R De Picciotto, Z Jiang, SH Simon, LN Pfeiffer, KW West, and AM Sergent. Impact of spin-orbit coupling on quantum Hall nematic phases. *Physical review letters*, 98(20):206804, 2007.

[3] AF Croxall, F Sfigakis, J Waldie, I Farrer, and DA Ritchie. Orientation of hole quantum Hall nematic phases in an out-of-plane electric field. *Physical Review B*, 99(19):195420, 2019.

[4] Igor Žutić, Jaroslav Fabian, and S Das Sarma. Spintronics: Fundamentals and applications. *Reviews of modern physics*, 76(2):323, 2004.

[5] Supriyo Datta and Biswajit Das. Electronic analog of the electro-optic modulator. *Applied Physics Letters*, 56(7):665–667, 1990.

[6] Pojen Chuang, Sheng-Chin Ho, Luke William Smith, Francois Sfigakis, Michael Pepper, Chin-Hung Chen, Ju-Chun Fan, JP Griffiths, Ian Farrer, Harvey Edward Beere, et al. All-electric all-semiconductor spin field-effect transistors. *Nature nanotechnology*, 10(1):35–39, 2015.

[7] Daniel Loss and David P DiVincenzo. Quantum computation with quantum dots. *Physical Review A*, 57(1):120, 1998.

[8] Denis V Bulaev and Daniel Loss. Spin relaxation and decoherence of holes in quantum dots. *Physical review letters*, 95(7):076805, 2005.

[9] Denis V Bulaev and Daniel Loss. Electric dipole spin resonance for heavy holes in quantum dots. *Physical review letters*, 98(9):097202, 2007.

[10] Sergei Studenikin, Marek Korkusinski, Alex Bogan, Louis Gaudreau, D Guy Austing, Andrew S Sachrajda, Lisa Tracy, John Reno, and Terry Hargett. Single-hole physics in GaAs/AlGaAs double quantum dot system with strong spin-orbit interaction. *Semiconductor Science and Technology*, 36(5):053001, 2021.

[11] VS Pribiag, S Nadj-Perge, SM Frolov, JWG Van Den Berg, I Van Weperen, SR Plissard, EPAM Bakkers, and LP Kouwenhoven. Electrical control of single hole spins in nanowire quantum dots. *Nature nanotechnology*, 8(3):170–174, 2013.

[12] Andrew P Higginbotham, TW Larsen, Jun Yao, Hao Yan, CM Lieber, CM Marcus, and Ferdinand Kuemmeth. Hole spin coherence in a Ge/Si heterostructure nanowire. *Nano letters*, 14(6):3582–3586, 2014.

[13] WA Coish and J Baugh. Nuclear spins in nanostructures. *physica status solidi (b)*, 246(10):2203–2215, 2009.

[14] Tzu-Kan Hsiao, Antonio Rubino, Yousun Chung, Seok-Kyun Son, Hangtian Hou, Jorge Pedrós, Ateeq Nasir, Gabriel Éthier-Majcher, Megan J Stanley, Richard T Phillips, et al. Single-photon emission from single-electron transport in a SAW-driven lateral light-emitting diode. *Nature communications*, 11(1):917, 2020.

[15] Takafumi Fujita, Kazuhiro Morimoto, Haruki Kiyama, Giles Allison, Marcus Larsson, Arne Ludwig, Sascha R Valentin, Andreas D Wieck, Akira Oiwa, and Seigo Tarucha. Angular momentum transfer from photon polarization to an electron spin in a gate-defined quantum dot. *Nature communications*, 10(1):2991, 2019.

[16] Louis Gaudreau, Alex Bogan, Marek Korkusinski, Sergei Studenikin, D Guy Austing, and Andrew S Sachrajda. Entanglement distribution schemes employing coherent photon-to-spin conversion in semiconductor quantum dot circuits. *Semiconductor Science and Technology*, 32(9):093001, 2017.

[17] A Srinivasan, I Farrer, DA Ritchie, and AR Hamilton. Improving reproducibility of quantum devices with completely undoped architectures. *Applied Physics Letters*, 117(18), 2020.

[18] A Shetty, F Sfigakis, WY Mak, K Das Gupta, B Buonacorsi, MC Tam, HS Kim, I Farrer, AF Croxall, HE Beere, et al. Effects of biased and unbiased illuminations on two-dimensional electron gases in dopant-free GaAs/AlGaAs. *Physical Review B*, 105(7):075302, 2022.

[19] Fabrizio Nichele. *Transport experiments in two-dimensional systems with strong spin-orbit interaction*. PhD thesis, ETH Zurich, 2014.

[20] R Winkler, Dimitrie Culcer, SJ Papadakis, B Habib, and M Shayegan. Spin orientation of holes in quantum wells. *Semiconductor science and technology*, 23(11):114017, 2008.

[21] Tenghua Gao and Kazuya Ando. Spin-orbit torques. *Handbook of Magnetic Materials*, 29:1–55, 2020.

[22] Roland Winkler. *Spin-orbit coupling effects in two-dimensional electron and hole systems*, volume 191. Springer, 2003.

[23] Charles Kittel and Ching-yao Fong. *Quantum theory of solids*. Wiley, 1987.

[24] Gene Dresselhaus. Spin-orbit coupling effects in zinc blende structures. *Physical Review*, 100(2):580, 1955.

[25] Yu A Bychkov and Emmanuel I Rashba. Oscillatory effects and the magnetic susceptibility of carriers in inversion layers. *Journal of physics C: Solid state physics*, 17(33):6039, 1984.

[26] Ulrich Rössler and Josef Kainz. Microscopic interface asymmetry and spin-splitting of electron subbands in semiconductor quantum structures. *Solid state communications*, 121(6-7):313–316, 2002.

[27] MV Durnev, MM Glazov, and EL Ivchenko. Spin-orbit splitting of valence subbands in semiconductor nanostructures. *Physical Review B*, 89(7):075430, 2014.

[28] E Marcellina, AR Hamilton, R Winkler, and Dimitrie Culcer. Spin-orbit interactions in inversion-asymmetric two-dimensional hole systems: A variational analysis. *Physical Review B*, 95(7):075305, 2017.

[29] M Altarelli, U Ekenberg, and A Fasolino. Calculations of hole subbands in semiconductor quantum wells and superlattices. *Physical Review B*, 32(8):5138, 1985.

[30] T Ihn. *Quantum states and electronic transport*. Oxford University Press, Oxford, 2010.

[31] Tsuneya Ando, Alan B Fowler, and Frank Stern. Electronic properties of two-dimensional systems. *Reviews of Modern Physics*, 54(2):437, 1982.

[32] CWJ Beenakker and H Van Houten. Semiconductor heterostructures and nanostructures. *Solid State Physics*, 44:1, 1991.

[33] BJ Van Wees, H Van Houten, CWJ Beenakker, J Gr Williamson, LP Kouwenhoven, D Van der Marel, and CT Foxon. Quantized conductance of point contacts in a two-dimensional electron gas. *Physical Review Letters*, 60(9):848, 1988.

[34] John Clarke and Alex I Braginski. *The SQUID handbook*, volume 1. Wiley Online Library, 2004.

[35] Clifford Plesha. Setup and design of a cryogenic testing station with focus on characterization of superconducting devices. Master's thesis, University of Waterloo, 2019.

[36] M Mück, D Hover, S Sendelbach, and R McDermott. Microstrip superconducting quantum interference device radio-frequency amplifier: Effects of negative feedback on input impedance. *Applied Physics Letters*, 94(13), 2009.

[37] Michael Mück, Marc-Olivier André, John Clarke, Jost Gail, and Christoph Heiden. Radio-frequency amplifier based on a niobium dc superconducting quantum interference device with microstrip input coupling. *Applied Physics Letters*, 72(22):2885–2887, 1998.

[38] Michael Mück. Increasing the dynamic range of a SQUID amplifier by negative feedback. *Physica C: Superconductivity*, 368(1-4):141–145, 2002.

[39] Michael Mück, JB Kycia, and John Clarke. Superconducting quantum interference device as a near-quantum-limited amplifier at 0.5 GHz. *Applied Physics Letters*, 78(7):967–969, 2001.

[40] AC Gossard. Modulation doping of semiconductor heterostructures. In *Molecular beam epitaxy and heterostructures*, pages 499–531. Springer, 1985.

[41] RP Taylor, PT Coleridge, M Davies, Y Feng, JP McCaffrey, and PA Marshall. Physical and electrical investigation of ohmic contacts to AlGaAs/GaAs heterostructures. *journal of Applied Physics*, 76(12):7966–7972, 1994.

[42] D Taneja, F Sfigakis, AF Croxall, K Das Gupta, V Narayan, J Waldie, I Farrer, and DA Ritchie. N-type ohmic contacts to undoped GaAs/AlGaAs quantum wells using only front-sided processing: application to ambipolar FETs. *Semiconductor Science and Technology*, 31(6):065013, 2016.

[43] WY Mak, K Das Gupta, HE Beere, I Farrer, F Sfigakis, and DA Ritchie. Distinguishing impurity concentrations in GaAs and AlGaAs using very shallow undoped heterostructures. *Applied Physics Letters*, 97(24):242107, 2010.

[44] Brandon Buonacorsi. *Quantum dot devices in silicon and dopant-free GaAs/AlGaAs heterostructures*. PhD thesis, University of Waterloo, 2021.

[45] V Umansky, R De-Picciotto, and Moty Heiblum. Extremely high-mobility two dimensional electron gas: Evaluation of scattering mechanisms. *Applied physics letters*, 71(5):683–685, 1997.

[46] Jian Huang, DS Novikov, DC Tsui, LN Pfeiffer, and KW West. Nonactivated transport of strongly interacting two-dimensional holes in GaAs. *Physical Review B*, 74(20):201302, 2006.

[47] Yong P Chen, G Sambandamurthy, ZH Wang, RM Lewis, LW Engel, DC Tsui, PD Ye, LN Pfeiffer, and KW West. Melting of a 2D quantum electron solid in high magnetic field. *Nature Physics*, 2(7):452–455, 2006.

[48] Talbot Knighton, Zhe Wu, Jian Huang, Alessandro Serafin, JS Xia, LN Pfeiffer, and KW West. Evidence of two-stage melting of Wigner solids. *Physical Review B*, 97(8):085135, 2018.

[49] JCH Chen, DQ Wang, O Klochan, AP Micolich, K Das Gupta, F Sfigakis, DA Ritchie, D Reuter, AD Wieck, and AR Hamilton. Fabrication and characterization of ambipolar devices on an undoped AlGaAs/GaAs heterostructure. *Applied Physics Letters*, 100(5):052101, 2012.

[50] Lin Tian, Francois Sfigakis, Arjun Shetty, Ho-Sung Kim, Nachiket Sherlekar, Sara Hosseini, Man Chun Tam, Brad van Kasteren, Brandon Buonacorsi, Zach Merino, et al. Stable electroluminescence in ambipolar dopant-free lateral pn junctions. *arXiv preprint arXiv:2306.10874*, 2023.

[51] WY Mak, F Sfigakis, K Das Gupta, O Klochan, HE Beere, I Farrer, JP Griffiths, GAC Jones, AR Hamilton, and DA Ritchie. Ultra-shallow quantum dots in an undoped GaAs/AlGaAs two-dimensional electron gas. *Applied Physics Letters*, 102(10):103507, 2013.

[52] T Obata, K Takeda, J Kamioka, T Kodera, WM Akhtar, K Sawano, S Oda, Y Shiraki, and S Tarucha. Charge-noise-free Lateral Quantum Dot Devices with Undoped Si/SiGe Wafer. In *Proceedings of the 12th Asia Pacific Physics Conference (APPC12)*, page 012030, 2014.

[53] WP Kirk and M Twerdochlib. Improved method for minimizing vibrational motion transmitted by pumping lines. *Review of Scientific Instruments*, 49(6):765–769, 1978.

[54] Nicholas Cockton. Setup of dry cryostat for measurements on superconducting microwave resonators. Master's thesis, University of Waterloo, 2019.

[55] Stephen J Sarkozy, Kantimay Das Gupta, Francois Sfigakis, Harvey Beere, Ian Farrer, Ruth Harrell, Dave Ritchie, and Geb Jones. Overcoming contact hurdles for investigating lower dimensional structures in undoped heterostructures. *ECS Transactions*, 11(5):75, 2007.

[56] B Habib, E Tutuc, Sorin Melinte, M Shayegan, D Wasserman, SA Lyon, and R Winkler. Spin splitting in GaAs (100) two-dimensional holes. *Physical Review B*, 69(11):113311, 2004.

[57] Fabrizio Nichele, Atindra Nath Pal, Roland Winkler, Christian Gerl, Werner Wegscheider, Thomas Ihn, and Klaus Ensslin. Spin-orbit splitting and effective masses in p-type GaAs two-dimensional hole gases. *Physical Review B*, 89(8):081306, 2014.

[58] HL Stormer, Z Schlesinger, A Chang, DC Tsui, AC Gossard, and W Wiegmann. Energy structure and quantized Hall effect of two-dimensional holes. *Physical review letters*, 51(2):126, 1983.

[59] JP Eisenstein, HL Störmer, V Narayanamurti, AC Gossard, and W Wiegmann. Effect of inversion symmetry on the band structure of semiconductor heterostructures. *Physical review letters*, 53(27):2579, 1984.

[60] AD Wieck, E Batke, D Heitmann, JP Kotthaus, and E Bangert. Lifting of the spin degeneracy of hole subbands in a surface electric field on silicon. *Physical review letters*, 53(5):493, 1984.

[61] Jian Ping Lu, Jeng-Bang Yau, SP Shukla, M Shayegan, L Wissinger, Ulrich Rössler, and R Winkler. Tunable spin-splitting and spin-resolved ballistic transport in GaAs/AlGaAs two-dimensional holes. *Physical review letters*, 81(6):1282, 1998.

[62] SJ Papadakis, EP De Poortere, HC Manoharan, M Shayegan, and R Winkler. The effect of spin splitting on the metallic behavior of a two-dimensional system. *Science*, 283(5410):2056–2058, 1999.

[63] Peter T Coleridge, M Hayne, P Zawadzki, and Andrew S Sachrajda. Effective masses in high-mobility 2D electron gas structures. *Surface science*, 361:560–563, 1996.

[64] SA Studenikin, G Granger, A Kam, AS Sachrajda, ZR Wasilewski, and PJ Poole. Nonlinear magnetotransport phenomena in high-mobility two-dimensional electrons in InGaAs/InP and GaAs/AlGaAs. *Physical Review B*, 86(11):115309, 2012.

[65] B Grbić, C Ellenberger, T Ihn, K Ensslin, D Reuter, and AD Wieck. Magnetotransport in C-doped AlGaAs heterostructures. *Applied Physics Letters*, 85(12):2277–2279, 2004.

[66] K Hirakawa, Y Zhao, MB Santos, M Shayegan, and DC Tsui. Anomalous cyclotron-resonance line splitting of two-dimensional holes in (311)A $Al_xGa_{1-x}As$/GaAs heterojunctions. *Physical Review B*, 47(7):4076, 1993.

[67] BE Cole, JM Chamberlain, M Henini, T Cheng, W Batty, A Wittlin, JAAJ Perenboom, A Ardavan, A Polisski, and J Singleton. Cyclotron resonance in ultra-low-hole-density narrow p-type GaAs/(Al, Ga) As quantum wells. *Physical Review B*, 55(4):2503, 1997.

[68] H Zhu, K Lai, DC Tsui, SP Bayrakci, NP Ong, M Manfra, L Pfeiffer, and K West. Density and well width dependences of the effective mass of two-dimensional holes in (100) GaAs quantum wells measured using cyclotron resonance at microwave frequencies. *Solid state communications*, 141(9):510–513, 2007.

[69] W Pan, K Lai, SP Bayrakci, NP Ong, Daniel Chee Tsui, LN Pfeiffer, and KW West. Cyclotron resonance at microwave frequencies in two-dimensional hole system in AlGaAs/GaAs quantum wells. *Applied physics letters*, 83(17):3519–3521, 2003.

[70] Z Schlesinger, SJ Allen Jr, Y Yafet, AC Gossard, and W Wiegmann. Cyclotron resonance in the two-dimensional hole gas in (Ga, Al) As/GaAs heterostructures. *Physical Review B*, 32(8):5231, 1985.

[71] Graziella Scandurra, Gianluca Cannatà, and Carmine Ciofi. Differential ultra low noise amplifier for low frequency noise measurements. *AIP Advances*, 1(2), 2011.

[72] B Habib, Mansour Shayegan, and R Winkler. Spin-orbit interaction and transport in GaAs two-dimensional holes. *Semiconductor science and technology*, 24(6):064002, 2009.

[73] S Keppeler and R Winkler. Anomalous magneto-oscillations and spin precession. *Physical review letters*, 88(4):046401, 2002.

[74] Boris Grbić, Renaud Leturcq, Thomas Ihn, Klaus Ensslin, Dirk Reuter, and Andreas D Wieck. Strong spin-orbit interactions and weak antilocalization in carbon-doped p-type GaAs/Al_xGaAs_{1-x} heterostructures. *Physical Review B*, 77(12):125312, 2008.

[75] E Zaremba. Transverse magnetoresistance in quantum wells with multiple subband occupancy. *Physical Review B*, 45(24):14143, 1992.

[76] ZQ Yuan, RR Du, MJ Manfra, LN Pfeiffer, and KW West. Landau level spectrum in a two-dimensional hole gas in C-doped (100) GaAs/$Al_{0.4}Ga_{0.6}As$ square quantum well. *Applied Physics Letters*, 94(5), 2009.

[77] A Srinivasan, LA Yeoh, O Klochan, TP Martin, JCH Chen, AP Micolich, AR Hamilton, D Reuter, and AD Wieck. Using a tunable quantum wire to measure the large out-of-plane spin splitting of quasi two-dimensional holes in a GaAs nanostructure. *Nano letters*, 13(1):148–152, 2013.

[78] Fabrizio Nichele, Stefano Chesi, Szymon Hennel, Angela Wittmann, Christian Gerl, Werner Wegscheider, Daniel Loss, Thomas Ihn, and Klaus Ensslin. Characterization of spin-orbit interactions of GaAs heavy holes using a quantum point contact. *Physical Review Letters*, 113(4):046801, 2014.

[79] Yashar Komijani, Miklos Csontos, Ivan Shorubalko, Ulrich Zülicke, T Ihn, Klaus Ensslin, Dirk Reuter, and Andreas D Wieck. Anisotropic Zeeman shift in p-type GaAs quantum point contacts. *Europhysics Letters*, 102(3):37002, 2013.

[80] Elizabeth Marcellina, Ashwin Srinivasan, DS Miserev, AF Croxall, DA Ritchie, Ian Farrer, OP Sushkov, Dimitrie Culcer, and AR Hamilton. Electrical control of the zeeman spin splitting in two-dimensional hole systems. *Physical Review Letters*, 121(7):077701, 2018.

[81] MJ Rendell, SD Liles, A Srinivasan, O Klochan, I Farrer, DA Ritchie, and AR Hamilton. Gate voltage dependent Rashba spin splitting in hole transverse magnetic focusing. *Physical Review B*, 105(24):245305, 2022.

[82] AR Hamilton, MY Simmons, FM Bolton, NK Patel, IS Millard, JT Nicholls, DA Ritchie, and M Pepper. Fractional quantum Hall effect in bilayer two-dimensional hole-gas systems. *Physical Review B*, 54(8):R5259, 1996.

[83] JD Watson, S Mondal, GA Csáthy, MJ Manfra, EH Hwang, S Das Sarma, LN Pfeiffer, and KW West. Scattering mechanisms in a high-mobility low-density carbon-doped (100) GaAs two-dimensional hole system. *Physical Review B*, 83(24):241305, 2011.

[84] JD Watson, S Mondal, G Gardner, Gabor A Csathy, and Michael J Manfra. Exploration of the limits to mobility in two-dimensional hole systems in GaAs/AlGaAs quantum wells. *Physical Review B*, 85(16):165301, 2012.

[85] Yoon Jang Chung, C Wang, SK Singh, A Gupta, KW Baldwin, KW West, M Shayegan, LN Pfeiffer, and R Winkler. Record-quality GaAs two-dimensional hole systems. *Physical Review Materials*, 6(3):034005, 2022.

[86] S Peters, Lars Tiemann, Christian Reichl, and Werner Wegscheider. Gating versus doping: Quality parameters of two-dimensional electron systems in undoped and doped GaAs/AlGaAs heterostructures. *Physical Review B*, 94(4):045304, 2016.

[87] Thomas Tschirky, Susanne Mueller, Ch A Lehner, Stefan Fält, Thomas Ihn, Klaus Ensslin, and Werner Wegscheider. Scattering mechanisms of highest-mobility InAs/$Al_xGa_{1-x}Sb$ quantum wells. *Physical Review B*, 95(11):115304, 2017.

[88] R Winkler, H Noh, E Tutuc, and M Shayegan. Anomalous Rashba spin splitting in two-dimensional hole systems. *Physical Review B*, 65(15):155303, 2002.

[89] Patrick Del Vecchio, Mario Lodari, Amir Sammak, Giordano Scappucci, and Oussama Moutanabbir. Vanishing Zeeman energy in a two-dimensional hole gas. *Physical Review B*, 102(11):115304, 2020.

[90] M Lodari, A Tosato, D Sabbagh, MA Schubert, G Capellini, A Sammak, M Veldhorst, and G Scappucci. Light effective hole mass in undoped Ge/SiGe quantum wells. *Physical Review B*, 100(4):041304, 2019.

[91] V Yu, M Hilke, PJ Poole, S Studenikin, and DG Austing. Phase diagram of quantum Hall breakdown and nonlinear phenomena for InGaAs/InP quantum wells. *Physical Review B*, 98(16):165434, 2018.

[92] Victor Yu. *Breakdown of the quantum Hall effect in InGaAs/InP quantum wells.* PhD thesis, McGill University (Canada), 2017.

[93] C-T Liang, Yu-Ming Cheng, Tsai Yu Huang, CF Huang, MY Simmons, DA Ritchie, Gil-Ho Kim, JY Leem, YH Chang, and YF Chen. Quantum magneto-transport in two-dimensional GaAs electron gases and SiGe hole gases. *Journal of Physics and Chemistry of Solids*, 62(9-10):1789–1796, 2001.

[94] Ikai Lo, WC Mitchel, RE Perrin, RL Messham, and MY Yen. Two-dimensional electron gas in GaAs/$Al_{1-x}Ga_xAs$ heterostructures: Effective mass. *Physical Review B*, 43(14):11787, 1991.

[95] HW Van Kesteren, EC Cosman, WAJA Van der Poel, and CT Foxon. Fine structure of excitons in type-ii GaAs/AlAs quantum wells. *Physical Review B*, 41(8):5283, 1990.

[96] VF Sapega, M Cardona, K Ploog, EL Ivchenko, and DN Mirlin. Spin-flip Raman scattering in GaAs/$Al_xGa_{1-x}As$ multiple quantum wells. *Physical Review B*, 45(8):4320, 1992.

[97] S Glasberg, Hadas Shtrikman, and Israel Bar-Joseph. Photoluminescence of a low-density two-dimensional hole gas in a GaAs quantum well: observation of valence-band Landau levels. *Physical Review B*, 63(20):201308, 2001.

[98] Yu G Sadofyev, A Ramamoorthy, B Naser, JP Bird, Shane R Johnson, and Y-H Zhang. Large g-factor enhancement in high-mobility InAs/AlSb quantum wells. *Applied physics letters*, 81(10):1833–1835, 2002.

[99] R Winkler, SJ Papadakis, EP De Poortere, and M Shayegan. Highly anisotropic g-factor of two-dimensional hole systems. *Physical review letters*, 85(21):4574, 2000.

[100] CL Yang, J Zhang, RR Du, JA Simmons, and JL Reno. Zener tunneling between Landau orbits in a high-mobility two-dimensional electron gas. *Physical review letters*, 89(7):076801, 2002.

[101] N Romero Kalmanovitz, AA Bykov, Sergey Vitkalov, and AI Toropov. Warming in systems with a discrete spectrum: Spectral diffusion of two-dimensional electrons in a magnetic field. *Physical Review B*, 78(8):085306, 2008.

[102] Zhenbing Tan, Changling Tan, Li Ma, GT Liu, L Lu, and CL Yang. Shubnikov-de Haas oscillations of a single layer graphene under dc current bias. *Physical Review B*, 84(11):115429, 2011.

[103] M Kawamura, H Takahashi, K Sugihara, S Masubuchi, K Hamaya, and T Machida. Electrical polarization of nuclear spins in a breakdown regime of quantum Hall effect. *Applied physics letters*, 90(2):022102, 2007.

[104] Minoru Kawamura, Kimitoshi Kono, Yoshiaki Hashimoto, Shingo Katsumoto, and Tomoki Machida. Spatial gradient of dynamic nuclear spin polarization induced by breakdown of the quantum Hall effect. *Physical Review B*, 83(4):041305, 2011.

[105] L Eaves. Quantum Hall effect breakdown steps: evidence for an instability induced by inter-Landau level scattering. *Physica B: Condensed Matter*, 298(1-4):1–7, 2001.

[106] L Eaves. An eddy viscosity model of the dissipative voltage steps in quantum Hall effect breakdown. *Physica E: Low-dimensional Systems and Nanostructures*, 9(1):45–53, 2001.

[107] JC Chen, Yuling Tsai, Yiping Lin, T Ueda, and S Komiyama. Negative differential conductivity of two-dimensional electron-gas systems in high magnetic fields. *Physical Review B*, 79(7):075308, 2009.

[108] Ching-Ping Lee, CC Chi, and Jeng-Chung Chen. Electric instability in a two-dimensional electron gas system under high magnetic fields. *Physical Review B*, 92(19):195410, 2015.

[109] G Nachtwei. Breakdown of the quantum Hall effect. *Physica E: Low-dimensional Systems and Nanostructures*, 4(2):79–101, 1999.

[110] G Eber, K Von Klitzing, K Ploog, and G Weinmann. Two-dimensional magneto-quantum transport on GaAs-$Al_xGa_{1-x}As$ heterostructures under non-ohmic conditions. *Journal of Physics C: Solid State Physics*, 16(28):5441, 1983.

[111] K v Klitzing, Gerhard Dorda, and Michael Pepper. New method for high-accuracy determination of the fine-structure constant based on quantized Hall resistance. *Physical review letters*, 45(6):494, 1980.

[112] F Kuchar, G Bauer, G Weimann, and H Burkhard. Non-equilibrium behaviour of the two-dimensional electron gas in the quantized Hall resistance regime of GaAs/$Al_{0.3}Ga_{0.7}As$. *Surface Science*, 142(1-3):196–202, 1984.

[113] S Komiyama, T Takamasu, S Hiyamizu, and S Sasa. Breakdown of the quantum Hall effect due to electron heating. *Solid state communications*, 54(6):479–484, 1985.

[114] H Iizuka, S Kawaji, and T Okamoto. Collapse of quantized Hall resistance and breakdown of dissipationless state in the integer quantum Hall effect: filling factor dependence. *Physica E: Low-dimensional Systems and Nanostructures*, 6(1-4):132–135, 2000.

[115] Beat Jeckelmann and Blaise Jeanneret. The quantum Hall effect as an electrical resistance standard. *Reports on Progress in Physics*, 64(12):1603, 2001.

[116] Beat Jeckelmann, A Rufenacht, Blaise Jeanneret, Frédéric Overney, Klaus Pierz, Aurel von Campenhausen, and Günter Hein. Optimization of qhe-devices for metrological applications. *IEEE Transactions on Instrumentation and Measurement*, 50(2):218–222, 2001.

[117] S Kawaji. Breakdown of the integer quantum Hall effect at high currents in GaAs/AlGaAs heterostructures. *Semiconductor Science and Technology*, 11(11S):1546, 1996.

[118] G Ebert, K Von Klitzing, C Probst, E Schuberth, K Ploog, and G Weimann. Hopping conduction in the landau level tails in gaas-alxga1-xas heterostructures at low temperatures. *Solid State Communications*, 45(7):625–628, 1983.

[119] O Makarovsky, A Neumann, LA Dickinson, L Eaves, PC Main, M Henini, S Thoms, and CDW Wilkinson. Quantum Hall effect breakdown: can the bootstrap heating and inter-Landau-level scattering models be reconciled? *Physica E: Low-dimensional Systems and Nanostructures*, 12(1-4):178–181, 2002.

[120] JA Alexander-Webber, AMR Baker, Philip Derek Buckle, T Ashley, and RJ Nicholas. High-current breakdown of the quantum Hall effect and electron heating in InSb/AlInSb. *Physical Review B*, 86(4):045404, 2012.

[121] ME Cage, RF Dziuba, BF Field, ER Williams, SM Girvin, AC Gossard, DC Tsui, and RJ Wagner. Dissipation and dynamic nonlinear behavior in the quantum Hall regime. *Physical review letters*, 51(15):1374, 1983.

[122] L Bliek, E Braun, G Hein, V Kose, J Niemeyer, G Weimann, and W Schlapp. Critical current density for the dissipationless quantum Hall effect. *Semiconductor science and technology*, 1(2):110, 1986.

[123] RJ Haug, K von Klitzing, and K Ploog. High Magnetic Fields in Semicond. Physics II. In *Springer Series in Solid-State Sciences*, volume 87, page 185. Springer Berlin, 1989.

[124] Marvin E Cage, G Marullo Reedtz, DY Yu, and CT Van Degrift. Quantised dissipative states at breakdown of the quantum Hall effect. *Semiconductor science and technology*, 5(4):351, 1990.

[125] Marvin E Cage. Dependence of quantized Hall effect breakdown voltage on magnetic field and current. *Journal of research of the National Institute of Standards and Technology*, 98(3):361, 1993.

[126] L Bliek, G Hein, V Kose, J Niemeyer, G Weimann, and W Schlapp. A New Quantum Effect in the Transverse Magnetoresistance of Two-Dimensional Conductors with a Narrow Constriction in the Conducting Channel. In *High Magnetic Fields in Semiconductor Physics: Proceedings of the International Conference, Würzburg, Fed. Rep. of Germany, August 18–22, 1986*, pages 113–117. Springer, 1987.

[127] AS Sachrajda, D Landheer, R Boulet, and T Moore. Evidence for an inhomogeneity size effect in narrow GaAs/$Al_xGa_{1-x}As$ constrictions. *Physical Review B*, 39(14):10460, 1989.

[128] L Eaves and FW Sheard. Size-dependent quantised breakdown of the dissipationless quantum Hall effect in narrow channels. *Semiconductor science and technology*, 1(6):346, 1986.

[129] RG Mani and JR Anderson. Inhomogeneous broadening and the breakdown of the quantum Hall effect in GaAs/AlGaAs. *Solid state communications*, 72(9):949–954, 1989.

[130] L Eaves, ST Stoddart, R Wirtz, AC Neumann, BL Gallagher, PC Main, and M Henini. Quantum Hall effect breakdown in two-dimensional hole gases. *Physica E: Low-dimensional Systems and Nanostructures*, 6(1-4):136–139, 2000.

[131] L Eaves. Quantum Hall effect breakdown: analogies with fluid dynamics. *Physica B: Condensed Matter*, 256:47–51, 1998.

[132] AM Martin, KA Benedict, FW Sheard, and L Eaves. Model for breakdown of laminar flow of a quantum Hall fluid around a charged impurity: comparison with experiment. *Physica E: Low-dimensional Systems and Nanostructures*, 22(1-3):205–209, 2004.

[133] P Streda and K Von Klitzing. Critical non-dissipative current of quantum Hall regime. *Journal of Physics C: Solid State Physics*, 17(19):L483, 1984.

[134] V Tsemekhman, K Tsemekhman, C Wexler, JH Han, and DJ Thouless. Theory of the breakdown of the quantum Hall effect. *Physical Review B*, 55(16):R10201, 1997.

[135] Susumu Komiyama and Yasushi Kawaguchi. Heat instability of quantum Hall conductors. *Physical Review B*, 61(3):2014, 2000.

[136] G Nachtwei, A Manolescu, N Nestle, and H Künzel. Bistable resistance switching in a ferromagnetic quantum Hall system induced by exchange enhancement of the Zeeman energy. *Physical Review B*, 63(4):045306, 2000.

[137] G Nachtwei, A Manolescu, N Nestle, and H Künzel. Ferromagnetism in a quantum Hall system due to exchange enhancement in a GaInAs quantum well. *Physica E: Low-dimensional Systems and Nanostructures*, 12(1-4):20–23, 2002.

[138] Y Hirayama, G Yusa, K Hashimoto, N Kumada, T Ota, and K Muraki. Electron-spin/nuclear-spin interactions and NMR in semiconductors. *Semiconductor science and technology*, 24(2):023001, 2009.

[139] Jason R Petta, Alexander Comstock Johnson, Jacob M Taylor, Edward A Laird, Amir Yacoby, Mikhail D Lukin, Charles M Marcus, Micah P Hanson, and Arthur C Gossard. Coherent manipulation of coupled electron spins in semiconductor quantum dots. *Science*, 309(5744):2180–2184, 2005.

[140] Ronald Hanson, Leo P Kouwenhoven, Jason R Petta, Seigo Tarucha, and Lieven MK Vandersypen. Spins in few-electron quantum dots. *Reviews of modern physics*, 79(4):1217, 2007.

[141] Jonathan H Prechtel, Andreas V Kuhlmann, Julien Houel, Arne Ludwig, Sascha R Valentin, Andreas D Wieck, and Richard J Warburton. Decoupling a hole spin qubit from the nuclear spins. *Nature materials*, 15(9):981–986, 2016.

[142] Jing Qiao Zhang, Sergey Vitkalov, and AA Bykov. Nonlinear resistance of two-dimensional electrons in crossed electric and magnetic fields. *Physical Review B*, 80(4):045310, 2009.

[143] Scott Dietrich, Sean Byrnes, Sergey Vitkalov, DV Dmitriev, and AA Bykov. Quantum oscillations of dissipative resistance in crossed electric and magnetic fields. *Physical Review B*, 85(15):155307, 2012.

[144] ZT Wang, Michael Hilke, Norm Fong, DG Austing, SA Studenikin, KW West, and LN Pfeiffer. Nonlinear transport phenomena and current-induced hydrodynamics in ultrahigh mobility two-dimensional electron gas. *Physical Review B*, 107(19):195406, 2023.

[145] Ivan A Dmitriev. Nonequilibrium magnetooscillations in spatially non-uniform quantum Hall systems. In *Journal of Physics: Conference Series*, volume 334, page 012015. IOP Publishing, 2011.

[146] Sergey Vitkalov. Nonlinear transport of 2D electrons in crossed electric and quantizing magnetic fields. *International Journal of Modern Physics B*, 23(23):4727–4753, 2009.

[147] Yanhua Dai, ZQ Yuan, CL Yang, RR Du, MJ Manfra, LN Pfeiffer, and KW West. Magnetotransport in Zener tunneling regime in a high-mobility two-dimensional hole gas. *Physical Review B*, 80(4):041310, 2009.

[148] Q Shi, QA Ebner, and MA Zudov. Hall field-induced resistance oscillations in a p-type Ge/SiGe quantum well. *Physical Review B*, 90(16):161301, 2014.

[149] MA Zudov, OA Mironov, QA Ebner, PD Martin, Q Shi, and David R Leadley. Observation of microwave-induced resistance oscillations in a high-mobility two-dimensional hole gas in a strained Ge/SiGe quantum well. *Physical Review B*, 89(12):125401, 2014.

[150] Tsai-Yu Huang, Chi-Te Liang, Yang Fang Chen, Michelle Y Simmons, Gil-Ho Kim, and David A Ritchie. Direct measurement of the spin gaps in a gated gaas two-dimensional electron gas. *Nanoscale research letters*, 8:1–6, 2013.

[151] Peter W Shor. Algorithms for quantum computation: discrete logarithms and factoring. In *Proceedings 35th annual symposium on foundations of computer science*, pages 124–134. Ieee, 1994.

[152] Lov K Grover. A fast quantum mechanical algorithm for database search. In *Proceedings of the twenty-eighth annual ACM symposium on Theory of computing*, pages 212–219, 1996.

[153] Hartmut Häffner, Christian F Roos, and Rainer Blatt. Quantum computing with trapped ions. *Physics reports*, 469(4):155–203, 2008.

[154] John Clarke and Frank K Wilhelm. Superconducting quantum bits. *Nature*, 453(7198):1031–1042, 2008.

[155] Christoph Kloeffel and Daniel Loss. Prospects for spin-based quantum computing in quantum dots. *Annu. Rev. Condens. Matter Phys.*, 4(1):51–81, 2013.

[156] JM Elzerman, R Hanson, LH Willems van Beveren, B Witkamp, LMK Vandersypen, and Leo P Kouwenhoven. Single-shot read-out of an individual electron spin in a quantum dot. *nature*, 430(6998):431–435, 2004.

[157] R Hanson, LH Willems van Beveren, IT Vink, JM Elzerman, WJM Naber, FHL Koppens, LP Kouwenhoven, and LMK Vandersypen. Single-shot readout of electron spin states in a quantum dot using spin-dependent tunnel rates. *Physical review letters*, 94(19):196802, 2005.

[158] M Field, CG Smith, Michael Pepper, DA Ritchie, JEF Frost, GAC Jones, and DG Hasko. Measurements of Coulomb blockade with a noninvasive voltage probe. *Physical review letters*, 70(9):1311, 1993.

[159] Jeffrey Mason. *RF-QPC Charge Detector and S-T_+ Qubit in a Lateral Double Quantum Dot Device*. PhD thesis, University of Waterloo, 2017.

[160] Christian Barthel, Morten Kjærgaard, J Medford, Michael Stopa, Charles Masamed Marcus, MP Hanson, and Arthur C Gossard. Fast sensing of double-dot charge arrangement and spin state with a radio-frequency sensor quantum dot. *Physical Review B*, 81(16):161308, 2010.

[161] Leif Roschier, P Hakonen, Kevin Bladh, Per Delsing, KW Lehnert, Lafe Spietz, and RJ Schoelkopf. Noise performance of the radio-frequency single-electron transistor. *Journal of applied physics*, 95(3):1274–1286, 2004.

[162] DJ Reilly, CM Marcus, MP Hanson, and AC Gossard. Fast single-charge sensing with a rf quantum point contact. *Applied Physics Letters*, 91(16), 2007.

[163] MC Cassidy, AS Dzurak, RG Clark, KD Petersson, I Farrer, DA Ritchie, and CG Smith. Single shot charge detection using a radio-frequency quantum point contact. *Applied Physics Letters*, 91(22), 2007.

[164] RJ Schoelkopf, P Wahlgren, AA Kozhevnikov, P Delsing, and DE Prober. The radio-frequency single-electron transistor (RF-SET): A fast and ultrasensitive electrometer. *science*, 280(5367):1238–1242, 1998.

[165] Julie Helen Love. *Resolved dynamics of single electron tunneling using the RF-SET*. PhD thesis, Yale University, 2007.

[166] John Daniel Teufel. *Superconducting tunnel junctions as direct detectors for submillimeter astronomy*. PhD thesis, Yale University, 2008.

[167] David M Pozar. *Microwave engineering*. John wiley & sons, 2011.

[168] Florian Vigneau, Federico Fedele, Anasua Chatterjee, David Reilly, Ferdinand Kuemmeth, M Fernando Gonzalez-Zalba, Edward Laird, and Natalia Ares. Probing quantum devices with radio-frequency reflectometry. *Applied Physics Reviews*, 10(2), 2023.

[169] Jose Aumentado. Superconducting parametric amplifiers: The state of the art in Josephson parametric amplifiers. *IEEE Microwave magazine*, 21(8):45–59, 2020.

[170] Michael Mück and Robert McDermott. Radio-frequency amplifiers based on dc SQUIDs. *Superconductor Science and Technology*, 23(9):093001, 2010.

[171] JM Elzerman, R Hanson, JS Greidanus, LH Willems Van Beveren, S De Franceschi, LMK Vandersypen, S Tarucha, and LP Kouwenhoven. Few-electron quantum dot circuit with integrated charge read out. *Physical Review B*, 67(16):161308, 2003.

[172] LMK Vandersypen, JM Elzerman, RN Schouten, LH Willems van Beveren, R Hanson, and LP Kouwenhoven. Real-time detection of single-electron tunneling using a quantum point contact. *Applied Physics Letters*, 85(19):4394–4396, 2004.

[173] Michael Mück. ez squid. http://www.ez-squid.de/Home.htm. Accessed: 2023-06-30.

[174] MP DeFeo and BLT Plourde. Superconducting microstrip amplifiers with sub-Kelvin noise temperature near 4 ghz. *Applied Physics Letters*, 101(5):052603, 2012.

[175] Yutian Wen, N Ares, FJ Schupp, T Pei, GAD Briggs, and EA Laird. A coherent nanomechanical oscillator driven by single-electron tunnelling. *Nature physics*, 16(1):75–82, 2020.

[176] Matthew A Morgan and Tod A Boyd. Reflectionless filter structures. *IEEE Transactions on Microwave Theory and Techniques*, 63(4):1263–1271, 2015.

[177] Leonardo Ranzani, Lafe Spietz, and José Aumentado. Broadband calibrated scattering parameters characterization of a superconducting quantum interference device amplifier. *Applied Physics Letters*, 103(2), 2013.

[178] Leonardo Ranzani, Lafe Spietz, Zoya Popovic, and Jose Aumentado. A 4: 1 transmission-line impedance transformer for broadband superconducting circuits. *IEEE transactions on applied superconductivity*, 22(5):1500606–1500606, 2012.

[179] FJ Schupp, F Vigneau, Yutian Wen, A Mavalankar, J Griffiths, GAC Jones, I Farrer, DA Ritchie, CG Smith, LC Camenzind, et al. Sensitive radiofrequency readout of quantum dots using an ultra-low-noise SQUID amplifier. *Journal of Applied Physics*, 127(24), 2020.

[180] VA Khlus. Current and voltage fluctuations in microjunctions between normal metals and superconductors. *Zh. Eksp. Teor. Fiz*, 93:2179, 1987.

[181] GB Lesovik. Excess quantum noise in 2D ballistic point contacts. *Soviet Journal of Experimental and Theoretical Physics Letters*, 49:592, 1989.

[182] A Aassime, D Gunnarsson, K Bladh, P Delsing, and R Schoelkopf. Radio-frequency single-electron transistor: Toward the shot-noise limit. *Applied physics letters*, 79(24):4031–4033, 2001.

[183] Thomas Müller, Bruno Küng, S Hellmüller, P Studerus, Klaus Ensslin, Thomas Ihn, Matthias Reinwald, and Werner Wegscheider. An in situ tunable radio-frequency quantum point contact. *Applied Physics Letters*, 97(20), 2010.

Appendix A

Fourier analysis of the SdH oscillations

This section presents the details of the Fourier analysis employed to isolate the frequencies within the Shubnikov-de Hass (SdH) oscillations. In the context of a single degenerate subband in transport, the SdH oscillations exhibit periodicity as a function of the inverse magnetic field (1/B). The subband population can be derived from the oscillation frequency via the relation $p = f \cdot e/h$. Given the presence of a beating pattern in the SdH oscillations within our GaAs 2DHGs, we conducted Fourier analysis to isolate the individual subband densities. The Fourier analysis was performed using the fast Fourier transform (FFT) algorithm within the *SciPy* package in Python.

The SdH oscillations are collected by slowing sweeping the magnetic field at a rate of 0.5 T/hour and measuring the longitudinal voltage V_{xx} across the Hall bar. An example of such oscillations are shown in Fig. A.1a, where the B-field was swept from 0.1 T to 0.7 T. The SdH oscillations in B (11,374 points from 0.1 T to 0.7 T) are converted to 1/B, where the spacing between points is unequal. The FFT algorithm requires the data be equally spaced. To obtain equally spaced data in 1/B, the data is interpolated using a cubic spline to 50,000 points. The Fourier transform of the interpolated oscillations is shown in Fig. A.1b. A large peak at zero frequency (dc term) is present from the finite background of the oscillations ($\sim$ 50 Ω). The slowly varying background is captured by fitting the interpolated data to a six

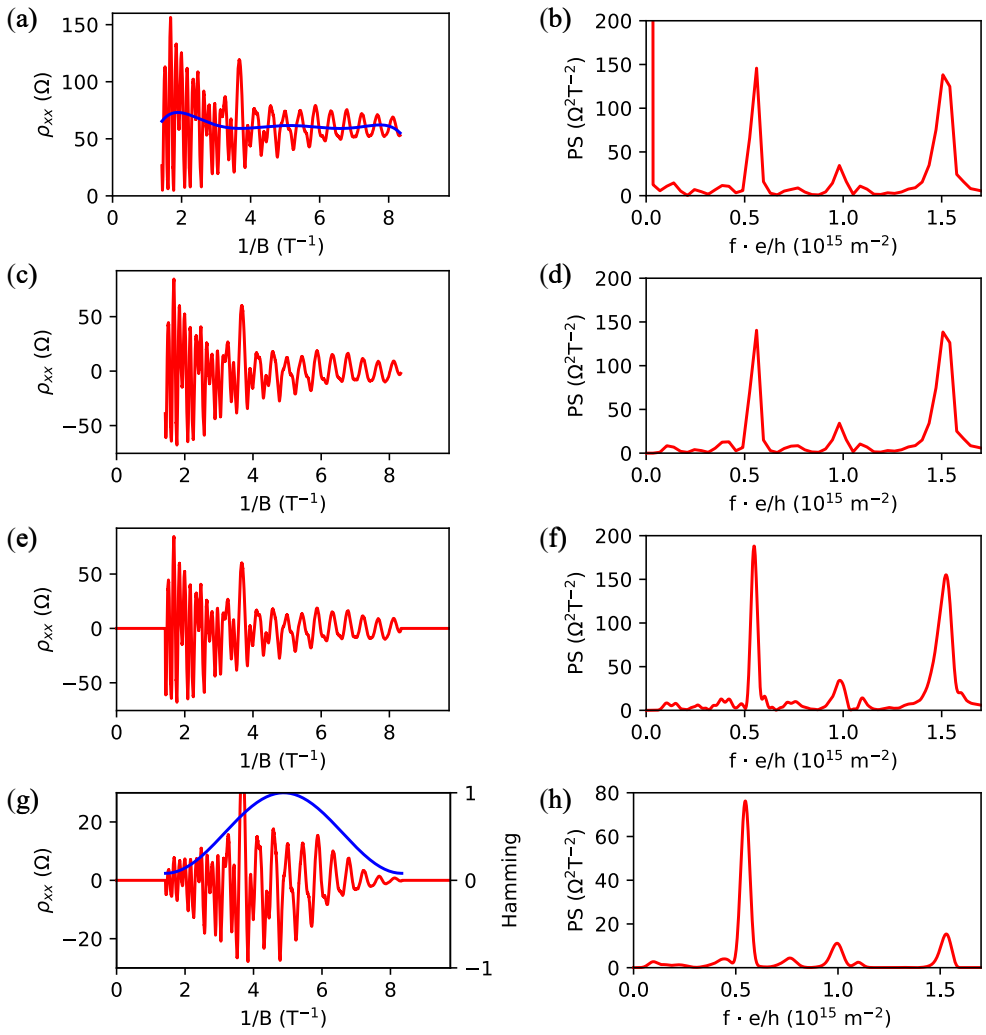


Figure A.1: Preparation of the Shubnikov-de Haas (SdH) oscillations for the fast Fourier transform (FFT) algorithm. (a) Raw data with six order polynomial fit (blue trace). (b) Power spectrum (PS) of the raw data in panel (a) with no operations applied. (c) Raw data in panel (a) subtracted from the polynomial fit. (c) Power spectrum of data in panel (c). (e) Zero-padded data in panel (c). (f) Power spectrum of data in panel (e). (g) Data in panel (e) after multiplication with a Hamming window (blue trace). (h) Power spectrum of data in panel (g), with all operations applied (background subtraction, zero-padding, multiplication with Hamming window.

order polynomial (blue trace in Fig. A.1b). The background of the oscillations is removed by subtracting the interpolated data from the polynomial fit, and is shown in Fig. A.1c. The corresponding Fourier transform is shown in Fig. A.1d. We further enhanced our analysis by extending the SdH oscillations in 1/B symmetrically with zeros, as shown in Fig. A.1e. This zero-padding approach refines the transformed data interpolation without actually increasing the frequency resolution. It's especially beneficial when analyzing a dataset with limited number of oscillations, facilitating a more accurate estimation of the amplitude of the peaks in the spectrum. To ensure a smoother power spectrum, we padded our 50,000 data points symmetrically with an additional 500,000 zeros. When the FFT algorithm encounters a dataset lacking an integer number of periods, spectral leakage can occur. This results in the true frequency's energy in the power spectrum seeming to "leak" into adjacent frequencies. To mitigate this, we can diminish the abrupt discontinuity at the boundaries with a windowing function. One popular choice for spectral analysis is the Hamming window, defined by

$$w(n) = 0.54 - 0.46\cos\left(\frac{2\pi n}{N}\right) \tag{A.1}$$

Where $0 \leq n \leq N$. Fig. A.1g shows the Hamming window (blue trace) and the multiplication by the SdH oscillations. Finally, Fig. A.1h shows the transformed data in Fig. A.1g with all operations applied to the SdH oscillations: background subtraction, zero-padding, and multiplication by a Hamming window.

Appendix B

Extended data

B.1 Effective mass analysis at other hole densities

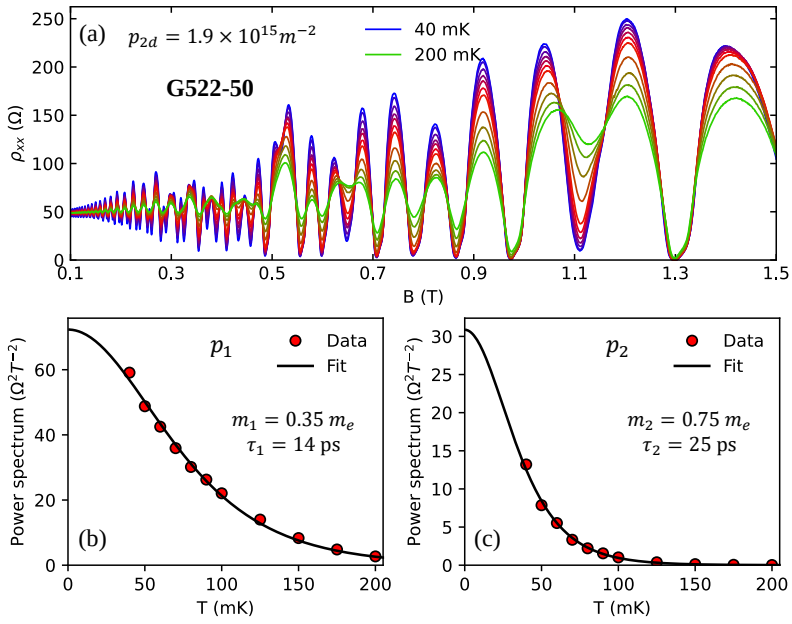


Figure B.1: Extension of Sec.4.3.7. (a) Temperature-dependence of the SdH oscillations at $p_{2d} = 1.9 \times 10^{15}$ m^{-2}. FT peak heights of (b) p_1 and (c) p_2 fitted to Eq. 4.1.

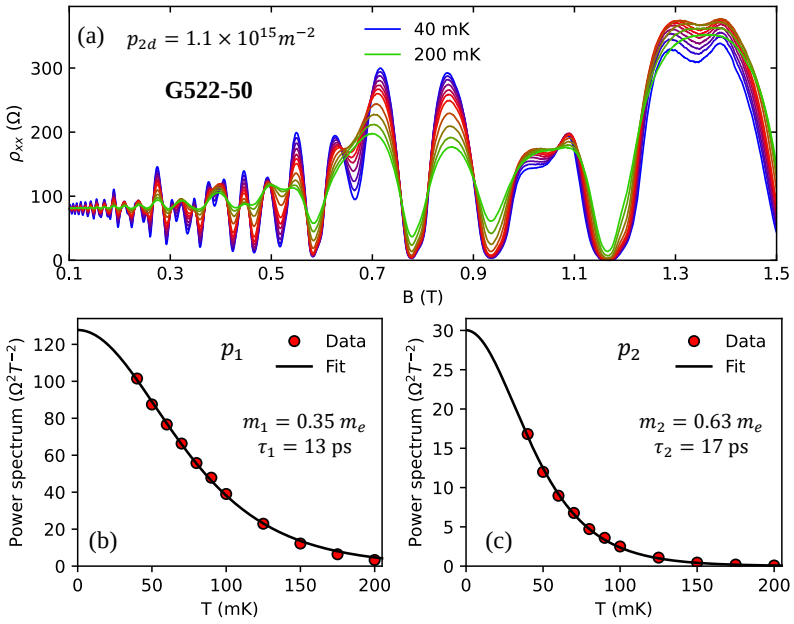


Figure B.2: Same as Fig.B.1 but at $p_{2d} = 1.1 \times 10^{15}$ m^{-2}.

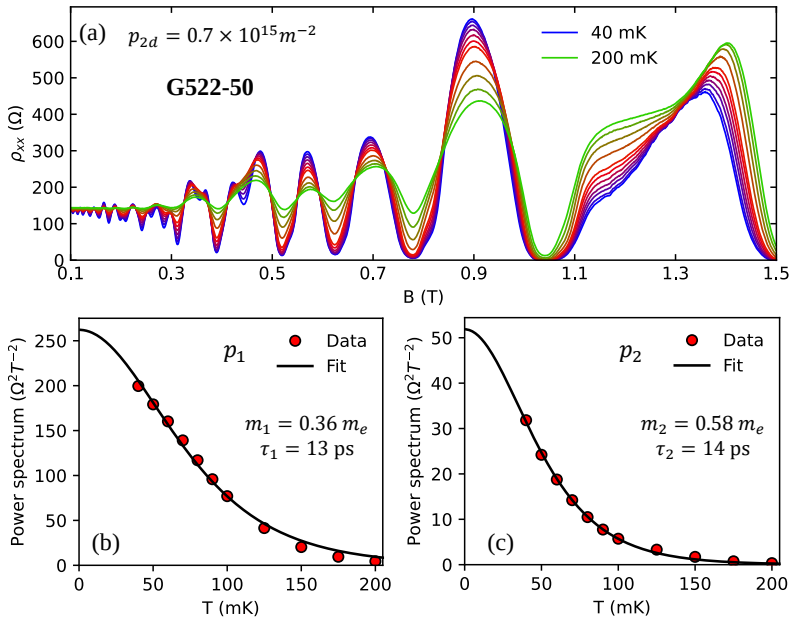


Figure B.3: Same as Fig.B.1 but at $p_{2d} = 0.7 \times 10^{15}$ m^{-2}.

B.2 Activation energies at other hole densities

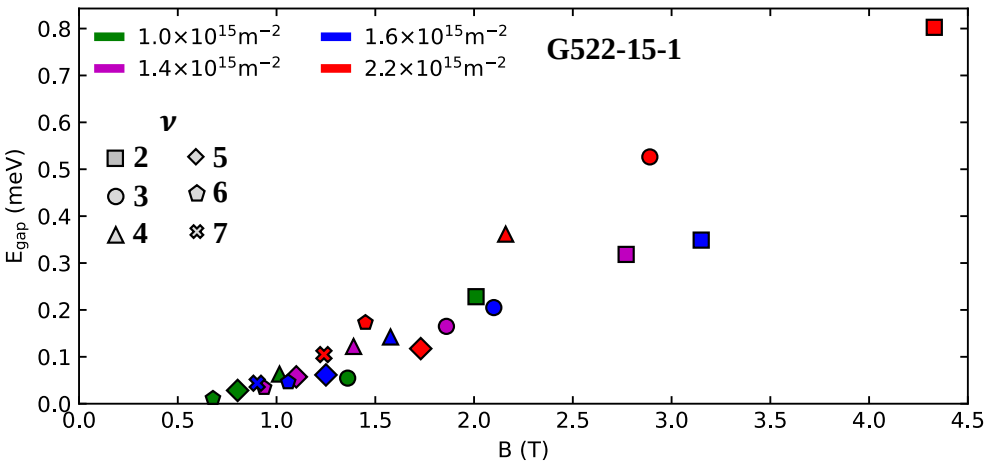


Figure B.4: Extension of Sec.4.3.10. Energy gaps E_{gap} as a function of B-field at different hole densities and filling factors. E_{gap} is extracted from temperature-dependence of ρ_{xx} minima, from an Arrhenius plot of $\rho_{xx} \sim \exp(\mathrm{E_{gap}}/2\mathrm{k_B T})$.

B.3 Temperature dependence of the low B-field positive magnetoresistance

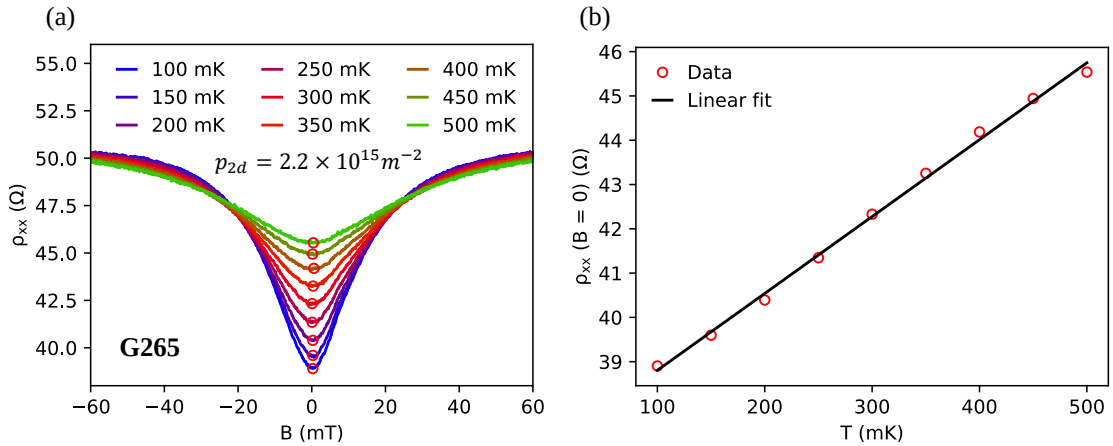


Figure B.5: (a) Low B-field magnetoresistance (ρ_{xx}) as a function of temperature. The positive magnetoresistance in ρ_{xx} is consistent with classical two-subband transport [19].(b) $\rho_{xx}(B = 0)$ as a function of temperature. The solid line is a least-squares linear fit of the data.

Appendix C

RF-QPC readout noise temperature and power dependence

C.1 RF-QPC noise temperature

Here, we outline the shot noise measurement used to evaluate the RF-QPC readout noise temperature, denoted as T_N. T_N is a sum of all noise contributions from thermal noise, instrumentation noise, and gate voltage noise. Electrical shot noise arises from the discrete nature of electric charge and follows a Poissonian process. For an average current I flowing through a device, the Schottky expression for the spectral density of shot noise is given by $S_P = 2eI$. The Poisson value of shot noise, represented as S_P, is a classical result that doesn't account for the fact that electrons obey Fermi-Dirac statistics. When quantum statistics are considered, the noise is suppressed relative to its Poisson value by the Fano factor η. For the specific case of a QPC constriction with a conductance of $G = (1 - \eta)(2e^2/h)$, the degree of suppression of shot noise from the Poissonian value is given by $S = 2eI\eta$ [180, 181], where $0 \leq \eta \leq 1$.

Following Refs. [163, 159], the system noise temperature of the RF-QPC readout is estimated by measuring the shot noise of the QPC as a function of the source-drain bias,

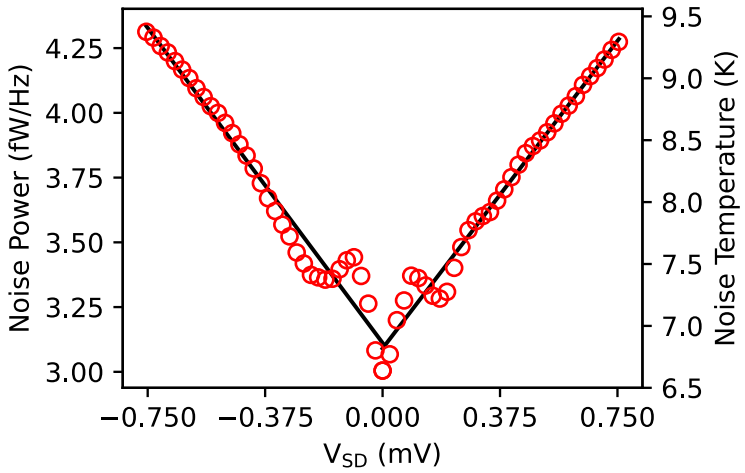


Figure C.1: Noise power per unit bandwidth of the RF-QPC readout as a function of V_{SD} across the QPC. The QPC conductance is set to 0.4 $\times 2e^2/h$ ($\eta = 0.6$). Red circles are data points and solid lines are linear fits. The right-axis is the total system noise temperature, which includes the shot noise contribution. Using the extracted slope and intercept, the intrinsic noise temperature of the rf readout ($V_{SD} = 0$) is approximately 6.6 K.

V_{SD}. The output noise power per unit bandwidth as a function of V_{SD} is given by [182]

$$P/B = Ak_BT_N + \frac{1}{2}Ae\eta|V_{SD}| \tag{C.1}$$

where A represents the total system gain (linear power ratio), B is the bandwidth (Hz), k_B is the Boltzmann constant, and e is the elementary charge. Fig. C.1 shows the noise power per unit bandwidth as a function of V_{SD}, collected using a spectrum analyzer at the RF-QPC readout frequency (143 MHz). The spectrum analyzer was configured with a resolution bandwidth of 1 MHz, and the 'MKNOISE' function was employed to convert the noise to a 1 Hz bandwidth. The QPC conductance was set to $G = 0.4(2e^2/h)$, corresponding to $\eta = 0.6$. For small source-drain biases $|V_{SD}| \lesssim 0.25$ mV, non-linear behaviour was observed, the origin of which is not understood. Nonetheless, we applied a linear fits to the data, for positive and negative V_{SD}, as indicated by the solid lines. The linear fit yields a gain of $A = 3.16 \times 10^7$ or 75 dB, which is expected from the components (net amplification) in the RF-QPC readout. Utilizing this gain value, the intrinsic system noise

temperature ($V_{SD} = 0$) is estimated to be approximately 6.6 K (as shown on the right-axis of Fig. C.1).

Treating the readout as a three stage amplifier chain, a value of T_N can be calculated from the following expression

$$T_N = (L-1)T_{phys} + LT_{n1} + \frac{LT_{n2}}{A_1} \tag{C.2}$$

The first stage considers the net attenuation and average physical temperature between the QPC and the first stage cryogenic amplifier. We estimate this attenuation to be L = 1.26 (1 dB). As an upper bound, we can set $T_{phys} = 2.8$ K, the temperature of the PTR 2nd stage where the cryogenic amplifier is mounted. The second stage is the cryogenic semiconductor amplifier, with a gain of 37 dB ($A_1 = 5012$) and noise temperature of $T_{n1} = 2.3$ K at 150 MHz. The room temperature Mini-Circuit amplifiers are the third stage and have an equivalent noise temperature of $T_{n2} = 35.5$ K. Substituting these values into Eq. C.2, we get $T_N = 3.6$ K. The higher T_N obtained from the shot noise measurement is consistent with the result in Ref. [159].

C.2 RF-QPC power dependence

Fig. C.2 shows the signal-to-noise ratio (SNR) of the lower sideband (LSB) as a function of carrier power. The measurement was collected using a spectrum analyzer with R_{QPC} = 59 kΩ, where the optimal sensitivity of the RF-QPC was determined (see Sec. 6.3.4). The LSB is generated with a 1 mV_{rms}, 1 MHz sine wave applied to gate RP. The solid line represents a linear fit applied to the data for a carrier power less than -85 dBm. For carrier powers greater than -80 dBm, the SNR is no longer linear with carrier power. A similar result was found in Ref. [159] for carrier powers greater than -75 dBm. The non-linearity at high carrier power is attributed by heating effects which flattens the QPC resistance curve [183].

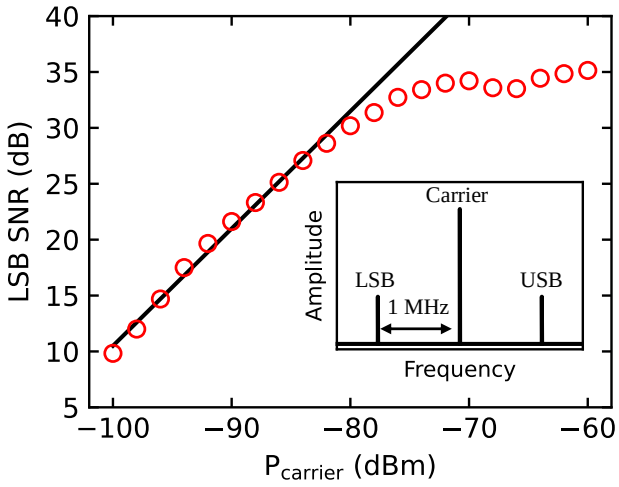


Figure C.2: SNR of the LSB as a function of $P_{carrier}$ measured with a spectrum analyzer. The resolution bandwidth on the spectrum analyzer was set to 300 Hz. Inset: Simulated example of a power spectrum as a function of frequency for amplitude modulated carrier.